



**HAL**  
open science

# Microscopie de surface multimodale appliquée aux technologies pour la santé

Amanda Gomes de Carvalho

► **To cite this version:**

Amanda Gomes de Carvalho. Microscopie de surface multimodale appliquée aux technologies pour la santé. Chimie analytique. Université Paris sciences et lettres, 2021. Français. NNT : 2021UPSLC008 . tel-03956169

**HAL Id: tel-03956169**

**<https://pastel.hal.science/tel-03956169>**

Submitted on 25 Jan 2023

**HAL** is a multi-disciplinary open access archive for the deposit and dissemination of scientific research documents, whether they are published or not. The documents may come from teaching and research institutions in France or abroad, or from public or private research centers.

L'archive ouverte pluridisciplinaire **HAL**, est destinée au dépôt et à la diffusion de documents scientifiques de niveau recherche, publiés ou non, émanant des établissements d'enseignement et de recherche français ou étrangers, des laboratoires publics ou privés.

**THÈSE DE DOCTORAT**  
DE L'UNIVERSITÉ PSL

Préparée à l'Ecole Nationale Supérieure de Chimie de Paris

# Multimodal surface microscopy applied to healthcare technologies

Soutenue par

**Amanda GOMES DE  
CARVALHO**

Le 30 Septembre 2021

Ecole doctorale n° 388

**Chimie Physique et Chimie  
Analytique de Paris Centre**

Spécialité

**Chimie Analytique**



ParisTech

Composition du jury :

Vincent, SEMETEY DR CNRS, Chimie ParisTech	<i>Président</i>
Christine, DUPONT Professeure, Univ. Louvain-La-Neuve, B	<i>Rapporteuse</i>
Didier, LEONARD Professeur, Université de Lyon 1	<i>Rapporteur</i>
Christelle, PRINZ Professeure, Lund University, S	<i>Examinatrice</i>
Catherine, PICART Professeure, CEA-IRIG	<i>Examinatrice</i>
Anouk, GALTAYRIES MCF HDR, Chimie ParisTech	<i>Directrice de thèse</i>
Jean-Paul, BARNES Dr. Ingénieur de recherche, CEA-LETI	<i>Encadrant de thèse</i>



# PUBLICATIONS AND COMMUNICATIONS

---

## PUBLISHED PAPER DURING THESIS

Amanda Gomes de Carvalho, Jean-Paul Barnes, Olivier Renault, Denis Mariolle, Christophe Gaude, David Ratel and Anouk Galtayries. **Combining surface-sensitive microscopies for analysis of biological tissues after neural device implantation.** *Biointerphases* 15, 031016 (2020). (Embedded in chapter 4)

## CONFERENCE ABSTRACTS

O. Renault, A. G. de Carvalho, J-P. Barnes, A. Galtayries (2021) **Correlative surface microscopy for healthcare technologies** abstract submission for oral presentation (15 min) to 16<sup>th</sup> European Vacuum Conference, EVC 16, 22-26 November 2021, Marseille, France.

A. G. de Carvalho, J. P. Barnes, O. Renault, D. Mariolle, C. Gaude, D. Ratel and A. Galtayries (2020) **Microscopies de surface combinées pour l'analyse des tissus biologiques après implantation d'un dispositif neuronal** abstract submission for oral presentation (15 min – in French) to Journées des spectroscopies d'électrons 2020, JSE2020, 21-22 January 2020, Paris, France.

A. G. de Carvalho, J. P. Barnes, O. Renault, D. Mariolle, C. Gaude, D. Ratel and A. Galtayries (2019) **Correlative surface microscopy for analysis of biological tissues after neural device implantation** abstract submission for oral presentation (15 min) to the 22<sup>nd</sup> International Conference on Secondary Ion Mass Spectrometry, SIMS-22, 20-25 October 2019, Kyoto, Japan.

## SEMINARS

A. G. de Carvalho and Anouk Galtayries (2020) **Combined surface-sensitive microscopies for analysis of biological tissues after neural device implantation** seminar presentation at Materials doctoral School of the Cadiz University, 11 November 2020, Webinar.

## AWARDS AND RECOGNITIONS

**Scientific highlight at CEA-Leti Scientific Report 2020** at PhD research at CEA-Leti section (pag. 86), 2020.

**Scientific highlight at American Institute of Physics (AIP) Scilight 2020** entitled Combined surface-sensitive microscopies analyze tissue damaged by neural devices (by Savannah Mandel), 26 June 2020.

Biointerphases Prize for the **Best Biointerface Presentation** at the 22<sup>nd</sup> International Conference on Secondary Ion Mass Spectrometry (SIMS22), 20-25 October 2019, Kyoto, Japan.



# ACKNOWLEDGEMENTS

---

Je remercie tout d'abord mes encadrants de thèse au CEA-Leti à Grenoble, Jean-Paul Barnes et Olivier Renault, qui m'ont confié ce travail doctoral, pour tout l'enseignement que j'ai reçu dans un environnement scientifique et technique très privilégié. Je remercie très chaleureusement ma directrice de thèse, Anouk Galtayries, que même basée à Paris était toujours présente avec de bons conseils dans chaque étape de ce travail. Un grand merci pour tout l'enseignement enthousiasmant qu'elle m'a procuré.

J'adresse mes sincères remerciements à Vincent Delaye, chef du Service de Métrologie et Caractérisation Physique du CEA-Leti, ainsi que Nicolas Chevalier, chef du Laboratoire d'analyse de surfaces et d'interfaces au sein du service, pour leur accueil, engagement professionnel et bienveillance. Je remercie également Armelle Ringuedé, directrice adjointe de l'École Doctorale Chimie Physique et Chimie Analytique de Paris-Centre, pour son suivi et son écoute devant plusieurs questions administratives posées concernant l'École Doctorale.

Je remercie les membres du jury pour leur évaluation ainsi que les remarques et questions qui ont permis d'apporter davantage d'éclaircissements et précisions aux résultats présentés dans ce manuscrit. Je remercie les rapporteurs Christine Dupont et Didier Leonard, ainsi que les examinateurs Christelle Prinz, Catherine Picart et Vincent Semetey, président du jury, pour tous les échanges stimulants dont ils m'ont fait l'honneur ainsi que leur accueil chaleureux lors de la soutenance.

Dans les différents services du CEA-Leti, dont j'ai eu la riche expérience de travailler ensemble, je remercie David Ratel et Cristophe Gaude, à Clinatec, pour leur disponibilité à échanger sur le projet BCI et aussi pour tout le soutien en m'apportant des échantillons biologiques étudiés dans ce travail. Merci également à Antoine Hoang et Claire Verplanck, au Département micro-Technologies pour la Biologie et la Santé (DTBS), pour tout leur soutien dans le projet TRAIL, merci également pour la fabrication des systèmes d'administration de médicaments à base d'hydrogel. Ce fut un honneur de contribuer à des projets aussi importants pour la santé que ceux auxquels vous êtes impliqué.

Dans mon groupe à la plate-forme de nano-caractérisation (PFNC), je remercie François Bertin pour tous nos échanges sur les statistiques multivariées et les outils de *machine learning* appliqués au traitement des données. Ses encouragements ont été très importants dans le développement des compétences en science des données que j'ai acquises au cours de ma thèse. Je remercie Denis Mariole, mon conseiller en microscopie en champ proche, qui m'a accompagné dans les tentatives les plus diverses d'analyse AFM de nos systèmes biomédicaux. Je remercie chaleureusement Marc Veillerot, François Pierre et Claire Guyot qui ont partagé le même bureau avec moi tout au long de mon séjour. Ce fut une expérience merveilleuse de travailler avec vous, merci pour la gentillesse de tous les matins, pour les rires et pour tous les goodies que nous avons l'habitude de manger ensemble. Je tiens également à remercier Anass Benayad, Eugénie Martinez, Nicolas Gauthier et Pierre-Marie Deleuze

pour tous les échanges que nous avons eu l'occasion d'avoir tout au long de mon doctorat. Ce fut un plaisir de vous avoir comme collègues de laboratoire.

Une thèse n'existerait pas s'il n'y avait pas de thésards. J'ai eu la chance de croiser le chemin de nombreuses et belles personnes tout au long de mon passage. Je remercie d'abord à El Mostafa Barik, qui m'a toujours épaulé, avec une constante amitié, gaieté et indispensable gaillardise. Je te souhaite le meilleur pour la suite. Je remercie Walter Pessoa pour son amitié et pour les précieux conseils qui m'ont accompagné de João Pessoa, au Brésil, jusqu'à Grenoble. Je te remercie pour les discussions très variées que nous avons eues, tu as été un exemple pour moi. Merci à Camila Cavalcante pour l'amitié et pour tous les échanges que nous avons eu pendant ces années de thèse. Grâce à toi et ton joli accent je me suis toujours senti plus proche du Brésil et aussi de la région du Nord-Est du Brésil que j'aime tant. Sois heureuse ! Merci également à Aurelio Borzi pour nos déjeuners toujours très amusants et pour toutes ses tentatives pour m'apprendre l'italien. Je te souhaite d'atteindre tout ce que tu vises ! Je remercie également tous les doctorants, stagiaires et amis que j'ai eu tant de chance de rencontrer durant ce travail, Maigid Moreno, Manon Berthault, Valentin Aubriet, Maxime Gay, Amal Ben Hadj, Maria Planells, Jorge Morales, Carla Xena, Taylor Bure, Roderic Cravero, Alexandre Blaizot, Tarek Spelta, Roberto Fantin, Steven Bel, Nathan Chatelet, Thomas Meyer.

Cette thèse a pu voir le jour grâce au support inconditionnel de ma famille et de mes amis. J'adresse mes premières pensées et remerciements à mes parents. Vous m'avez appris à ne pas baisser les bras, à être curieuse et à vouloir aller au bout des choses ; c'est grâce à vous que j'ai pu mener à terme ce travail, pour toutes les valeurs que vous m'avez enseignées. Je remercie mes frères et ma sœur, pour leur soutien et compréhension que malgré la distance je garde toujours l'affection de chacun avec moi. Merci à mes amis brésiliens et compatriotes à Grenoble. Merci à mes très chers amis étudiants de longue date.

Enfin, je remercie très amoureusement Rafael Biriba qui m'a tant soutenu, aidé et encouragé mais aussi supporté ! Tu m'as fait voir la vie sous une autre optique, et ta présence a été si bénéfique durant ce travail qu'elle m'a été d'une valeur infinie.

# CONTENTS

---

Abbreviation index .....	xi
1 Introduction.....	1
1.1 Importance of surfaces in biology and medicine .....	1
1.2 Main challenges in imaging biological surfaces .....	4
1.2.1 Fragile systems.....	4
1.2.2 Challenging for UHV .....	4
1.2.3 Insulator specimens.....	5
1.2.4 Complex systems .....	5
1.2.5 Analytical limitations .....	5
1.2.6 Data analysis .....	6
1.3 Imaging techniques: state-of-the-art instrumentation in biomedical surface science.....	6
1.3.1 Optical microscopy .....	6
1.3.2 Vibrational imaging .....	7
1.3.3 Electron microscopy .....	9
1.3.4 Proximal probe microscopy .....	11
1.3.5 X-ray spectromicroscopy .....	13
1.3.6 Mass spectrometry imaging.....	15
1.4 Implantable technologies and interfaces between synthetic and biological environments ...	19
1.4.1 Neuromodulator devices.....	21
1.4.2 Drug Delivery Systems (DDS).....	25
1.5 Objectives of this thesis.....	27
1.6 Thesis outlines.....	29
2 Experimental description.....	31
2.1 Multimodal surface imaging approach.....	31
2.2 Protocols of sample preparation.....	33
2.2.1 Preparation of hydrogel-based drug delivery systems .....	33
2.2.2 Cross section of biological tissues embedded in resin.....	35
2.2.3 Neural tissue hosting a Drug Delivery System .....	36
2.2.4 Glial scar tissue formed surrounding a neural electrode .....	37
2.3 Analytical methods.....	40
2.3.1 Time-of-flight secondary ion mass spectrometry (ToF-SIMS).....	41
2.3.2 Tandem mass spectrometry (Tandem MS).....	51
2.3.3 Atomic force microscopy (AFM) .....	52
2.3.4 X-ray photoelectron spectroscopy (XPS) .....	54
2.3.5 Photoemission electron microscopy (PEEM) .....	70
3 Multimodal ToF-SIMS, AFM and XPS approach for surface analysis of drug delivery systems ...	79

3.1	Imaging of ketorolac tromethamine and gellan gum microcapsules in HA hydrogel by ToF-SIMS	80
3.1.1	Individual chemical markers of HA hydrogel, ketorolac tromethamine and gellan gum....	80
3.1.2	Mapping of ketorolac tromethamine and gellan gum microcapsules in HA hydrogel .....	84
3.2	Imaging gellan gum microcapsules by AFM.....	86
3.3	Quantification of chemical environments of ketorolac tromethamine and gellan gum in hydrogel by XPS .....	87
3.3.1	Survey spectra analysis of pure HA hydrogel .....	88
3.3.2	Survey spectra analysis of HA hydrogel containing ketorolac tromethamine .....	89
3.3.3	Core level spectra analysis of HA hydrogel and ketorolac tromethamine.....	92
3.3.4	Survey spectra analysis of HA hydrogel containing gellan gum microcapsules .....	100
3.3.5	Core level spectra analysis of HA hydrogel with gellan gum microcapsules .....	101
3.4	Multimodal approach discussion .....	105
3.5	Conclusions .....	106
4	Multimodal ToF-SIMS, Tandem MS, XPS and XPEEM approach for surface chemical analysis of optimal cutting temperature compound .....	111
4.1	Imaging chemical features in the resin hosting a biological tissue by ToF-SIMS .....	111
4.1.1	Ions from silicon substrate .....	113
4.1.2	Ions from the biological tissue .....	114
4.1.3	Ions from the resin .....	115
4.2	Imaging chemical features in the resin by Tandem MS .....	124
4.3	Chemical quantification in the resin by XPS.....	126
4.3.1	Survey spectra analysis from S1 and S2-OCT regions.....	126
4.3.2	Core level spectra analysis from S1 and S2-OCT regions.....	128
4.4	High-resolution chemical state imaging of chemical features in the resin by X-PEEM.....	132
4.4.1	Secondary electron PEEM images: identification of the S1 and S2-OCT regions.....	132
4.4.2	Core level X-PEEM images: chemical state analysis.....	133
4.5	Multimodal approach discussion .....	139
4.6	Conclusions .....	141
5	Multimodal ToF-SIMS, XPS and X-PEEM approach for surface chemical analysis of brain and glial scar tissues in contact with implantable biomedical technologies .....	145
5.1	Brain tissue .....	147
5.2	Imaging hydrogel in a rodent's brain coronal section by ToF-SIMS.....	148
5.2.1	Imaging of the main chemical structures present in the cortectomy region .....	148
5.2.2	Comparison between ToF-SIMS imaging and cresyl violet staining of a rodent's brain tissue	150
5.3	Glial scar tissue .....	151
5.4	Imaging a glial scar tissue by ToF-SIMS.....	154
5.4.1	Identification of the main biomolecules present in the glial scar tissue by applying PCA on ToF-SIMS data .....	154

5.4.2	Imaging chemically distinct features in the scar tissue by applying PCA on ToF-SIMS data	158
5.4.3	Identification of metals in the glial scar tissue by ToF-SIMS .....	163
5.5	Chemical quantification performed in the glial scar tissue by XPS .....	165
5.5.1	Survey spectra analysis from ECM and PM-rich regions .....	166
5.5.2	Core level spectra analysis from ECM and PM-rich regions .....	167
5.6	High-resolution chemical state mapping by X-PEEM.....	170
5.6.1	Secondary electron X-PEEM image: identification of a zone of interest .....	171
5.6.2	C 1s core level X-PEEM imaging: chemical-state analysis .....	172
5.7	Multimodal approach discussion .....	175
5.8	Conclusions .....	177
	Final conclusions and prospects .....	181
	Bibliography .....	187
	Appendix.....	199
1.	Glial scar tissue and scheme of tissue cross section's location .....	199
2.	Parameters used for principal component analysis of slices SA09 and SA18.....	200
3.	PCA scores from ToF-SIMS negative spectrum of slice SA18 .....	200
	Extended summary of the thesis in French .....	201
	Microscopie multimodale de surface pour des applications en technologies pour la santé .....	201



## ABBREVIATION INDEX

---

<b>AFM</b>	Atomic force microscope
<b>BCI</b>	Brain Computer Interface
<b>CNS</b>	Central nervous system
<b>DDS</b>	Drug Delivery Systems
<b>ECM</b>	Extracellular matrix
<b>ECoG</b>	Electrocorticography
<b>EEG</b>	Electroencephalography
<b>FAs</b>	Fatty Acids
<b>FoV</b>	Field of view
<b>GFPA</b>	Glial fibrillary acidic protein
<b>H&amp;E</b>	Hematoxylin and eosin
<b>HA</b>	Hyaluronic Acid
<b>IBA1</b>	Ionized calcium-binding adapter molecule
<b>MS</b>	Mass spectrometry
<b>MWCNT</b>	Multi-walled carbon nanotube
<b>NSAID</b>	Nonsteroidal anti-inflammatory drug
<b>O.C.T.<sup>TM</sup></b>	Optical coherence tomography
<b>PC</b>	Phosphatidylcholine
<b>PCA</b>	Principal Component Analysis
<b>PE</b>	Phosphatidylethanolamine
<b>PEEM</b>	Photoemission electron microscopy
<b>PEG</b>	Polyethylene glycol
<b>PI</b>	Phosphatidylinositol
<b>PM</b>	Plasma membrane
<b>PVA</b>	Polyvinyl alcohol
<b>ROI</b>	Region of interest
<b>SE</b>	Secondary electron
<b>SM</b>	Sphingomyelin
<b>SXI</b>	Scanning x-ray image

**ToF-SIMS**

Time-of-flight secondary ion mass spectrometer

**UHV**

Ultra-high vacuum

**XPS**

X-ray photoelectron spectroscopy

# 1 INTRODUCTION

---

Beyond nature's use of biological interfaces in biological processes, surface concepts have been adopted in medical and biological technology over the years to support human health. However, a more deeply understanding of such processes at bio-interfaces remains essential in the elaboration of emerging biomedical technologies that are simultaneously functional and biocompatible. To fill this gap, sensitive-surface microscopies commonly applied in microelectronics, catalysis, corrosion and tribology research fields have migrated to biomedical research aiming to provide detailed information from biological surfaces. In order to introduce this topic, we present in the beginning of this chapter (1.1) the importance of surfaces in biology and medicine followed by (1.2) the main challenges in imaging biological surfaces. The (1.3) state-of-the-art instrumentation in biomedical surface science, and (1.4) the implantable technologies and the interface between synthetic and biological environments whose interfaces are addressed in this work are also presented. The (1.5) objectives of this thesis and (1.6) the thesis outlines are given at the end of this chapter.

## 1.1 IMPORTANCE OF SURFACES IN BIOLOGY AND MEDICINE

In each living being in nature we can find surfaces and interfaces of extreme importance. These surfaces are generally responsible for supporting important biological processes, very unlike the common idea that processes in the organism occur preferably in solution phase. It might be explained by the high accessibility of surfaces for reactions. The low energy barrier to mobility in the plane of the surface can be either considered the main characteristic used to facilitate complex reactions in the organism. Some examples to consider are clustering of molecules on the surface of living cells to collaborate in a variety of biological events and burial of proteins in cell membranes that is essential to cell signaling or molecular transportation.

Beyond the natural use of biological surfaces in biological processes, surface concepts have been adopted in biomedical research to support human health over past years. Important phenomena such as epitaxy, molecular recognition and self-assembly readily implemented at surfaces are examples of surface concepts that have been widely applied in the development of new biomedical technologies [1-3]. With this growing intention of using surface concepts in biomedical technologies designed to improve human life, almost twenty years ago, David G. Castner and Buddy D. Ratner, were able to point examples of interfaces where these surface concepts would potentially be applied and that would be at the same time of great importance in biology and medicine for the coming decades such as cell/synthetic material, ECM/cell, hydrated tissue/air (lung) and mineral/protein (bone) [4]. These interfaces are still nowadays included in expanding research fields in biomedical surface science and represent guidelines for scientific research in the future.

It is worth emphasizing that "biomedical surface science" is considered in this work as a synonym of "biological surface science" whose according to Bengt Kasemo's definition says that it is an

interdisciplinary subfield of surface science where properties of biological and synthetic surfaces are investigated in order to fabricate bioengineered surfaces for medical applications [5]. In this field, the biomedical surface addressed is not necessarily a surface of a biological sample extracted from living organisms such as cells and tissues but can also be functionalized materials developed to be in contact with the biological matter.

Among the interfaces of great importance cited by David G. Castner and Buddy D. Ratner, the cell surface/synthetic material is a typical interface of importance for implantable technologies and the one of most interest in this work. Implantable technologies are usually made of biomaterials, which are considered distinguished materials due to their ability to generate an appropriate response of the host in a specific application [6]. This biocompatibility usually requires that implantable surfaces do not leach biologically reactive substances allowing healing in the body after implantation and, at the same time, allow the controlled development of a scar tissue 50-200  $\mu\text{m}$  thick that encapsulates the biomedical technology without jeopardizing its operation. Examples of implantable technologies include brain electrodes and drug delivery systems. Figure 1.1 shows schematically a sequence of important events that contribute to the formation of a scar tissue around a biomedical technology after implantation surgery. In cases of bio-incompatibility, this encapsulation is not controllable and triggers stages of severe inflammation in the surgery site. A controlled encapsulation is then typical of a minimized inflammatory response.

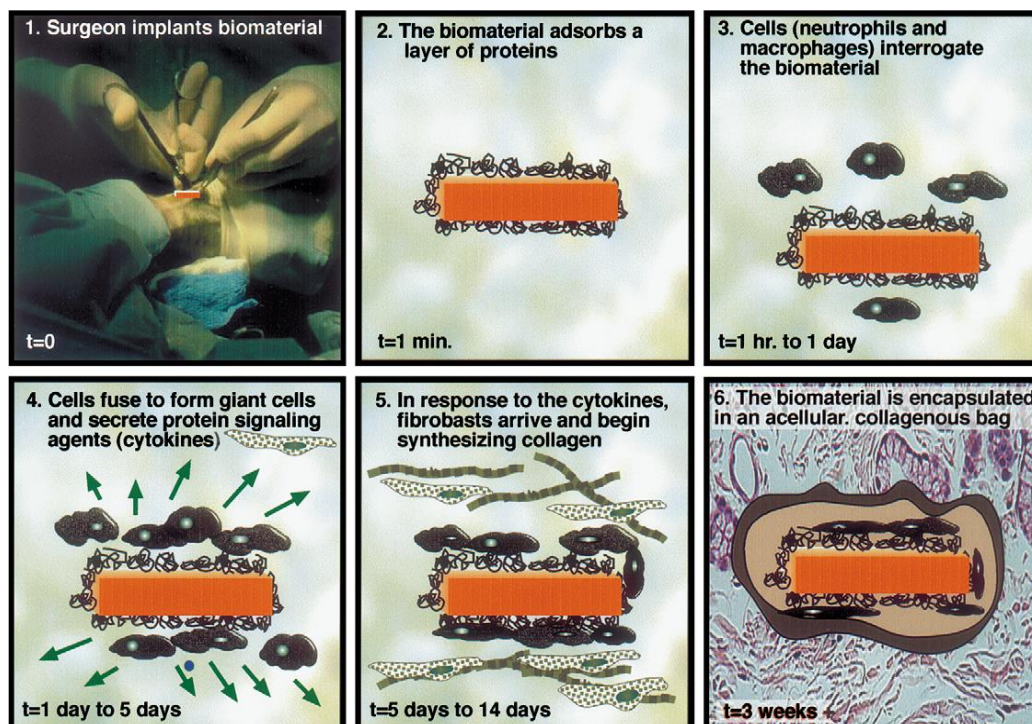


Figure 1.1. Schematic view of the organism's natural reaction and encapsulation of a synthetic device after implantation surgery. [4]

Similarly, the ECM/cell surface is considered an interface of great biomedical importance due its application in tissue engineering. The ECM is a three-dimensional environment made of several large proteins and glycosaminoglycans that support cells into tissue. Most cells are adherent and remain connected to the ECM during growth, division, differentiation and even death. The adhesion of cells and the host subsequent signalling events are mediated by specific interactions between cell-surface receptors and ligands of the matrix. Approaches to tissue engineering centre on the need to provide signals to cell populations to promote cell proliferation and differentiation in an orderly way that results in tissue/organ formation. The strategy for repair of lost body function in this case is to produce a real functioning tissue from a cell culture by making it grow *ex vivo* in a suitable environment. It usually requires a synthetic scaffold that simulates the ECM for the growing cells/tissue. Since differentiated tissue and organs are ultimate goals in tissue engineering, different parts of the scaffold may require different surface functionalities, *i.e.* different surface chemistries and topographies [5, 7, 8].

Other purely biological interfaces are of great importance in understanding biological processes inherent to life and in the development of new biomedical technologies. The hydrated tissue surface/air interface is an example. It is found throughout the respiratory system and enables gas exchange in the lungs. The alveolus are the cohesive units responsible for providing a barrier between the external environment and the organism while promoting together with the cardiovascular system an efficient O<sub>2</sub>/CO<sub>2</sub> exchange via surface diffusion. Structural damage of these units due the pathogenesis of lung diseases, however, can impair its normal functions. In the case of the alveolar epithelium, for example, its injury may include disassembly of the tight junctions, holes in the plasma membranes, or loss of cells [9]. Approaches to alveolar tissue repair focus on *in vitro* proliferation and transdifferentiation of alveolar epithelial type II cells, after type I cells death, to replace lost type I cells [10]. Critically, lung tissue regeneration requires coordinated responses by multiple cell types (and the matrix) that can occur through cell-cell signalling or juxtaposition. Whether these *in vitro* cell cultures are functionally integrated into host lung tissue, are long-lived, and retain expression of a complete lung transcriptomic program are still open questions that will need to be addressed in further alveolar surface analysis before these cells can be referred to as “engrafted” [11].

Similar to hydrated tissue surface/air interfaces, the mineral/protein interface is also a purely biological interface of great interest in medicine for bone studies. The bone is known to consist of a matrix of proteins embedded in a complex calcium phase dominated by hydroxyapatite. The mechanism that sticks them together is yet very little known but remains important in understanding how bone works as a material, how it is tough, and rigid enough to support our bodies and their movement [12]. In osteoporotic therapy, the administration of several drugs appears to affect the interface of carbonated hydroxyapatite with its surroundings aiming to slow down bone resorption or stimulate bone formation [13-15]. In dentistry, the interfacial interaction between crystals of hydroxyapatite and proteins is also fundamental in the formation and conferring of mechanical properties to dental structures such as enamel, dentin and cementum [16].

At this point we can notice how surfaces are critically important to many aspects of biology and medicine. Surfaces are responsible for biological reactions that range from breathing to body sustaining, in addition to orchestrating the acceptance or not of implantable technologies. Nevertheless, although these purely biological or synthetic material/biological interfaces are found within living organisms, many biomedical studies have smartly focused on biological models that could reproduce the *in vivo* behaviour [17]. However, over the last years, biomedical surface science has increasingly been associated with surface chemical state imaging studies of truly biological surfaces such as cells and tissues [18-21]. This has been happening mainly due to the growing need to learn even more about the relationship between chemical structure and physical property of natural and complex structures. Such learning is considered invaluable in the manufacture of new advanced functionalized materials for biomedical applications in the future. Nevertheless, acquiring detailed information from biological surfaces such as cells and tissues is not trivial and can be challenging in different ways.

## **1.2 MAIN CHALLENGES IN IMAGING BIOLOGICAL SURFACES**

Despite the growing interest about truly biological surfaces in the biomedical field, characterization of cells and tissues extracted from living organisms remain considered highly challenging when regarding the use of surface imaging techniques well known in traditional surface science. Below we have listed the main challenges in imaging biological surfaces and what have been done in biomedical surface science to overcome difficulties.

### **1.2.1 Fragile systems**

Biological specimens such as cells and tissues are considered fragile in comparison with bulk materials normally faced in other research areas and, for this reason, usually require special care when analysed. The use of energetic surface probes normally employed in the most diverse analytical techniques can easily damage molecules at the surface and change the chemistry and morphology of the sample. In the mass spectrometry field, this obstacle has been overcome by the use of cluster ion beam technology that has the ability to characterize surface composition with minimal damage that is essential for bioimaging applications [22]. [See more details about the use of clusters beams in mass spectrometry in the subsection 2.3.1.3.]

The degradation that biological specimens can suffer during storage and sample preparation may also modify their initial state and lead then to a less representative or unrepresentative description of the biological surface.

### **1.2.2 Challenging for UHV**

Biological specimens are also not ideal for ultra-high vacuum (UHV) environments required for most surface analytical techniques. Since biological systems are normally functional only in aqueous media, the draining of the aqueous part can create a new system also less representative than that one once

found *in vivo* (e.g., proteins can denature and unfold) [23]. Insufficiently dried specimens that remain humid during analysis may also degas and degrade the required vacuum for analysis. As an alternative, cryogenic analysis based on sample freezing are currently performed in biological research aiming to access a closer *in vivo* environment. Recent advances in atmospheric pressure ionization techniques are also contributing as an alternative to characterize biological tissues in an environment with less alteration of natural conditions [24-26].

### 1.2.3 Insulator specimens

Other constraints are based on the fact that biological specimens are insulator systems. Since it is considered an undesirable specimen property for most surface analytical techniques that normally use photons and accelerated electrons or ions beams for analysis. In cases of biological systems susceptible to adaptation, appropriate methodologies to overcome specimen insulation must be well planned and carefully applied.

### 1.2.4 Complex systems

Another critical constraint in analysing cells and tissues lies in the fact that biological specimens exhibit a complex structure-property relationship that exists at multiple-length scales with an elegant hierarchical organization that is hard to describe. A wide variety of molecules that present different three-dimensional (3D) arrangements and which are made of the same atomic building blocks can be found within these structures. Therefore, surface and in-depth characterization of truly biological surfaces such as found in cells and tissues has increasingly required techniques with sufficient spatial resolution to distinguish patterns at small scales that can vary until the nanometric order, as well as high sensitivity to detect traces of species or molecules.

Here, the use of ion beam technologies clusters has also allowed for molecular depth profiling in biological samples with excellent spatial (100 nm or less) and depth (5 nm) resolutions [27-29]. It also provides a surface-localized damage that preserves the chemical structure in the subsurface region being then ideal for surface cleaning applications aiming to remove surface contamination that could affect results and increase the surface complexity [30]. These features were unheard of with previously employed monatomic ion beam sources.

### 1.2.5 Analytical limitations

Despite the laterally and in-depth resolved information able to be acquired through the available state-of-the-art instrumentation, realize important questions such as how molecular orientation and consequently the molecular reactivity that are associated to the shape of molecules, e.g. as found in enzymatic reactions, still represents a main difficulty in the analysis of biological surfaces. The technical sensitivity of imaging instrumentation can also represent a great challenge when imaging traces or even light species such as hydrogen is intended.

However, new surface tools capable of providing more comprehensive information about a wide range of complex biological surfaces and interfaces of interest have been developed. It includes new protocols of sample preparation and analysis. Among the protocols of sample analysis we have the use of multi-technique approaches that provides analytical results from different perspectives and a complete surface characterization of biological materials [31].

### **1.2.6 Data analysis**

Other constraint includes the fact that large amounts of data are often generated during analysis and they eventually require high-performance computers to be processed when complex surfaces are imaged. The meaningful interpretation of the large volume of data may also be challenging. In this case, multivariate statistical analysis (MVA) has been effectively implemented to reduce large complex datasets to a small number of more useful variables, discarding noise and discerning trends and patterns in the data. Among all MVA methods, principal component analysis (PCA) is the most commonly used for exploratory analysis of data in surface chemical state imaging studies of cells [32-34] and tissues [30, 35-37].

In summary, although biological specimens need special care and their accessibility remains a major challenge in biomedical surface science, new analytical features, experimental protocols and data analysis methods have emerged as powerful surface tools aiming to overcome the main challenges in imaging biological surfaces. In the next section we will focus on introducing state-of-the-art instrumentation in the imaging field and understand how the information acquired through each technique has been important in modern biomedical research.

## **1.3 IMAGING TECHNIQUES: STATE-OF-THE-ART INSTRUMENTATION IN BIOMEDICAL SURFACE SCIENCE**

In order to learn even more about the relationship between chemical structure and physical property of biological complex structures, biomedical surface science has increasingly applied spatially resolved surface techniques capable of distinguishing important features that might be present in such systems. Here we present a brief overview of the state-of-the-art in surface state imaging techniques that provides insights into a variety of problems faced nowadays in the biomedical field.

### **1.3.1 Optical microscopy**

Optical microscopy or light microscopy is the most traditional form of microscopy that uses one or a series of lenses to magnify images of small samples to a higher resolution using visible light, invented before the 18<sup>th</sup> century and still commonly used nowadays [38]. This is considered a very used technique in modern cell biology mainly because its resolution is well-matched to the sizes of subcellular structures and also because the availability of fluorescent probes makes it possible to visualize autofluorescent cellular structures, fluorescent dyes or stains, or to analyze the expression, modification and/or

localization of proteins using fluorescent antibodies by immunofluorescence. Besides that, the relatively nonperturbing nature of light means that living cells can be imaged for long periods of time to follow their dynamics [39].

Because of biological tissues has little inherent contrast in light microscope, staining is employed to give both contrast to the tissue as well as highlight particular features of interest. Hematoxylin and eosin (H&E stain) is one of the most commonly used stains in histology to show the general structure of biological tissues. Hematoxylin stains cell nuclei blue; eosin, an acidic dye, stains the cytoplasm and other tissues in different stains of pink. The Cresyl Violet staining, on the other hand, is used to stain Nissl substance in the cytoplasm of neurons being then commonly used to identify the neuronal structure in brain and spinal cord tissue. It uses basic aniline dye to stain RNA blue, while the Nissl substance (rough endoplasmic reticulum) appears dark blue due to the staining of ribosomal RNA, giving the cytoplasm a mottled appearance.

### 1.3.2 Vibrational imaging

Vibrational imaging techniques are considered powerful tools for chemical state imaging of biological systems. They can provide label-free molecular information about complex surfaces without the necessity to place the biological specimen under UHV conditions [40]. The main imaging techniques based on vibrational spectroscopic signatures are Infrared (IR) absorption and Raman scattering. From the excitation of biological matter with incident photons at wavelengths ranging from the visible light to the infrared spectrum, these techniques provide a vibrational spectrum from a sampling volume about 1  $\mu\text{m}$  (deeper than the extreme surface) that is something like a structural "fingerprint" of the biological specimen since it is characteristic of chemical bonds in a specific molecule.

IR spectroscopy is a straightforward technique for vibrational imaging. Fourier transform IR (FTIR) microscopy with scanning options allows chemical mapping with lateral resolution about tens of microns. In cancer research, it has been possible to distinguish between benign and malignant tumours in tissue samples of brain [41], breast [42-44], colon [45-47], lung (see Figure 1.2) [48-50] and prostate [51, 52] along with cervical cytology or biopsies [53, 54]. In addition, liquids samples can also be examined directly in IR spectroscopy, which makes it also an ideal tool for the study of biofluids such as urine, saliva, serum or whole blood [55-57].

Raman microscopy is also an analytical tool applied in cancer research that allows identification of malignant tumours in human tissue specimens [58, 59]. Raman microscopy has also contributed over the past years in the study of chronic diseases such as hypertension, atherosclerosis and diabetes. These are diseases commonly related to alterations in the vessel wall and, particularly, in the endothelium, the innermost layer of the vessel wall. Since the endothelial dysfunction is an early feature of such pathologies, the implementation of Raman imaging to study them is, therefore, aimed at identifying subtle differences in chemical and structural composition and in distribution of components in the endothelium [60-62].

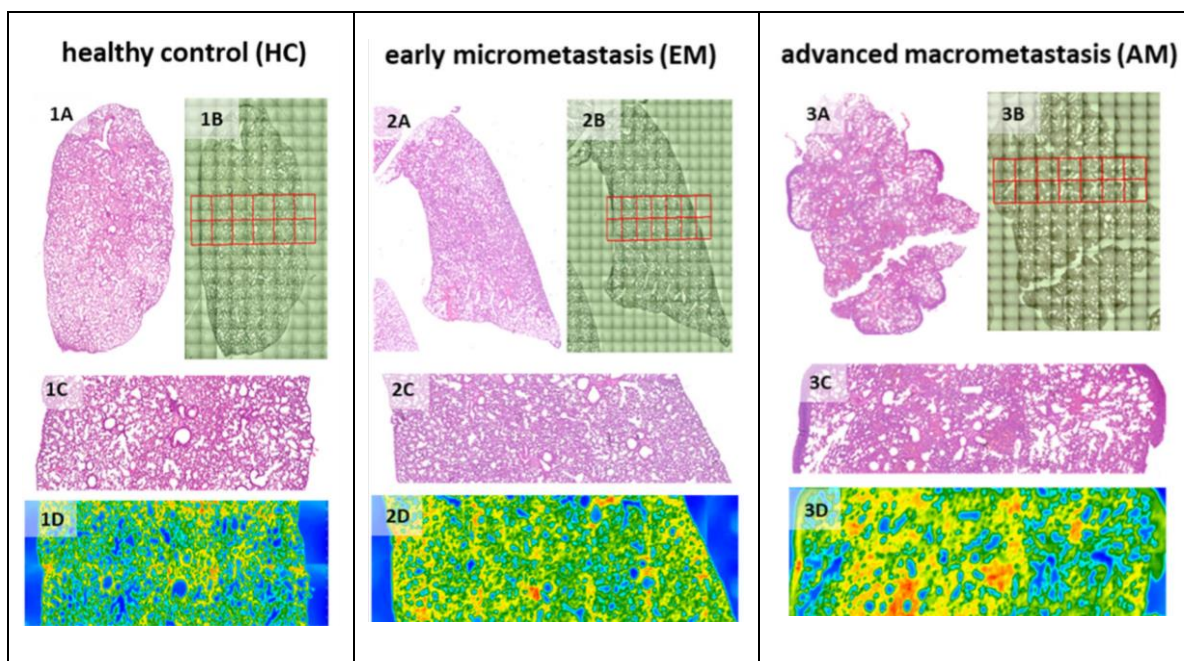


Figure 1.2. Label-free FTIR spectroscopic imaging of lung cross-sections of murine. Three tissues: healthy control (HC), early micrometastasis (EM) and advanced macrometastasis (AM); after orthotopic inoculation with viable 4T1 tumor cells. (A) H&E stained cross-sections (magnification 20 $\times$ ). (B) White light images with marked regions of interest (ROI; magnification 15 $\times$ ). (C) Magnified H&E stained ROIs. (D) IR images for the protein distribution (amide I: 1702–1610  $\text{cm}^{-1}$ ). One red square corresponds to the area of 700 $\times$ 700  $\mu\text{m}^2$ . [50]

Coherent anti-Stokes Raman Scattering (CARS) imaging may be the most successful Raman imaging technique. Although the first CARS microscope was reported in 1982 [63], it was not until the development of a new detection scheme in 1998 that high-quality, 3D images of biological samples became possible [64]. Since there has been a continuous evolution of the detection schemes and laser sources for CARS microscopy. It has allowed imaging lipid-rich structures of living cells and live skin tissues with resolution of 0.3  $\mu\text{m}$  in the lateral plane and 1.5  $\mu\text{m}$  in the axial direction (see Figure 1.3) [65-67].

However, techniques such as IR and Raman are still considered limited in lateral resolution in the analysis of biological specimens, even with the latest optical technology [68]. FTIR is limited by diffraction [69]. And although, in principle, Raman techniques can produce images with spatial resolution on a submicron scale, this requires high intensity incident beams that can damage the biological specimen [70]. The integration of IR absorption and Raman scattering into near-field scanning optical microscopy (SNOM) has been an innovative approach to *in situ*, non-destructive and high spatial resolution imaging. For applications in the chemical characterization of biological specimens, it improved the spatial resolution of Raman scattering and IR spectroscopy to below the optical diffraction limit ( $\geq 0.2 \mu\text{m}$ ) [71, 72].

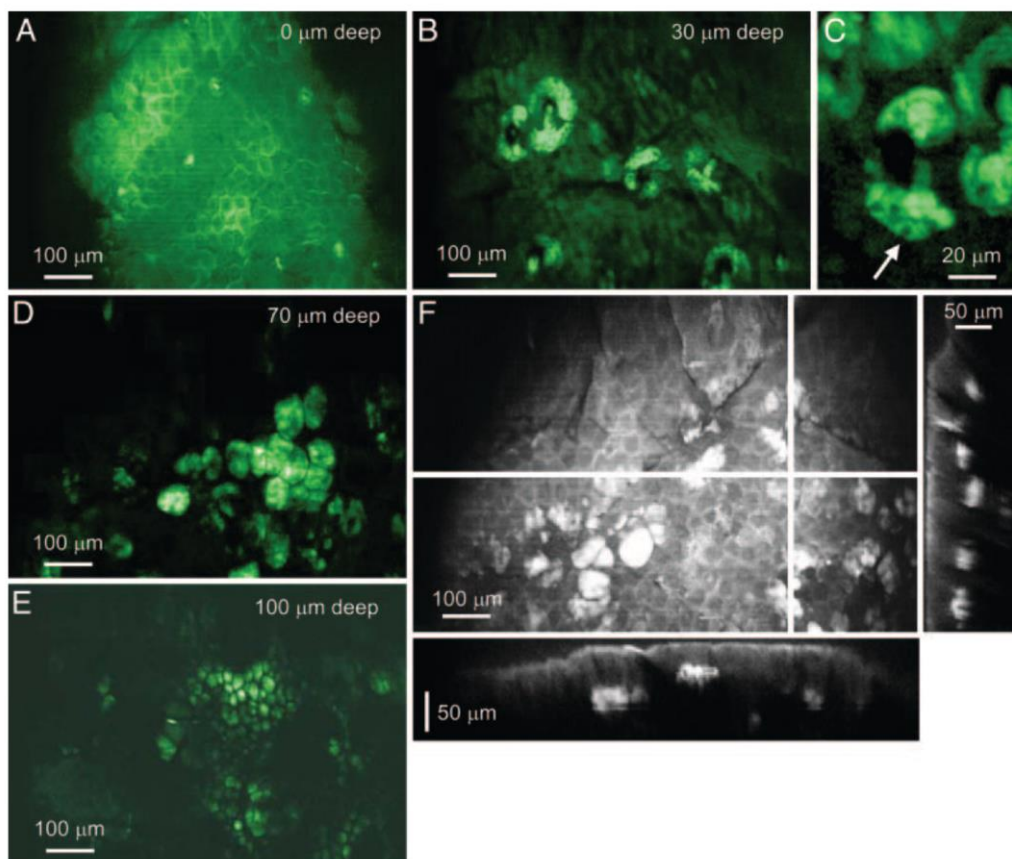


Figure 1.3. Images of a hairless mouse ear. The Raman shift is set at  $2,845\text{ cm}^{-1}$  ( $\omega_p=816.8\text{ nm}$ ) to address the lipid  $\text{CH}_2$  symmetric stretch vibration. The frames are averaged for 2 s. (A) Stratum corneum with bright signals from the lamellar lipid intercellular space that surrounds the polygonal corneocytes. Bright punctuated dots are ducts of sebaceous glands. (B) Sebaceous glands at  $\approx 30\text{ }\mu\text{m}$  from skin surface. (C) Individual cells of the gland compartment can be recognized, with nuclei visible as dark holes (arrow). (D) Adipocytes of the dermis at  $\approx 60\text{ }\mu\text{m}$  from skin surface. (E) Adipocytes of the subcutaneous layer at a depth of  $\approx 100\text{ }\mu\text{m}$ . (F) 2D projection of 60 depth-resolved slices separated by  $2\text{ }\mu\text{m}$ . Panels to the right and under F show the yz and xz cross sections taken at the white lines, respectively. [65]

### 1.3.3 Electron microscopy

Since its first prototype developed by Ernst Ruska and Max Knoll in 1931, electron microscopy (EM) has become a remarkably versatile imaging tool. Nowadays, almost all major R&D organizations (universities, industrial laboratories, national labs) in the world have EM facilities that can accommodate the EM well-established imaging techniques. Despite its apparent maturity, new techniques continue to be developed, not only exceeding the resolution limits of EM, but also expanding the range of samples and environments in which it can be used.

The utility of electrons for imaging comes from the fact that the electron wavelength is about 1000 times shorter than that of visible light, which ensures less pronounced diffraction effects currently faced in optical microscopy and provides a probe with much higher spatial resolution (about 10 nm). According

to the energy of the incident electron beam (ranging from few to hundreds of kiloelectronvolts, or keV), its interaction with the matter can generate emissions that carry characteristic topographic or chemical information from different sampling volume ranging from near the surface (about 10 nm) to few micrometres depth.

There are two main types of electron microscope — the scanning EM (SEM) and the transmission EM (TEM). The signal used by an SEM to produce a topographic image results from the interaction of an incident electron beam with an average energy of a dozen of keV and the detection of secondary electron (SE) and back-scattered electron (BSE) emissions. SEs have very low energies (about 50 eV). Then, SEs can only escape from the top few nanometres of the surface of a sample. On the other hand, BSEs are beam electrons that are reflected from the sample by elastic scattering. Since they have much higher energy than SEs (close to the energy of the incident electron beam), they emerge from deeper locations within the specimen and, consequently, the resolution of BSE images is less than SE images. However, BSE is more applied along with the spectra of the characteristic X-ray emission. Since the intensity of BSE is strongly related to the atomic number of the specimen, it can provide information about the distribution, but not the identity, of different elements in the sample. Nonetheless, the energy or wavelength of characteristic X-ray emission can be measured by Energy-dispersive X-ray spectroscopy (EDS) or Wavelength-dispersive X-ray spectroscopy (WDS) and used to identify and measure the abundance of elements in the sample and map their distribution. Conversely, TEM is used to view thin specimens (less than 100 nm) through which electrons with an average energy of hundreds of keV can pass generating a projection image.

However, there are significant limitations to their use in biomedical applications, such as the need for a vacuum to produce and transmit electrons and electron beam damage to biological samples. For SEM, besides specimens are required to be completely dry, biological specimens require chemical fixation to preserve and stabilize their structure. The dry biological specimen is also required to be sputter-coated with heavy metals, such as gold, for better electron conduction before examination. For TEM, besides specimens less than 100 nm thick, biological samples may be embedded in resin to withstand the high vacuum and to enable cutting tissue into electron transparent thin sections. For these reasons, the applications of EM in biomedical surface science have been mostly in the observation of the surface of biomaterials, such as, for example, the study of porosity and morphology of scaffolds for applications in tissue engineering [73, 74].

Nevertheless, the development of a variety of EM techniques has had a tremendous impact in fields ranging from condensed matter physics to structural biology. One advance is the use of rapid freezing to transfer hydrated specimens into an electron microscope, a process known as cryo-EM. This process preserves the biological sample in a thin layer of vitreous, non-crystalline ice in a near native state. This has been a very useful tool, for example, in the structural analysis of biomolecules from brain tissues associated with Alzheimer's disease, which has major implications for the understanding of the disease and for the development of new compatible therapeutic treatments [75, 76].

Applications of focused ion beam (FIB), which has the ability to sputter away a few nanometres of matter at a time, combined with EM have been also a useful approach in biomedical surface analysis. If applied to sputter the surface of the sample in repeated cycles of exposed surface imaging, a sequence of images can be produced highlighting 3D structures. FIB-SEM has been considered an essential tool for imaging of sections of neural tissue for connectome tracing, at resolutions  $<10$  nm in the x, y and z axis (see Figure 1.4) [77], as well as for imaging of subcellular features for the study of membrane trafficking, organelle architecture and cytoskeletal arrangement in the volume of the cell [78].

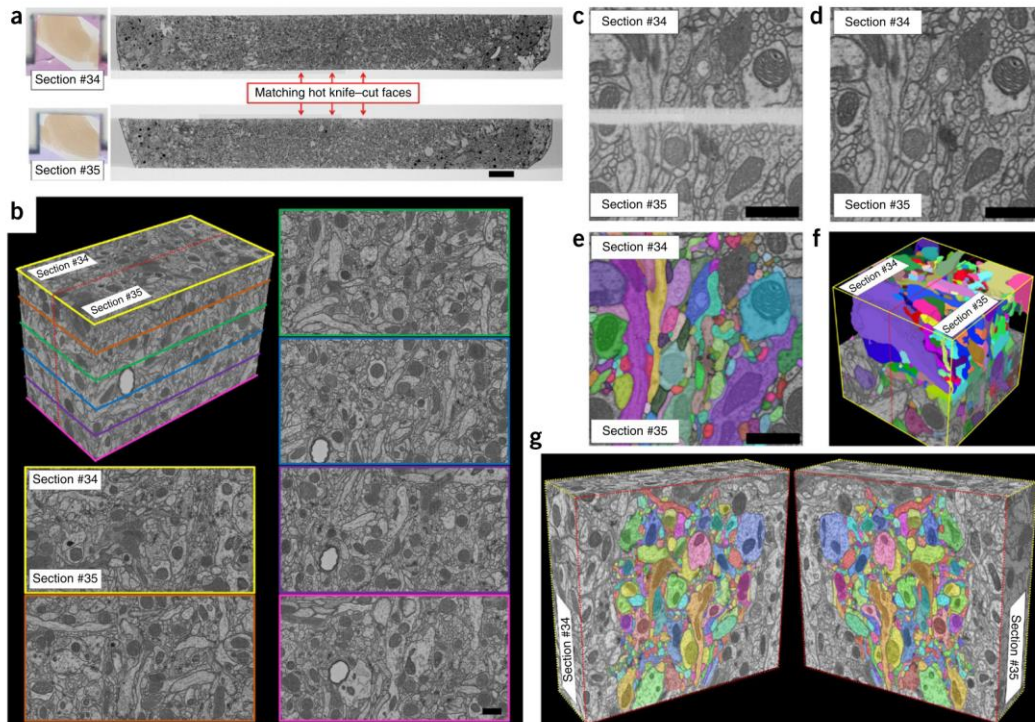


Figure 1.4. Volume stitching on C-PLT-prepared *Drosophila* brain. (a) FIB-SEM images of two sequential 20- $\mu\text{m}$  ultrathick sections. (b) Volume stitching over an 8  $\mu\text{m}$   $\times$  12  $\mu\text{m}$  cropped region. The dotted red line on the 3D volume shows the stitch plane. Images with coloured borders correspond to cut planes through this 3D stitched volume. (c,d) Aligned hot-knife cut edges before (c) and after (d) algorithmic flattening and stitching. (e,f) Volume tracing of the 4  $\mu\text{m}$   $\times$  4  $\mu\text{m}$   $\times$  4  $\mu\text{m}$  volume from which c,d were obtained. (g) 9  $\mu\text{m}$   $\times$  10  $\mu\text{m}$  cropped region that has been split open along the stitch plane. Scale bars, 10  $\mu\text{m}$  (a) and 1  $\mu\text{m}$  (b–e). [77]

#### 1.3.4 Proximal probe microscopy

Since the advent of the scanning tunnelling microscope (STM) in the early 1980s [79, 80], a wide variety of related microscopies using similar experimental principles and instrumentation have been developed for imaging samples based on their electronic, optical, chemical, mechanical, and magnetic properties. Among them, we can mention atomic force microscopy (AFM) [81], near-field scanning optical microscopy (NSOM) [82, 83], and scanning electrochemical microscopy (SECM) [84] all find broad applications in high-resolution imaging experiments. These different techniques are called “proximal probe microscopies” because they employ a small probe that is positioned very close to the sample of

interest for the purposes of recording an image of the sample, performing spectroscopic experiments, or manipulating the sample.

As it uses a physical probe to obtain images of surfaces, sample preparation for scanning probe imaging is relatively simple, and no freezing, metal coating, vacuum or dye is required, which are ideal conditions for imaging biological samples. Another important advantage in studies of biological samples is the capability of scanning probes operating in air as well as in liquid, so samples can be scanned in their physiological buffer solutions. In STM, image contrast is derived from spatial variations in current flowing between the proximal probe and the sample. Then, despite many applications of STM in observations and manipulation of adsorbed organic molecules in self-assembly and molecular recognition studies [85, 86], its use has been limited in the biological field because samples need to be electrically conductive.

On the other hand, in AFM the physical scanning is based on attractive and repulsive atomic forces, does not requiring conductive samples, with lateral resolution limited by the finite size of the physical tip that is generally 5 to 10 nm and with a vertical resolution about 0.1 nm capable to probe an atomic monolayer. Thus, shortly after the emergence of AFM in the 1980s, the first applications of AFM in the study of biological matter emerged. Since then, different applications in the imaging of biological samples include visualization of virus morphology and investigation of mechanisms of virus assembly in virology studies [87-89]. Imaging of deoxyribonucleic acid (DNA) and protein-DNA complexes [90]. Study of chromatin and metaphase chromosome structures [91]. Imaging of changes on cell surface during bacteria life cycle induced by alteration in condition or treatment with antimicrobial agents that leads to a better design of antimicrobial drugs to combat the problems created by the increasing resistance to antibiotics (see Figure 1.5) [92-94]. Imaging of specific cellular structures such as cytoskeletons, filopodia, lamellipodia and microvilli in mammalian cells aiming to observe morphological changes in cancer cells after treatment with anticancer agents [95]. Visualization of interactions between proteins and misfolding proteins that usually evoke malfunctions such as seen in Alzheimer's disease [96].

Similarly, SECM has been applied to a variety of studies of biological interest at high resolutions comparable with those achieved using AFM. The studies include characterization of biological samples, studies of enzymes and membranes, electrochemical imaging and studying the uptake or release of chemical species due to processes in cells, and probing inside cells [97-99].

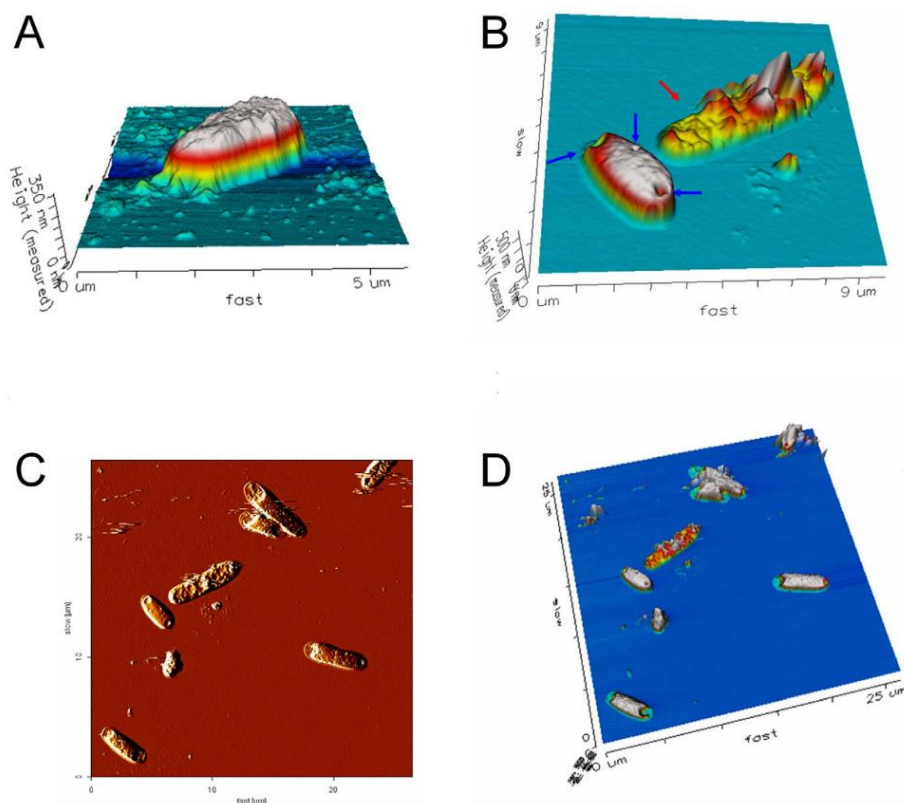


Figure 1.5. Representative AFM topographic images of photocatalyzed *E. coli* cells. The AFM images showed the cellular morphology of *E. coli* that was treated before (A) and after (B–D) C200-photocatalysis (visible light 1 minute). Compared to the control cell (A), C200-mediated photocatalysis greatly damaged certain bacteria, which appeared to be flattened (red arrow in B). Many of the bacteria cells were only partially damaged and many of them showed signs of beginning stage of the deformations. Holes are found on the cell surfaces (blue arrows in B). A two-dimensional vertical deflection image shows the best contrast and provide a clearer detail on the top of the cells (C). The height information indicated in figure D. Most of the bacterial damage appeared near the poles of the rod-shape bacteria (C, D). [94]

### 1.3.5 X-ray spectromicroscopy

X-ray spectroscopy is a general term for several spectroscopic techniques that use X-ray excitation (based on short-wavelength/high-energy photons). On reaching the surface of the sample X-rays interact with the matter much more deeply than either visible light or electrons and generate emissions based on processes of X-ray absorption or scattering (Fluorescence, Rayleigh scatter, Compton scatter, Photoelectron emission, Auger emission). By examining the energies from a determined emission, it is possible to determine the identity and local configuration of atoms present in a sample. The spectra also contain finer details, which can reveal chemical information specific to the sample studied.

Combining this X-ray spectral information with X-ray imaging is termed spectromicroscopy. This measures the local atomic-scale details of the structural and electronic environment of a chosen atomic species. X-ray photoelectron spectroscopy (XPS), also called electron spectroscopy for chemical

analysis (ESCA), is a type of long-wavelength X-rays (around 1 to 15 nm) spectromicroscopy elucidated by Kai Siegbahn in 1954, and the most widely used UHV surface analysis technique. Based on the photoelectric effect, observed in 1887 by Heinrich Rudolf Hertz and in 1902 by Philipp Lenard, and explained by Albert Einstein in 1905, it has the ability to provide elemental and chemical structure information of the extreme surface of biological samples (sampling depth of about 3 nm).

In biomedical surface science, XPS spectroscopy has been extensively used in the surface chemistry characterization of biological models to detect adventitious contaminants that may affect the biological interactions [100]. Also, in the optimization of surface modifications of titanium dental implants for better bone integration [101], as well as in monitoring of biological interactions such as adsorption of proteins and other biomolecules onto surfaces [102]. Due to similarities in the chemical composition of most biomolecules such as proteins, XPS is not ideal for fundamental chemical differentiation of amino acids, but still provides a great opportunity to elucidate information regarding the surface coverage and layer thickness [103]. Similarly, the applications of XPS spectromicroscopy in the biomedical field have been only on the surface chemical state image analysis of DNA microarrays (see Figure 1.6) [104, 105]. The lower applications in imaging biological systems may be due the fact that XPS optimal spatial resolution is still limited to 5-10  $\mu\text{m}$  due to the aberrations that occur inside the spherical photoelectron analyser, which leads to applications mainly in spectroscopy instead of microscopy mode.

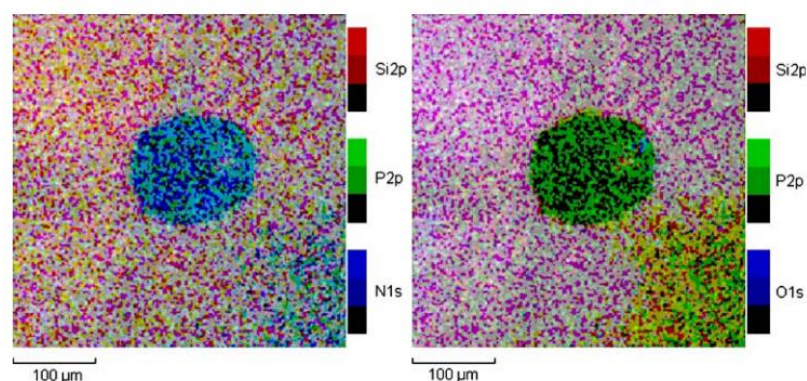


Figure 1.6. XPS images of a spot of an *E. coli* microarray printed on an amino-functionalized slide as an overlay of N 1s, Si 2p, and P 2p (left) and Si 2p, O 1s, and P 2p images (right), respectively. [104]

Photoemission electron microscopy (PEEM), however, is more appropriate to obtain images with chemical state information. Despite the first images PEEM were published in the early 1930s [106], it was only from 1972 the first applications of this technique in the imaging of tissues [107], cells [108-110], viruses [111, 112] and DNA [111, 113, 114]. Based on the same photoelectric principle as XPS, in PEEM photoelectrons are refocused into a real space image by the use of an aperture and a series of electron lenses. Recent advances in terms of aberration corrected lenses and light source facilities have led to an improved resolution of 5  $\mu\text{m}$  on biological samples ideal for microscopy. Its application in contemporaneous biomedical research is still rare and few recent studies have been found in the

literature. The most recent studies found in the matter include surface chemical mapping of blood cells and immune system cells activated by nanoparticles (see Figure 1.7) [115-117].

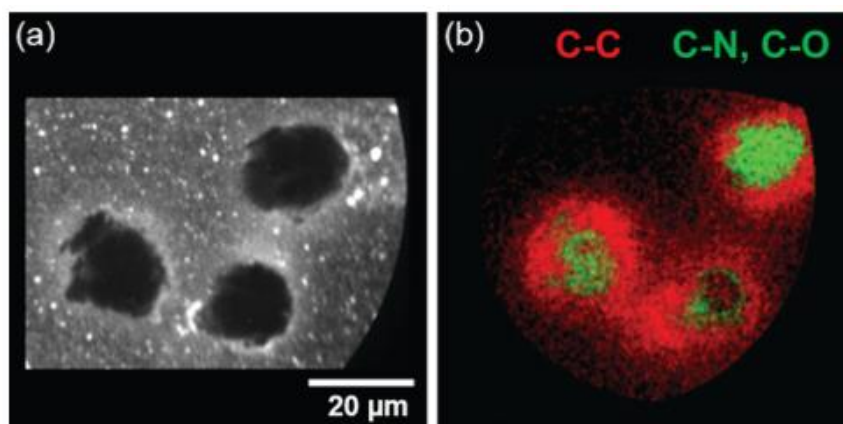


Figure 1.7. Energy-filtered PEEM image of neutrophil interactions with a silicon surface at  $E\text{-}EF = 4.0$  eV using monochromatized  $AlK\alpha$  x-ray excitation where neutrophils appear in dark and the silicon surface is bright in shades of grey (a). Spatially resolved chemical map of  $C1s$  core level distribution for C-C (red) appearing mainly in the cell membrane and C-N and C-O (green) appearing mainly in the cell nucleus (b). [116]

### 1.3.6 Mass spectrometry imaging

Mass spectrometry imaging (MSI) has also been widely applied as a technique for chemical imaging of biological surfaces. Introduced in the early 1960s using secondary ion mass spectrometry (SIMS) to study semiconductor surfaces, it was only in the late 1990s that matrix-assisted laser desorption/ionization (MALDI) was applied in the study of large biomolecules. Despite MALDI is the current dominant technology with regard to clinical and biological applications of MSI, recent advances in other ionization techniques such as SIMS have made them suitable to biological applications.

The MALDI technique is based on the mixing of the biological sample with a laser energy-absorbing matrix to generate ions from large molecules with minimal fragmentation. It has been mainly used as imaging technique for relatively large molecules due to its soft ionization method, however, at spatial resolution that ranges from 50 to 200  $\mu\text{m}$ . Lipidomic and proteomic studies for clinical diagnosis of cancers and neurodegenerative diseases have been some of the biomedical research field most benefited with its application (see Figure 1.8) [118-121].

In contrast, the SIMS technique is based on the sputtering of the surface of the sample using a focused primary ion beam and collecting and analysing ejected secondary ions. The SIMS imaging can be achieved by focusing and rastering the primary ion beam over a selected area, where the secondary ion intensity for a given mass-to-charge ( $m/z$ ) ratio is monitored as a function of position on the sample. Some common sources of primary ion beam are  $Cs^+$ ,  $O_2^+$ ,  $Ar^+$  and  $Ga^+$ , which have high energy per ion that causes high fragmentation of large molecules being then not appropriate to characterize biological surfaces. However, in the last two decades,  $Bi_3^+$ ,  $SF_5^+$ ,  $Au_3^+$ ,  $C_{60}^+$  and  $Ar_n^+$  ( $500 \leq n \leq 2500$ ) cluster ions

have also proved to be outstanding for surface characterization by SIMS. It is mainly because their ability to characterize surfaces and in-depth compositions with high secondary yields, minimal damage, high spatial resolutions ranging from 50 to 100 nm and high sensitivities for bioimaging applications.

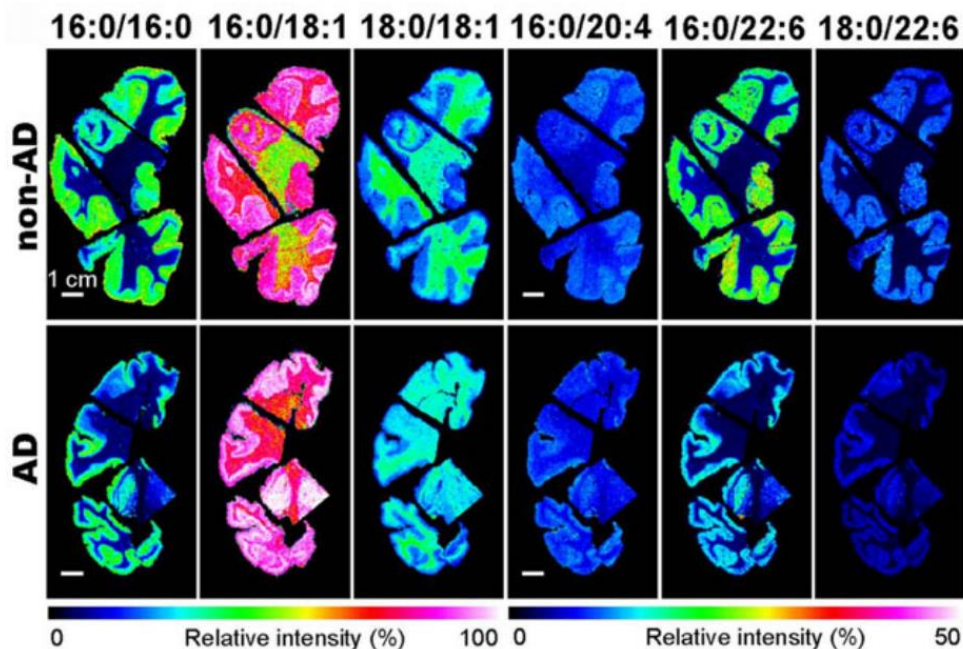


Figure 1.8. The distributions and intensities of phosphatidylcholines species in coronal sections of postmortem non-Alzheimer's disease (non-AD) and Alzheimer's disease (AD) human brains as analysed by MALDI-MSI e.g., PC molecular species containing PC (18:0/22:6) was selectively depleted in the grey matter of patients with AD. The scale bars show 1 cm. [121]

There are three basic types of SIMS instruments where the cluster technology can be applied: (1) Time-of-Flight Secondary Ion Mass Spectrometer (ToF-SIMS) that provides a mass spectrum based on the time of ejected secondary ions spend to travel along a known flight path to the detector. As the velocity of a given ion is inversely proportional to its mass, its flight time will vary accordingly, and heavier ions will arrive at the detector later than lighter ions. (2) Magnetic Sector SIMS instruments that are based on the deflection of ejected secondary ions by a combination of electrostatic and magnetic sectors analysers. As lighter ions deflect more than heavy ions, the ions of different mass will physically separate into distinct beams for later detection. (3) Quadrupole SIMS instruments that are based on a resonating electric field, where only ions with selected masses have stable trajectories through a given oscillating field. Although these are common designs in SIMS community, new instrument designs have emerged such as the combination of continuous ion beams with multiple mass spectrometers e.g., quadrupole/ToF for Tandem Mass Spectrometry (Tandem MS) analysis.

Because of the higher operating currents and continuous beams, both Magnetic Sector SIMS and Quadrupole SIMS instruments are not as ideal for surface analysis and characterization of samples that will charge and/or damage readily such as biological specimens. Due to the high primary ion dose

applied during an analysis, these are generally thought of as “dynamic SIMS” instruments. In ToF-SIMS analysis, however, the operating current is pulsed which allows the use of a primary ion beam dose that minimises the interaction of the primary ion beam with the top layer of molecules of the biological surface. This therefore limits the ion beam dose that can be used during an analysis to  $\approx 10^{12}$  to  $10^{13}$  ions  $\text{cm}^{-2}$ , which is known as static limit, and explain why this instrument is known as “static SIMS”.

ToF-SIMS has found since then many applications in biomedical surface science as follows. Visualization of lipids and proteins fragments directly from tissues and cells for studies on breast cancer and neurodegenerative disease [19, 30, 122, 123]. Mapping in vitro drug release through biodegradable membranes as well as imaging ex vivo drug distribution in diversified tissues after delivery system implementation [124-126]. Even more recent studies include SIMS imaging in the visualization of influenza viral envelope composition and depletion of virus assembly [127], simultaneous visualization of mineralized and non-mineralized bone tissue as well as bone implant interphases in osteoporotic bone research [128] and visualization of cocaine and methylphenidate effects on major lipids in *Drosophila* brain (see Figure 1.9) [129, 130].

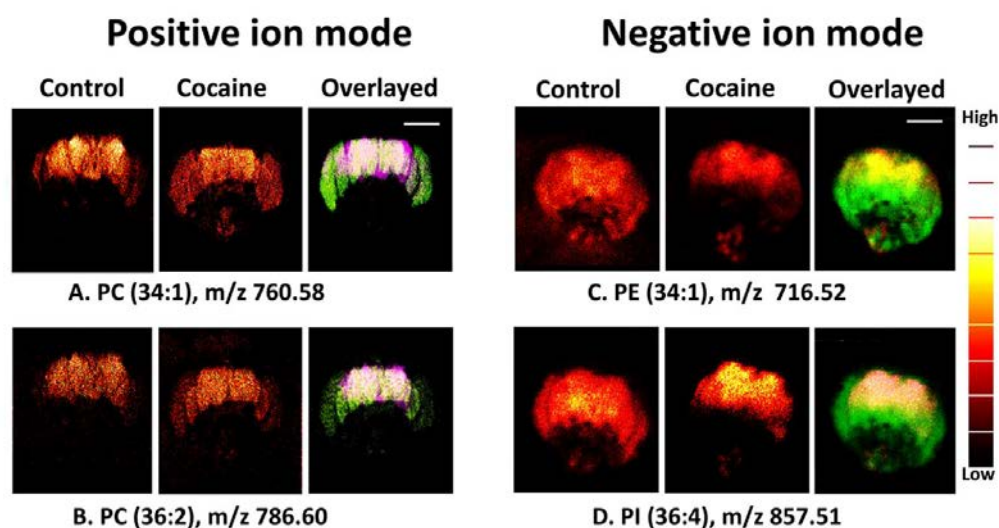
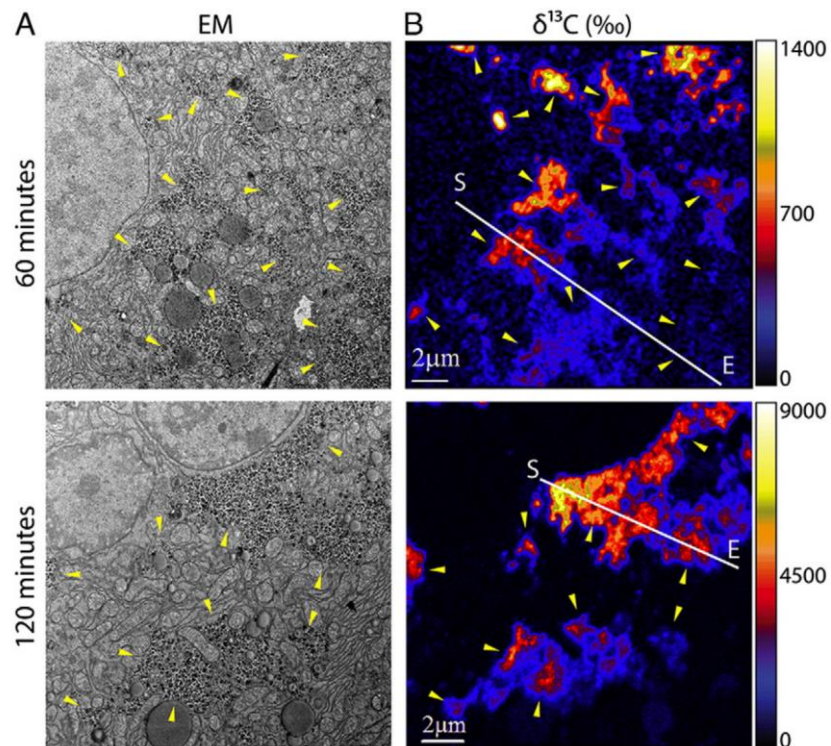


Figure 1.9. Distribution of phospholipids in the *Drosophila* brain before and after cocaine treatment by ToF-SIMS in positive and negative ion modes. Image area:  $800 \times 800 \mu\text{m}^2$  and  $256 \times 256$  pixels; pixel size,  $\sim 3 \mu\text{m}$ . [129]

The Nanoscale SIMS (NanoSIMS), also referred to as multi-isotope imaging mass spectrometry (MIMS), is a variation of SIMS instrumentation that was introduced in biology in the first half of the 2000s with the measurement of carbon and nitrogen isotopes of eukaryotic cells [131]. The NanoSIMS processes high lateral resolution of few tens of nanometres ideal to distinguish small patterns in the biological structure, but is still limited to the collection of elements and small fragments. Recent studies in biomedical surface science with the use of NanoSIMS include subcellular chemical exploration of cells and tissues [132, 133], intracellular measurement of accumulations and fluxes of molecules containing various stable isotopes aiming to reveal the location of several cellular proteins [134], and determination of the spatial distribution of nanoparticles and drugs such as within tumour tissues [135]. A large variety

of tissues have also been studied using nanoSIMS mainly through the application of isotopic-labelling techniques where main biochemical processes occurring within tissues could be followed. In heart tissues some examples include analysis of cardiomyocytes proliferation [136], and quantification of selenoproteins and lipoproteins in aortic endothelial cells [137, 138]. While in liver and brain tissues examples include imaging the spatiotemporal distribution of glycogen, neuromelanin and other neuroproteins in hepatic and cerebral metabolism (see Figure 1.10) [139-141].



*Figure 1.10. Nanometre scale imaging of liver glycogen synthesis from  $[U\text{-}^{13}\text{C}]$  glucose. (A) EM image of liver thin section prepared from a fasted mouse 60 min (top) and 120 min (bottom) after the first injection of  $[U\text{-}^{13}\text{C}]$  glucose, respectively; yellow arrowheads point to glycogen granules; (B) Quantitative NanoSIMS  $^{13}\text{C}$ -enrichment map of precisely the same region on the same thin sections. [139]*

In summary, each surface microscopy has its strengths and limitations when it comes to the analysis of biological systems. In addition to observing whether requirements such as UHV and electrical conductivity are compatible with the analysed biomedical system, technical parameters such as sensitivity and lateral resolution must be strongly taken into account when it comes to investigating biomedical issues. It is also important to be aware of how deeply a surface can be analysed. In terms of chemical analysis, among the aforementioned microscopies, vibrational imaging techniques are those with the highest sampling volume, while the spectromicroscopies are those with the lowest one, thus generating information from only the first monoatomic layers of the analysed surface. However, despite this "limitation", some microscopes are able to perform depth profiles, thus generating information from surfaces at different depths and consequently producing information from deeper areas.

Now that we got knowledge about the main surface microscopies currently used in biomedical research, we will introduce in the next subsection the use of medical implants such as neural electrode technologies and drug delivery systems at the same time as putting in evidence how some of the surface microscopy techniques seen above can be useful in the diagnosis and improvement of such biomedical technologies.

## **1.4 IMPLANTABLE TECHNOLOGIES AND INTERFACES BETWEEN SYNTHETIC AND BIOLOGICAL ENVIRONMENTS**

Over the past few decades, the tremendous advance in nanoelectronics, biocompatible systems and nanomaterials has led to the development of implantable devices capable of considerably improving the quality and effectiveness of healthcare. An implant is a medical device, which is used to replace or support any damaged body organs, improve the functioning of body organs, or treat defects in normal body functions. These can be surgically implanted either permanently or temporarily in the human body, and can be removed when necessary.

From the first pacemaker implant in 1958, the number of patients treated with cardiovascular implantable devices, artificial limbs, neuromodulators and drug delivery systems have been increasing. The pacemaker is the most well-known implanted medical device for heart patients used to treat irregular heartbeats known as arrhythmias, and provides electrical pulses to restore normal rhythm when irregular heartbeats are detected. Artificial hips and knees are commonly replaceable devices in chronic disabled patients with hips and knees damaged due to stress during lifetime or degenerative bone diseases. Neuromodulators are neural devices usually applied to substitute a motor, sensory or cognitive modality that might have been damaged as a result of a brain injury or disease. Some examples of neuromodulators comprise spinal cord stimulators (SCS), deep brain stimulators (DBS), Vagus nerve stimulators (VNS), sacral nerve stimulators (SNS) and transcranial magnetic stimulators (TMS). Drug delivery systems can be implantable devices that enable the introduction of a therapeutic substance in the body and improves its efficiency and safety by controlling the rate, time and place of release of drugs in the body in a wide range of chronic diseases.

With a worldwide active market worth USD 23.1 Billion in 2020 and expected to reach USD 33.6 Billion by 2025 with a 7.76% compound annual growth rate (CAGR), the implantable medical devices market represents an important part of the world economy [142]. In Table 1.1 below the previously cited and others contemporary implantable technologies are summarized with respect to the number of yearly users only in France, total market share, and CAGR.

Table 1.1. Worldwide users per year, total market size and CAGR for the most commonly clinically used implants.

<b>Device</b>	<b>Average users/yr only in France</b>	<b>Total Market Size in 2019 [\$Billion]</b>	<b>CAGR [%] for forecast 2020-2027</b>
Artificial knees	40,000	9.4	4.3
Coronary stents	200,000	5.9	6.7
Injectable drug delivery	Not found <sup>(1)</sup>	483.4	12.9
		<b>Total Market Size in 2018 [\$Billion]</b>	<b>CAGR [%] for forecast 2019-2026</b>
Cardioverter defibrillator	10,000	6.6	2.8
Cardiac pacemaker	40,000	4	3
Artificial hips	140,000	7.1	5
Dental implants	60,000	3.8	5.1
Hearing aids (devices & implants)	250,000	8.3	7.2
Neuromodulator devices	Not found <sup>(2)</sup>	4.5	9.5

<sup>(1)</sup> Injectable drugs is the most used way for medication in the world.

<sup>(2)</sup> It is estimated that more than 150,000 people globally have received a DBS implant.

Source: Business Fortune Insights | [www.fortunebusinessinsights.com](http://www.fortunebusinessinsights.com); published reports from 2019 and 2020.

Being electro-mechanical systems and still in the development phase, electronic implantable systems such as neuromodulators are inevitably prone to various types of failures. Design errors and technology limitations are certainly causing unavoidable and typical failures, mostly because the bio-environment inside a living being is reactive for the non-biological materials used to create electronics, electrodes, and system packaging. Thus, long term interaction with the human body may cause implant material degradation and eventual failure of the system. Nonetheless, consequences of implant failure could be as simple as a temporary discomfort, such as replacement of a broken tooth, or danger for a person, for example failure of a pacemaker. So, from an engineering perspective, the design of implantable devices must be constrained by a set of specific technology requirements such as biocompatibility, resistance to the reactive biological environment, density matched to biological tissue, and minimal tethering to adjacent structures [143].

### 1.4.1 Neuromodulator devices

In the nervous system, massive numbers of neurons constantly generate and transmit electrophysiological signals to communicate between neurons and brain regions. These signals have a critical role in coordinating the activity of different regions of the brain, including brain areas responsible for body motor control, and synchronizing neuronal assemblies involved in complex processes and functions, such as memory formation and neuroplasticity [144-146]. Nonetheless, the proper functioning of neural activities is directly linked to brain health and can be seriously compromised if injured or suffering from any disorder.

#### 1.4.1.1 Deep Brain Stimulation (DBS)

In people suffering from neurodegenerative disorders as diverse as Alzheimer's disease, Parkinson's disease, prion diseases, Huntington's disease, frontotemporal dementia, and motor neuron disease, a common aggregation and deposition of abnormal proteins in the intracellular and extracellular spaces is the main reason for intoxication of neuron cells from brain areas responsible for bodies motor control [147]. Once neuron cells are intoxicated, they consequently start to die and important neurotransmitters such as dopamine that participates in a number of functions in motor coordination, emotions, memory, reward mechanism and neuroendocrine regulation stop to be secreted. Figure 1.11 presents a schematic view of the brain region affected in particular by Parkinson's disease and its aggregation of misfolded proteins.

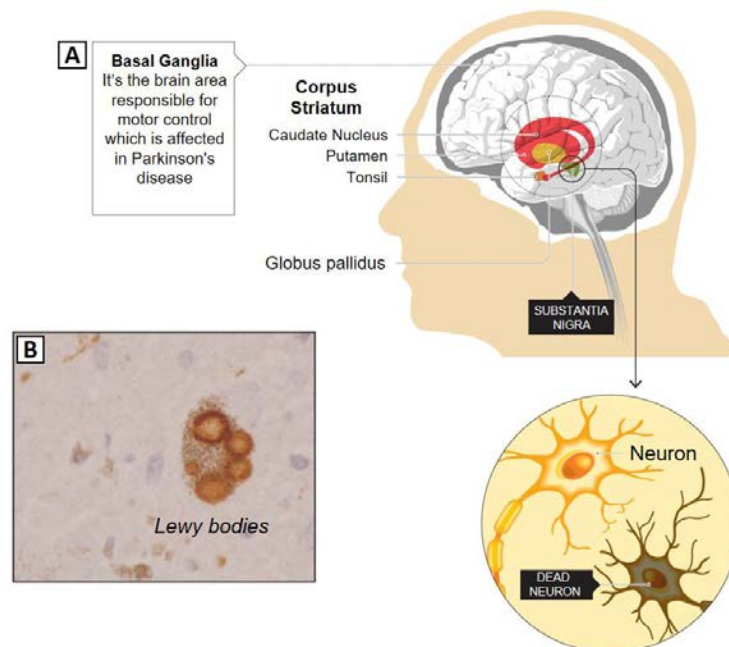
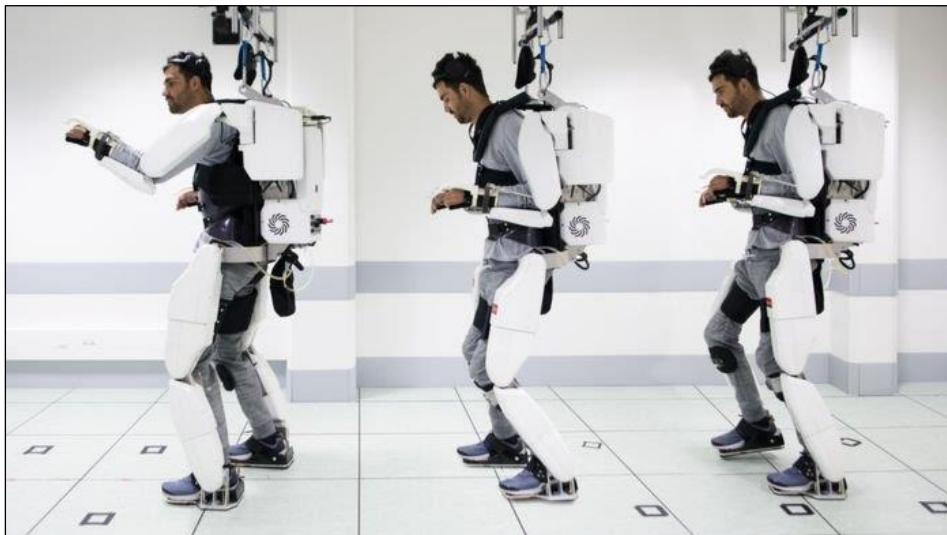


Figure 1.11. (A) A schematic view indicating the localization of the substantia nigra: the basal ganglia structure affected by Parkinson's disease and (B) optical image showing an aggregation of Lewy bodies in a nigral neuron. Magnification,  $\times 40$ . Adapted from [147].

In this regard, the clinical use of neural electrode technologies for stimulation of neural activities has provided remarkable benefits for people with a variety of neurologic conditions. In treatments based on the deep brain stimulation (DBS) technique, high-frequency electrical impulses are continuously sent to specific targets in the brain for mimicking the brain's normal electrical activity [148]. This stimulation is then capable of exciting neurons and axons to support again neurotransmitters creation and transmission, and consequently relieve symptoms such as bradykinesia, rigidity, tremor, and walk difficulties associated with Parkinson's disease, besides relieving dementia symptoms and memory loss evoked in Alzheimer's disease [149, 150].

#### 1.4.1.2 Brain Computer Interface (BCI)

In people suffering from neuromuscular impairments the nerves that control voluntary muscles and the nerves that communicate sensory information to the brain are affected and consequently limbs and torso movements are compromised. Such impairments can be caused by illness as diverse as stroke, amyotrophic lateral sclerosis, multiple sclerosis and Huntington's disease or damage to the brain or the spinal cord at a high level due to lifelong accidents. Since some neuromuscular impairments do not affect the mental functioning but only the communication of nerve cells with the brain, the clinical use of neural recording electrode technologies has made prominent contributions to modern neuroscience. It has been enabled detection of broadband neural signals from the extracellular space around neurons which can be largely used in brain-computer interface (BCI) technology as a radically new communication option for those with reduced mobility. It has been providing a new hope to reduced mobility patients allowing them move again through the control of neuroprosthesis and exoskeletons [151, 152].



*Figure 1.12. A man who did not walk doing his first steps in a robotic arms and legs controlled by the decoding of his motor cortex activity in real-time at Clinatex, France. (Photo by Louis Korczowski, 2019)*

The central element in BCI technology seen above in Figure 1.12 is a translation algorithm that converts electrophysiological input from the user into output that controls external devices [153]. The input is usually given by electrodes in contact with neurons recording neural broadband signals from the extracellular space that can be processed to extract signals in different frequency bands and voltages. At least two different types of voltage signals can be recorded — the slow-varying local field potentials (LFPs), which reflect collective transmembrane currents from multiple neurons, and high-frequency action potentials or spikes, which last on the order of milliseconds from individual neurons or single units. The latter represents the key activity to understanding the inner working of the brain besides the electrophysiological input of interest in BCI technology.

In general, the emplacement of neural devices is varied and includes applications on the surface of the scalp, on the surface of the brain or even inside the brain as we can see below in see Figure 1.13.

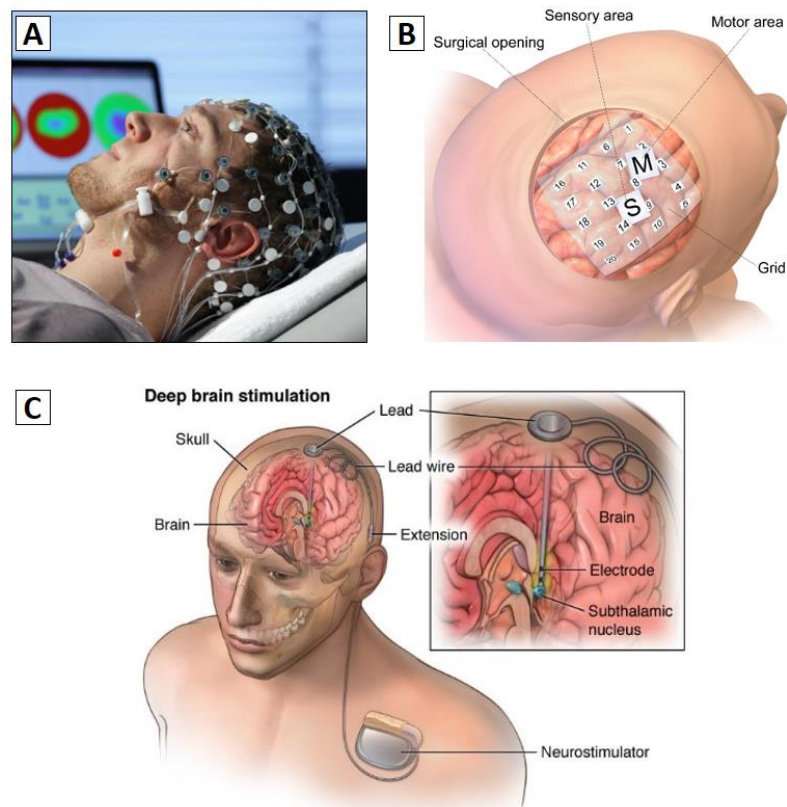


Figure 1.13. Possible emplacement of neural devices. (A) The surface of the scalp where an electroencephalography (EEG) monitoring is possible. (B) The surface of the brain where an electrocorticography (ECoG) monitoring is possible. Both emplacements are commonly used in BCI. (C) Emplacement of an invasive deep brain stimulation device inside the brain.

These different emplacements have their own advantages and disadvantages and directly depend on the purpose of the application. From the surface of the scalp, it is possible to establish an electroencephalography (EEG) monitoring of the brain electrical activity fundamental to diagnose epilepsy, sleep disorders, anesthesia, among others. Despite monitoring from the scalp being a non-

invasive method, devices with this emplacement have low spatial and temporal signal resolution. In contrast, from the surface of the brain cortex it is possible to establish an electrocorticography (ECoG) monitoring with higher signal-to-noise ratio in a partially invasive method that allows better recording of electrical activities for BCI applications. Conversely, through penetration electrodes positioned close to the neurons inside the brain we can monitor but also stimulate individual neurons or small neural populations inside the brain, which is ideal for DBS treatments.

However, despite the widespread application of neural electrode implants and their remarkable support for advances in neuroscience, their chronic use is still limited by technical difficulties such as chronic immune response, shear motion of implanted probes, chemical instability of electrodes, delamination and degradation of insulating layers and potential infection through percutaneous [144]. The uncontrolled chronic immune response is considered the main cause of device signal loss due to increased electrical impedance attributed to the brain tissue reaction against the neural device (see Figure 1.1). This immunological response consists in several inflammatory phases initially evoked from the mechanical mismatch between the soft neural tissue and stiff implants that ultimately result in loss of neurons in implant vicinity and the formation of a dense fibrous sheath of hundreds of micrometres that encapsulates the device [154-156]. In Figure 1.14 is given a comparison between the stiffness of common materials used in the manufacture of neural devices and living cells.

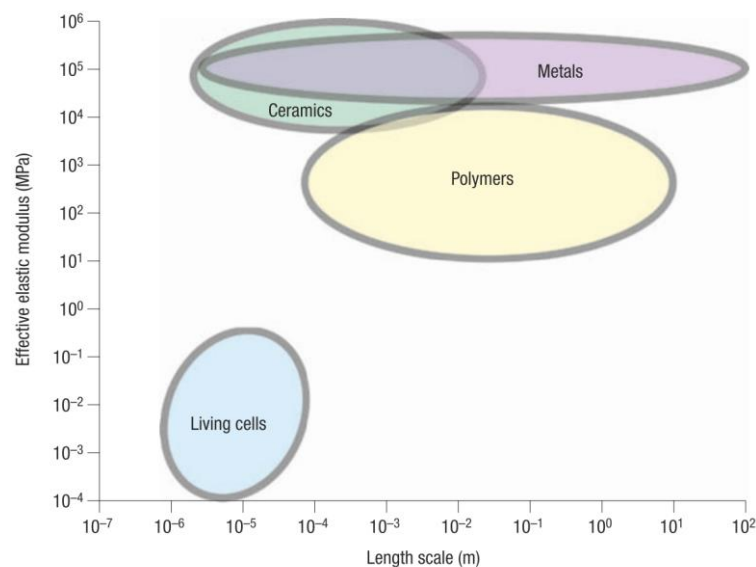


Figure 1.14. Approximate range of values for the elastic modulus of biological cells and comparisons with those of engineering metals, ceramics and polymers. [157]

Since these inflammatory reactions mainly occur at interfaces between synthetic materials and biological environments, a stable electrode–brain interface should minimize the chronic immune response and avoid disturbing the natural distribution of neurons and other non-neuronal cells. Thus, the development of new neural technologies aiming to achieve long term recording or stimulation stability strongly

depends on previous interfacial knowledge [5, 144]. In this context, microscopic correlative approaches can be extremely useful in observing interfacial properties between implantable synthetic materials and biological environments allowing evaluation of topographic and chemical characteristics of neural devices after implantation time as well as of the biological tissue in contact with them. In cases of reaction of the cortical tissue against the chronic use of implantable electrodes, combined analysis approaches can be used to discover the main interfacial causes of incompatibility, including possible chemical instability of implantable devices that usually intoxicate neurons through involuntary release of toxic elements, as well as to follow the main characteristics of biological tissues under inflammation.

#### **1.4.2 Drug Delivery Systems (DDS)**

In clinical medicine, drugs and other therapeutic agents are commonly administered in patients to treat specific diseases and disorders with the goal of achieving desired pharmacological effects with minimum side effects. Nevertheless, physiological barriers to efficient drug delivery, such as transport in the circulatory system and drug movement through cells and tissues, and side effects due to the drug interacting with healthy tissues that are not the target of the drug, can limit the development of optimal medications for many diseases.

In this regard, the application of drug delivery systems (DDS) is nowadays a central strategy to enhance the therapeutic efficacy and safety of drugs and therapeutic molecules. A DDS can be considered as a new method or process of administering a pharmaceutical compound able to ensure a higher and longer duration of drug bioavailability besides to control the location in the body where it is released. In spite of still having some drawbacks and limitations in specific applications, it has been increasingly used to maximize treatment impact for a wide range of chronic diseases, such as diabetes, cancer, atherosclerosis, myocardial ischemia, asthma, pulmonary tuberculosis, Parkinson's disease, and Alzheimer's disease [158].

The current research in DDS comprises studies in four broad categories: routes of delivery, delivery vehicles, cargo, and targeting strategies. The central goal in (1) routes of delivery research is to improve current delivery methods such as by swallowing, inhalation, absorption through the skin or injection, as well as designing new ones that can enhance the use of existing medications. Conversely, in (2) delivery vehicles research the main goal is the development of suitable and biocompatible drug delivery vehicles [159]. A wide variety of organic, inorganic, polymeric and metallic nanostructures, including functionalized dendrimers, micelles, solid lipid nanoparticles, carbon nanotubes, hydrogels and liposomes, are frequently used as targeted and controlled drug delivery vehicles. Moreover, (3) cargo research focuses on the medication themselves where, in addition to drugs and novel vaccines, researchers are also exploring the use of genes, proteins and stem cells as treatments. Whereas, (4) targeting strategies aim to improve the targeting of whole organs (heart, lung, brain), tissue types (muscle, nerve), disease-specific structures (tumour cells), or structures inside of cells.

### 1.4.2.1 DDS in brain cancer treatment

In patients suffering from malignant brain cancers, such as anaplastic astrocytoma and glioblastoma, surgery is currently the first-line treatment for tumour resection. However, despite surgical intervention, recurrent tumours, which have the same characteristics as the original one, grow in close vicinity to the original site due to the infiltrating nature of the tumour cells. Herein, surgical brain injury due to surgical intervention can also contribute to glioma recurrence at the resection margin [160]. This association is related to the fact that chronic inflammation and post-lesional angiogenesis act as tumour promoters. In Figure 1.15 we can see an example of glioma recurrence after surgical procedure. Therefore, inflammation mediators and other components of the central nervous system wound-healing process as well as growth factors found in injured brains known to promote tumour growth can be considered valuable therapeutic targets in a possible drug delivery treatment [161].

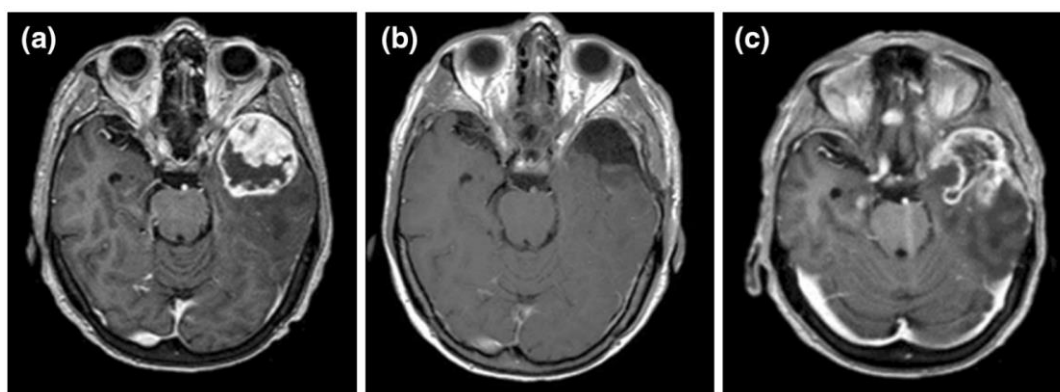


*Figure 1.15. Glioma recurrence at the resection margin. (a) Contrast-enhanced MRI scan at the time of diagnosis showing a temporal glioblastoma with typical peripheral hyper-intense lesion surrounding a necrotic hypo-intense core. (b) 48 h post-operative MRI scan, showing a macroscopically complete resection with no residual hyper-intense signal. (c) Local recurrence occurring 6 months later in the margin of the surgical cavity. [161]*

Injectable biodegradable hydrogels have been a combined type of route and vehicle widely utilized for cell/drug delivery applications in cancer therapy [162, 163]. Intratumor drug delivery with injectable biodegradable hydrogels has attracted much attention because they can provide a sustained and controlled drug delivery within the target tumour site while minimizing the adverse effects of systemic exposure to the drug. In addition, localized therapy with injectable hydrogels present high solubility, which lessen the required amount of drug and increase the amount that reaches the tumour site [164, 165].

In terms of medication, nonsteroidal anti-inflammatory drugs (NSAIDs) are of great interest in cancer treatment. Besides their use as analgesics in primary cancer surgery, studies suggest that NSAIDs could prevent cancer development and progression. Especially in therapies based on the use of ketorolac tromethamine [166]. In this context, microscopic approaches can be extremely useful in observing the resorption of hydrogel and diffusion of drugs in the neural tissue. This type of information

is extremely important to understand the behaviour of the routes of delivery selected and if the drug has reached or not its therapeutic target.

## 1.5 OBJECTIVES OF THIS THESIS

As we noticed in the previous sections, as long as medical science is increasingly engaged to overcome the limitations of the human organism through the use of implantable technologies, the interface between synthetic and biological environments will be of critical importance in the development of more efficient and biocompatible implantable technologies. In this context, advances in surface sensitive analysis methods, but also analytical approaches and data analysis techniques are increasingly considered to be fundamental of outmost importance for providing a better understanding of such complex interfaces.

With regards to the analytical approaches, multi-modal analysis that aim to correlate information from different surface sensitive imaging techniques has been specially highly required in the monitoring of biological interfaces. It is mainly because each method of analysis has its own advantages and disadvantages with respect to analysing complex surfaces such as the biological ones [167].

**General objective:** The general objective of this thesis will then consist in implementing a correlative surface imaging approach aiming at providing multimodal and multiscale imaging from a same target region of analysis. This will use a combination of modern surface analysis methods with the ultimate goal of acquiring chemical and morphological information from biomedical interfaces such as found in non-human brain tissues holding biomedical technologies e.g., drug delivery systems used in the treatment of glioblastoma and neural devices used as brain-computer interfaces.

One of the main scientific challenges currently faced in biomedical surface science and one which we address in this thesis is how to map out chemical and morphological properties of biomolecules directly in their biological environment in a similar way as has been done for simple molecules during the past decades in surface science [4].

**Intermediate objectives:** There are three intermediate objectives of this work:

- Identification of chemical surface species presents in the biological system,
- Identification of chemically and morphologically distinct regions in the biological system,
- Quantification of the surface composition in each distinct region.

The multimodal surface imaging approach that will be implemented in this work, and that will be explained in the next section (see subsection 2.1), will comprise the combination of surface analytical methods such as ToF-SIMS, Tandem MS, photoemission techniques such as XPS and PEEM, and AFM. This correlation should be capable of identifying and quantifying the main chemical elements, functional groups and molecules present in a biomedical surface as well as monitoring surface morphology. It is an approach never used before in the study of non-human brains in contact with drug

delivery systems or neural devices. Since massive amounts of data will be produced, data analysis techniques such as Principal Component Analysis (PCA) is also used to reduce large amounts of data to a small number of more useful variables, discarding noise and discerning trends and patterns in the data.

The aforementioned objectives of this thesis are achieved at three gradual levels of sophistication: first a multimodal surface imaging of non-biological samples at different zones of interest for analysis is implemented (level 1), then the multimodal surface imaging is applied on a same organic sample but still at different zones of interest for analysis (level 2); then finally, we considered a correlative multimodal surface imaging approach on a same biological sample in a same zone of interest for analysis. This gradual approach will allow us to identify possible problems in our analytical strategy without attributing them to the complexity of the biological surfaces studied. A schematic view of the three levels of sophistication of our multimodal surface imaging approach is given in Figure 1.16 and explained below.

### Levels of sophistication of the multimodal surface imaging approach

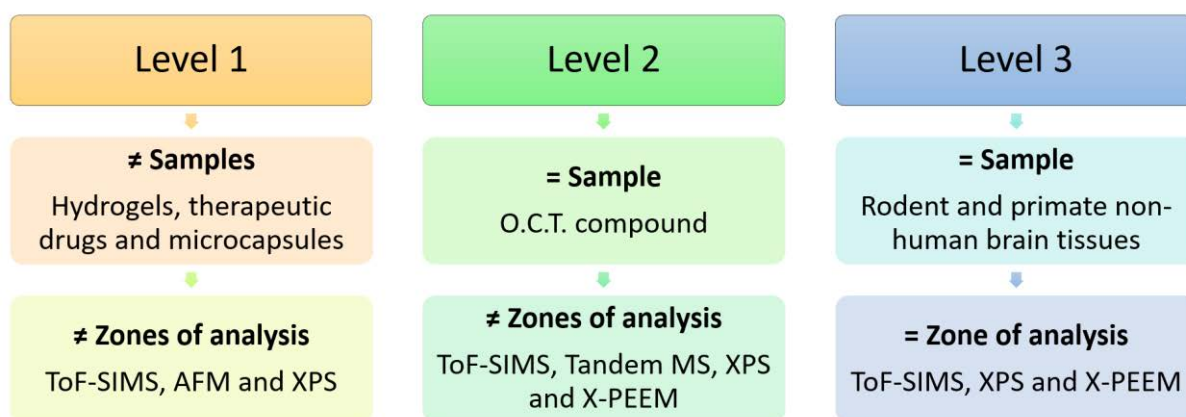


Figure 1.16. Three gradual levels of sophistication of the proposed multimodal surface imaging approach. The first stage will concentrate the correlative surface analysis from over different synthetic and biocompatible drug delivery systems at different zones of analysis. The second level of analysis will concentrate on a single O.C.T.<sup>TM</sup> Compound hosting a biological tissue at different zones of analysis. The third level will focus on a same target region of analysis on a same biological surface hosting biomedical technology.

In the first level of sophistication of our multimodal surface imaging approach, different samples and areas of interest for analysis will be explored. A synthetic and biocompatible drug delivery system that have not yet been injected into a non-human brain was chosen to be analysed in this first level. This drug delivery system will be a hydrogel that contains therapeutic drugs such as the anti-inflammatory ketorolac tromethamine and gellan gum microcapsules used as intelligent drug delivers, both are biomedical strategies used in the treatment of glioblastoma. The main interest in the use of a multimodal surface imaging approach here will be in the mapping of therapeutic drugs and microcapsules in hydrogel that is considered an important information in understanding their dispersion in hydrogel even for after implantation in living organs.

In the second level of sophistication of our multimodal surface imaging approach, a same sample at different areas of interest for analysis will be explored. A synthetic and biocompatible O.C.T.<sup>TM</sup> Compound hosting a non-human neural tissue commonly used in the preparation of biological samples. The main interest in the correlation of surface microscopies in this second level will be mainly in acquire chemical information from a same sample. The accomplishment of this analytical strategy on an organic compound will be extremely important in creating a know-how for the reoperation of regions of interest on biological surfaces.

In the third level of sophistication of our multimodal surface imaging approach, a same target zone of interest for analysis in a same biological sample will be explored. A rodent and a non-human primate brain hosting biomedical technologies will be explored. The main interest in the correlation of surface microscopies in this last stage will be in mapping hydrogels used in the treatment of glioblastoma after 3 months of implantation in a non-human brain. In addition, with the correlation of these surface microscopies we will seek to understand why an uncontrolled inflammatory reaction was triggered in a non-human brain around an implanted neural device.

## 1.6 THESIS OUTLINES

In chapter 2 all experimental information useful to understand the development of this work will be described. The first section will present the multimodal surface analysis approach proposed to be ultimately applied over biological tissues through combining ToF-SIMS, Tandem MS, XPS, PEEM and AFM in three levels of sophistication. The second section will present the protocols of sample preparation used in this work. It comprises information about the formulation of the drug delivery systems and the sample preparation protocol used over non-human brain tissues before analysis. Finally, the third section will present technical information about the main surface microscopy techniques used in this work.

In chapter 3 we will find the results of the first level of sophistication of our multimodal surface analysis approach on a synthetic and biocompatible system. In this first stage, we will see how ToF-SIMS enables the unprecedented visualization of the dispersion of ketorolac tromethamine in hydrogel as well as the dispersion of micro capsules used as intelligent drug deliverers. From the use of XPS we will be able to quantify chemical environments and determine C 1s high-resolution spectra characteristic of hydrogel systems containing ketorolac tromethamine and micro capsules. Finally, we will see how AFM will be used in exploring the morphology of micro capsules. The AFM analysis has great potential for application in studies of understanding mechanisms of absorption and release of drugs by these intelligent drug deliverers.

In chapter 4 we will see the results of the second level of sophistication of our multimodal surface analysis approach over an organic system hosting a non-human biological tissue. In this second stage, we will reach the correlation of all chemical analysis methods over different target regions of analysis in a same organic sample. We will also see how ToF-SIMS will be able to highlight regions of chemical

contrast over a same material, and how Tandem MS will be an important tool to confirm the existence of specific molecules in these regions of contrast. From XPS data we will be able to quantify the chemical environment in each of these regions of contrast and understand which types of molecules are mostly present in one region in relation to another. This is an important piece of information that could not be obtained over organic or biological systems only from mass spectrometry analysis. With the application of PEEM we will be able to obtain the same kind of information obtained by XPS from the regions of contrast but over a wider region and with detailed lateral distribution.

In chapter 5 we will find the results of the third level of sophistication of our multimodal surface analysis approach over non-human neural tissues containing hydrogel as a drug deliverer and neural device as a brain-computer interface. In addition to the identification of native biomolecules from biological tissues, biomedical technologies and the effects of these implantable technologies on the biological tissue will be imaged. From the application of ToF-SIMS imaging we will be able to identify the existence of hydrogel used as drug deliverer in a non-human brain after three months of implantation. With the mapping of the hydrogel, we will be able to confirm its good position over a target tissue in the treatment of glioblastoma. Similarly, the ToF-SIMS imaging of chemical patterns in the non-human neural tissue that was once in contact with a neural device used as brain-computer interface indicate severe inflammation on the biological tissue with an early case of necrosis. The presence of particles of metals spread in this tissue reveals a possible cause of uncontrolled encapsulation of the neural device and tissue necrosis. Quantification of the elemental composition and the imaging of the chemical bond states in areas of interest in the non-human neural tissue will be accomplished with XPS and X-PEEM analysis.

In chapter 6 we will find the manuscript ends with the general conclusions about the multimodal imaging approach applied to different biomedical systems and the perspectives of surface-sensitive microscopies for the analysis of biological interfaces in the future.

## 2 EXPERIMENTAL DESCRIPTION

---

In the first section of this second chapter (2.1), we will describe the multimodal surface imaging approach that should be applied in three gradual stages of validation: first on a synthetic and biocompatible drug delivery system, then on an organic system hosting a biological tissue, and finally, on a biological tissue that contains biomedical technologies such as hydrogel as drug deliver and neural device. In the second section of this second chapter (2.2), we will describe the protocols of sample preparation intended to be analysed in the three levels of the multimodal surface imaging approach. Firstly, we will describe the preparation of the HA hydrogel-based drug delivery system that contains ketorolac tromethamine and gellan gum microcapsules. Next, we will present the O.C.T.<sup>TM</sup> Compound commonly used in the embedding and sectioning of biological tissues. Then, we will describe the implantation of biomedical technologies such as drug delivery systems and neural devices in non-human brains as well as the tissue sectioning for correlative surface analysis. In the third section of this second chapter (2.3), we will present the technical information about the main surface microscopy techniques used in this work.

### 2.1 MULTIMODAL SURFACE IMAGING APPROACH

As introduced in the previous chapter, a biomedical surface is not necessarily a surface of a biological sample extracted from a living organism but can also be organic and functionalized materials developed to be in contact with biomolecules. Knowing that, the following analytical strategy was developed in order to provide detailed multimodal and multiscale observations from biomedical surfaces as follows.

- **1<sup>st</sup> action: perform a chemical mapping of a large area on the sample.** The biomedical surface must initially be imaged with a large field-of-view (FoV) in order to identify areas of interest for correlative analysis based on chemical contrasts. Therefore, ToF-SIMS offers the option of acquiring mm size images over biomedical surfaces from putting images or tiles up to 500  $\mu\text{m}^2$  with 256  $\times$  256 pixels together. This kind of mm size image is what we will call by "macro image" or "mosaic image". The image resolution is associated with the pixel size and might be about 1.95  $\mu\text{m}$  for using these parameters. The mass resolution  $\left(\frac{M}{\Delta M}\right) \approx 4000$  of ToF-SIMS for these imaging parameters is also an advantage and allows us to measure the mass of ions of interest with good accuracy. In the case of chemical mapping of a large area is performed by ToF-SIMS on highly complex biomedical surfaces such as biological tissues, which have a large variety of biomolecules, PCA can be applied with the aim of highlight trends and patterns in the data.
- **2<sup>nd</sup> action: confirm the existence of certain molecules in regions of chemical contrast or explore morphological contrasts.** Once the zone of interest is identified, if there are doubts about the veracity of any molecule detected in the ToF-SIMS spectrum, Tandem MS can be used in order to study the fragmentation of that particular molecular ion. Conversely, if the zone of interest has chemical contrasts that may be associated with differences in topography on the

surface of the region of interest, AFM can be used to detect topographic variations up to 100  $\mu\text{m}$  (xy-direction) and 10  $\mu\text{m}$  (z-direction).

- **3<sup>rd</sup> action: quantification of chemical environments in regions of chemical contrast.** The quantification of the chemical environments presents in regions of interest showing chemical contrasts previously highlighted by ToF-SIMS or Tandem MS or even showing topological contrasts highlighted by AFM must be performed by XPS analysis.
- **4<sup>th</sup> action: imaging of chemical environments in regions of chemical contrast.** When regions of interest are already identified and characterised by correlative surface microscopy analysis, PEEM can be used for mapping of the distribution of chemical environments on the biomedical surface. This action must be considered the last one because among all the previous ones it will be considered a destructive analysis, that is, the organic or biological region of interest where correlative analysis was performed will be destroyed by the long exposure to X-rays and no more analysis in this same region will be possible.

Figure 2.1 summarizes the analytical protocol to be adopted described above.

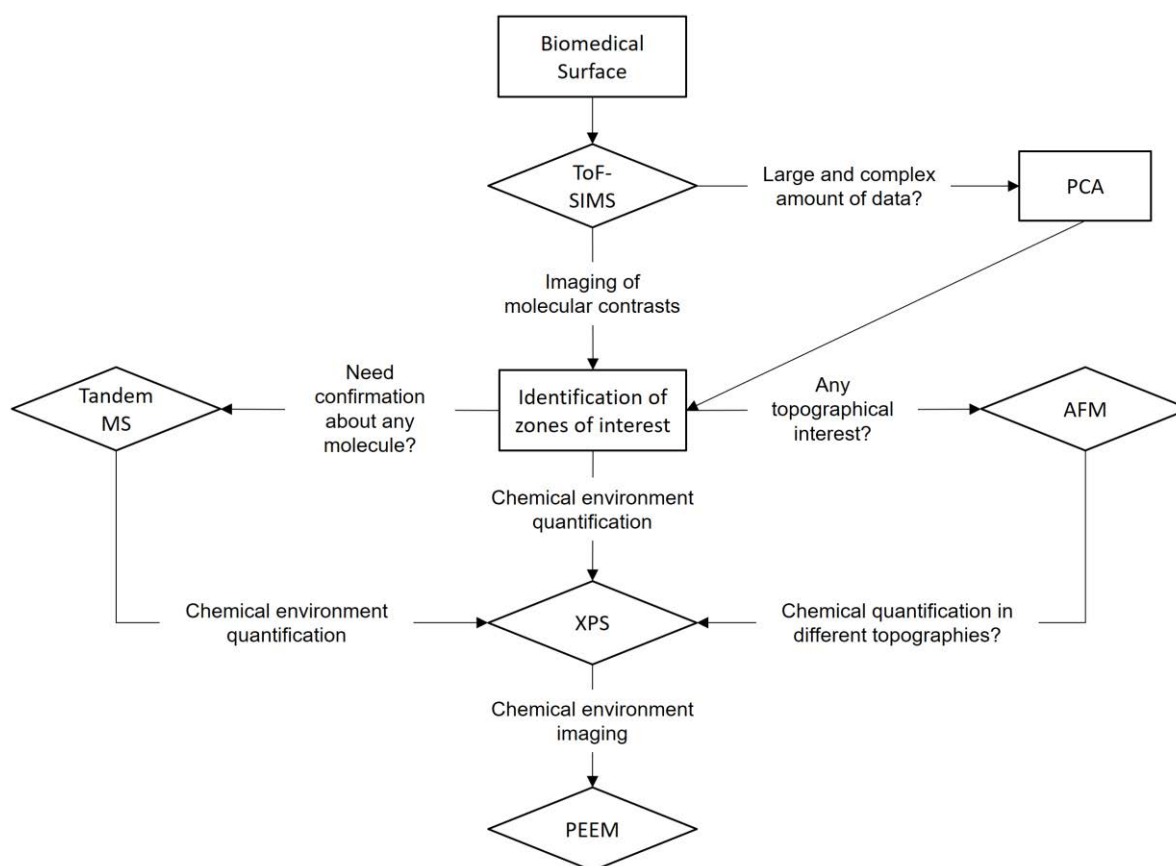


Figure 2.1. Schematic view of the analytical strategy developed for the ultimate analysis of biomedical interfaces.

## 2.2 PROTOCOLS OF SAMPLE PREPARATION

In this second section we will describe the preparation of samples used in this work.

- The preparation of hydrogel-based drug delivery system with ketorolac tromethamine and gellan gum microcapsules.
- Then we will be understanding about the organic compound used in the embedding and sectioning of the biological tissues.
- Then, we will describe the implantation of biomedical technologies in non-human brains as well as the tissue sectioning for combined analysis.

### 2.2.1 Preparation of hydrogel-based drug delivery systems

The hydrogel-based drug delivery systems fulfilled with ketorolac tromethamine and gellan gum microcapsules analysed in this work were fabricated by our collaborators Antoine Hoang and Claire Verplanck in the Department of Micro-Technologies for Biology and Health (DTBS) of CEA-Leti. The hyaluronic acid (HA) used by them as hydrogel is a natural linear polysaccharide that consists of alternating units of D-glucuronic acid and N-acetyl-D-glucosamine that has emerging as an appealing starting material for hydrogels design in brain drug delivery due to its biocompatibility, native biofunctionality, biodegradability and non-immunogenicity. Figure 2.2 shows the molecular structure of the hyaluronic acid.

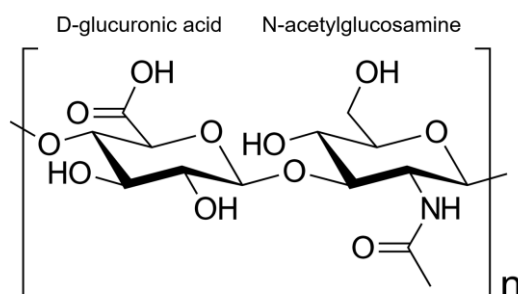


Figure 2.2. Molecular structure of hyaluronic acid.

The protocol of preparation of HA hydrogels used as drug deliver is given as follows. Initially, a hyaluronic acid (HA) and bis(oxymanine) linker (BOL) solution is prepared. The solution is then spilled into cylindrical moulds where crosslinking will occur. The cross-linked hydrogel is subsequently demoulded and freeze-dried at  $-47\text{ }^{\circ}\text{C}$  and 37 Pa. This step is essential for analyses performed under UHV environments. After the freeze-drying process, the hydrogel does not have a gelatinous aspect anymore and becomes a solid and fragile structure that can be broken into pieces. One of the small pieces of hydrogel is then placed into a  $1\text{ cm}^2$  silicon substrate compatible in size with all analytical methods used in the protocol of analysis.

A scheme of the preparation of hydrogel used as a drug deliver is illustrated in Figure 2.3.

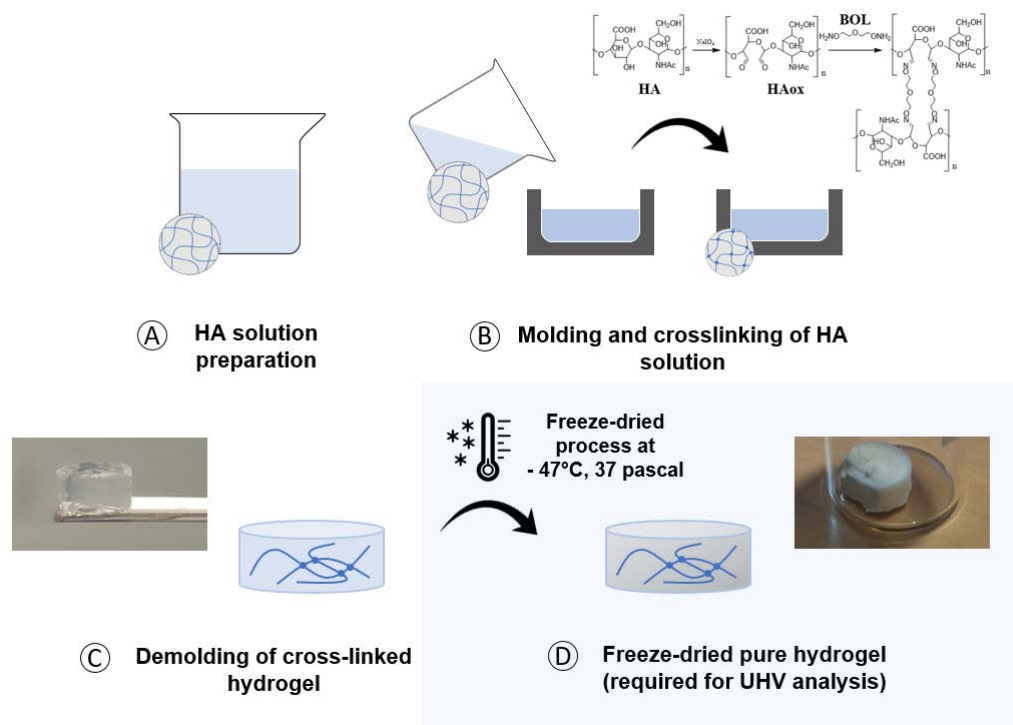


Figure 2.3. Schematic diagram for the preparation of hydrogel samples for analysis under UHV conditions. (A) Preparation of hyaluronic acid (HA) and bis(oxymanine) linker (BOL) solution. (B) Solution is spilled into cylindrical moulds where crosslinking occurs. (C) Demoulding of cross-linked hydrogels. (D) Lyophilized hydrogel.

The formulation protocol applied in the development of cylindrical and freeze-dried hydrogels is basically the same applied in the production of hydrogel formulations with ketorolac tromethamine and gellan gum microcapsules as we will see below.

### 2.2.1.1 Addition of ketorolac tromethamine in hydrogel formulations

The 2-amino-2-(hydroxymethyl)propane-1,3-diol;5-benzoyl-2,3-dihydro-1H-pyrrolizine-1-carboxylic acid also known as ketorolac tromethamine with the molecular formula  $C_{15}H_{13}NO_3$  (see molecular structure in Figure 2.4) is a non-steroidal anti-inflammatory drug with potent analgesic and moderate anti-inflammatory activity commonly used in the treatment of glioblastoma.

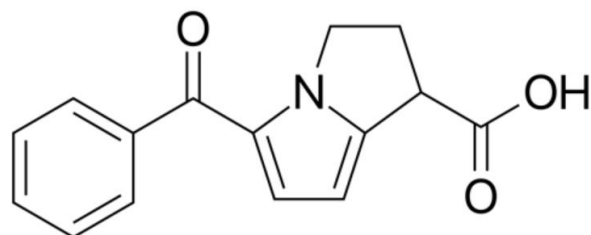


Figure 2.4. Molecular structure of ketorolac tromethamine.

In order to produce formulations of hydrogel containing ketorolac tromethamine, 2 and 10 mg of ketorolac tromethamine were added into the hyaluronic acid (HA) and bis(oxymanine) linker (BOL) solution. The HA solution containing ketorolac tromethamine is then spilled into cylindrical moulds where crosslinking will occur. Then, steps such as crosslinking, demoulding, freeze-drying, and placement of pieces of hydrogel containing ketorolac tromethamine into silicon substrate occur as the same mentioned for pure hydrogel.

### 2.2.1.2 Addition of gellan gum microcapsules in hydrogel formulations

The gellan gum is a biocompatible polysaccharide obtained from the bacteria *Sphingomonas elodea*. It is a linear anionic exopolysaccharide, with the repeating unit consisting of L-rhamnose, D-glucose and D-glucuronate in the molar ratios 1:2:1 (see Figure 2.5). It has specific gelling properties in different media leading then to the development of controlled release forms based on gellan. In the context of this work, gellan gum microcapsules were used as an alternative vehicle in drug delivery in order to replace the free presence of drugs such as ketorolac tromethamine in hydrogel.

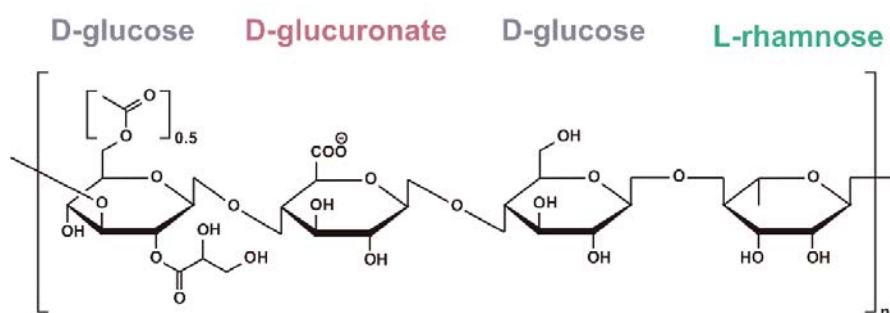


Figure 2.5. Molecular structure of high-acyl form of gellan gum consisting of D-glucose, D-glucuronate and L-rhamnose units.

The drug delivery via gellan gum microcapsules can be considered intelligent because when applied in environments with higher temperatures, such as inside the human body, it allows a slow and prolonged release of medication held inside the microcapsules.

However, the gellan gum microcapsules that size about 50  $\mu\text{m}$ , introduced in hydrogel formulations will not be fulfilled with ketorolac tromethamine but they will be introduced empty directly into HA solutions instead. Then, steps such as crosslinking, demoulding, freeze-drying, and placement of pieces of freeze-dried hydrogel containing gellan gum microcapsules into silicon substrate occur as the same mentioned for pure hydrogel and hydrogel containing ketorolac tromethamine. Details on the manufacture process of gellan gum microcapsules are not mentioned.

### 2.2.2 Cross section of biological tissues embedded in resin

The cross section of rat brain and glial scar tissue analysed in this work were prepared using a resin to facilitate tissue sectioning by our collaborators Christophe Gaudé and David Ratel in Clinatéc in the

context of the Brain-Computer Interface (BCI) project. The Optimal Cutting Temperature compound (O.C.T.<sup>TM</sup> Compound) used is a resin made of approximately 10.0% of polyvinyl alcohol (PVA), 4.5% of polyethylene glycol (PEG) and 85.5% of non-reactive ingredients that is commonly used to embed tissue samples prior to frozen sectioning on a microtome-cryostat. It also provides benefits in the analysis of biological tissues such as stabilizing the fine details of the tissue, preventing the samples from drying out, and allowing long-term preservation. Once the biological tissue is embedded in O.C.T.<sup>TM</sup> Compound, there are few reliable methods for separating them, so both are commonly sectioned and affixed together on a flat surface for analysis. The O.C.T.<sup>TM</sup> Compound will be present at the margins of the biological tissue along this work.

Figure 2.6 below illustrates this situation showing a random biological material embedded in O.C.T.<sup>TM</sup> Compound and an optical image of the O.C.T.<sup>TM</sup> Compound surrounding a biological tissue after section production and affixation onto 1 cm<sup>2</sup> silicon substrate.

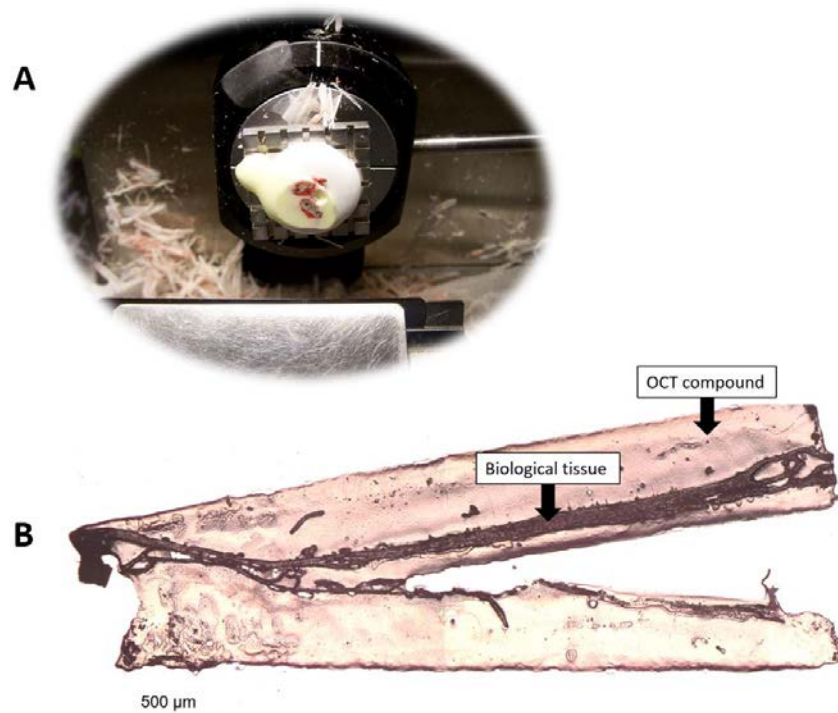


Figure 2.6. (A) Random biological material embedded in O.C.T.<sup>TM</sup> Compound, mounted on a chuck in a cryostat and ready for section production. (B) Optical image of O.C.T.<sup>TM</sup> Compound resin (in lighter colours) surrounding a biological tissue (in darker colours) after frozen sectioning and affixation onto 1 cm<sup>2</sup> silicon substrate. The surface of the silicon substrate is not visible due its ability to reflect the visible light.

### 2.2.3 Neural tissue hosting a Drug Delivery System

Hydrogel without any medication was prepared from hyaluronic acid (HA) and bis(oxymanine) linker (BOL) solution to be used as drug delivery vehicle and injected into a Wistar rat cortex by cortectomy surgery. The HA hydrogel remained then implanted inside the rat cortex for 3 months.

A schematic illustration of the implantation of crosslinked HA hydrogel in a rat brain is shown in Figure 2.7.

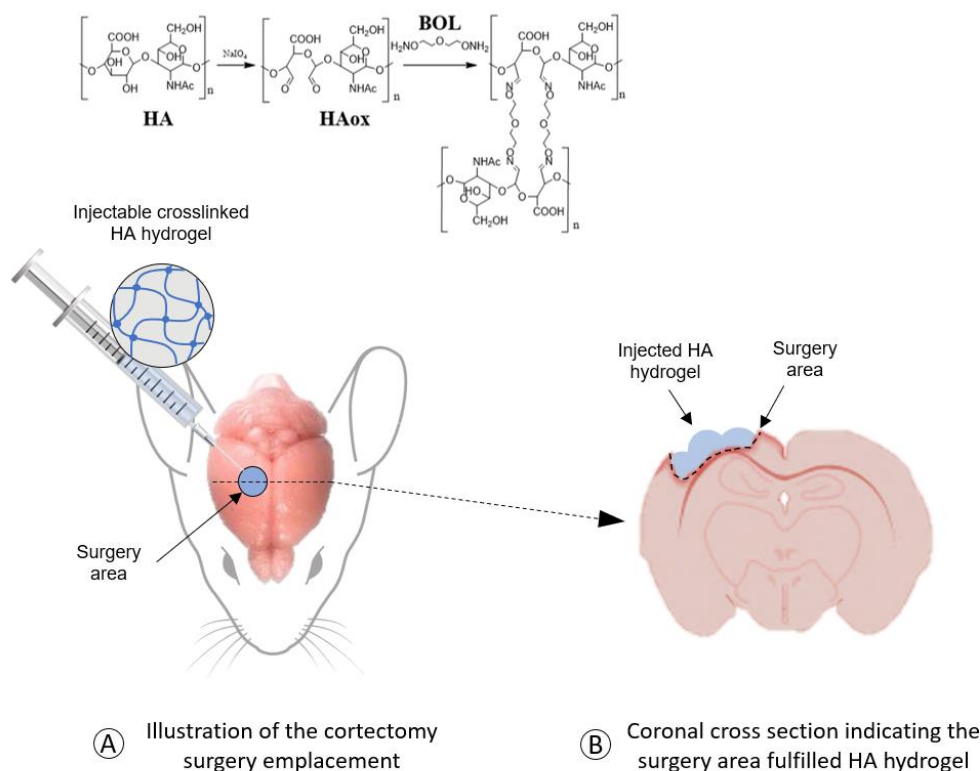


Figure 2.7. (A) Schematic diagram illustrating the procedure of injection of a crosslinked hyaluronic acid (HA) hydrogel in a rat brain area. The hydrogel remained implanted 3 months. (B) Coronal cross section view of the rat brain with its cavity fulfilled with HA hydrogel after 3 months of implantation.

The procedure followed to acquire tissue sections for combined analysis was the same applied for a non-human brain found in the [next] subsection 2.2.4, which concerns tissue fixation, dehydration, Tissue-Tek® O.C.T.™ Compound embedding, cryopreservation, sectioning and deposition into 1 cm<sup>2</sup> silicon substrate for posterior combined analysis. However, two caveats must be considered.

1. Rat brain with hydrogel received an additional washing in phosphate-buffered saline (PBS) solution with addition of 30% sucrose.
2. Rat brain with hydrogel was sectioned coronally 40 μm instead 20 μm thick using the freezing microtome (Leica CM3050S).

## 2.2.4 Glial scar tissue formed surrounding a neural electrode

One of the first generations of a wireless fully implantable ECoG neural device WIMAGINE® remained implanted on a nonhuman primate brain in order to record brain activity for a test period of approximately one year. The implantation surgery consisted of removing locally the layers of scalp, skull and part of the meninges laying the device directly in contact with the brain. After the one-year period, the implant

was found useless and completely enveloped by a dense glial scar tissue formed due to the uncontrolled immunological brain tissue response to the foreign object.

A schematic view of the emplacement of the neural device in nonhuman primate brain and some pictures from the brain and the neural device after the implantation period is shown in Figure 2.8.

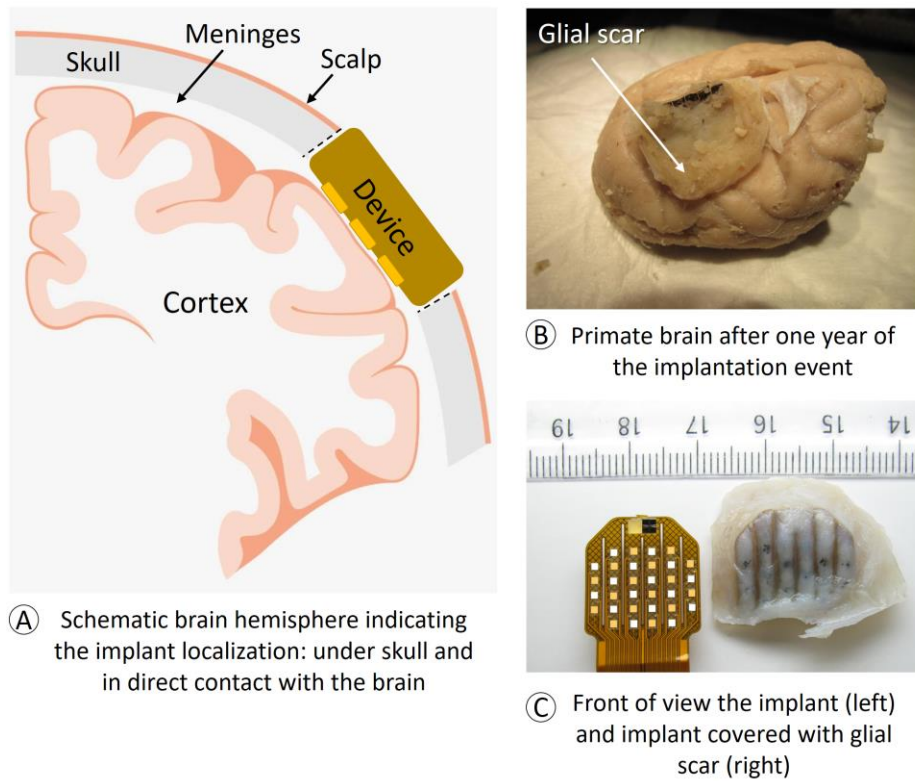


*Figure 2.8. (A) schematic view of the emplacement of the neural device in the nonhuman primate brain. It is placed under the skull, in direct contact with the brain. (B) Nonhuman primate brain (without scalp and skull) with the neural device attached to its lateral after one year of implantation. The neural device is completely enveloped by a glial scar tissue. (C) A control neural device (left) and the implanted neural device extracted from the nonhuman primate brain and completely enveloped by a glial scar (right).*

From the nonhuman primate brain seen in Figure 2.8B until obtaining slices of glial scar for combined surface analysis, the protocol of sample preparation is given as follows.

- The nonhuman primate brain and its attached and enveloped neural device are overnight fixed in a 10% formalin bath. The ensemble is then transferred through a series of increasingly concentrated ethanol solutions, ending in 100%, which removes all water.
- Once harvested from a formalin-fixed and dehydrated nonhuman primate brain, a small block from the biological system (neural device + glial scar) is selected for combined analysis.
- The selected tissue block (with a piece of neural device inside) is then embedded in Tissue-Tek® optimal cutting temperature (O.C.T.) compound (polyvinyl alcohol 10.24%, polyethylene glycol 4.26%, and nonreactive ingredient 85.50%) produced by PST Pty Ltd.

- After, the embedded tissue block is cryopreserved in a  $-80\text{ }^{\circ}\text{C}$  freezer.
- The glial scar tissue is then sectioned in  $20\text{ }\mu\text{m}$  thick slices from OCT-embedded blocks inside a Cryostat (Leica CM3050S) held at  $-20\text{ }^{\circ}\text{C}$  at the Clinattec Biomedical Research Center.
- The sections of glial scar (from approximately  $500\text{ }\mu\text{m}$  range of distance from the neural device) are placed onto  $1\text{ cm}^2$  ITO/glass or silicon substrates compatible in size with all instruments used in this work.
- Hereupon, these sections were left 2 h drying at ambient conditions in a fume cupboard plus 5 min at  $37\text{ }^{\circ}\text{C}$  in a dryer. Then, placed in a non-sealed container, which was stored under  $\text{N}_2$  atmosphere and just removed for analysis.

A schematic diagram of the protocol described above is shown in Figure 2.9. The same protocol was applied in the preparation of the meningeal layers.

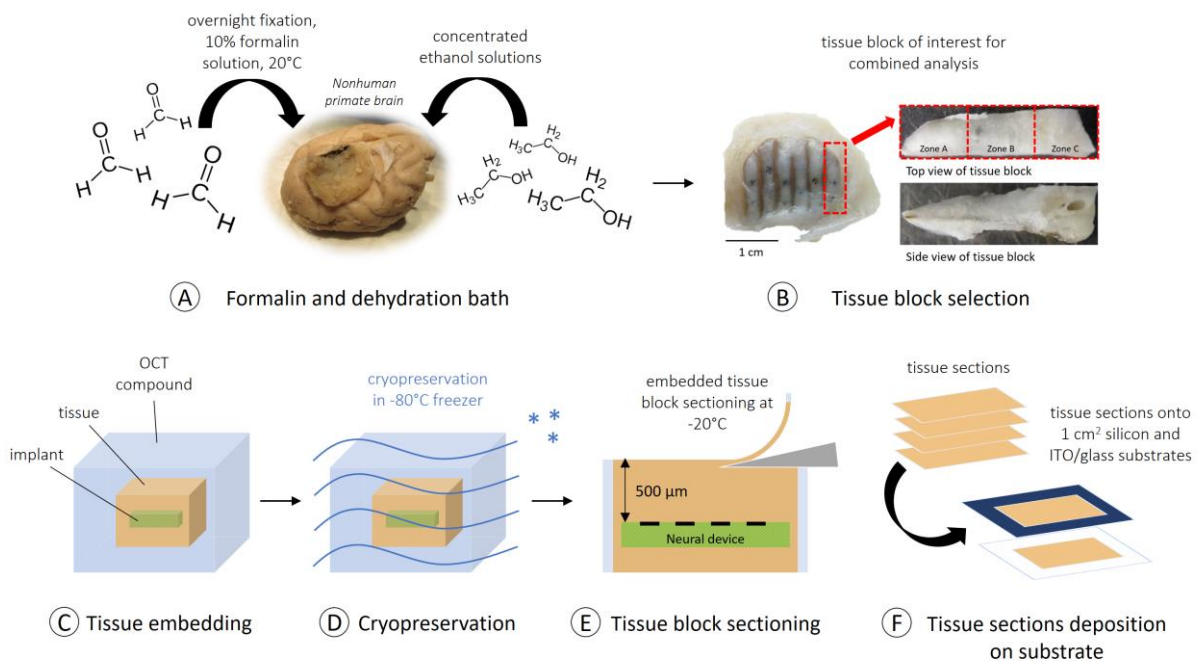


*Figure 2.9. Schematic diagram illustrating the procedure for embedding and sectioning the glial scar tissue. (A) Firstly, the procedure of fixation and dehydration of the nonhuman primate brain with the neural device and glial scar with formalin and isopropanol, respectively. (B) Formalin-fixed and dehydrated glial scar enveloping the neural device. The selected tissue block for combined analysis is given in a red dotted square. (C) The block of glial scar tissue (in peach) with a piece of neural device inside (in green) is embedded in Tissue-Tek® optimal cutting temperature (OCT) compound (in light blue). (D) The embedded block is cryopreserved in a  $-80\text{ }^{\circ}\text{C}$  freezer. (E) The glial scar tissue is sectioned from OCT-embedded blocks. (F) The sections of glial scar tissue are placed onto  $1\text{ cm}^2$  ITO/glass or silicon substrates.*

#### 2.2.4.1 H&E staining

Some of the sectioned non-human primate brain tissues were not used for combined microscopic analysis but instead prepared for hematoxylin and eosin (H&E) staining. In this case, the tissue sections

were fixed with an ethanol 50%/acetone 50% solution, and after rinsing, staining with hematoxylin for 4 min made it possible to stain the cell nuclei. Then, a differentiation in a 0.5% hydrochloric acid solution and a 0.25% ammonia solution of a few seconds each was carried out with rinses with water after each solution. Then, the slices were stained for a few seconds in eosin to stain collagen type I. Finally, the sections were mounted between superfrost plus slides and coverslips for analysis.

### 2.2.4.2 The neural device

The implanted neural device consists of two main parts: (1) the electrodes responsible for recording electrophysiological signals from the non-human primate brain and (2) a Kapton® matrix responsible for supporting the electrode network. The electrodes are made of 100 µm silicon chips with two different coatings. One based on titanium nitride (TiN) and other based on multi-walled carbon nanotubes (MWCNTs) directly grown on a titanium nitride layer with a 5nm catalyst nickel layer and glued with UV Master Bond [168]. The matrix is a Kapton® flex made up of 35 µm copper tracks with a classical Ni/Au stacking for electrode contact recovery. A conductive epoxy glue loaded with silver EPO-TEK® H20E is used to resume the contact of the copper tracks with the electrodes. An illustration of the neural device and its electrodes is shown in Figure 2.10.

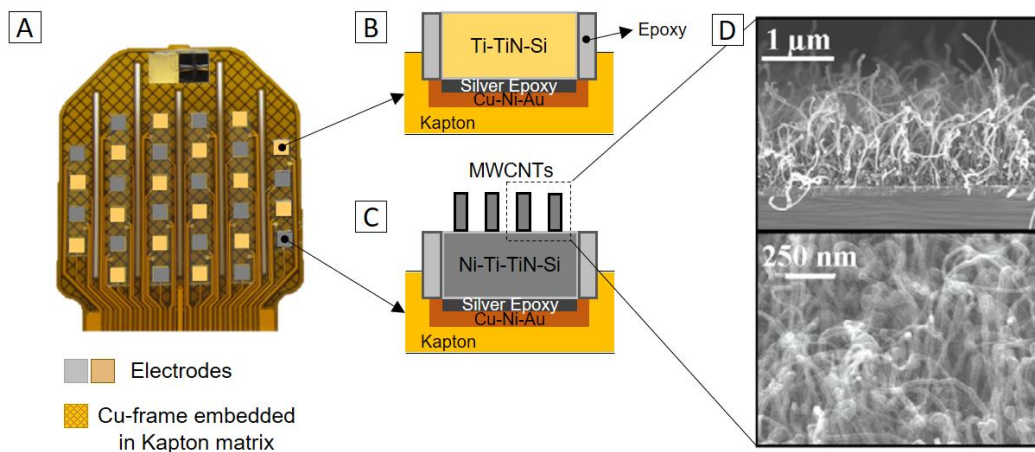


Figure 2.10. (A) Frontal vision of the neural device. The grey and yellow squares are part of an organized electrode network linked by copper connections and supported in a kapton matrix. This device uses two different types of electrodes based on silicon chips (B) coated with a titanium nitride (TiN) layer, and another (C) coated with multi-walled carbon nanotubes (MWCNTs) directly grown on a titanium nitride layer with a 5 nm catalyst nickel layer. (D) SEM images from a side view (upper panel) and a top view (lower panel) of the MWCNTs. Adapted from [168]

## 2.3 ANALYTICAL METHODS

In this third section of this second chapter, we will present the technical information about the main surface microscopy techniques used in this work. We will find described the principle as well as understanding the operational mode of Time-of-Flight Secondary Ion Mass Spectrometry (ToF-SIMS), X-ray Photoelectron Spectroscopy (XPS) and Photoemission Electron Microscopy (PEEM).

### 2.3.1 Time-of-flight secondary ion mass spectrometry (ToF-SIMS)

Time-of-Flight Secondary Ion Mass Spectrometry (ToF-SIMS) is a locally destructive physicochemical characterization technique that produces a crater size of a few hundred microns per side and few nanometres in depth, particularly dedicated to the analysis of elements, isotopes and molecules present in biological samples.

#### 2.3.1.1 Principle of ToF-SIMS

The physical principle of ToF-SIMS is based on bombarding the surface of a solid sample with a primary ion beam that causes a cascade of atomic collisions in the specimen leading to an ejection of its first atomic monolayers. Some of these ejected secondary ions (SI) can be spontaneously ionized as atoms or fragments of entire molecules being focused and accelerated towards a time-of-flight (ToF) mass spectrometer, located few millimetres of distance from the surface of the sample, for their separation in function of mass/charge ratio ( $m/z$ ) before detection. The acceleration of the secondary ions towards the ToF analyser is due the application of a potential difference of few kV between the sample and the analyser. A sputter beam for in-depth profiles is generally also available. The scheme in Figure 2.11 illustrate the principle of ToF-SIMS.

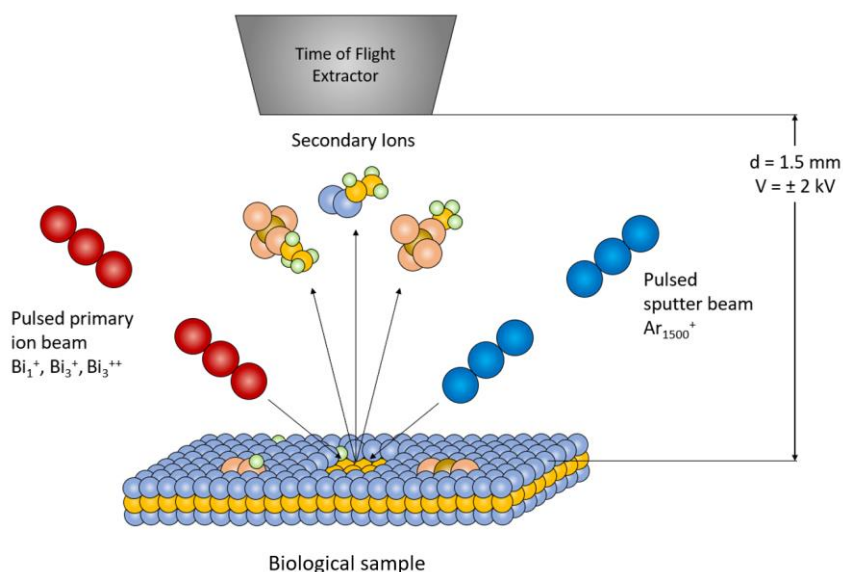


Figure 2.11. ToF-SIMS principle showing a bismuth primary ion beam colliding with the surface of a biological sample and generating characteristic secondary ions. The incidence of an argon cluster sputter beam with the surface of the sample is also illustrated.

#### 2.3.1.2 Modes of analysis in ToF-SIMS

Three operational modes are typically available using ToF-SIMS: surface spectroscopy, surface imaging and depth profiling. These three operational modes are illustrated in Figure 2.12.

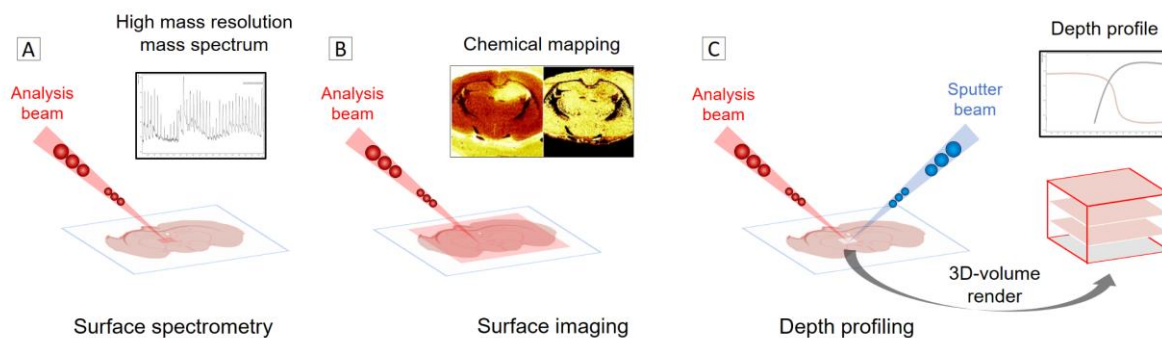


Figure 2.12. Illustrations of the different acquisition modes: (A) analysis of the extreme surface composition of a biological tissue by acquisition of mass spectra, (B) imaging of the extreme surface of a biological tissue and (c) depth profiling using a “Dual beam” mode and projection of the ionic images in a 3D rendering configuration.

- The surface spectrometry mode allows mass spectra to be generated from a locally interaction of the primary ion beam with the surface of the biological sample.
- The surface-imaging mode allows obtaining a spatial distribution of the intensity of characteristic secondary ions from a selected zone in the biological surface. In this mode the primary ions sweep across the surface of the sample and for each pixel in the image is associated a mass spectrum.
- The depth-profiling mode allows analysis of the composition of the sample over its volume. The operating configuration include the use of a primary ion beam for analysis and a sputter beam for removal of the surface monolayers.

### 2.3.1.3 The cluster effect

Some common sources of primary ion beam are monatomic ( $\text{Ar}^+$ ,  $\text{Cs}^+$ ,  $\text{Bi}^+$ ,  $\text{Ga}^+$ , etc) or biatomic ( $\text{O}_2^+$ ,  $\text{O}_2^-$ , etc) projectiles that have high energy per ion and causes high fragmentation of large molecules. It is then not appropriate for the characterization of biological surfaces. The use of cluster beams ( $\text{Bi}_n^+$ ,  $\text{SF}_5^+$ ,  $\text{Au}_n^+$ ,  $\text{C}_{60}^+$ ,  $\text{Ar}_n^+$ ), however, is capable of providing characterization of surfaces and in-depth compositions with minimal damage favouring the ejection of larger and less fragmented ions. This is possible due the fact that sputtering yields can be enhanced when an atomic projectile is replaced by a cluster ion with the same incident energy [169, 170]. Besides that, clusters lead to smaller damage accumulation in bombarded organic solids. In monatomic projectiles, most of the primary energy is deposited deep inside the material and cannot contribute to ejection of large molecules due to high fragmentation, however, for cluster projectiles, the primary kinetic energy is partitioned between many constituent atoms as the projectile breaks up upon impact. The energy of individual atoms in a cluster projectile is, therefore, low, which results in a small penetration. Consequently, the primary energy is deposited near the surface, and the ejection of secondary ions is very efficient [50]. In Figure 2.13 we can observe the impact of  $\text{Ar}_{9000}$  and  $\text{Ar}_{2953}$  clusters with different initial kinetic energies on a thin organic layer of sec-butyl-terminated polystyrene tetramer (PS4) deposited onto Ag111 substrate. Similar behaviour occurs at biological surfaces.

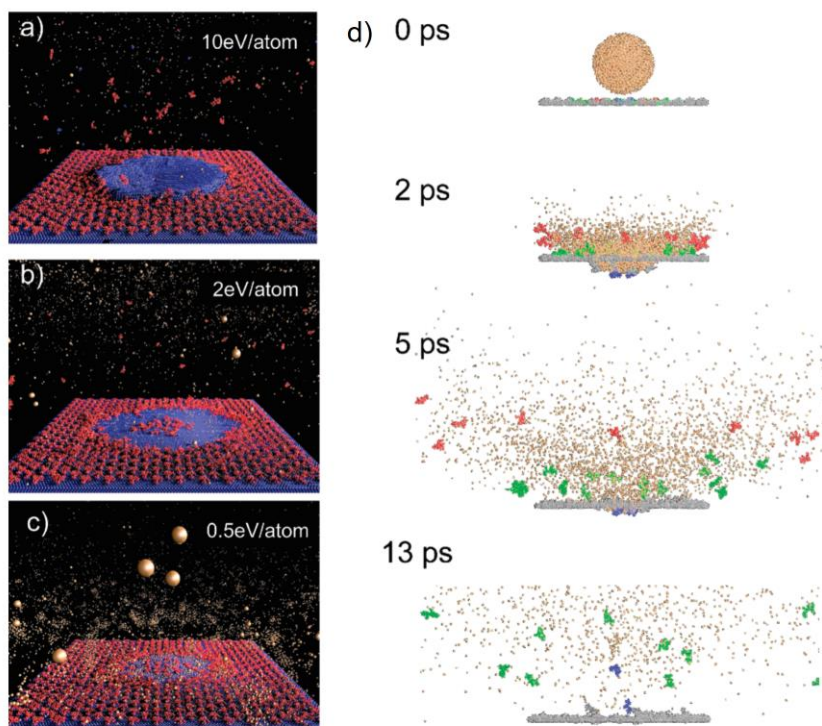


Figure 2.13. Molecular dynamics computer simulation of the ejection mechanism of PS4/Ag111 system bombarded with Ar<sub>9000</sub> projectiles having different kinetic energies of (a) 10 eV, (b) 2 eV, and (c) 0.5 eV per atom at 36 ps after the ion impact. The greater the primary energy employed, the greater the ejection of secondary ions is observed. (d) Side view of the temporal evolution of the collision events stimulated by 15 keV Ar<sub>2953</sub> impact at the same PS4/Ag111 system at normal incidence. Peach spheres depict Ar atoms. Ejected PS4 molecules with different total kinetic energy are depicted in red, green and blue. Grey spheres depict PS4 molecules that were not sputtered from the surface. [50]

#### 2.3.1.4 The ToF-SIMS V

The TOF-SIMS V equipment from IonToF GmbH (Münster, Germany) used in this work is equipped with a dual beam primary ion source, a pulsed one for analysis in static mode and another dedicated to sputtering the sample. The analysis beam is a pulsed source of primary ions based on a new generation of Liquid Metal Ion Source (LMIS) using a bismuth-manganese alloy with a maximum acceleration voltage of 30 kV. The sputtering cannon uses an ionic source of argon to generate clusters. All beams reach the sample at 45°. An electron gun is available to compensate for the charge effects due to ionic bombardment. The mass analyser is equipped with an electrostatic lens for compensation of kinetic energy variations (Reflectron). After going through the mass analyser all secondary ions reach a detector. The detector consists of microchannels (MCPs) for ion-electron conversion, a scintillator for electron-photon conversion and a photomultiplier.

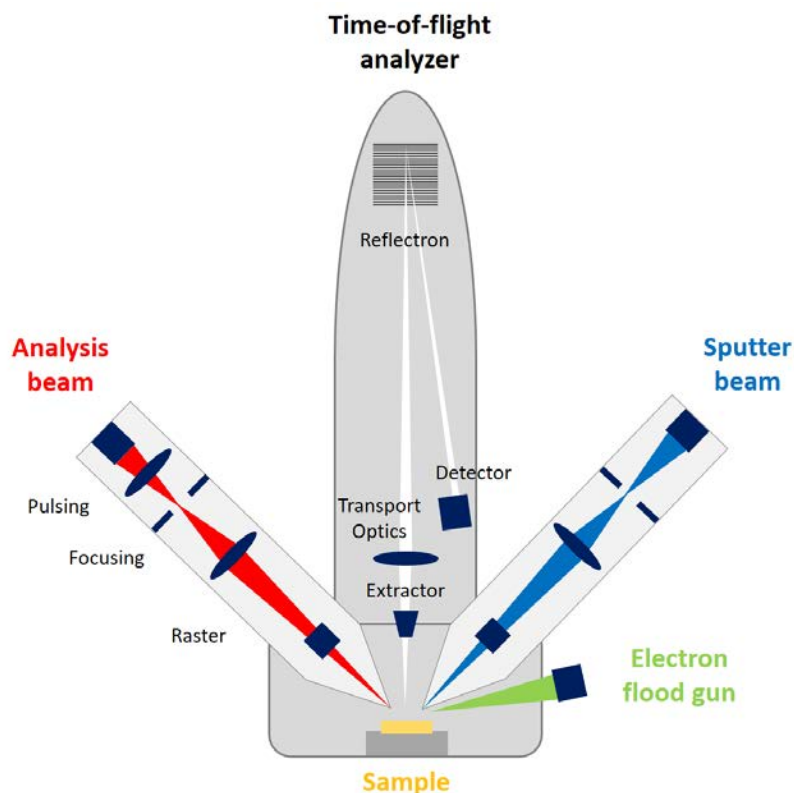


Figure 2.14. Schematic diagram of the ToF-SIMS V instrument from IonToF GmbH.

#### 2.3.1.4.1 Primary ion source

The analysis beam used in this work was a polyatomic bismuth ion beam ( $\text{Bi}_n^+$ ) provided by a LMIS. The principle of a LMIS is illustrated in Figure 2.15. The emissive part of the source is composed of a metal reservoir containing a needle. The entire source is localized inside the analysis gun and is connected to a positive high voltage power supply with a heating filament attached to the metal reservoir. Once enough heat is generated by the filaments, the metal melts and flows from the reservoir to the needle. When the extractor reaches high potentials (from -5 to -10 kV), an intense electric field is created around the tip covered by a very small volume of liquid metal. In response to the electrostatic force, positive metal ions near the tip are ejected, while electrons travel down the tip. The source thus reaches a state of dynamic equilibrium with a constant flow of ion current. The formation of a stable Taylor cone then depends on the balance between the surface tension and the electrostatic forces opposing the surface of the metal. The assembly therefore leads to the emission of ions in the gas phase from the top of the tip. These emitted ions can be singly charged species, but also doubly charged ions and clusters [171].

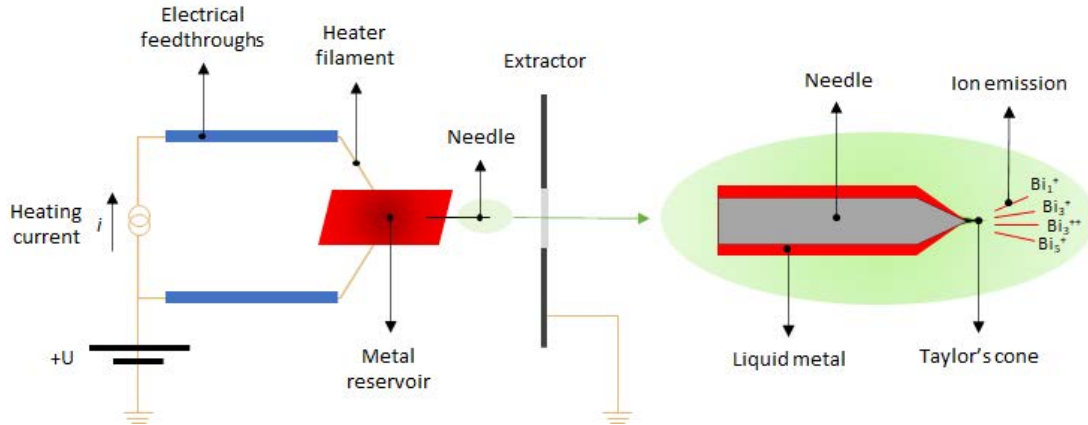


Figure 2.15. Schematic view of a LMIS emitter. [172]

Since the LMIS emits direct current (DC) beams containing several kinds of ions ( $\text{Bi}^+$ ,  $\text{Bi}_2^+$ ,  $\text{Bi}_3^+$ ,  $\text{Bi}_3^{++}$ ,  $\text{Bi}_5^+$ , and so on), the beams must not only be pulsed but the primary ion must also be mass selected. This mass selection can be accomplished either with a Wien filter or a dual set of deflection plates. Both systems have specific advantages and drawbacks. The Wien filter is capable of a high transmission but suffers from poor resolution and does not eliminate the need for a blanking plate to pulse the beam. The dual set of deflection plates have a better resolution but a lower transmission. In the TOF-SIMS V equipment used in this work the primary ion beam pulsing and mass selection are done thanks to deflection plates as the schematic view shown in Figure 2.16.

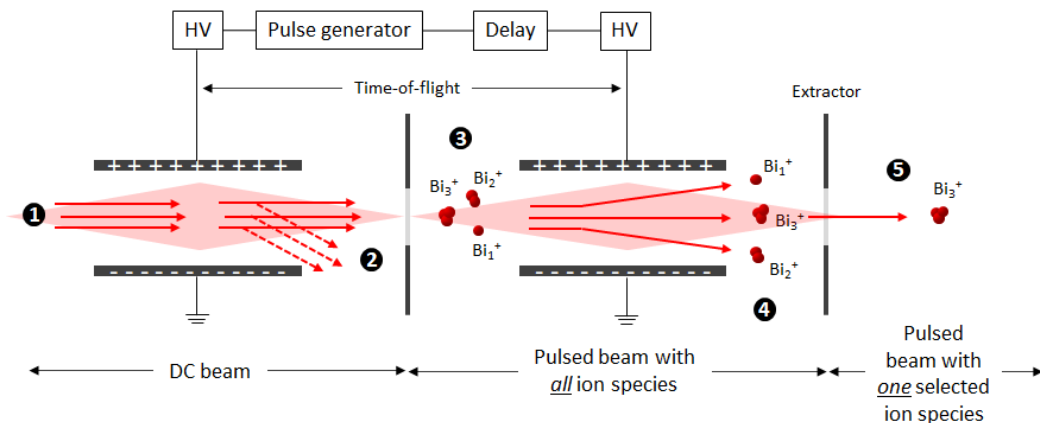


Figure 2.16. Schematic view of dual blanking plates that ensure both pulsation of the DC primary ion beam and mass selection among the different cluster ions emitted. [172]

According to the schematic view presented above, the deflection plates work as follows. Initially, the DC emission of different bismuth ions reaches the first set of plates (1). Then, the emission beam becomes periodically deflected due to a potential difference applied between the plates (2). Once the beam is deflected no current pass through the first extractor. This action is responsible for producing a pulsed emission beam. After, the pulsed beam with all bismuth species reaches the second set of plates (3). Since ions of different mass-to-charge ratios fly at different velocities, the second set of plates operating

at a controlled time delay after the first set can precisely select ions corresponding to a particular  $m/z$  (4). A pulsed beam with one selected ion species is then ultimately obtained (5).

In order to ensure good mass resolution for the TOF-SIMS spectrometer, a pulse of ions arriving at the sample must have a very short duration, about 1 ns or less. The simplest way is to produce very short pulses with the deflection plates. Unfortunately, such short pulses have relatively poor intensities, which consequently increase the acquisition time. In addition, the energy spread of the primary ions, although small, causes the pulse duration to increase as the primary ions fly from the deflection plates to the sample surface. Consequently, the pulsed primary ion beams need to be bunched by variable electrostatic fields in order to achieve pulse durations at the sample shorter than 1 ns (without bunching, pulse durations can be several tens of nanoseconds). For a given ion  $m/z$  ratio and energy, the pulse duration corresponds directly to the spatial extent of the pulse. It is possible, therefore, to shorten this pulse in time by compressing the ion packet in space. A bunching device is made with two plates, each with an aperture on the beam axis. These plates are separated by a distance greater than the spatial extent of the ion pulse. While the ion pulse is flying between the two plates, a voltage is applied to the rear plate in order to accelerate the ions. The ions at the rear of the pulse, which were originally the slowest, are accelerated over a greater distance than the ions at the front of the pulse, which were originally the fastest. Consequently, the ions at the rear acquire speeds slightly greater than those at the front of the pulse and, thus, catch up with the latter at some position downstream of the buncher.

#### 2.3.1.4.2 Sputter ion source

The sputter beam used in this work was an argon cluster ion beam ( $\text{Ar}_n^+$ ) provided by a Gas Cluster Ion Beam (GCIB). This source is also convertible as an ion-sputtering source or as an ion source for analysis [173]. Obtaining the clusters requires a complex architecture such as shown schematically in Figure 2.17. Neutral clusters are initially formed by expansion of an argon source gas at high pressure (around 25 bar) through a supersonic nozzle into vacuum (in the order of  $10^{-3}$  mbar). The directed axial stream of clusters emerging from the nozzle is allowed to pass through an aligned skimmer, which blocks downstream transmission of most of the excess gas as shown in Figure 2.18.

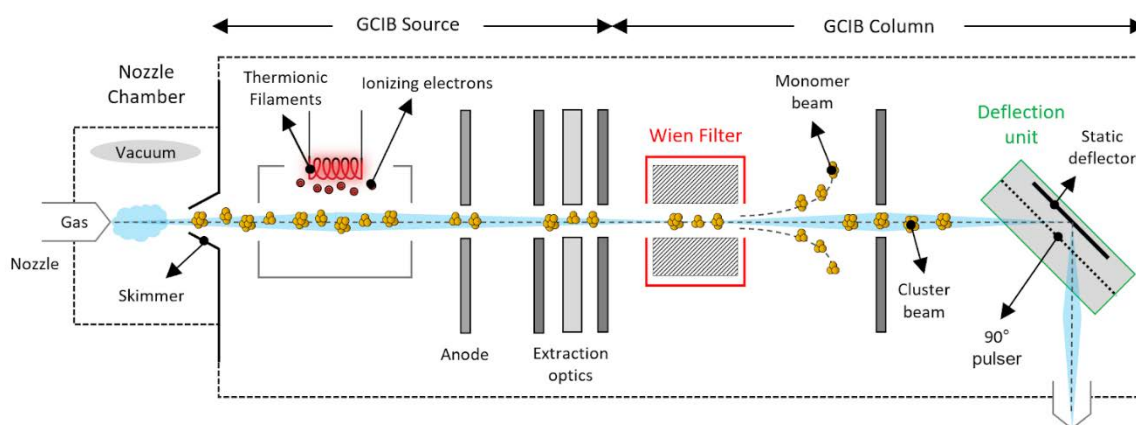


Figure 2.17. Schematic configuration of GCIB. [173]

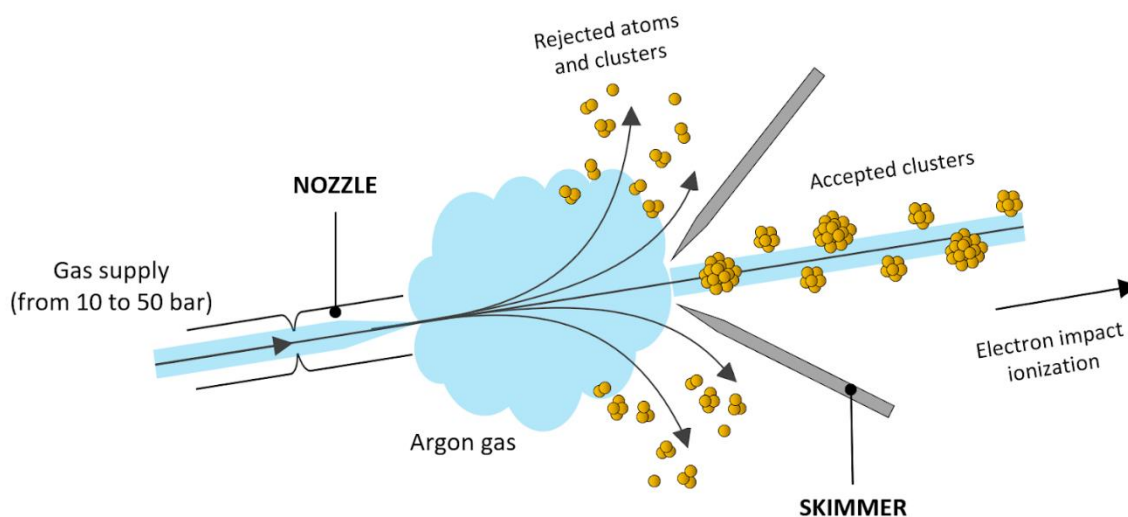


Figure 2.18. Schematic diagram of the formation of aggregates by adiabatic expansion of a gas. [174]

Clusters passing through the skimmer to a second vacuum stage are ionized by electron impact and then accelerated to high potential, typically a few kilovolts to a few tens of kilovolts, depending upon the intended use for the beam. Magnetic filtering of the extracted ion beam to eliminate monomer ion contamination results in a beam composed only of cluster ions with size distribution ranging from a few hundred to several thousand atoms. A cluster mass filtering is therefore essential to control the ion beam employed in an argon cluster ion source. The mass selection is then performed inside a Wien filter whose structure is shown in Figure 2.19.

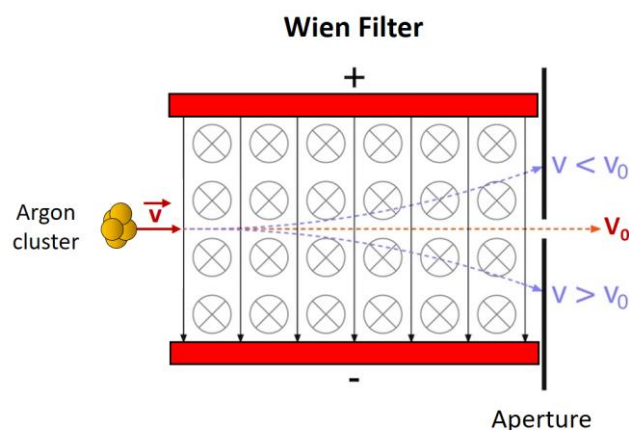


Figure 2.19. Diagram of ion mass selection by a Wien filter in an argon cluster ion source. [174]

This type of filter consists of two deflection plates that generate an electric field. The electric field is perpendicular to the velocity vector of the ions and exerts a force of  $qE$  on the ions. The magnetic field is perpendicular to both the velocity vector and the electric field. The magnetic force has magnitude  $qvB$ , and is opposite in direction to the electric force. The forces balance when:

$$qE = qvB \quad (2.1)$$

$$v = \frac{E}{B} \quad (2.2)$$

For ions with a larger speed the magnetic force exceeds the electric force and those ions are deflected out of the beam. Ions with a smaller speed are deflected out of the beam in the other direction, because for those ions the electric force is larger than the magnetic one. For higher  $m/z$  ratios, the cluster speed will be reduced as well as the deflection induced by the magnetic field. Thus, the filter will become less efficient with the increase in the number of argon atoms per cluster for the same charge. The beam then undergoes a deflection of  $90^\circ$  to refine the distribution of the clusters resulting from the Wien filter. This consists of a deflector plate for static deviations and a deflector plate for a  $90^\circ$  pulsation. Two operating modes are accessible and offer the possibility of obtaining an ion beam with argon clusters suitable either for the acquisition of spectra or for the depth profile.

In the depth profile mode, all ions that have the same energy have the same flight path through the Deflection Unit. In principle, the deflection unit is not able to separate ions based on the  $m/z$  ratio. However, their course is modified if there is a correlation between the  $m/z$  ratio and the kinetic energy of the species, as is the case for Argon clusters. The heavier clusters thus have more kinetic energy and therefore have a longer distance to cover in the deflection unit. The beam is then spatially distributed in energy to pass through the downstream opening, which separates the ion clusters according to the  $m/z$  ratio.

## 2.3.1.4.3 ToF analyser

After the collision of primary ions with the surface of the sample and the formation of characteristic SI, these are collected and separated according to their  $m/z$  ratio before detection. The ToF-SIMS technique uses a ToF analyser, which principle involves the separation of SI based on the time SI take to travel through a flight tube with known length and reach the detector. The trajectory of the ions through a ToF analyser depends on its momentum and kinetic energy due to an applied pulsed acceleration voltage and  $m/z$  ratios of the ions.

Based on classical physics, ions with lower  $m/z$  will travel the fastest and arrive at the detector first while ions with larger  $m/z$  will travel the slowest and arrive at the detector last. The time it takes for the secondary ions to move across the flight tube between the ion source and detector allows us to determine the  $m/z$  ratios. In the ToF spectrum, the recorded peak for any  $m/z$  will correspond to the sum of signals corresponding to multiple and independent ions arriving at the mass detector. A ToF layout is shown in Figure 2.20.

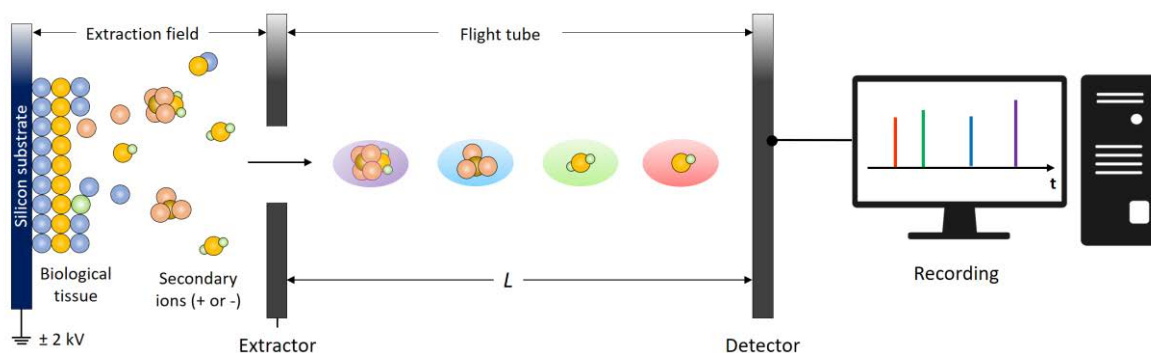


Figure 2.20. Schematic diagram of the time-of-flight analyser in a simplified geometry. [174]

The following derivation to describe a ToF analyser dynamics was adapted from E. Hoffman and V. Stroobant, 2007 [175]. This can be shown in the following equations where the potential energy given to ions in the extraction field is converted to kinetic energy for all ions:

$$zeU = \frac{1}{2}mv^2 \quad (2.3)$$

Where  $z$  is the number of elementary charges,  $e$  is the elementary charge,  $U$  is the extraction voltage and  $m$  is the mass of the ion. Resolving the previous equation for velocity  $v$ :

$$v = \sqrt{\frac{2zeU}{m}} \quad (2.4)$$

Since velocity is equal to the drift path length  $L$  divided by time:

$$v = \frac{L}{t} \therefore t = \frac{L}{v} \quad (2.5)$$

Then, solving for time  $t$  and we get the following equation used to describe time in a ToF analyser:

$$t = \sqrt{\left(\frac{m}{z}\right) \left(\frac{L^2}{2eU}\right)} \quad (2.6)$$

By algebraically rearranging the equation above, an expression of  $m/z$  is determined as shown below.

$$\frac{m}{z} = \left(\frac{2eU}{L^2}\right) t^2 \quad (2.7)$$

We can also describe mass resolution for ions by differentiating the equation above with respect to mass and time we get the following relation:

$$\frac{1}{z} dm = \left(\frac{2eU}{L^2}\right) 2t dt \quad (2.8)$$

Manipulating the equation above, we get the following relation used to express mass resolution:

$$\frac{m}{dm} = \frac{t}{2dt} \therefore \frac{t}{2\Delta t} = \frac{m}{\Delta m} = R \quad (2.9)$$

However, one of the drawbacks for using a linear ToF is poor mass resolution. Factors that cause poor mass resolution are shown in Figure 2.21. The starting times and locations of ions before they are accelerated into the flight tube are different and affect resolution. In addition, different kinetic energies for ions and initial orientation of ions also affect mass resolution and give poor results [176].

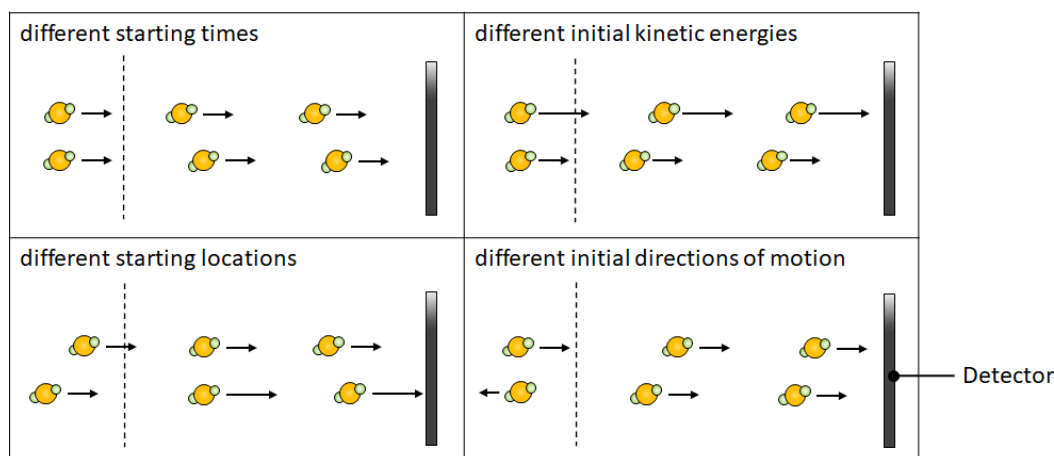


Figure 2.21. Factors affecting mass resolution in a linear ToF mass analyser. [174]

To correct for poor mass resolution, an electrostatic mirror or Reflectron is added to the ToF analyser. A layout of a Reflectron ToF is shown in Figure 2.22.

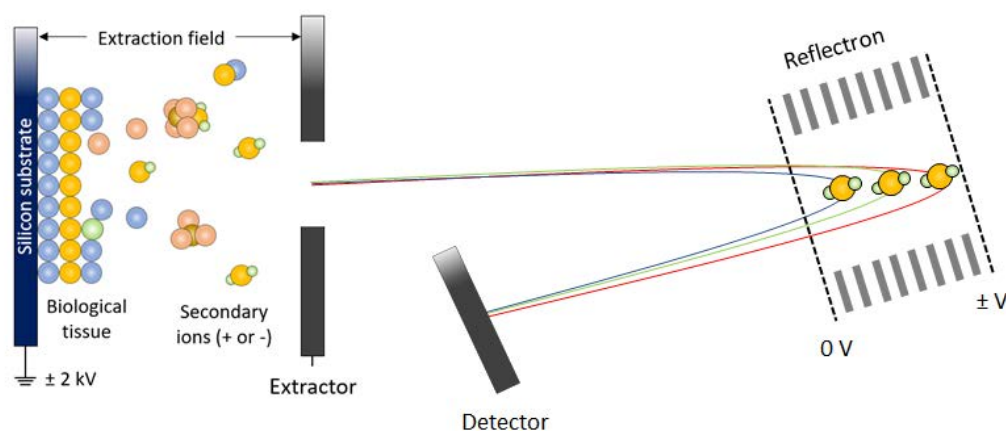


Figure 2.22. Schematic illustration of a Reflectron ToF analyser. In the reflection, the higher energy ion takes a longer path but arrives at the detector at the same time as the lower energy ion of the same mass. [174]

The reflectron consists of a series of electrodes charged to increasing potentials, forming a uniform electric field that will repel secondary ions. The principle of operation is based on the temporal refocusing of ions of the same  $m/z$  ratio so that they reach the detector at the same time, without modifying the kinetic energy. In practice, an ion will penetrate the deeper into the "reflectron" the greater is its kinetic energy. The trajectory it will take will then be longer. Therefore, two ions of the same  $m/z$  ratio but of different initial speeds will be reflected separately to arrive at the detector at the same time.

### 2.3.2 Tandem mass spectrometry (Tandem MS)

The Tandem mass spectrometry, also known by MS/MS or MS<sup>2</sup>, is distinguished from other mass spectrometry techniques by the presence of two or more mass analysers coupled together using an additional reaction step to increase its ability to analyse samples that contains complex chemistry composition. The equipment used to perform this technique in this work was the PHI *nanoToF* II ToF-SIMS which principle is based on the already discussed ToF-SIMS and the use of a parallel imaging MS/MS capability.

#### 2.3.2.1 MS/MS principle

The fragments of molecules of a given sample are ionized and the first spectrometer (designated MS1) separates these ions by their mass-to-charge ratio ( $m/z$ ). Ions of a particular  $m/z$ -ratio coming from MS1 are selected and then made to split into smaller fragment ions by collision-induced dissociation (CID). These fragments are then introduced into the second mass spectrometer (MS2), which in turn separates the fragments by their  $m/z$ -ratio and detects them. This additional fragmentation step makes it possible

to identify and separate ions that have very similar  $m/z$ -ratios in regular mass spectrometers as we can see in the scheme of Figure 2.23.

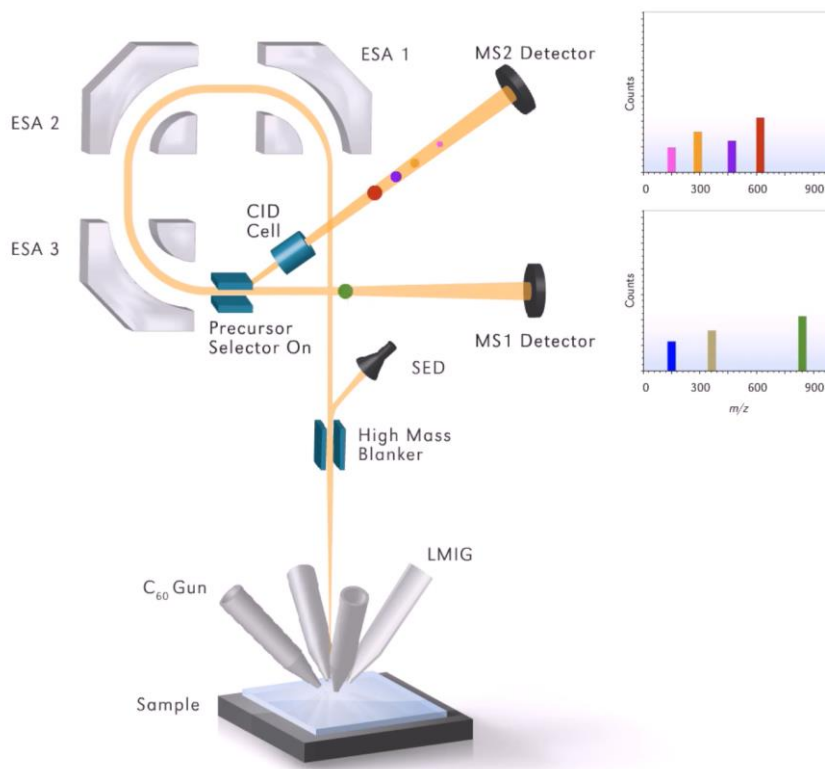


Figure 2.23. Schematic of the PHI nanoTOF II with MS/MS. [177]

In this instrument, the entire TOF-SIMS spectrum (except the precursor ions) is detected simultaneously with the MS/MS spectrum. No secondary ions are discarded while operating in the MS/MS mode of analysis. We refer to this as “Parallel Imaging MS/MS ToF-SIMS” because secondary ions are recorded at the standard ToF-SIMS detector at the same time that MS/MS fragment ions are recorded at the linear TOF detector. More information about the PHI *nanoToF* II ToF-SIMS can be found published by Fisher, G. L. et al., 2016. [177]

### 2.3.3 Atomic force microscopy (AFM)

Developed in 1986 by Binnig, Quate, and Gerber as a collaboration between IBM and Stanford University [81], the atomic force microscope (AFM) was created to overcome the main limitation of the scanning tunnelling microscopy, the surface imaging of exclusively conductive samples. AFM is still nowadays largely used in biology and considered a multifunctional imaging platform that allows biological samples, from single molecules to living cells, to be visualized and manipulated. [178]

### 2.3.3.1 Principle of AFM

An AFM uses a cantilever with a very sharp tip to scan over a sample surface. As the tip approaches the surface, the close-range, attractive force between the surface and the tip cause the cantilever to deflect towards the surface. However, as the cantilever is brought even closer to the surface, such that the tip makes contact with it, increasingly repulsive force takes over and causes the cantilever to deflect away from the surface. The curve in Figure 2.24 shows the attractive and repulsive forces according to the distance between the tip and the sample.

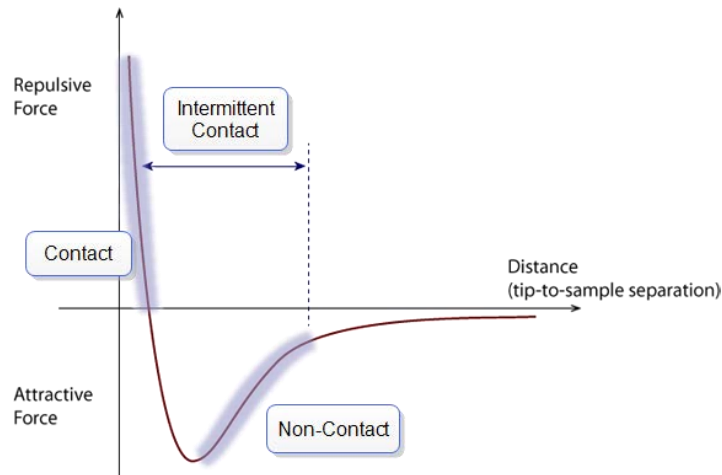


Figure 2.24. The effect of tip-to-sample distance on the force interaction between tip and sample. Three regimes are shown: attractive, repulsive and no forces. The AFM operation modes are represented in the curve: the contact mode in the repulsive regime, the non-contact mode in the attractive regime and the intermittent-contact that includes the repulsive to the attractive mode. [179]

A laser beam is used to detect cantilever deflections towards or away from the surface. By reflecting an incident beam off the flat top of the cantilever, any cantilever deflection will cause slight changes in the direction of the reflected beam. A position-sensitive photo diode (PSPD) can be used to track these changes. Thus, if an AFM tip passes over a raised surface feature, the resulting cantilever deflection (and the subsequent change in direction of reflected beam) is recorded by the PSPD. Figure 2.25 shows a schematic view of the placement of the tip on the cantilever and the lased beam in the AFM.

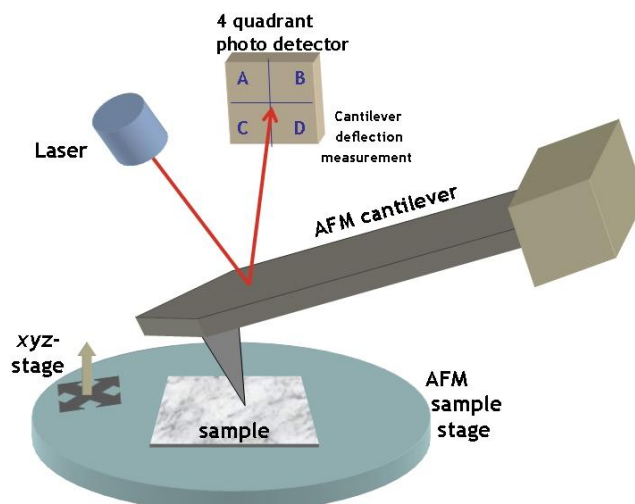


Figure 2.25. Schematic view of the main components of an AFM. [179]

An AFM images the topography of a sample surface by scanning the cantilever over a region of interest. The raised and lowered features on the sample surface influence the deflection of the cantilever, which is monitored by the PSPD. By using a feedback loop to control the height of the tip above the surface—thus maintaining constant laser position—the AFM can generate an accurate topographic map of the surface features.

### 2.3.4 X-ray photoelectron spectroscopy (XPS)

The X-ray photoelectron spectroscopy (XPS) is a non-destructive surface characterization technique particularly interested in measuring the kinetic energy of core level photoelectrons emitted from ionised atoms in the material during exposition to X-ray radiation. The ultimate objective is to access the characteristic binding energy of each photoelectron emitted based on their detected kinetic energy. It allows the study of elemental composition as atomic percentages of materials for all detectable elements (all except H and He) as well as characterize the chemical environment of elements thanks to the observation of light shifts in the electrons binding energy.

#### 2.3.4.1 Principle of XPS

The physical principle of XPS is based on the photoelectric effect that consists in the emission of electrons from the surface of the sample when it is hit by electromagnetic radiation. It is due the interaction of a photon with sufficient energy  $h\nu$  with the matter that results in the emission of an electron from its surface. Electrons emitted in this manner are called photoelectrons. The photon radiation is capable to induce electrons not only from the outer shells, but also from core-levels of elements, which are of interest in XPS analysis. If the photon energy is sufficient to reach the photoionization threshold value characteristic of the atom of the sample, an electron leaves from its atomic orbital and following extracted from the surface with a kinetic energy  $E_{kin}$ .

For ultraviolet and soft X-ray excitations, the process can be described by the energy conservation equation:

$$E_{kin} = h\nu - E_{bin} - \phi_{sam} \quad (2.10)$$

Where  $E_{bin}$  is the aimed photoelectron binding energy characteristic of each element, and  $\phi_{sam}$  is the work function of the sample or the energy necessary for the emitted electron escape through the surface barrier into free-electron-like states of the vacuum. Thus, measuring the kinetic energy  $E_{kin}$  and knowing the energy of the photon source  $h\nu$  and the work function of the sample  $\phi_{sam}$ , the binding energy  $E_{bin}$  can be determined.

The same equation can be expressed in terms of spectrometer as follows:

$$E_{bin} = h\nu - E'_{kin} - \phi_{spe} \quad (2.11)$$

Where  $E'_{kin}$  is the photoelectron kinetic energy measured inside the spectrometer and  $\phi_{spe}$  is the work function of the spectrometer, or the energy necessary for the core photoelectron across the spectrometer analyser. An energy scheme of the sample and spectrum of ejected electrons is illustrated below in Figure 2.26.

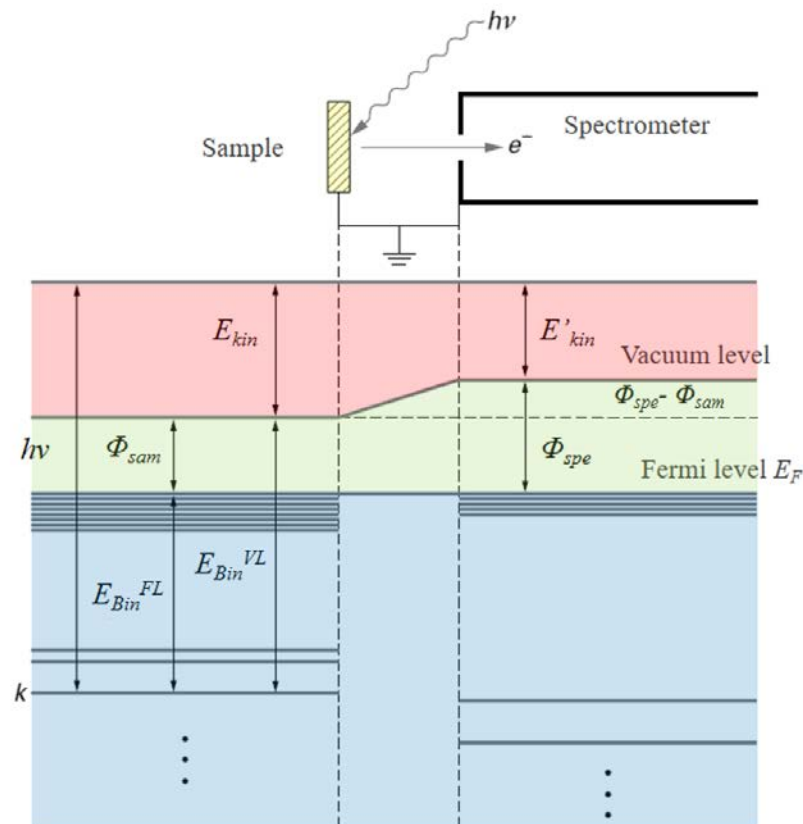


Figure 2.26. Scheme of the conservation of total energy during a photoelectric phenomenon after X-ray's exposure. [180]

Although the kinetic energy of the core photoelectron leaving the sample  $E_{kin}$  depends on the work function of the sample  $\phi_{sam}$ , the measured energy  $E'_{kin}$  only depends on the work function of the spectrometer  $\phi_{spe}$ . The work function of the spectrometer  $\phi_{spe}$  as well as the energy of the incident photons  $h\nu$  are known parameters of the experimental setup. Then, by measuring the kinetic energy of the photoelectrons  $E'_{kin}$ , it is possible to access the binding energy  $E_{bin}$  of the electronic level from which the core photoelectron originates.

Since electrons can occupy different orbitals around the same atomic nucleus, each chemical element will generate one or more characteristic peaks on the XPS spectrum. An example of an XPS survey spectrum is given in Figure 2.27.

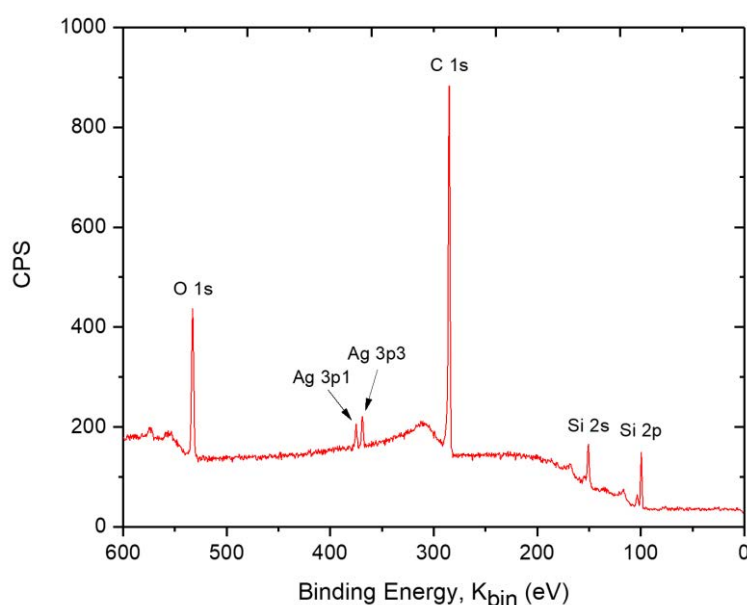


Figure 2.27. XPS spectrum showing core level emissions from Si, C, Ag and O from a unique acquisition.

This spectrum consists of several photoelectron emission peaks, characteristic of the electronic levels of the elements present in the material. The x-axis represents the binding energy  $E_{bin}$  of the detected photoelectrons and the y-axis represents their counts per second inside the instrument detector. The more counts per second of a given photoelectron, the more intense the peak in the XPS spectrum will be. The measured intensity depends on the instrument transmission, the emitting elemental concentration, the atomic photoionization cross-section  $\sigma$  of the considered atomic level, and the depth probed. The depth probed depends on the inelastic mean free path  $\lambda$ .

#### 2.3.4.1.1 Photoionization cross section $\sigma$

The photoionization cross-section  $\sigma$  represents the probability of an incident photon to ionize an orbital for a given element. It depends on the atomic number of the atom, the core level considered, and the photon energy  $h\nu$ . Values are typically taken from calculations of Scofield [181] and Yeh and Lindau

[182] and can be represented graphically as follows in Figure 2.28 for the carbon and oxygen core-levels 1s, 2s and 2p with an  $Al K_{\alpha}$  excitation.

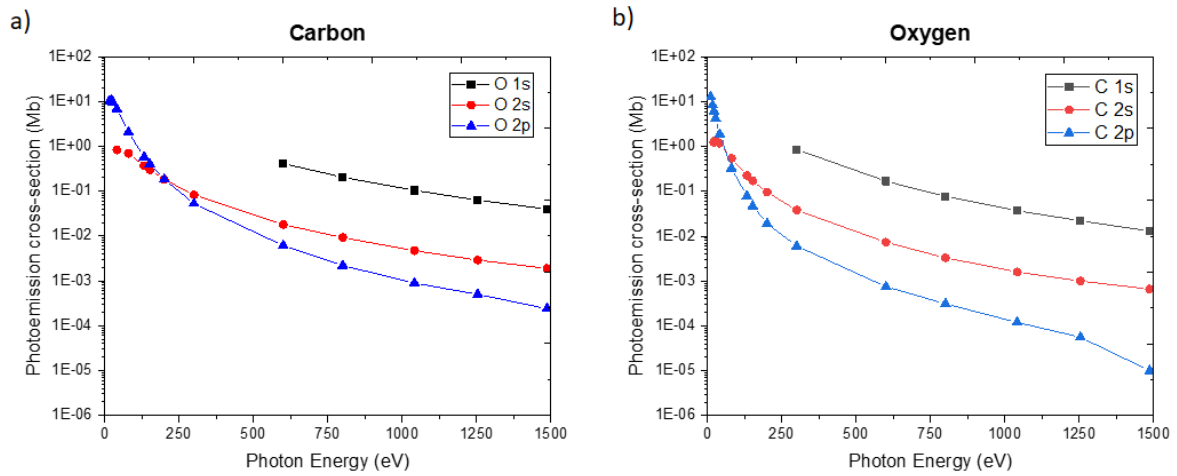


Figure 2.28. Photoemission cross-section  $\sigma$  for a) carbon and b) oxygen. For photon energy range from 0 to 1500 eV, the  $\sigma$  of the core-levels decrease as the photon energy increases. The cross-section unit is given in Mb: 1 Mb =  $10^{-18}$  cm<sup>2</sup>. [181]

#### 2.3.4.1.2 Inelastic mean free path $\lambda$

The inelastic mean free path  $\lambda$  is the average distance that an electron with a given energy travels between successive inelastic collisions. It strongly depends on the kinetic energy of the electron and varies with materials in terms of density and nature. Figure 2.29 below shows the experimental values of  $\lambda$  in angstroms (Å) for incident electrons from 100 eV to 10keV energies in guanine [183].

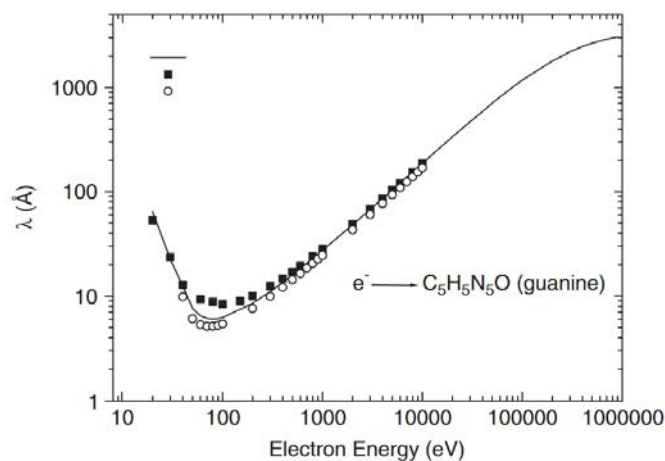


Figure 2.29. Inelastic mean free path  $\lambda(E)$  results for incident electron energies in guanine. —, experimental study; ■ and ○, theoretical results. [183]

As we can see on the curve, the inelastic mean free paths  $\lambda$  at these energies are about 5-110 Å. This makes XPS a surface-sensitive technique for chemical analysis. In general, the inelastic mean free path  $\lambda$  in the biological matter can be comparable with those acquired for guanine and is drastically reduced in comparison with some metals. It is because biological samples are made up of complex molecular arrangements, and the larger the radius of a molecule, the space between them decreases, causing them to run into each other more often. Therefore, reducing the average distance that an electron can travel without collisions.

#### 2.3.4.1.3 Detection limit

The detection limit of an element  $A$  is a function of the intensity  $I_A$  of the specific signal of that element, the intensity of the continuous background  $I_{BF}$  and the statistical fluctuations of these signals. The detection limit is the intensity of the minimum detectable signal. For a signal to be detectable, that is, to come out of the background noise  $\sigma$ , its intensity must be greater than the statistical fluctuations of the background signal (see Figure 2.30).

It is generally accepted that the amplitude of the minimum detectable signal,  $S_{min}$ , should be equal to or greater than three times the background noise  $\sigma$  [184]:

$$S_{min} = I_{S_{min}} t = 3\sigma \quad (2.12)$$

Where  $t$  is the counting time. In terms of the minimum detectable concentration,  $C_{min}$ , we have:

$$C_{min} = C_0 \frac{3}{\sqrt{I_0} \sqrt{\frac{I_0}{I_{BF}}} \sqrt{t}} \quad (2.13)$$

Where  $S_0$ ,  $I_0$  and  $C_0$  are respectively the area of the peak XPS (in number of strokes), the intensity (number of strokes/s) and the atomic concentration of the standard sample, in general a pure element.

Then, according the  $C_{min}$  relation, the factors directly influencing the detection limits in XPS are the intensity of the specific signal  $I_0$ , the signal-to-background ratio  $I_{BF}$  and the accumulation time  $t$ , which are equally weighted.

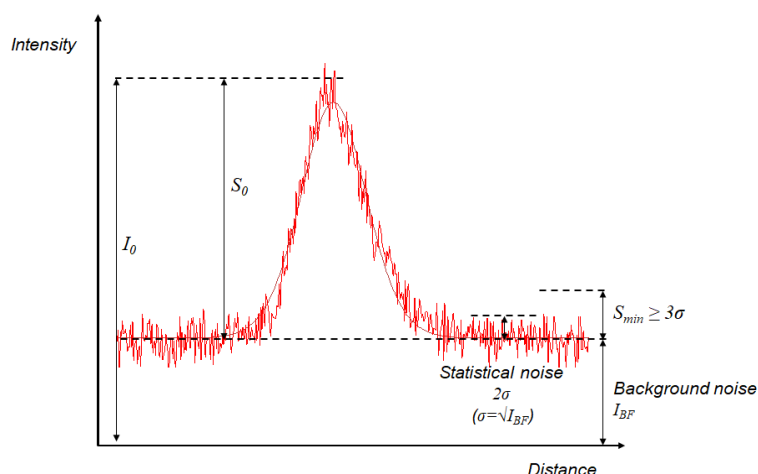


Figure 2.30. Continuous background, statistical noise, minimum detectable signal and limit of detection. [184]

### 2.3.4.2 Core level analysis

The core level peaks appearing in a XPS survey spectrum are not infinitely sharp, but have particular shape due to slight variations in terms of binding energy. These variations are associated with the initial chemical environment of the atom of interest but also with the interaction of the emitted photoelectron with the all-other electrons in the sample. Peak broadening may also occur due to different reasons associated with the sample but also with the instrument. Below we will detail the main characteristics of core-level peaks.

#### 2.3.4.2.1 Core level chemical shifts

The detected binding energy  $E_{bin}$  differs from the theoretical value because the atom is not isolated. This slight change in binding energy may be related to the sensitivity of the electron to its chemical environment, but also to photoelectric effects.

There are four main contributions for variations in the detected binding energy  $\Delta E_{bin}$  [185]:

$$\Delta E_{bin} = \Delta \varepsilon_l + \Delta E_R + \Delta E_F + \Delta E_C \quad (2.14)$$

Where,

$\Delta E_{bin}$  is the difference between the theoretical bond energy and that obtained when the atom is no longer isolated.

$\Delta \varepsilon_l$  is the chemical shift that reflects the effect of the atom chemical environment. It is due to a change in the potential of an electron level when an atom chemically bonds to another. For instance, for two atoms A and B with the same valance band but an electronegativity  $\chi_A < \chi_B$ , B tends to attract electrons

from the valence band of atom A. The charge transfer of an electron from A to B gives rise to a contraction of both core hole and core-levels of the atom A, as shown in Figure 2.31. Thus, an increase in positive charge is therefore accompanied by an increase in binding energy, this is why atoms such as C when linked to N or O in biomolecules present a higher binding energy.

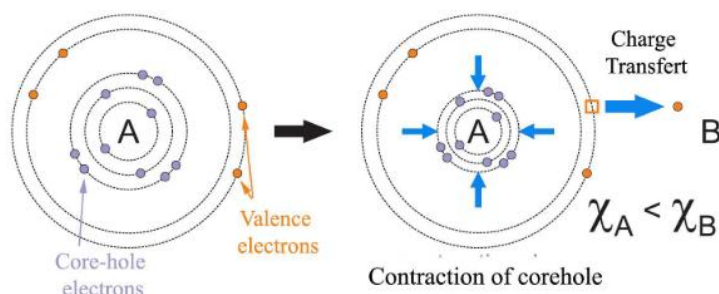


Figure 2.31. Schematic representation of the binding energy on a core-level before photoemission effects. When the A atom loses a valence electron for a more electronegative B atom, the binding energy of core-level electrons in the A atom increases.

$\Delta E_R$  is the post-photoemission relaxation that results from the photoemission of an electron. When a core electron leaves the atom after photoelectric phenomenon, as seen in Figure 2.32, the valence orbitals contract around the hole created. The positive charge is then shielded with electrons orbiting slightly closer, which causes a decrease in the energy of the final state of the atom and therefore a decrease in the binding energy.

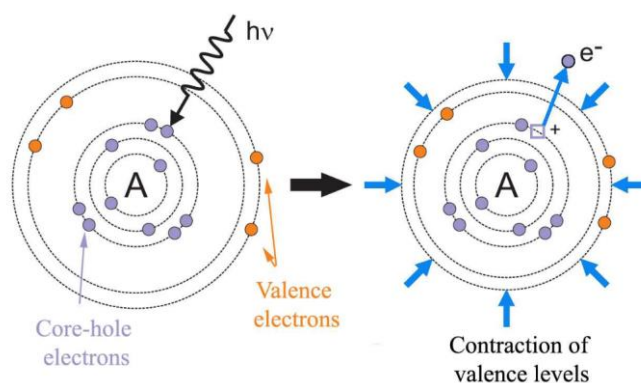


Figure 2.32. Schematic representation of the binding energy on a core-level after photoemission effects. When a core-hole is created in an A atom due to a photoemission process, the valence levels contract to compensate the positive charge and, consequently, the binding energy of core-level electrons in the A atom decreases.

$\Delta E_F$  is the variation of Fermi energy that takes place in cases where the sample is an insulator or a semiconductor. This phenomenon corresponds to a static displacement of all atomic orbitals in the same direction, which changes the bond energy in the same way for all core electrons, regardless of the type of atom.

$\Delta E_C$  is the charge effect that takes place when the material studied is an insulator. It is mainly because when the photoelectrons are ejected, they leave behind uncompensated positive charges. The sample then charges positively. The surface potential, which appears slowing down the photoelectrons, has the effect of shifting the binding energies towards higher energies. This phenomenon can be suppressed by using an electron gun that sends electrons to the surface of the sample compensating then for the positive charges created during the phenomenon of photoionization.

#### 2.3.4.2.2 Shape of photoemission peaks

A range of physically possible line profiles for fitting core-level peaks is possible. In general, simply Gaussian or Lorentzian functions are very rarely adequate. In the case of bio-organic samples, it has been shown that symmetric peak shape can be well described by the Gauss-Lorentz (Voigt) profile [186-188].

However, resolving peaks due to different chemical states depends on their energy separation and the experimental resolution. The best experimental resolution the XPS instrument can achieve during analysis is closely related to the width of a peak in the energy spectrum, which has a width  $\Delta E$  defined as the full-width-at-half-maximum (FWHM) of the peak after background subtraction. The total contributions to the broadening of the spectral lines can be approximated by the overall energy resolution of the instrument by:

$$\Delta E_T^2 = \Delta E_n^2 + \Delta E_s^2 + \Delta E_A^2 \quad (2.15)$$

Where,  $\Delta E_n$  is the natural linewidth of the core level associated to the decay of the core-hole state when another electron relaxes to fill it according to an associated lifetime that causes Lorentzian broadening of the photoemission peak,  $\Delta E_s$  is the photon bandwidth and  $\Delta E_A$  is the analyser resolution, both measurement process are described by a Gaussian. The  $\Delta E_A$  analyser resolution will be discussed in subsection 2.3.4.5.4.

#### 2.3.4.2.3 Background subtraction of a core-level peak

The background that appears in the photoemission spectra is due to scattered electrons that have lost energy in inelastic interactions but still had enough energy to escape from the surface of the sample. Then, in order to estimate the real peak shape from an experimental spectrum, the background is usually required to be subtracted. Different models background shape include: linear, Shirley and Tougaard. A simply linear-type background can be used for fast spectral analysis, whereas for more accurate line shape analysis, more sophisticated background is preferred. The Shirley background is a smoothed step function which is a good approximation to fit the background intensity. The Tougaard background is a more complex smooth step background used to account for inelastic process. For all core level photoemission spectra in this thesis, a Shirley background has been subtracted.

### 2.3.4.3 Quantitative analysis

The absolute concentration determination is not carried out in an XPS experiment because some parameters needed are difficult to access such as, for example, the flow of photons over the surface analysed. However, based on the intensity  $I_i$  of the XPS signal, a relative quantitative analysis is possible either by expressing the stoichiometric ratio of the atomic concentrations of two elements A and B [184]:

$$\frac{N_A}{N_B} = \frac{\frac{I_A}{\sigma_A \lambda_A T(E_A)}}{\frac{I_B}{\sigma_B \lambda_B T(E_B)}} \quad (2.16)$$

Where,  $\sigma_i$  and  $\lambda_i$  are respectively the photoionization cross section and the mean free path of an element  $i$ ,  $T$  is the spectrometer transmission function, which combines the transmittance of the analyser and the efficiency of the detector, and  $E_i$  is the detected kinetic energy.

The stoichiometry of an element can also be expressed in terms of the sum of all the elements detected. This is then the concentration in relative atomic percentage:

$$X_A = \frac{N_A}{\sum_i N_i} = \frac{\frac{I_A}{\sigma_A \lambda_A T(E_A)}}{\sum_i \frac{I_i}{\sigma_i \lambda_i T(E_i)}} \quad (2.17)$$

The intensity of a XPS signal is given by:

$$I(\theta) = I_\infty \left[ 1 - e^{-\frac{z}{\lambda \sin \theta}} \right] \quad (2.18)$$

Where,  $I_\infty$  is the XPS signal obtained from the contribution of electrons for an infinitely layer,  $z$  is the thickness of a surface layer that contributes in signal and  $\lambda \sin \theta$  is the escape depth.  $\lambda$  is the mean free path and  $\theta$  is a given direction of the emitted electron. The escape depth is determined as the distance normal to the surface of the sample at which specified particles or radiations escape without significant energy loss due to inelastic processes.

### 2.3.4.4 Other physical effects

The XPS spectrum can also show binding energies relative to different electrons aside from those coming from core levels. Many electronic effects are the origin of these peaks: Auger transitions, peaks due to plasmon excitation or even satellite peaks of shake-up and shake-off.

## 2.3.4.4.1 X-ray excited Auger electron transition

The Auger emission follows the core level ionization. Three atomic levels are involved in the Auger emission (as seen in Figure 2.33). For example, an ionization of the K shell is filled by an electron from an upper L shell, the energy of this transition is not dissipated in radiative form but communicated to a third L electron which is ejected, which triggers a Auger KLL transition series and its lines can also be seen in the XPS energy spectrum. Auger electron energies are also sensitive to the chemical environment of emitting atoms. Its shift can be used in addition to that from the main photoelectron lines in order to obtain better information on the chemical structure of the compounds studied.

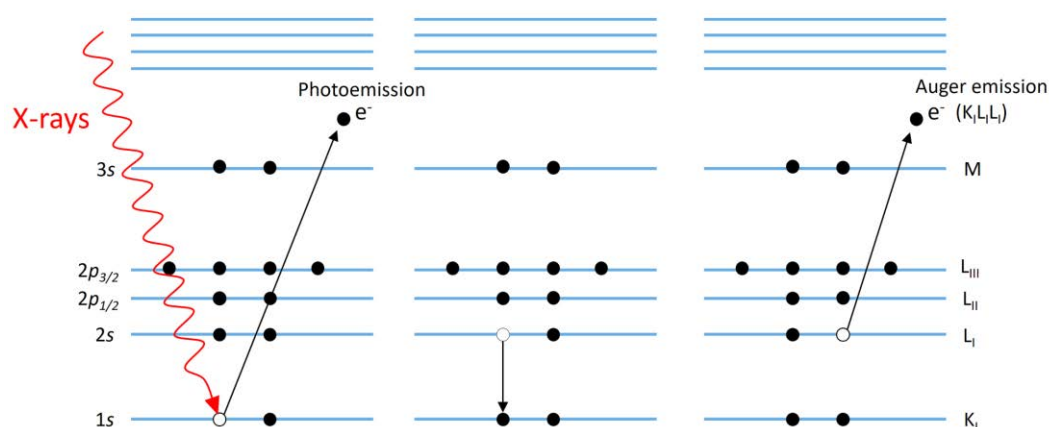


Figure 2.33. Auger transition principle for a KLL emission. [189]

## 2.3.4.4.1.1 Shake-up and shake-off satellites

One of the consequences of the relaxation effects in response to the creation of core holes by photoionization is the appearance of the so-called shake-up and shake-off satellites. The satellites formation mechanism is shown schematically in Figure 2.34. The spectrum in this figure shows three types of  $1s$  core level photoemission mechanism. The peak on the right is the main peak associated with the previous presentation of one core electron emission. The orbitals configuration shown above the main peak represent the final ionized state with one missing electron on the  $1s$  monoenergetic orbital and the remaining residual electrons frozen on their un-relaxed orbitals ( $1s^2 2s^2 2p^6$ ).

However, photoionization of core levels, such as a  $1s$  orbital, creates a final state with a very high excitation energy, part of which can be communicated to the residual electrons of the ionized atom, in particular to weakly bound valence electrons or, in other words, “shake” the valence electrons, as the term shake-up suggests. Thus, if an unoccupied level is at a sufficiently low energy and close to the last occupied levels of the ionized atom, an electron occupying these valence orbitals can be excited and sent to that unoccupied level. In our example case then, an  $2p$  electron of the main ionized configuration ( $1s^2 2s^2 2p^6$ ) is excited on the unoccupied  $3p$  orbital to give the final excited  $1s^2 2s^2 2p^5 3p^1$  configuration of lower energy. The energy of the transition shake-up from the orbital  $2p$  to the orbital  $3p$

accompanying the photoemission is to be subtracted from the kinetic energy of the photoelectron emitted. The photoelectron participating of this process has then a lower kinetic energy from that of the main peak. This is the reason for appearing satellites peaks close to the main peak at higher binding energies.

The energy of the transition shake-up can increase until the excitation limit of the  $2p$  electron on a free level and therefore of its emission, hence the term shake-off. As the free levels form a continuum, the shake-off satellites do not appear in the form of peaks but in the form of a continuous band following the shakeup satellite peaks.

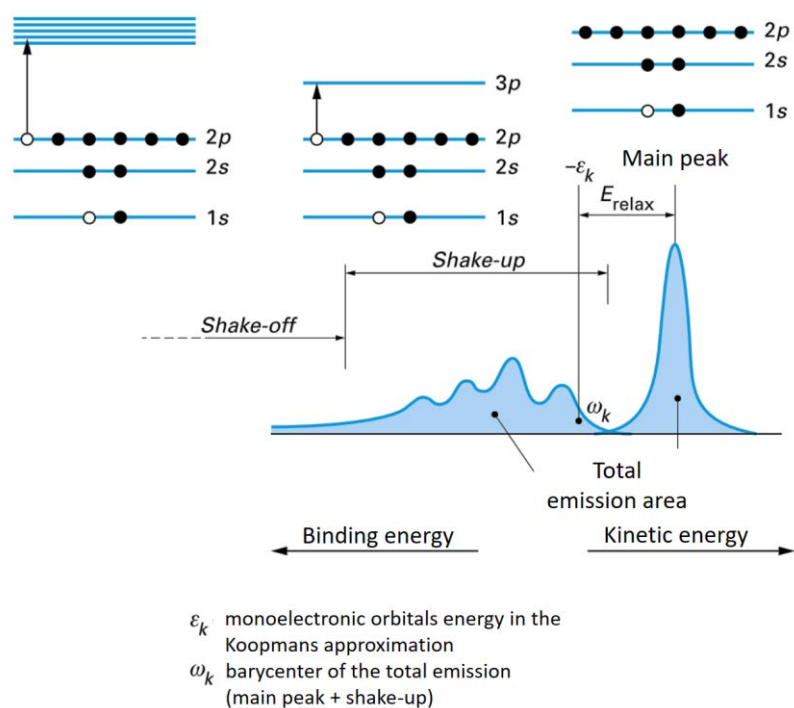


Figure 2.34. Shake-up and shake-off process. [184]

#### 2.3.4.5 The VersaProbe II

The PHI Versaprobe II equipment from ULVAC-PHI (Physical Electronics Inc., Chanhassen, MN, USA) used in this work basically consists of the following tools. An X-ray source with a monochromator, a sample handler, a collection lens set, a hemispherical electron analyser (HSA), a detection system for electron and data processing by computer and an ultra-vacuum pump to obtain a high vacuum (of the order of  $10^{-9}$  mbar).

A schematic view of the XPS instrumentation is illustrated in Figure 2.35. The X-ray source, the monochromator and the photoelectron analyser will be described below.

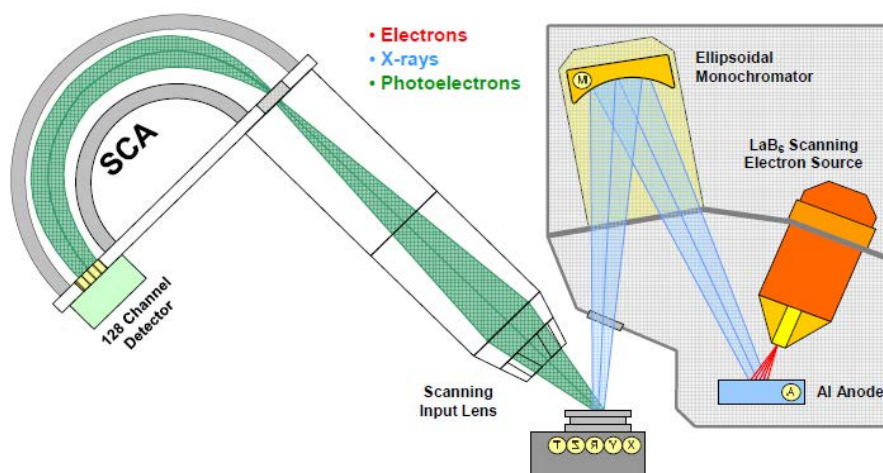


Figure 2.35. Schematic view of a monochromatized XPS instrument with a hemispherical energy analyser (HSA) and multi-channel detector.

### 2.3.4.5.1 The X-ray source

Within an X-ray source, radiation is produced from the interaction of electrons emitted by a cathode with a metallic anode. The energy loss of the incident electron is sufficient to generate focused X-rays of importance for a XPS experiment. A  $\text{LaB}_6$  (Lanthanum Hexaboride or “Lab Six”) crystal is mounted as a sharp crystal point on a single-piece stress-free nonreactive graphite carbon which is heated resistively to raise the temperature of the emitter. This heating causes thermionization of the electrons in the filament. These electrons are then accelerated through an electric field formed due application of a high potential difference (up to 20kV) until hitting the metal anode. This interaction generates an X-ray emission.

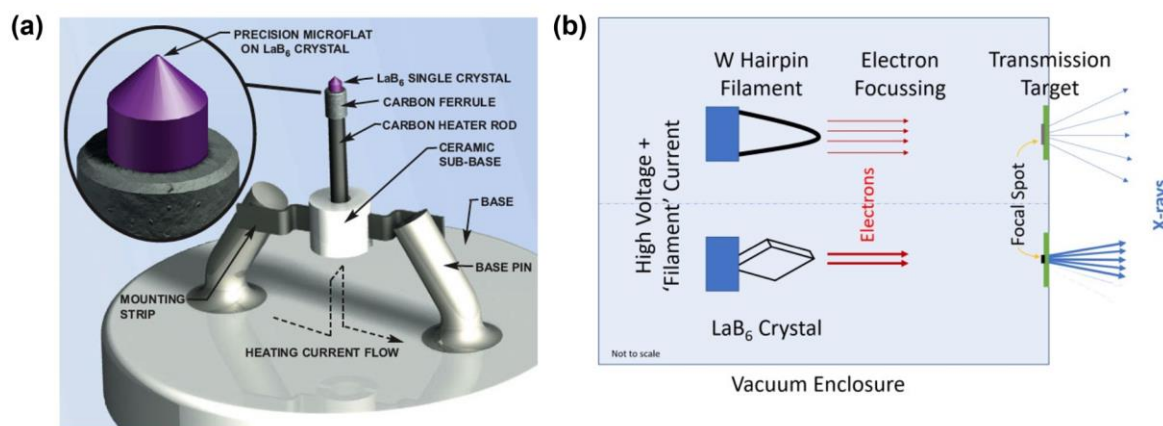


Figure 2.36. (a) Schematic view of a Lanthanum Hexaboride ( $\text{LaB}_6$ ) cathode used in an X-ray source for XPS equipment. (b) Schematic of a comparison of open, transmissive-target X-ray tubes using either a traditional Tungsten (W) hairpin filament or  $\text{LaB}_6$  crystal for electron generation and the relative effects these have on focal spot size and X-ray emission (flux). Emission is actually from almost  $180^\circ$  from the target exit surface but ray diagram is simplified for clarity.

There are two types of X-rays radiation that take place simultaneously during this process: the characteristic X-rays and the Bremsstrahlung X-rays. The characteristic X-rays are created when the incident electron knocks a low energy electron out of the shells of the atom in the metal anode and an electron in higher energy level drops down to fill the vacancy left by the knocked electron. This radiation is called characteristic because the energy of this emission is characteristic of the chemical element that serves as the anode material. In the case of an aluminium anode, the  $K_{\alpha}$  line has an energy of 1486.7 eV with a FWHM of 0.85 eV. Conversely, the Bremsstrahlung is created when the incident negatively charged electron is slowed down when passing close to the positively charged nucleus of the atom in the anode. This Bremsstrahlung radiation composes the continuous white spectrum, also known as the background noise seen in subsection 2.3.4.2.3. In order to avoid damaging the anode, which heats up during multiple electron impacts, a cooling circuit is used to lower its temperature. This process is specially done under UHV so as not to damage the filament as well as other elements of the source subjected to high voltage but also to avoid the interaction of electrons and photons with impurities.

#### 2.3.4.5.2 Monochromator

A monochromator is employed to select a single line of the unresolved  $K_{\alpha_{1,2}}$  doublet of X-rays, to eliminate satellite peaks and to suppress the continuous white spectrum. The monochromator is based on the diffraction of the X-ray polychromatic beam on a crystal cut parallel to a family of reticular planes, where only the wavelengths that meet a selective reflection condition are reflected. This reflection condition is given by the Bragg's law:

$$n\lambda = 2d \sin \theta \quad (2.19)$$

Where  $n$  is a positive integer representing the diffraction order,  $\lambda$  is the wavelength of the reflected emission wave,  $d$  is the inter-reticular distance of the crystal, and  $\theta$  is the scattering angle. Figure 2.37a shows a diagram of a monochromator that allows both to select a wavelength and focus the beam on the sample, and Figure 2.37b shows the difference of an Al  $K_{\alpha_{1,2}}$  line detection with and without a monochromator:

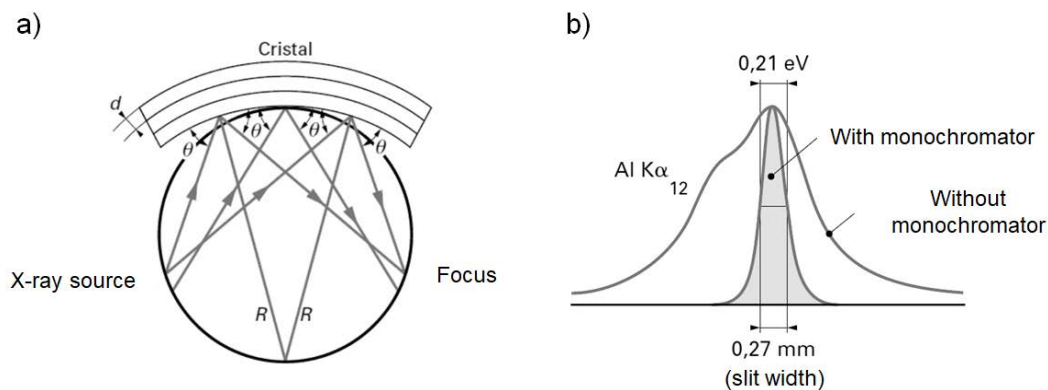


Figure 2.37. a) A monochromator that allows both to select a wavelength and focus the beam on the sample under Bragg condition, and b) an Al  $K_{\alpha 12}$  line profile with and without using a monochromator. [184]

Generally, a quartz crystal is suitable for this kind of application, since it is slightly flexible and not too thick allowing then to diffract (first order) the Al  $K_{\alpha}$  line for an angle of Bragg of  $78.5^{\circ}$ .

#### 2.3.4.5.3 Photoelectron analyser

After the X-ray beam monochromatization and focusing on the surface of the samples, characteristic photoelectrons are ejected from the extreme surface of the sample. These photoelectrons are then collected, differentiated according to their kinetic energy and analysed inside a specific analysis system. This system is divided into: an optic input, composed of electrostatic lenses with the purpose of collect the photoelectrons and focus them on the input slit of the analyser, the hemispheric energy analyser (HSA) which allows the selection of photoelectrons according to their kinetic energy, and the detector which counts the number of photoelectrons.

A detailed representation of the HSA analyser is given in Figure 2.38.

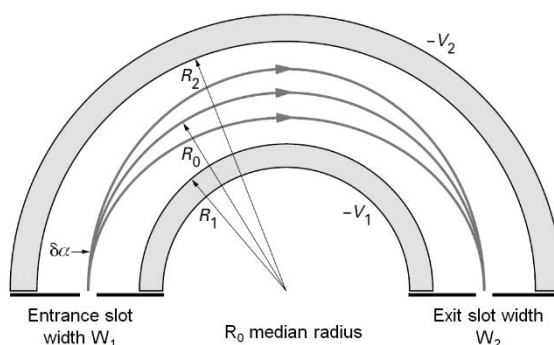


Figure 2.38. Scheme of a  $180^{\circ}$  hemispherical analyser commonly used in XPS. [184]

This analyser consists of two concentric hemispheres, one of radius  $R_1$  and the other of radius  $R_2$ . The  $R_0$  corresponds to the median radius. Fixing the potential of the internal sphere to  $-V_1$  and that of the

external sphere to  $-V_2$ , an electric field of direction normal to the surface of the spheres is formed. This electric field has the effect of dispersing the path of the photoelectrons as a function of their kinetic energy ( $\delta$ ) when compared to an energy of analysis  $E_a$ , which depends on the geometry of the analyser and on the potential difference  $V_2 - V_1$ :

$$E_a = ke (V_2 - V_1) \quad (2.20)$$

Where  $e$  is the charge of the electron and  $k$  is a constant spectrometer parameter based on  $R_1$  and  $R_2$  radius.

Then, photoelectrons entering in the analyser with energy less than  $E_a$  will be strongly deflected by the electric field and strike the inner sphere, and those with energy greater than  $E_a$  will be weakly deflected and crash into the outer sphere. Thus, a priori only electrons of energy  $E_a$  can pass through the analyser by taking the median circular path, as shown in Figure 2.39:

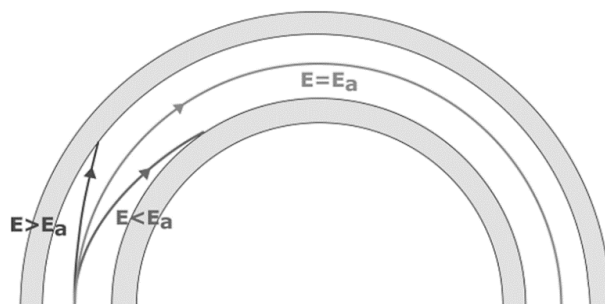


Figure 2.39. Electrons path through the analyser according to their input energy. [184]

The situation described in Figure 2.39 is an extreme case. A practical situation of analytical interest takes into account a range of energy, where  $E$  is an interval  $[E_a - \delta, E_a + \delta]$ , with  $\delta \approx 10\%E_a$  that allows dispersion at the output.

#### 2.3.4.5.4 Energy resolution

The energy resolution  $\Delta E$ , or the emission lines width, is an important parameter in XPS. It due mainly because if the difference in energy between two neighbours peaks, each corresponding to a different chemical environment, is less than the energy resolution  $\Delta E$ , it becomes impossible to differentiate their information and these two environments are consequently lost.

The total energy resolution  $\Delta E_T$  of an XPS experiment counts on three energy contributions. The  $\Delta E_n$  that is the natural line width related to the lifetime broadening. The  $\Delta E_s$  that is the X-ray source resolution. The  $\Delta E_A$  that is the analyser resolution. These terms are related by the following equation, as previously seen in subsection 2.3.4.2.2:

$$\Delta E_T^2 = \Delta E_n^2 + \Delta E_s^2 + \Delta E_A^2 \quad (2.21)$$

For a monochromated Al K $\alpha$  the photon bandwidth is of 0.26 eV. While  $\Delta E_A$  depends on the pass energy  $E_a$  in the HSA, the mean radius  $R_0$ , the angle of electrons entering the analyser at the entrance slit  $\delta_\alpha$ , and the entrance  $w_1$  and exit  $w_2$  slit width (see Figure 2.38):

$$\Delta E_A = E_a \left( \frac{(w_1 + w_2)}{2R_0} + (\delta_\alpha)^2 \right) \quad (2.22)$$

Since the optimal resolution is reached when  $(\delta_\alpha)^2 = \frac{w}{R_0}$ ,

$$\Delta E_A = E_a \left( \frac{(w_1 + w_2)}{2R_0} \right) \quad (2.23)$$

Thus, the analyser resolution  $\Delta E_A$  decreases with the pass energy  $E_a$  and with the width of the slits. However, the instrument sensitivity increases with  $E_a$ . A balance is therefore necessary.

In addition, aiming to detect electrons with different kinetic energies, electrons can be delayed at the detector input by a potential  $R$  up to the pass energy  $E_a$ :

$$E_a = E_{kin} - eR \quad (2.24)$$

Thus by varying  $R$ , it is possible to sweep the energy spectrum. Another way to proceed is to vary the voltages applied to the hemispheres ( $V_1$  and  $V_2$ ), in order to vary  $E_a$ , while keeping the voltage  $R$  constant.

#### 2.3.4.5.5 The Channeltron detector

The detector is a channel electron multiplier (Channeltron) placed in the analyser exit plane. It amplifies the current of a single photoelectron by a factor  $10^7$  to  $10^8$ . The principle is as follows. When a potential is applied between the input and output end of the microchannel plate (Figure 2.40a), the resistive surface forms a continuous dynode (Figure 2.40b). A dynode has the property of emitting secondary electrons when primary particles (photoelectrons, in this case) impinge upon it. These secondary particles are accelerated down the channel by a positive bias. Upon striking the interior surface of the channel walls, these electrons then generate further secondary electrons. The resulting avalanche process produces an easily detectable output pulse of charge containing up to  $10^8$  electrons with duration FWHM of about 8 nanoseconds. If the electron avalanche is collected with an anode, a single pulse is produced that appears on the oscilloscope as shown in Figure 2.40c. These output pulses are then detected using a discriminator, a preamplifier and a pulse counter.

The recorded spectra are sets of data containing the intensity corresponding to the total counts versus the electron kinetic energy referred to the sample Fermi level ( $E - E_F$ ). The intensity is most of the time given in counts per second. Either the energy scale can be expressed in terms of measured kinetic energy or, if the position of the Fermi level is known, in terms of binding energy.

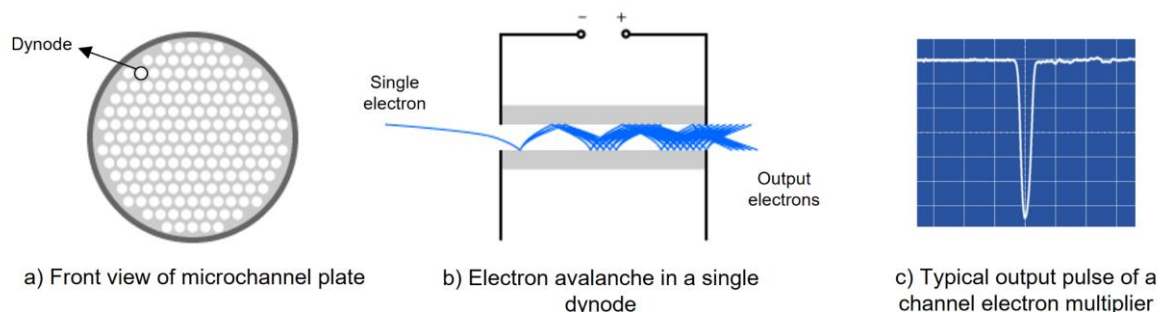


Figure 2.40. Front view of a microchannel plate, the generation of an electron avalanche with a single incident electron, and the typical output pulse of a channel electron multiplier.

### 2.3.5 Photoemission electron microscopy (PEEM)

The photoemission electron microscopy (PEEM) is based on the same photoelectric principle as XPS. It is also interested in measuring the kinetic energy of photoelectrons emitted from ionised atoms in the sample during exposition to electromagnetic radiation aiming to access the characteristic binding energies of these photoelectrons. Moreover, a high-performance imaging system is reached in this technique using an additional spherical mirror analyser consisting of two concentric hemispheres and a delay-line detector system which records position-sensitive spectra allowing record local variations in electron emission to generate image contrast.

#### 2.3.5.1 The NanoESCA

The NanoESCA MkI spectromicroscope (Scienta Omicron) used in this work consists of a photon source, a PEEM column that leads the photoemitted electrons through the spectrometer, a twin hemispherical energy analyser for aberration corrections, a detection system and data processing by computer and an ultra-vacuum pump to obtain a UHV of the order of  $10^{-9}$  mbar.

##### 2.3.5.1.1 Excitation sources

The NanoESCA is equipped with two types of photon sources:

- Low energy photons – emitted in ultraviolet (UV) mercury (Hg) discharge lamp at 4.9 eV and vacuum ultraviolet (VUV) helium I or II discharge lamp at 21.2 eV and 40.8 eV, respectively.

- High energy photons – include monochromatized Al K $\alpha$  or Mg K $\alpha$  X-rays with photon energies of 1486.7 eV and 1253.6 eV, respectively.

The low energy photons can only probe the outermost electrons broadened in the valence band. The experiment using these photons is called UV-PEEM. In other hand, the high energy photons can probe core level electrons. The experiment using these high energy photons is called X-PEEM. These incident photons reach the surface of the sample at an angle of  $\sim 77^\circ$  with respect the normal *i.e.* Brewster's angle. This is necessary because the maximum resolution of the instrument is achieved only when there is a short working distance between the anode and the sample ( $\sim 4$  mm) [190].

The Al K $\alpha$  photon source is the same used in the XPS experiment and is already described in subsections 2.3.4.5.1 and 2.3.4.5.2.

### 2.3.5.1.2 Operating modes

As mentioned before, the photon radiation is capable to induce electrons from innermost and outermost shells of elements. With a photon source of chosen energy, the generated photocurrent contains photoelectrons with kinetic energy ranging from zero to  $h\nu - \phi_{sam}$ . The kinetic energy distribution of the emitted electrons is schematically shown in Figure 2.41 [191].

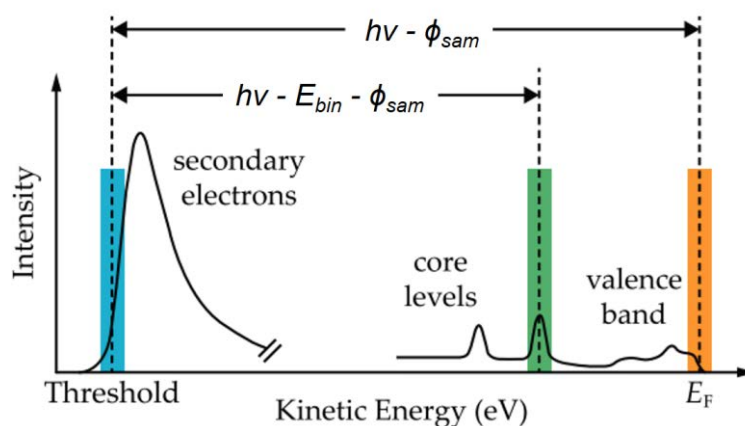


Figure 2.41. Schematic of a full photoemission spectrum. The intensity of the collected photoelectrons is plotted as a function of kinetic energy. The coloured areas represent the high intensity photoemission threshold corresponding to secondary electrons of low kinetic energy (blue), the core level region (green) and the valence band (orange). Adapted from [191]

These all photoelectrons collected inside the spectrometer can take different paths according to the microscope-operating modes:

1. Direct non-energy filtered PEEM mode,
2. Spectroscopy mode using a Channeltron detector,
3. Energy filtered PEEM imaging mode.

A schematic view of the PEEM instrumentation is illustrated below in Figure 2.42.

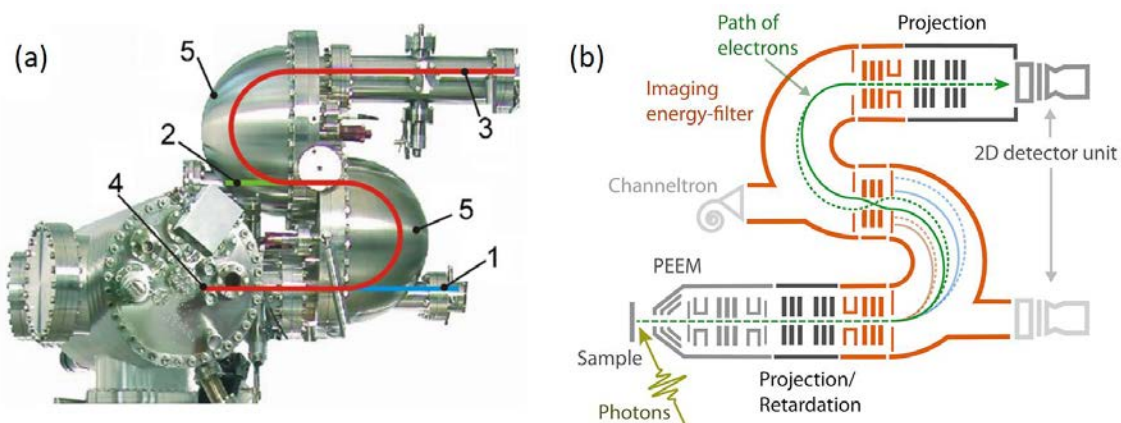


Figure 2.42. (a) Photo and (b) equivalent schematic layout of the NanoESCA Mk1 spectromicroscope (Scienta Omicron) instrument. Three operating modes are possible: (1) direct non-filtered photoelectron emission microscopy (PEEM) mode, (2) selected area spectroscopy or Channeltron mode, and (3) energy-filtered PEEM imaging mode. (4) Indicate the sample position and (5) the hemispherical analyser. Adapted from [192]

These three different operational modes will be detailed in the following subsections.

### 2.3.5.2 Non-energy filtered PEEM mode

In the PEEM direct imaging mode, the photoelectrons are magnified onto an image detection unit without passing through any energy analyser. The image formed contains the entire set of photoelectron energies seen in Figure 2.41.

#### 2.3.5.2.1 Electron optics: the PEEM column

In the PEEM column, the sample is near ground potential. The extractor anode that is part of the first lens in the immersion objective is at high positive voltage (about 15 kV). The sample is held at a high negative potential and an electric field is created between it and a grounded anode, which allows collecting photoelectrons emitted with large angles. The whole column is biased to negative voltage to focus the photoelectrons on the image plane. The PEEM column consists of the following magnetic elements. An immersion objective lens with an adjustable contrast aperture situated in the back focal plane of this objective lens, an electrostatic octupole stigmator, a field aperture or iris aperture in the first image plane, and two projective lenses. The adjustable iris aperture is used to select a defined FoV for selected area spectroscopy. The projective lenses are either used to project the first intermediate image onto the screen for direct non-energy-filtered imaging or to adapt the electron beam to the pass energy of the analyser. The PEEM column is seen in Figure 2.43.

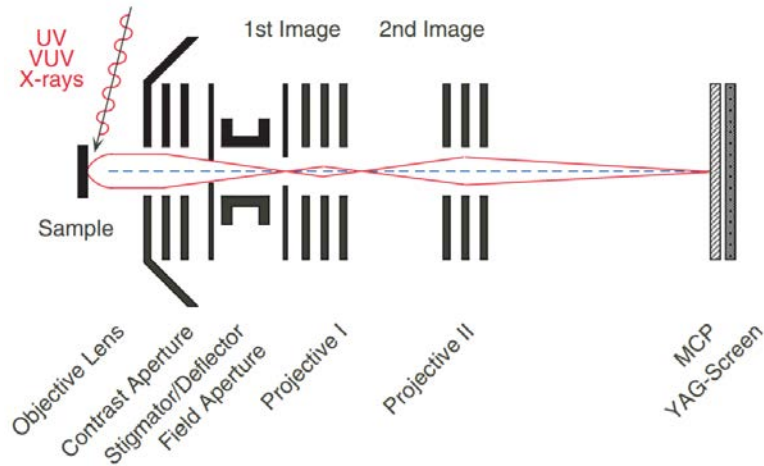


Figure 2.43. General technical layout of an electron emission microscope utilizing photoexcitation (PEEM). [193]

### 2.3.5.2.2 PEEM transmission

The combination of immersion objectives lens and contrast aperture has a retardation filter behaviour. As we can see in Figure 2.44, secondary electrons yield sees its distribution in energy decrease after passing through the magnetic optics [193]. The retardation behaviour also depends on the contrast aperture diameter placed in the focal plane. The smallest the aperture, the smaller energy width and the lower the intensity of the secondary electron spectrum [194].

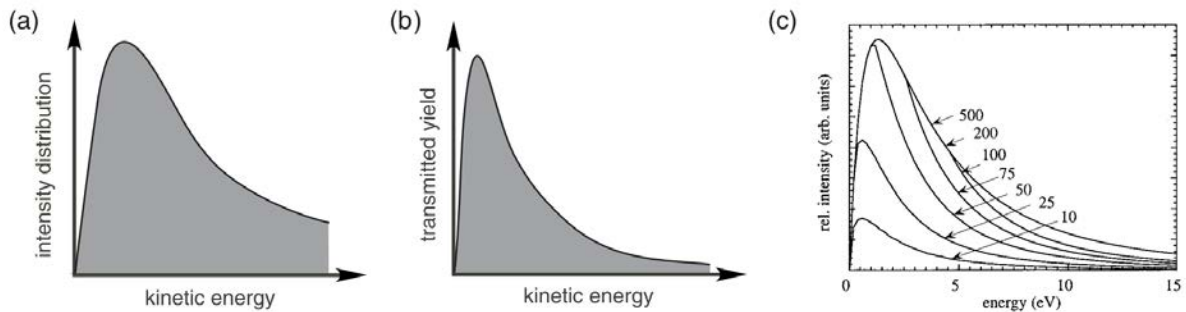


Figure 2.44. Schematic secondary electron spectrum before (a) and after passing through the electron emission microscope optics (b). (c) Energy distribution of electrons transmitted through a PEEM column using apertures of different diameters (in  $\mu\text{m}$ ). [193, 194]

### 2.3.5.2.3 The detection system

The detector consists of three elements: microchannel plates, a fluorescent screen and a camera that contains a charged-coupled device (CCD). The objective using these three elements is to convert the electronic signal collected by the column in an optical signal, which can be recorded by the camera. In summary, the electrons are firstly multiplied thanks to an avalanche multiplication system inside the

microchannel plates. Then, accelerated onto a YAG crystal fluorescent screen that emits a photon when hit by an electron. A cooled CCD equipped with a lens collects these photons. The optical image resulting on the fluorescent screen corresponds to the electronic image of the surface obtained by the PEEM.

### **2.3.5.3 Spectroscopy or Channeltron mode**

In the Channeltron mode, is possible to acquire a spectrum from a selected area. Applying proper electron optics settings, photoelectrons of chosen kinetic energy are slowed down at the entrance of the analyser to a kinetic energy that matches the band pass of the energy analyser  $E_a$ . Hence, chosen photoelectrons can travel inside the analyser, giving access to the binding energy of the initial photoelectrons, according to equation 2.11. The photoelectrons are collected using a channel electron multiplier (Channeltron) after the first hemispherical analyser. The Channeltron detector operation is already described in subsection 2.3.4.5.5.

### **2.3.5.4 Energy filtered PEEM mode**

In the energy-filtered PEEM mode, selected electrons are allowed to travel inside the second analyser, which corrects the spherical aberrations generated by the first analyser, before reach an image unit composed of microchannel plates, a fluorescent screen and a CCD camera. This image unit is already described in subsection 2.3.5.2.3.

#### **2.3.5.4.1 Double energy analyser IDEA**

The analyser of the NanoESCA, called the imaging double energy analyser (IDEA), consist of two hemispherical energy analysers (HAS). The action of the two analysers is shown in Figure 2.45. In the closed spherical field, similar to planetary motion (Kepler ellipses), the trajectories of the electrons coincide after a complete revolution, independent of the star energy or start angle, generating a perfect achromatic image without aberrations. This is mainly because the second half of the elliptical orbit compensates the aberrations of the first half. In the IDEA analyser the same aberration compensation is observed with the support of a transfer lens placed leaving the first hemisphere and entering in the second hemisphere [195].

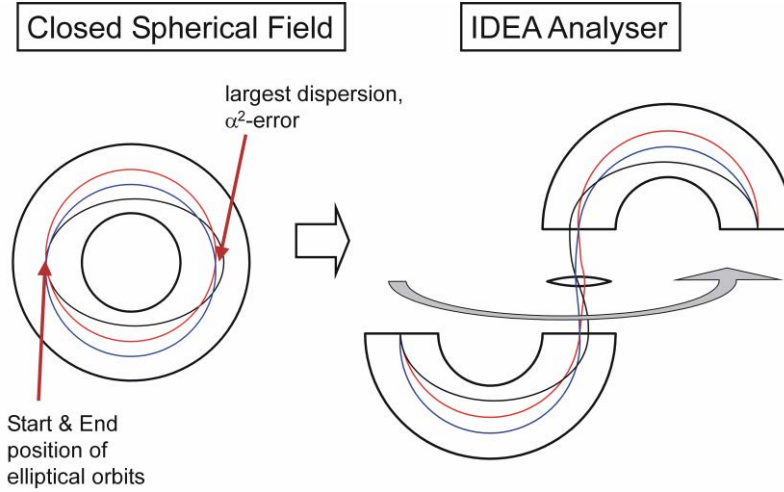


Figure 2.45. Schematic illustration of the basic design for the Imaging Double Energy Analyzer (IDEA). The different coloured particle trajectories are drawn for the same kinetic start energy.

#### 2.3.5.4.2 Energy resolution

The energy resolution of the IDEA analyser is identical to the energy resolution of a single HSA seen previously in equation 2.22 [192].

$$\Delta E_A = E_a \left( \frac{(w_1 + w_2)}{2R_0} + (\delta_\alpha)^2 \right) \quad (2.25)$$

Where  $E_a$  is the electron pass energy,  $R_0$  is the hemisphere mean radius,  $\delta_\alpha$  is the angle of electrons entering the analyser at the entrance slit, and the entrance  $w_1$  and exit  $w_2$  slit width. In normal operations, the entrance slits are smaller than those of the exit are. Thus, the exit slits determine the effective slit width (the sum of both entrance and exit slits width).

#### 2.3.5.4.3 Lateral resolution

The lateral resolution of a PEEM experiment is not limited by the IDEA system since the second hemispherical analyser always compensates the dispersion of the first one. Hence, contrary to the imaging XPS that the diffraction aberration can be neglected as large apertures must be used, the lateral resolution of the NanoESCA depends only on the aberrations of both the extracting field and the optics before and behind the IDEA, but especially those of the cathode objective lens [196, 197].

According to M. Escher *et al.* [192], the total resolution can be approximated by the disc diameter:

$$d_{tot} = 2 \sqrt{d_{r_c}^2 + d_{r_s}^2 + d_{r_d}^2} \quad (2.26)$$

Where  $d_{r_c}^2$ ,  $d_{r_s}^2$  and  $d_{r_d}^2$  are respectively the chromatic, the spherical and the diffraction contributions to the disc radius.

In biological samples such as tissues and cells, which normally have significant topography, spherical aberrations are currently introduced as the emitted electrons are ejected in various angles. Similarly, samples of multiple chemical components with different characteristic photoionization energies introduce chromatic aberrations as the emitted electrons are ejected at different kinetic energies [190].

For M. Escher *et al.* [192], the aberrations due diffraction can be reduced by using a smaller angular spread during the extraction of electrons. The larger angles are usually cut by the contrast aperture. The aperture size can be reduced until diffraction at the aperture plays the dominant role. They also highlight the fact that resolution is more easily deteriorated by diffraction at higher extraction potentials.

Astigmatism is also an important factor that must be taken into account on PEEM lateral resolution. It is due problems of misalignment between the sample and the optical column, or due to the misalignment between the different lenses of the PEEM column.

### **2.3.5.5 Types of contrasts in PEEM imaging**

The contrast observed in PEEM images are not trivial to interpret. They originate from spatial variations of the electron yield, either of the secondary electrons in non-energy filtered PEEM mode or from electrons of a specific energy in filtered PEEM mode. In non-filtered PEEM mode, the contrasts are consequence of lateral variations of work function and morphology. The same contrast mechanism can be seen in energy-filtered PEEM mode using low energetic electrons (SE electrons). However, using high-energy electrons as excitation source in energy-filtered PEEM mode, core-levels and valence bands are probed.

#### **2.3.5.5.1 Work function contrast**

The work function contrast happens when photon excitation energies are in the range of the photoemission threshold of low energy (*e.g.*, UV discharge lamp near 5 eV). Regions of the biological sample where the SE photoemission threshold is greater than the photon excitation energy have low SE photoelectron yield and appear darker while regions where the SE photoemission threshold function is exceeded by the photon energy generally appear brighter. For materials in general, the work function depends on many factors including surface chemical composition, crystal orientation, surface dipole, and phase [198].

For local work function maps to be generated, images over the photoemission threshold are recorded by varying the SE photoelectron kinetic energy ( $E - E_F$ ). For each recorded energy, an image is acquired, which generates three-dimensional image stacks where the spatial contrast will also be a function of the SE photoelectron kinetic energy  $I(x, y, E - E_F)$ .

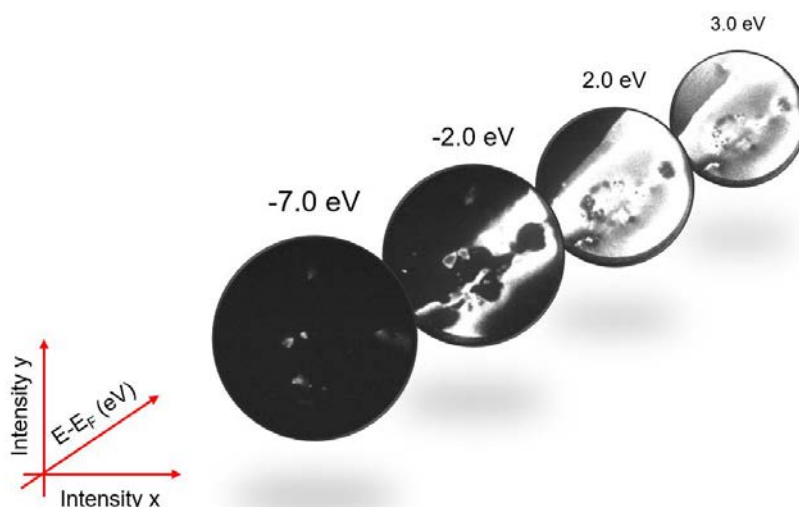


Figure 2.46. Image stack representation in 3D:  $I(x, y, E - E_F)$ . Work function contrast over the resin (O.C.T. compound) obtained from a range of  $E - E_F$  from -7.0 to 3.0 eV.

The work function  $\phi$  can be calculated by fitting the SE photoemission threshold with the following error function:

$$I(E - E_F) = \frac{I_{max}}{2} \cdot \text{erfc} \left[ \frac{\phi - (E - E_F)}{\sigma\sqrt{2}} \right] + I_{off} \quad (2.27)$$

Where  $I_{max}$  is the maximum intensity of the spectrum for each image pixel,  $I_{off}$  represents a constant offset,  $\phi$  is the work function, and  $\sigma$  is the standard variation of the Gaussian due to the energy broadening of the analyser at the pass energy used.

Other corrections and filtering in order to suppress instrumental artefacts superimposed by the microchannel plates and the CCD camera such as isochromatic effect, Schottky effect, dark- and flat field can be performed post measurement. More details about these corrections can be found elsewhere [192, 199, 200].

#### 2.3.5.5.2 Core-level contrast

The core-level contrast is due the lateral variations in the kinetic (binding) energy of determined core-level photoelectron of interest over a selected zone of analysis. The contrast generated is directly associated with the chemical environment the core-level electron was originally in, as previously seen in subsection 2.3.4.2.1 for a XPS experiment. Inside a CCD camera, core-levels images can have lower signal-to-noise ratio (SNR) than SE imaging, it is usually then necessary to acquire several series of image in the same range of kinetic energies, which makes the analysis long and ready after many hours

(an average of 6-8 hours for each core-level spectrum). Thus, the addition of the several images acquired can improve the SNR.

Figure 2.47 presents an example of a region of interest imaged at the O 1s transition with an Al K $\alpha$  source at 1486.7 eV.

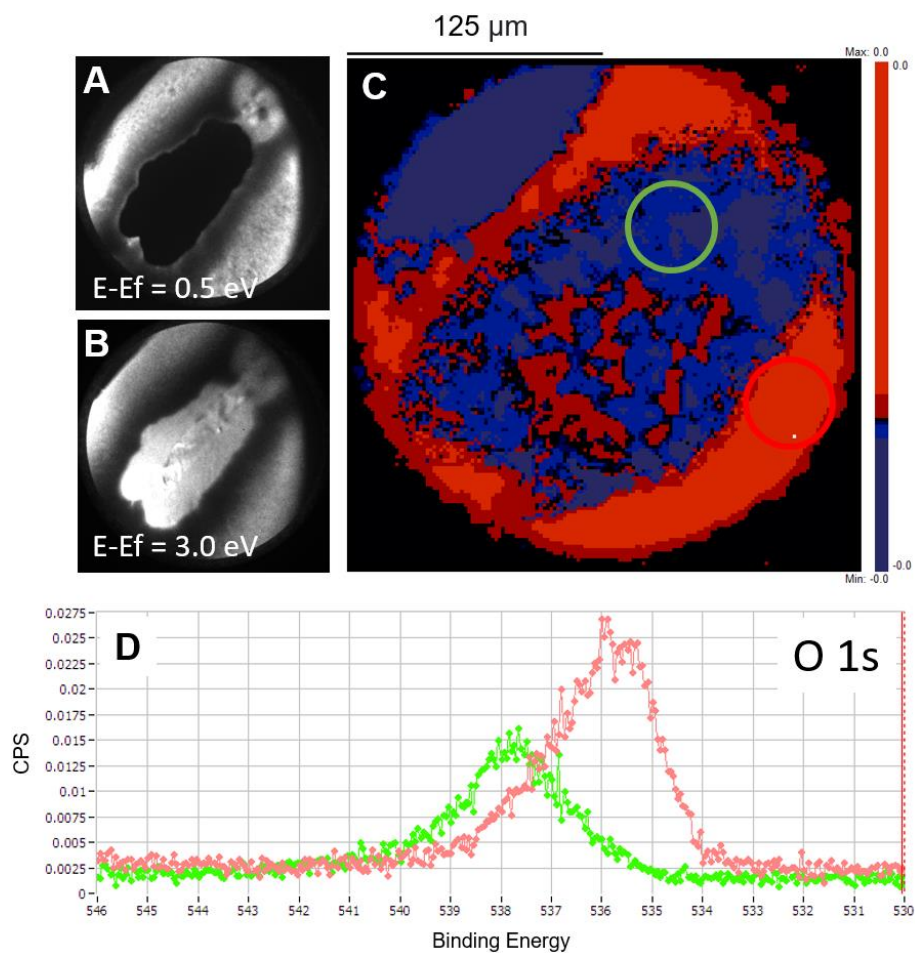


Figure 2.47. Work function contrast over an organic compound at (A)  $E - E_F = 0.5$  eV and (B)  $E - E_F = 3.0$  eV. (C) Filtered energy PEEM image showing differences in the O 1s chemical environment in the same region where the work function image was obtained. The blue and red colours highlight the chemical differences in this region. The O 1s core level spectrum for each blue (green spectrum) and red (red spectrum) regions were obtained by selecting a small circular zone in the region of interest and can be found in (D).

### 3 MULTIMODAL TOF-SIMS, AFM AND XPS APPROACH FOR SURFACE ANALYSIS OF DRUG DELIVERY SYSTEMS

In this third chapter, we will see the first level of application of our multimodal surface imaging approach to different synthetic and biocompatible drug delivery systems that have not yet been injected into a living brain. The drug delivery systems discussed here will be a HA hydrogel formulation that contains ketorolac tromethamine used as a cargo in the treatment of glioblastoma or gellan gum microcapsules used as an intelligent drug delivery vehicle. The preparation of these formulations was already described in section 2.2.1. The main interest in the use of surface microscopies here will be in the mapping of therapeutic drugs and microcapsules in HA hydrogel, which is considered an important information in understanding the dispersion of these components in HA hydrogel in the context of this localized therapy. The analysis of pure HA hydrogel, pure ketorolac tromethamine and pure gellan gum will also be performed in order to provide reference spectra that will be used later to distinguish these compounds when they are mixed into a drug delivery system. A schematic view of the multimodal planning of analysis of all pure and mixed systems that will be discussed in this chapter can be seen in Figure 3.1.

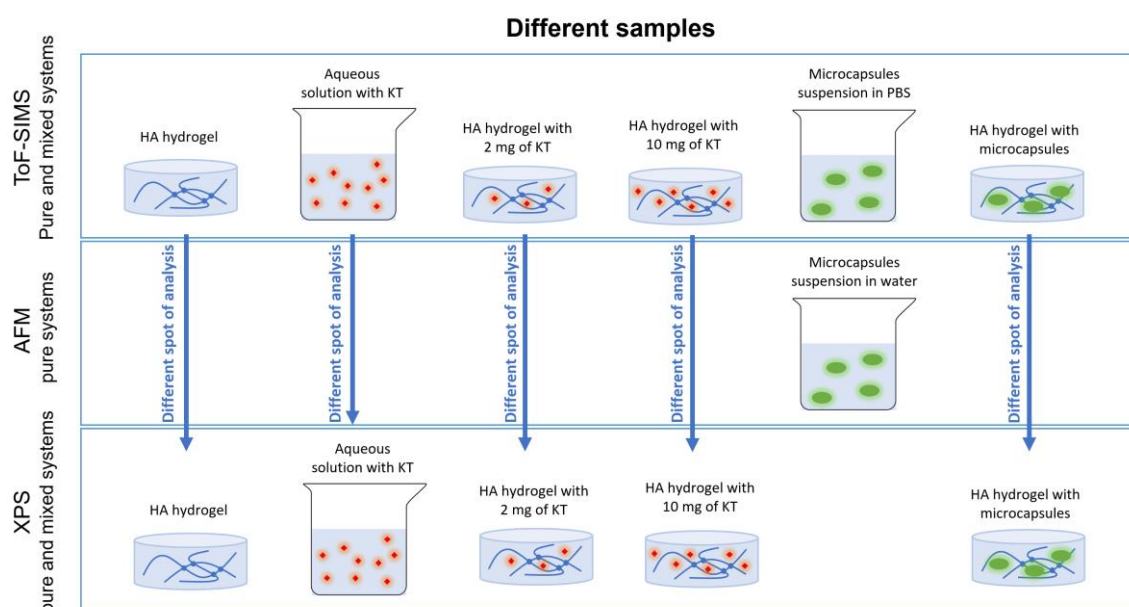


Figure 3.1. Schematic view of the planning of analysis of the different compounds part of the drug delivery systems that will be discussed in this chapter.

In the first section of this third chapter (3.1), we see how ToF-SIMS image analysis is a key tool in mapping the dispersion of ketorolac and gellan gum microcapsules in HA hydrogel. Here, we will mostly exploit on chemical contrasts generated by characteristic molecular fragments of ketorolac tromethamine, gellan gum and HA hydrogel when imaging the sample. In the second section of this third chapter (3.2), we present application of AFM in the topographical analysis of the surface of gellan gum

microcapsules. This can be an important information in the understanding of the mechanisms of absorption and release of drugs in these gellan gum microcapsules. In the third section (3.3), we see how XPS is a useful tool in identifying and quantifying chemical environments in HA hydrogel formulations containing ketorolac and gellan gum microcapsules. Then we present how the information obtained by ToF-SIMS and XPS can be punctually correlated. While an analytical method can generate qualitative molecular information about a target surface and give us the spatial distribution of these molecules (ToF-SIMS), only with the use of XPS we are able to measure and quantify the chemical environments present that correspond to the characteristic molecules highlighted by ToF-SIMS. This can be considered a possible approach in drug mapping and *in situ* measuring of drug reabsorption even for after implantation in living organs. Details about the multimodal imaging approach can be found in the fourth section (3.4). Conclusions for this chapter are given in the fifth section of this third chapter (3.5).

### **3.1 IMAGING OF KETOROLAC TROMETHAMINE AND GELLAN GUM MICROCAPSULES IN HA HYDROGEL BY TOF-SIMS**

In order to map the chemical distribution of 2-amino-2-(hydroxymethyl)propane-1,3-diol;5-benzoyl-2,3-dihydro-1H-pyrrolizine-1-carboxylic acid also known as ketorolac tromethamine and gellan gum microcapsules in HA hydrogel, we first identify by ToF-SIMS analysis the peaks or molecular ions characteristic of these three systems by ToF-SIMS analysis, individually before they are mixed. Then, we proceed with the chemical mapping of ketorolac tromethamine and gellan gum microcapsules in HA hydrogel formulations based on the chemical markers we found in the previous step.

#### **3.1.1 Individual chemical markers of HA hydrogel, ketorolac tromethamine and gellan gum**

To identify molecular ions characteristic of HA hydrogel, ketorolac tromethamine and gellan gum used as components of a drug delivery system in the treatment of glioblastoma, we initially acquired a mass spectrum over a  $500 \times 500 \mu\text{m}^2$  region on a pure hydrogel sample (freeze-dried sample), on a dry drop of aqueous solution containing ketorolac tromethamine and on a dry drop of PBS solution containing gellan gum microcapsules deposited onto a silicon substrate. The care taken in the preparation of freeze-dried samples or evaporating drops of aqueous or saline solution containing the sample of interest for analysis are necessary given the UHV system employed in surface microscopies such as ToF-SIMS and XPS.

##### **3.1.1.1 Chemical markers of pure HA hydrogel**

Figure 3.2 shows the resulting mass spectrum acquired on the pure and freeze-dried HA hydrogel. In order to make easier the visualization of the fragments of interest in this system, we selected the  $m/z$  range from 20 to 120.

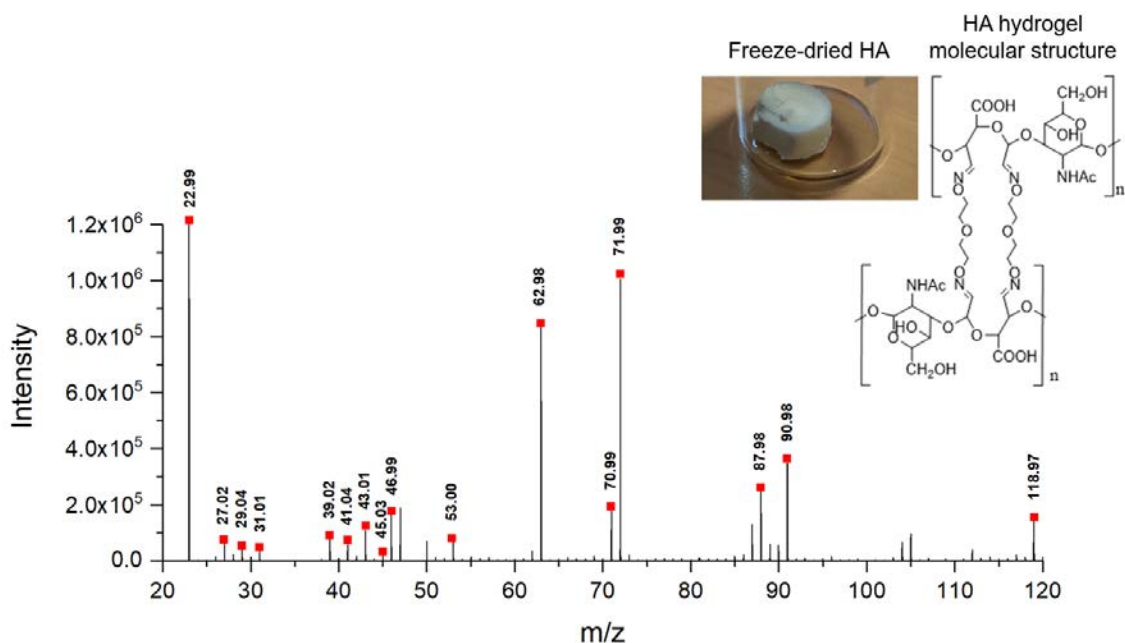


Figure 3.2. ToF-SIMS mass spectrum acquired in positive ion mode on a freeze-dried HA hydrogel.

According to A. Shard *et al.* [201], the ions between  $m/z = 27$  and  $53$  can be assigned to species such as  $C_2H_3^+$  ( $m/z = 27.02$ ),  $CHO^+$  ( $m/z = 29.00$ ),  $CH_2OH^+$  ( $m/z = 31.01$ ),  $C_3H_3^+$  ( $m/z = 39.02$ ),  $C_3H_5^+$  ( $m/z = 41.04$ ),  $CH_3CO^+$  ( $m/z = 43.01$ ),  $CH_5CO^+$  ( $m/z = 45.03$ ) and  $C_3HO^+$  ( $m/z = 53.00$ ). Further peaks characteristic of the HA hydrogel are noted at even higher mass, typically appearing at  $m/z = 62.98$ ,  $70.99$ ,  $71.99$ ,  $87.98$ ,  $90.98$  and  $118.97$ . The strong peak appearing at  $m/z = 22.99$  is due to sodium.

These peaks characteristic of HA hydrogel are listed below in Table 3.1.

Table 3.1. List of molecular ions identified on freeze-dried HA hydrogel samples.

	m/z (experimental)	m/z (theoretical)	Assignment
<b>Positive ions</b>	27.02	27.02	$C_2H_3^+$
	29.00	29.00	$CHO^+$
	31.01	31.01	$CH_2OH^+$
	39.02	39.02	$C_3H_3^+$
	41.04	41.03	$C_3H_5^+$
	43.01	43.01	$CH_3CO^+$
	45.03	45.03	$CH_5CO^+$
	53.00	53.00	$C_3HO^+$
	62.98	-	-
	70.99	-	-
	71.99	-	-
	87.98	-	-
	90.98	-	-
	118.97	-	-

### 3.1.1.2 Chemical markers of ketorolac tromethamine

Figure 3.3 shows the resulting mass spectrum acquired on a dry drop of aqueous solution containing ketorolac tromethamine. In order to make easier the visualization of the fragments of interest in this system, we selected the  $m/z$  range from 70 to 260.

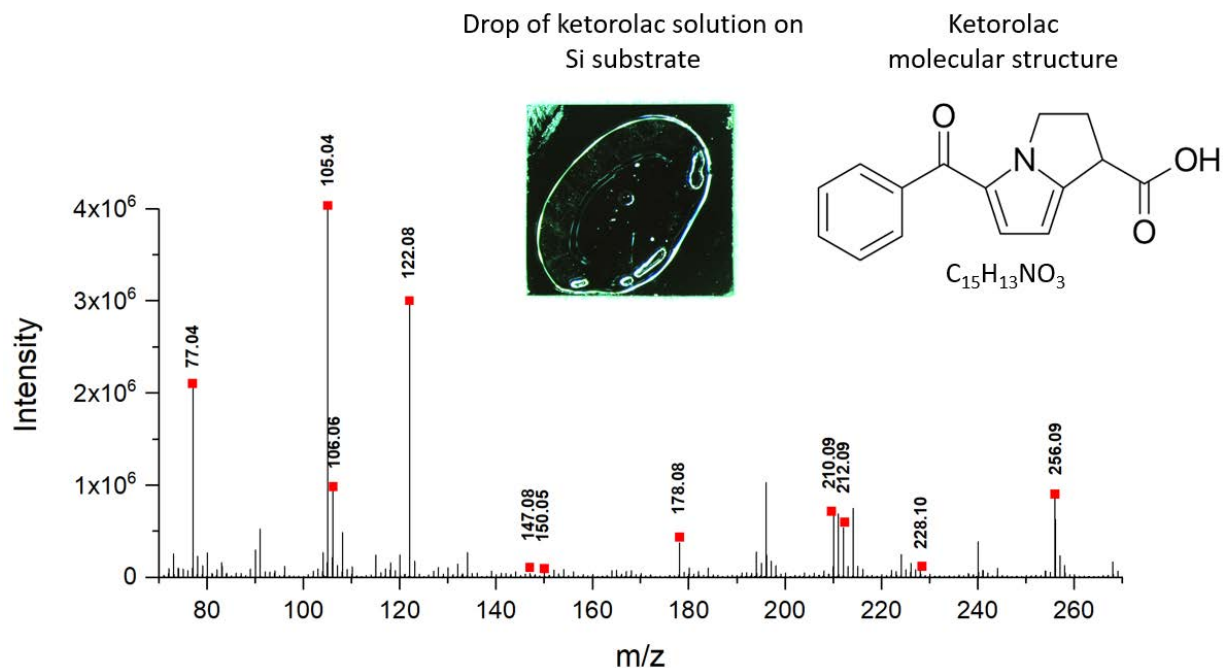


Figure 3.3. ToF-SIMS mass spectra acquired in positive ion mode from a dried drop of aqueous solution containing ketorolac tromethamine on silicon substrate.

According to R. Bandu *et al.* [202, 203],  $C_6H_5^+$  ( $m/z = 77.04$ ),  $C_7H_5O^+$  ( $m/z = 105.04$ ),  $C_7H_8N^+$  ( $m/z = 106.06$ ),  $C_7H_8NO^+$  ( $m/z = 122.08$ ),  $C_8H_8NO_2^+$  ( $m/z = 150.05$ ),  $C_9H_8NO_3^+$  ( $m/z = 178.05$ ),  $C_{14}H_{12}NO^+$  ( $m/z = 210.09$ ),  $C_{14}H_{14}NO^+$  ( $m/z = 212.10$ ),  $C_{14}H_{14}NO_2^+$  ( $m/z = 228.10$ ) and  $C_{15}H_{14}NO_3^+$  ( $m/z = 256.09$ ) are direct fragments of ketorolac tromethamine.

These peaks characteristic of ketorolac tromethamine are listed below in Table 3.2.

Table 3.2. List of molecular ions identified on a dry drop of aqueous solution containing ketorolac tromethamine.

	m/z (experimental)	m/z (theoretical)	Assignment
<b>Positive ions</b>	77.04	77.03	C <sub>6</sub> H <sub>5</sub> <sup>+</sup>
	105.04	105.03	C <sub>7</sub> H <sub>5</sub> O <sup>+</sup>
	106.06	106.06	C <sub>7</sub> H <sub>8</sub> N <sup>+</sup>
	122.08	122.06	C <sub>7</sub> H <sub>8</sub> NO <sup>+</sup>
	150.05	150.05	C <sub>8</sub> H <sub>8</sub> NO <sub>2</sub> <sup>+</sup>
	178.05	178.05	C <sub>9</sub> H <sub>8</sub> NO <sub>3</sub> <sup>+</sup>
	210.09	210.10	C <sub>14</sub> H <sub>12</sub> NO <sup>+</sup>
	212.10	212.12	C <sub>14</sub> H <sub>14</sub> NO <sup>+</sup>
	228.10	228.10	C <sub>14</sub> H <sub>14</sub> NO <sub>2</sub> <sup>+</sup>
	256.09	256.12	C <sub>15</sub> H <sub>14</sub> NO <sub>3</sub> <sup>+</sup>

### 3.1.1.3 Chemical markers of gellan gum microcapsules

Figure 3.4 shows the resulting mass spectrum acquired on a dry drop of PBS solution containing gellan gum microcapsules. In order to make easier the visualization of the fragments of interest in this system, we selected the m/z range from 30 to 110, then from 170 to 210.

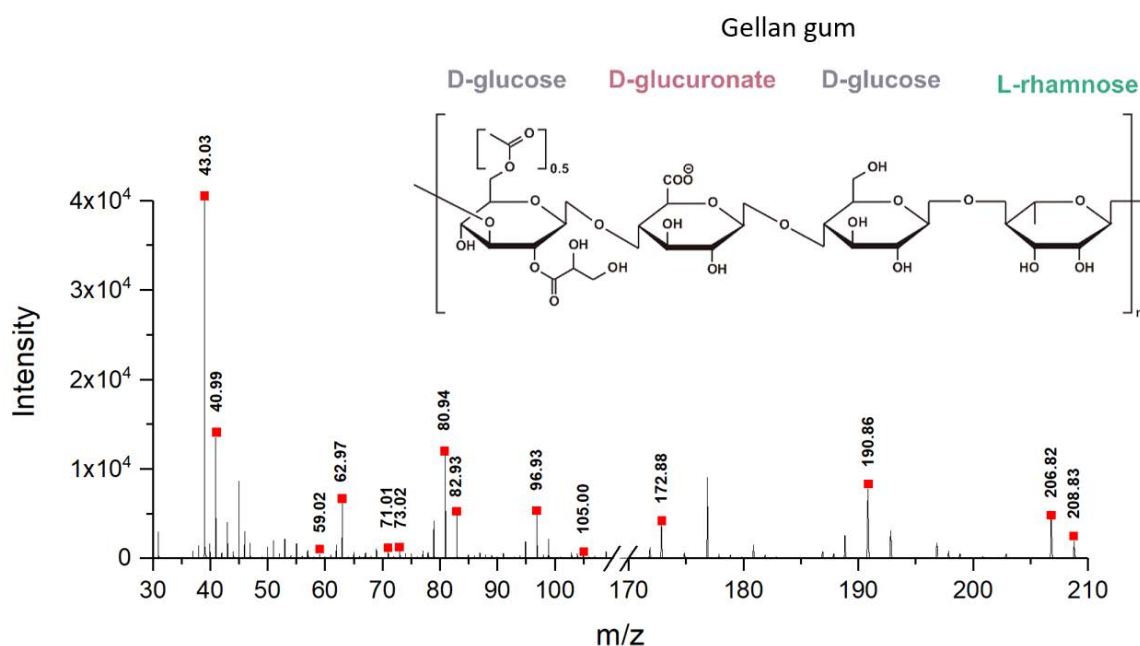


Figure 3.4. ToF-SIMS mass spectra acquired in positive ion mode from a dried drop of PBS solution containing gellan gum microcapsules on silicon substrate.

The peaks at m/z = 40.99, 43.03, 59.02, 62.97, 71.01, 73.02, 80.94, 82.93, 96.93 and 105.00 directly identified in the mass spectrum might be related to the D-glucose, D-glucuronate and L-rhamnose units. Further peaks at higher mass also appearing as characteristic of gellan gum include m/z = 172.88, 190.86, 206.82 and 208.83. These characteristic peaks of gellan gum are listed below in Table 3.3.

Table 3.3. List of molecular ions characteristic of gellan gum microcapsules.

	<b>m/z (experimental)</b>	<b>Assignment</b>
<b>Positive ions</b>	40.99	-
	43.03	-
	59.02	-
	62.97	-
	71.01	-
	73.02	-
	80.94	-
	82.93	-
	96.93	-
	105.00	-

The assignment for each m/z is not shown in order to avoid false assignments since these m/z were identified directly in the mass spectrum of a drop of PBS solution containing gellan gum microcapsules deposited on silicon and no reference about the gellan gum fragmentation in mass spectrometry was used to confirm possible assignments for these m/z.

### **3.1.2 Mapping of ketorolac tromethamine and gellan gum microcapsules in HA hydrogel**

Once the characteristic peaks or molecular ions of pure HA hydrogel, ketorolac tromethamine and gellan gum microcapsules have been identified, we can now proceed with the imaging of freeze-dried HA hydrogel samples containing ketorolac tromethamine or microcapsules in hydrogel.

#### **3.1.2.1 Imaging ketorolac tromethamine in HA hydrogel**

In order to highlight the dispersion of ketorolac tromethamine, formulations of HA hydrogel containing 2 and 10 mg of ketorolac tromethamine were analysed. Figure 3.5 shows the dispersion of ketorolac tromethamine in two different amounts in HA hydrogel through a field of view of  $500 \times 500 \mu\text{m}^2$ .

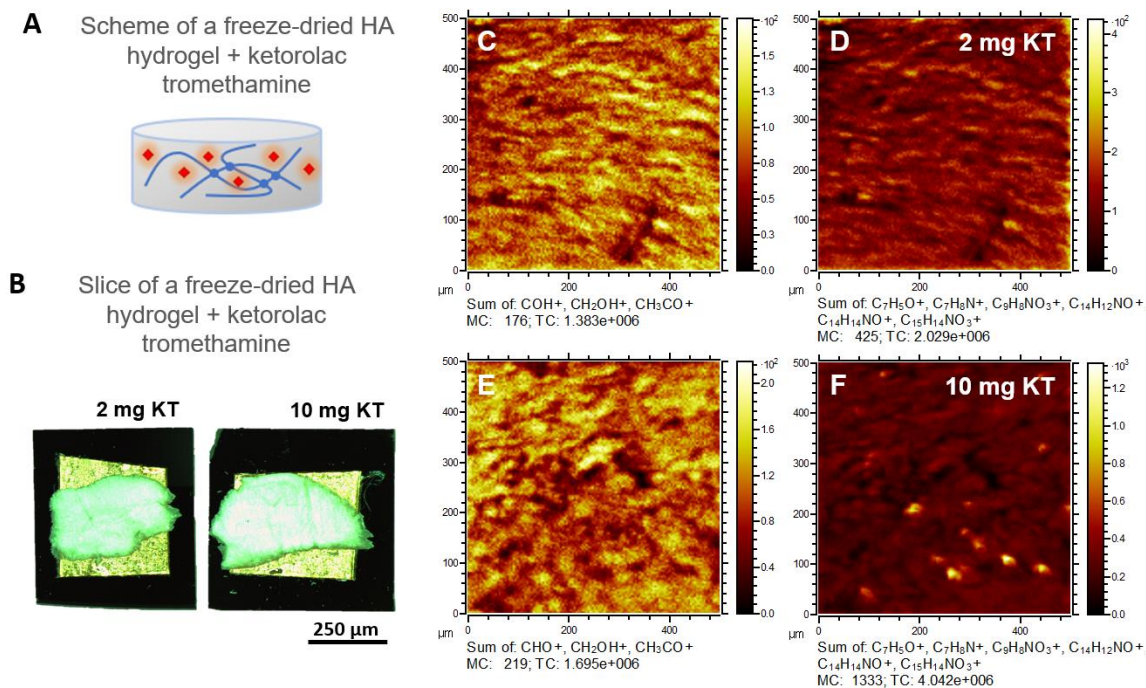


Figure 3.5. (A) Scheme illustrating the analysed freeze-dried HA hydrogel system containing ketorolac tromethamine. (B) Optical image of the two freeze-dried HA hydrogel formulations containing 2 mg and 10 mg of ketorolac tromethamine glued to the silicon substrate with the help of copper tape. The two formulations of HA hydrogel cannot be distinguished with the naked eye. ToF-SIMS 500×500 μm<sup>2</sup> images showing the sum of intensities of (C) hydrogel and (D) ketorolac tromethamine species from the formulation containing 2 mg of ketorolac tromethamine in hydrogel. Similarly, we can see the sum of intensities of (E) hydrogel and (F) ketorolac tromethamine species from the formulation containing 10 mg of ketorolac tromethamine in hydrogel.

As we can see, the formulation containing 2 mg of the drug ketorolac tromethamine in hydrogel shows a more homogeneous distribution (see Figure 3.5B). Conversely, the formulation containing 10 mg of ketorolac tromethamine shows localized spots with a high intensity of molecular ions characteristic of ketorolac tromethamine in the hydrogel (see Figure 3.5D), which indicates that 10 mg of ketorolac tromethamine is probably a high dose of medication for used hydrogel. This same approach was performed in four other regions of interest on the surface of the freeze-dried HA hydrogel formulations containing 2 and 10 mg of ketorolac tromethamine and the same result was obtained, which further supports the idea of drug saturation in formulations containing 10 mg of ketorolac tromethamine compared to formulations containing only 2 mg.

### 3.1.2.2 Imaging gellan gum microcapsules in HA hydrogel

Similarly, the dispersion of gellan gum microcapsules in freeze-dried HA hydrogel can be seen in Figure 3.6 but this time with a larger field of view 1500 × 1500 μm<sup>2</sup>.

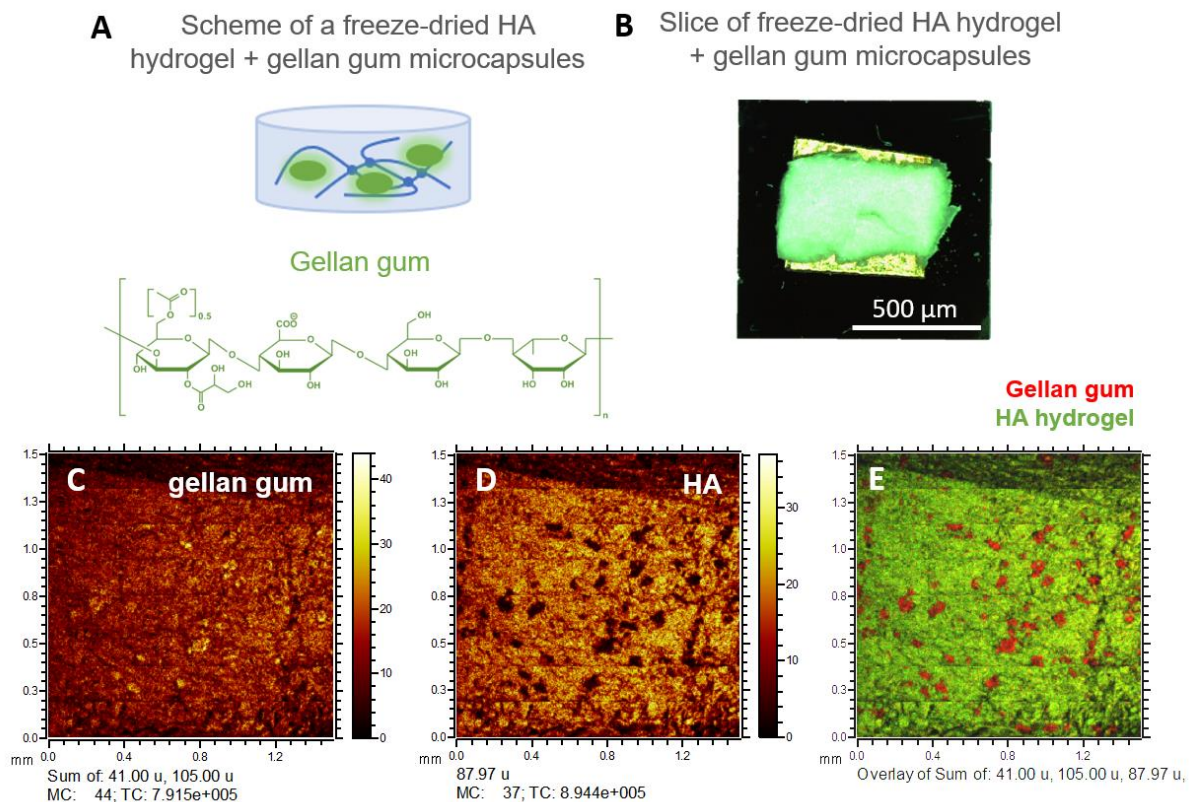


Figure 3.6. (A) Scheme illustrating the analysed freeze-dried HA hydrogel system containing gellan gum microcapsules. (B) Optical image of the freeze-dried HA hydrogel formulations containing gellan gum microcapsules glued to the silicon substrate with the help of copper tape. ToF-SIMS image from a large FoV of  $1500 \times 1500 \mu\text{m}^2$  over hydrogel formulation containing gellan gum microcapsules showing (C) a sum of  $m/z = 41.00$  and  $105.00$  intensities related to gellan gum microcapsules, (D)  $m/z = 87.97$  intensity related to hydrogel, and (E) an overlay of red:(C) and green:(D).

As we can see, we were able to observe the dispersion of gellan gum microcapsules in the hydrogel from a wider field of view. This visualization is based on a chemical contrast generated by an overlay of false colours attributed to the intensity of molecular ions characteristic of gellan gum such as  $m/z = 41.00$  and  $105.00$  and hydrogel such as  $m/z = 87.97$  that were identified in the previous subsection. This visualization shows a dispersion of gellan gum microcapsules without agglomerations on the analysed surface. Two others similar analyses were performed on the surface of HA hydrogel formulations containing gellan gum microcapsules and similar results were obtained. This same type of analysis could be used in the mapping of microcapsules directly in biological tissues seeking to visualize the drug release from microcapsules as well as to know if the drug has reached or not its therapeutic target. Once again, ToF-SIMS imaging proves to be a useful tool in drug vehicle mapping and DDS research.

### 3.2 IMAGING GELLAN GUM MICROCAPSULES BY AFM

After having demonstrated the mapping gellan gum microcapsules directly in hydrogel from mm sizes areas by ToF-SIMS imaging, we were interested in knowing the morphology of gellan gum

microcapsules at high spatial resolution. The microcapsules were initially dried and then placed on a flat surface for AFM analysis. The dehydrated state of the microcapsules allowed formation of clusters of microcapsules, thus making it difficult to identify single microcapsules. Figure 3.7 shows topographic contrasts over a  $2 \times 2 \mu\text{m}^2$  region on the surface of a cluster of microcapsules.

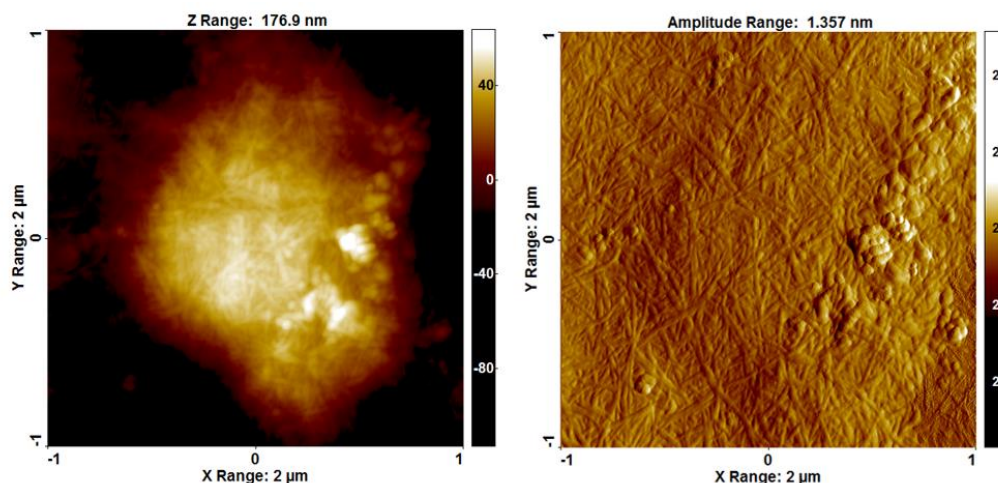


Figure 3.7. Atomic force microscopy (AFM) image from a same spot on the surface of a cluster of gellan gum microcapsules. The left side shows the topographic image and the right side the error-signal image of the same spot. Field of view  $2 \times 2 \mu\text{m}^2$ .

The left side image represents the topography of the surface of a cluster of gellan gum microcapsules. The right-side image represents the error-signal of the topographic image. It makes possible to remove the low frequency present on the topographic image and thus allowing us to see the fibrillar aspect of the surface of the cluster of gellan gum microcapsules. The morphology of these microcapsules is still little explored; however, it has a great potential in giving indications of how the absorption and release of therapeutic drugs can happen through these surfaces.

### 3.3 QUANTIFICATION OF CHEMICAL ENVIRONMENTS OF KETOROLAC TROMETHAMINE AND GELLAN GUM IN HYDROGEL BY XPS

Although ToF-SIMS analysis is capable of detecting most elements and many of the molecules in a region of interest, quantifying the signal is difficult without standard or using another technique. The identification and quantification of the chemical environments present in formulations of HA hydrogel containing ketorolac tromethamine and gellan gum microcapsules were possible thanks to XPS analysis. We divided this chemical investigation by XPS into three steps: first we will discuss the chemical environments found in freeze-dried pure HA hydrogel, then we will move on to the analysis freeze-dried HA hydrogels containing ketorolac tromethamine and then freeze-dried HA hydrogels containing gellan gum microcapsules. All survey and core level spectra discussed in this chapter were acquired using a  $200 \mu\text{m}$  diameter x-ray spot for analysis.

### 3.3.1 Survey spectra analysis of pure HA hydrogel

To identify and quantify chemical environments in HA hydrogel formulations and provide a chemical basis for further comparison with formulations of HA hydrogel containing ketorolac tromethamine and gellan gum microcapsules, we obtained a survey spectrum from a 200  $\mu\text{m}$  diameter analysis spot on a freeze-dried HA hydrogel sample. Figure 3.8 below shows the survey spectra for this freeze-dried HA hydrogel sample.

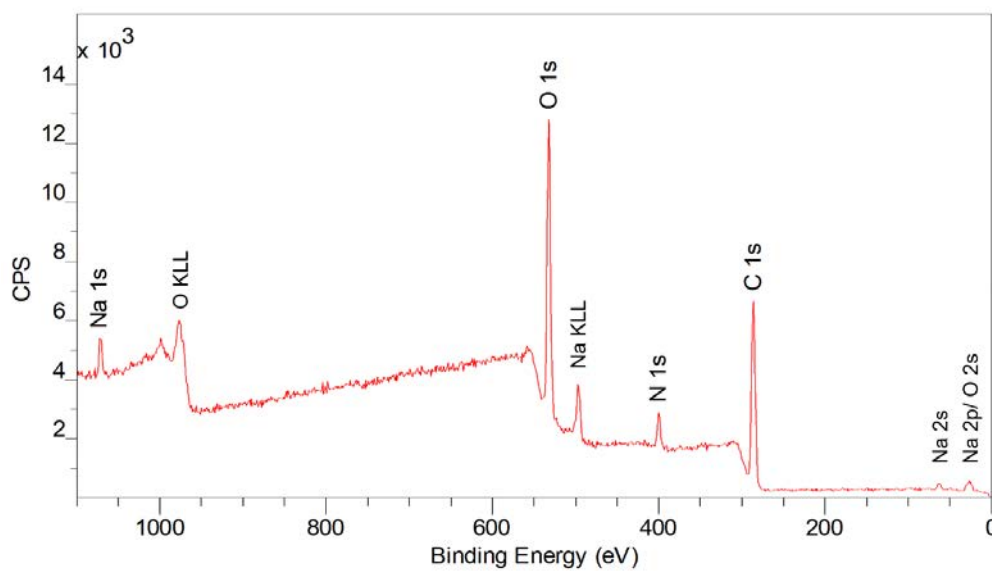


Figure 3.8. Survey spectra acquired from a 200  $\mu\text{m}$  diameter analysis spot on a freeze-dried HA hydrogel sample.

According to the spectra above, a quantifiable presence of carbon, oxygen, nitrogen and sodium were identified. This is an expected result, since the hyaluronic acid, which is basically formed of carbon, oxygen and nitrogen, was oxidized in the presence of sodium periodate to obtain a functionalized hydrogel before gelation.

The different relative amounts of carbon, oxygen, nitrogen and sodium found in the freeze-dried HA hydrogel can be found below in Table 3.4.

Table 3.4. Core levels and their corresponding peak binding energies (eV) and experimental atomic concentrations (at. %) from survey spectra of freeze-dried HA hydrogels.

Core level	Peak BE (eV)	HA	
		at. %	at. %
C 1s	285	62.2	62.9
N 1s	398	5.2	5.2
O 1s	531	31.5	31.9
Na 1s	1070	1.1	Not considered

The stoichiometric atomic values found for the freeze-dried HA hydrogel cannot be directly compared with the theoretical values for the functionalized HA hydrogel molecule because it includes the atomic

concentration of sodium that is not supposed to be part of the HA hydrogel molecular structure. However, if we do not consider the atomic concentration of sodium, we will reach an experimental atomic ratio of 12:1:6 that is completely different to the theoretical values of the functionalized HA hydrogel molecule, whose atomic ratio of carbon, nitrogen and oxygen is 16:3:12. The identification of sodium indicates that residues from the process of functionalization of hydrogel may still be present in the HA hydrogel formulations, which means that theoretical values for the HA hydrogel cannot be reached and it can therefore explain why higher amounts of carbon and sodium as well as lower amounts of nitrogen and oxygen have been found in experimental data in comparison with those expected for theoretical values. The molecular structure of the functionalized HA hydrogel used as a drug vehicle in this work is shown below in Figure 3.9. The oxygen and nitrogen atoms are highlighted in different colours for better identification purposes.

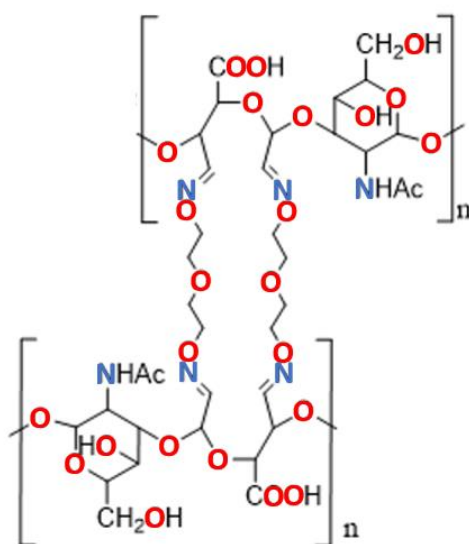


Figure 3.9. Resulting molecular structure of HA hydrogel after functionalization and crosslinking.

Unfortunately, the study of core-level spectra from XPS analysis of freeze-dried HA hydrogel sample cannot be discussed here because they presented a large broadening on both energy sides of C 1s, O 1s and N 1s peaks, probably due to surface charge effects, making it impossible to decompose them correctly.

### 3.3.2 Survey spectra analysis of HA hydrogel containing ketorolac tromethamine

Similarly, in order to identify and quantify chemical environments in HA hydrogel formulations containing ketorolac tromethamine, we firstly obtained a survey spectrum from a 200  $\mu\text{m}$  diameter x-ray analysis spot on a dry drop of aqueous solution containing ketorolac tromethamine aiming to highlight chemical environments only characteristic of the therapeutic drug and then on freeze-dried HA hydrogel formulations containing 2 and 10 mg of ketorolac tromethamine. Figure 3.10 below shows the survey spectra for a dry drop of aqueous solution containing ketorolac tromethamine and for the freeze-dried formulations of HA hydrogel containing 2 and 10 mg of ketorolac tromethamine.

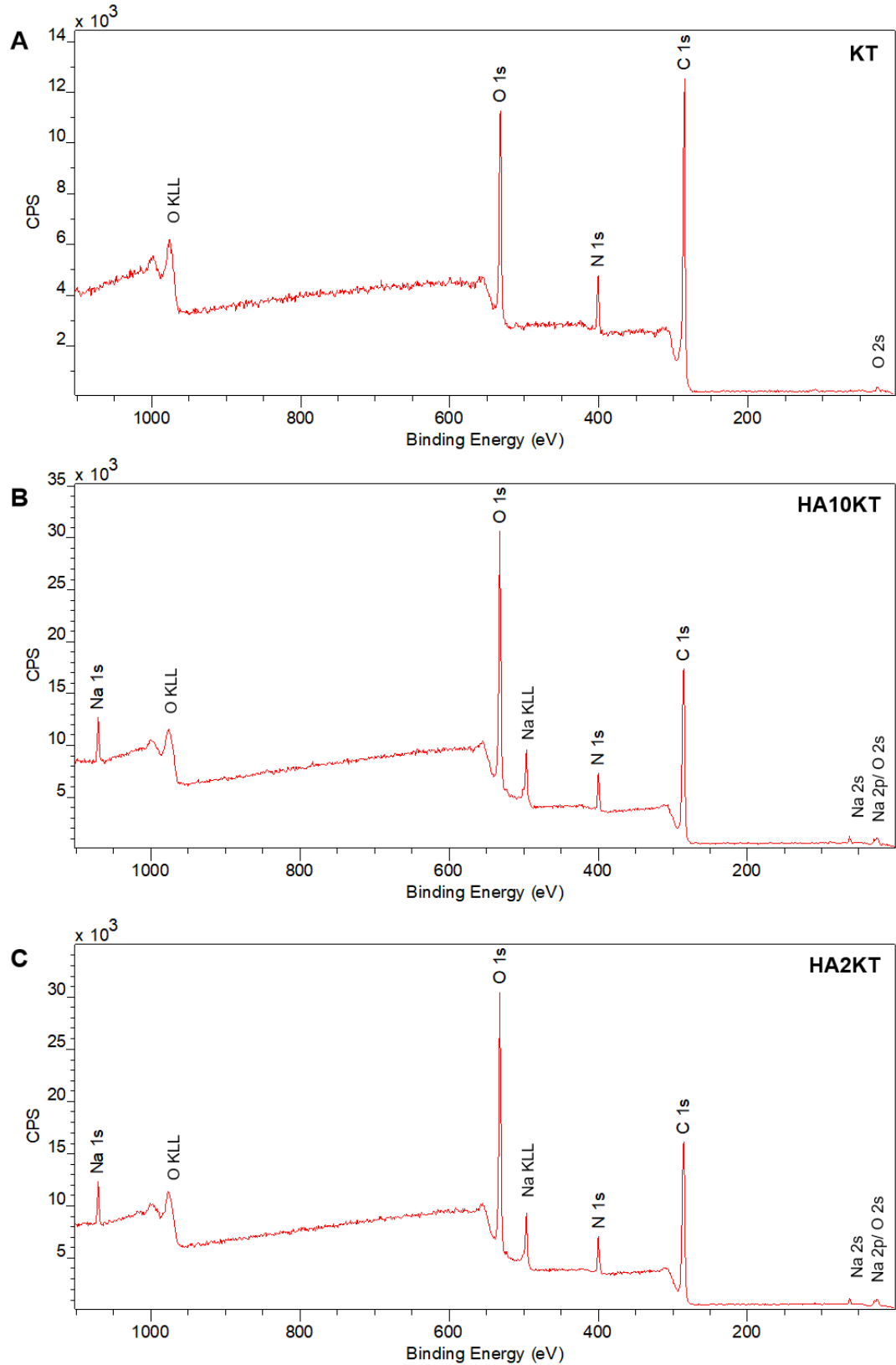


Figure 3.10. Survey spectra from (A) a dry drop of aqueous solution containing ketorolac tromethamine (KT) and from freeze-dried formulations of HA hydrogel containing (B) 10 mg (HA10KT) and (C) 2 mg (HA2KT) of ketorolac tromethamine.

According to the spectra of Figure 3.10, quantifiable presence of carbon, oxygen and nitrogen were identified in all formulations. However, sodium was only identified in formulations with HA hydrogel. This can be explained by the use of sodium periodate in the functionalization of the HA hydrogel before gelation as seen in the previous subsection.

The different relative atomic amounts in a dry drop of aqueous solution containing ketorolac tromethamine and for the freeze-dried formulations of HA hydrogel containing 2 and 10 mg of ketorolac tromethamine can be found below in Table 3.5.

Table 3.5. Core levels and their corresponding peak binding energies (eV) and experimental atomic concentrations (at. %) from survey spectra of a dried drop of aqueous solution of ketorolac tromethamine (KT) and freeze-dried HA hydrogel samples containing 2 mg (HA2KT) and 10 mg (HA10KT) of ketorolac tromethamine. The rightmost column brings the atomic concentrations for the pure HA hydrogel found in the previous subsection.

Core level	Peak BE (eV)	KT	HA10KT	HA2KT	HA
		at. %	at. %	at. %	at. %
C 1s	285	75.5	66.3	65.6	62.2
N 1s	398	6.4	5.7	5.6	5.2
O 1s	531	18.1	26.7	27.5	31.5
Na 1s	1070	–	1.3	1.3	1.1

The approximate stoichiometric ratios found in a dry drop of aqueous solution containing ketorolac tromethamine (12:1:3) are different to the theoretical values for the ketorolac tromethamine molecule, whose atomic ratio of carbon, nitrogen and oxygen is 19:2:6. It means to say that the experimental stoichiometric ratios show less carbon and more nitrogen and oxygen than expected for a ketorolac tromethamine molecule. This might be explained by the fact that the pure ketorolac tromethamine was analysed from a dried drop of aqueous instead of analysing the ketorolac tromethamine salt. The molecular structure of ketorolac tromethamine is shown in Figure 3.11. The oxygen and nitrogen atoms are highlighted in different colours for better identification purposes.

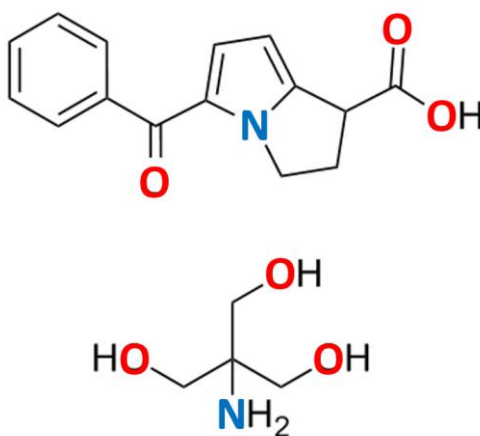


Figure 3.11. Molecular structure of ketorolac tromethamine ( $C_{19}H_{24}N_2O_6$ ) with oxygen and nitrogen atoms highlighted in red and blue, respectively.

In addition, as the experimental stoichiometric ratios of ketorolac tromethamine has a higher carbon and lower oxygen content compared to the stoichiometric values found for the HA hydrogel [see columns of Table 3.5] labelled as KT and HA], it is expected that the stoichiometric ratios of HA hydrogel formulations containing 2 and 10 mg of ketorolac tromethamine will have an increase in the atomic percentage of carbon and a decrease in the atomic percentage of oxygen if compared to pure HA hydrogel formulations as observed. A slight increase in the amount of nitrogen is also associated with the addition of ketorolac tromethamine in formulations based on HA hydrogel. Sodium from the HA hydrogel was also expected to be found in hydrogel formulations containing ketorolac tromethamine. Comparing now only ketorolac-containing hydrogel formulations, we have experimental evidence that XPS is able to detect different atomic ratios due to changes of few milligrams in the concentration of therapeutic drugs such as ketorolac tromethamine used in hydrogel-based drug delivery systems.

### 3.3.3 Core level spectra analysis of HA hydrogel and ketorolac tromethamine

Besides the atomic identification and quantification in HA hydrogel formulations containing ketorolac tromethamine, the high-resolution C 1s, N 1s, and O 1s core level spectra can also be studied aiming to identify and quantify the chemical bonding states present in the dry drop of aqueous solution containing ketorolac tromethamine as well as in HA hydrogel formulations containing ketorolac tromethamine.

The XPS spectra from a dry drop of aqueous solution containing ketorolac tromethamine is shown in Figure 3.12.

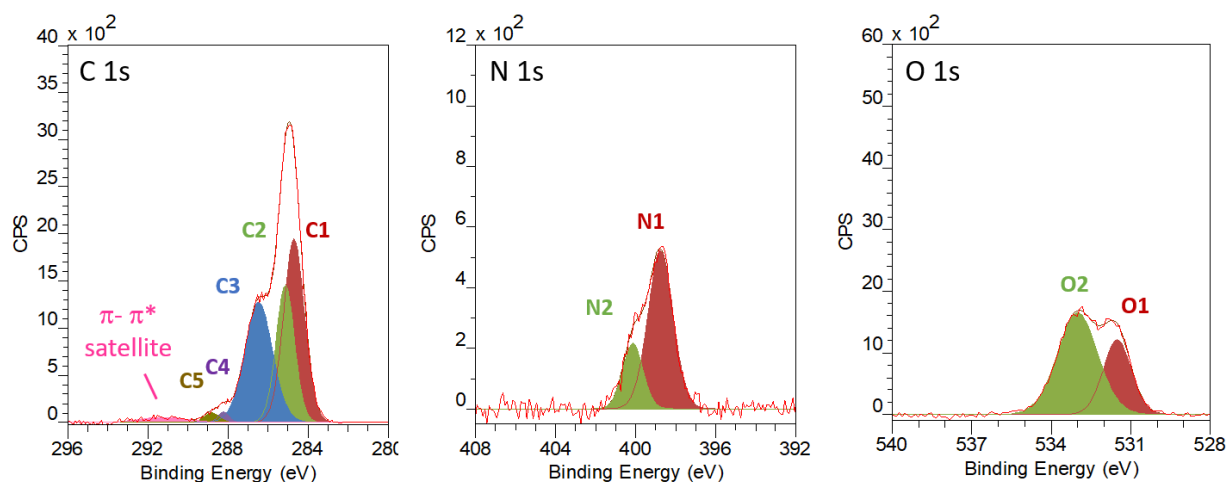


Figure 3.12. Curve fitting of the high-resolution spectra of C 1s, N 1s and O 1s core levels from a dry drop of aqueous solution containing ketorolac tromethamine.

The XPS spectra from freeze-dried formulations of HA hydrogel containing 10 mg (HA10KT) and 2 mg (HA2KT) of ketorolac tromethamine, and their corresponding fitting are shown in Figure 3.13.

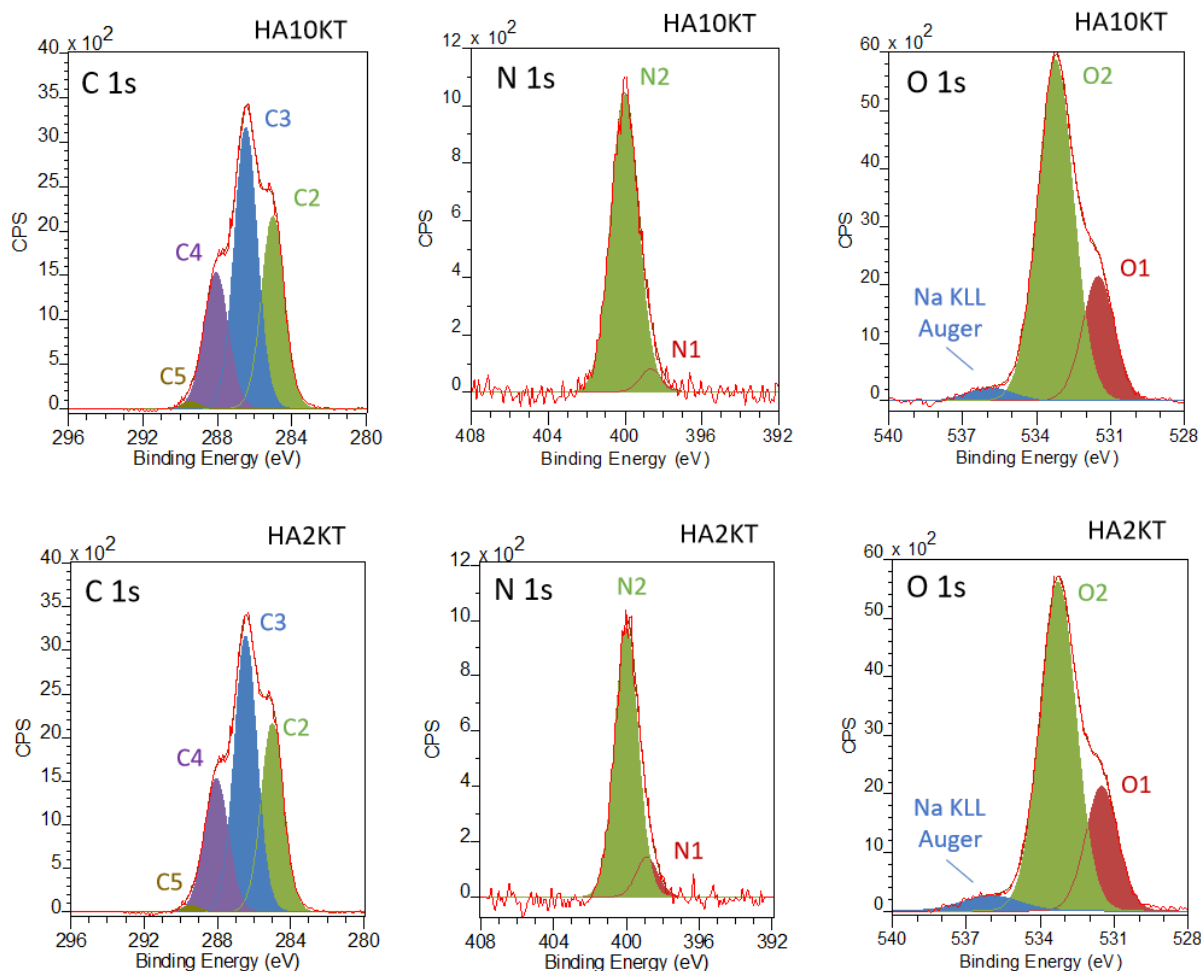


Figure 3.13. Curve fitting of the high-resolution spectra of C 1s, N 1s and O 1s core levels of freeze-dried formulations HA hydrogel containing 10 mg (HA10KT) and 2 mg (HA2KT) of ketorolac tromethamine.

A comparative study of the C 1s, N 1s and O 1s spectra shows different bonding states for a dry drop of aqueous solution containing ketorolac tromethamine and freeze-dried HA hydrogel formulations containing 2 and 10 mg of ketorolac tromethamine.

The identified amounts of C 1s, N 1s, and O 1s for these formulations can be seen in Table 3.6.

Table 3.6. Peak fitting parameters of high-resolution XPS analysis of a dried drop of ketorolac tromethamine solution (KT) and freeze-dried HA hydrogel formulations containing 10 mg (HA10KT) and 2 mg of ketorolac tromethamine (HA2KT).

Core level	Position (eV)	Assignment	Bonding state	KT	HA10KT	HA2KT
				Area (%)	Area (%)	Area (%)
<b>C 1s</b>	284.6	C1	C–H/C–C(arom.)	34.6	–	–
	285.0	C2	C–H/C–C(aliph.)	23.0	34.5	30.8
	286.2, 286.3	C3	C–OH/C–N	40.3	42.3	45.3
	287.9, 288.0	C4	C=O/O=C–N	0.8	22.7	23.1
	289.2	C5	O=C–OR	1.3	0.5	0.8
<b>N 1s</b>	398.5	N1	N–H	65.8	13.2	12.1
	400.0	N2	C–N/C=N	34.2	86.8	87.9
<b>O 1s</b>	531.5, 532.0	O1	C=O/O=C–OH	33.8	22.0	22.8
	533.0	O2	O–C–O/C–OH	66.2	78.0	77.2

From the data shown in Table 3.6, we can see that despite the disparity of chemical environments between formulations of pure ketorolac tromethamine and HA hydrogel formulations containing ketorolac tromethamine, in general, both HA2KT and HA10KT showed very similar amounts of carbon, oxygen and nitrogen environments. We will understand what each number of chemical environments represents in each of these formulations in the following subsections.

### 3.3.3.1 Chemical state assignments for pure ketorolac tromethamine (KT)

Regarding the pure ketorolac tromethamine (KT), there were found five different carbon bonding states after analysis of a dried drop of aqueous solution with ketorolac tromethamine as indicated in Table 3.6.

- The carbon from the aromatic ring structure (C1: —C—H/—C—C—) at 284.6 eV.
- The carbon from aliphatic hydrocarbon structures (C2: —C—H/—C—C—) at 285.0 eV.
- The carbon from the heterocyclic ring structure containing an atom of nitrogen, amine or hydroxyl environments (C3: —C—N—/—C—OH) at 286.2 eV.
- The carbon from the carbonyl environment (C4: —C=O) at 287.9 eV.
- The carbon from the carboxylic acid environment (C5: O=C—OH) at 289.2 eV.
- It is also possible to notice the presence of shake-up satellites in the C 1s spectrum at energies around 291.5 eV (see Figure 3.13).

The C1<sub>KT</sub> (31.5 at. %) amount related to aromatic ring structures, the C2<sub>KT</sub> (23.0 at. %) amount related to the aliphatic carbon bonds and the C3<sub>KT</sub> (40.3 at. %) amount related to amine or carbon-nitrogen environments indicate an approximate chemical ratio of 6:4:7 similar that is found for C1:C2:C3 in the ketorolac tromethamine molecule. However, the C4<sub>KT</sub> (0.8 at. %) and C5<sub>KT</sub> (1.3 at. %) amounts show

less than 4 times the expected theoretical ratios for these chemical environments in the ketorolac tromethamine molecule. In part, this might be explained by the presence of shake-up satellites appearing at high binding energies very close to those of carboxylic environments, which ends up interfering with the decomposition of the C5 component and consequently in the C4 as well. The molecular structure of ketorolac tromethamine showing these five chemical environments mentioned above is shown in Figure 3.14.

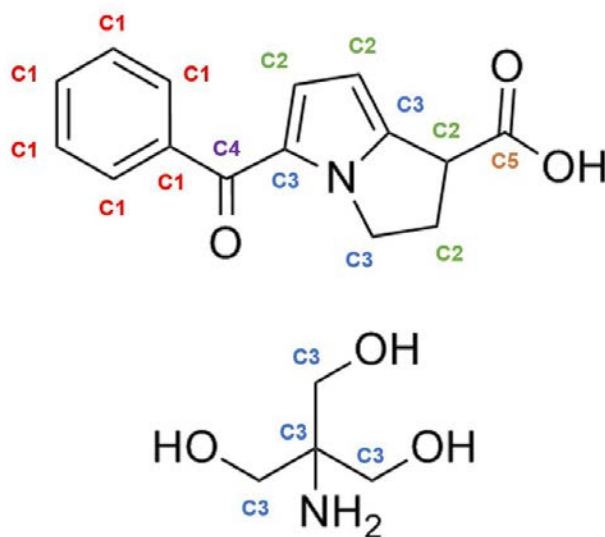


Figure 3.14. Molecular structure of ketorolac tromethamine showing the C1: aromatic carbon, C2: aliphatic carbon, C3: carbon-nitrogen bond in a heterocyclic ring structure, C4: carbonyl bond and C5: carboxyl environment.

Regarding the N 1s core level spectra from pure ketorolac tromethamine (KT) shows two different nitrogen bonding states.

- The nitrogen of amino groups (N1: —N—H) at 398.5 eV,
- The carbon-nitrogen bond from the heterocyclic ring structure (N2: —N—C—) at 400.0 eV.

In contrast, the N1<sub>KT</sub> (65.8 at. %) amount related to amine groups and the N2<sub>KT</sub> (34.2 at. %) amount related to carbon-nitrogen structures indicate a 2:1 stoichiometry different from the 3:1 found in the ketorolac tromethamine molecule. This might indicate that part of the amine groups found do not belong to ketorolac tromethamine and must come from the interaction of ketorolac tromethamine salt with water or other substances that may be present in this aqueous system.

Regarding the O 1s core level spectrum for pure ketorolac tromethamine (KT), two different oxygen bonding states are indicated.

- The oxygen from the carbonyl or carboxyl groups (O1: —O=C—OH) at 531.5 eV,
- The oxygen from hydroxyl groups (O2: —O=C—OH) at 533.0 eV.

In accordance with our previous stoichiometric results, the greater amount of O<sub>2KT</sub> (66.2 at.%) indicates that most of the oxygen present in the dry drop of aqueous solution containing ketorolac tromethamine is in the form of hydroxyl, while the lowest amount indicated in O<sub>1KT</sub> (33.8 at.%) is related to carbonyl environments seen in the ketorolac tromethamine molecule (Figure 3.14).

As we can see, despite the interference of shake-up satellites in the C 1s spectrum that made the decomposition of the C5 component and therefore of the C4 component a hard task, in general, with the decomposition of the C 1s, N 1s and O 1s spectra we are able to obtain coherent quantitative information about the chemical environments present in the target system with excellent accuracy. Either identifying and quantifying those environments belonging to the ketorolac tromethamine molecule or even from external chemical environments probably present in the aqueous system.

### 3.3.3.2 Chemical state assignments for freeze-dried HA hydrogel formulations with ketorolac tromethamine

In both freeze-dried HA hydrogel formulations containing ketorolac tromethamine (HA2KT and HA10KT) there were found four different carbon bonding states as indicated in Table 3.6.

- The carbon from hydrocarbon structures (C2: —C—H/—C—C—) at 285.0 eV.
- The carbon from amine, hydroxyl or ether groups (C3: —C—N—/—C—OH/—C—O—C) at 286.2 eV.
- The carbon from the carbonyl and imine environments (C4: —C=O/—C=N—) at 288.0 eV.
- The carbon from the carboxylic acid environment (C5: O=C—OH) at 289.2 eV.

The amount of C<sub>2HA2KT</sub> (30.8 at.%) and C<sub>2HA10KT</sub> (34.5 at.%) indicate the presence of hydrocarbon structures present in the HA hydrogel as well as carbons from aromatic and aliphatic structures from ketorolac tromethamine. However, the amount of ketorolac tromethamine seems to play an important role in the C2 amount. The higher C<sub>2HA10KT</sub> (34.5 at.%) amount can be explained by the fact that in this HA hydrogel formulation there is more ketorolac tromethamine in comparison with the C<sub>2HA2KT</sub> (30.8 at.%). The higher C<sub>3HA2KT</sub> (45.3 at.%) and C<sub>3HA10KT</sub> (42.3 at.%) amounts were already expected because these are mainly related to the presence of amine, hydroxyl and ether environments strongly present in the HA hydrogel structure but also related to the carbon-nitrogen and hydroxyl environments characteristic of ketorolac tromethamine structure. However, in this case, the addition of ketorolac tromethamine appears to reduce the C<sub>3HAKT</sub> amounts as ketorolac tromethamine is added. The possible explanation for this behaviour is that although ketorolac tromethamine has a large C<sub>3KT</sub> amount that could increase the C<sub>3HAKT</sub> amounts, most of its composition is actually due to hydrocarbon environments [seen in C<sub>1KT</sub> and C<sub>2KT</sub> amounts in the previous subsection] and when ketorolac tromethamine is then incorporated into HA hydrogel formulations, the C<sub>3HAKT</sub> environments is less increased in comparison with the hydrocarbon environments. On the other hand, the higher C<sub>4HA2KT</sub> (23.0 at.%) and C<sub>4HA10KT</sub> (22.6 at.%) amounts are unexpected when the cross-linked hydrogel molecule is kept in mind (see Figure 3.15). Even with the contribution of the carbonyl environment present in the ketorolac

tromethamine molecule [ $C4_{KT}$  (0.8 at. %)], this component appears to present very high concentrations and seems have its concentration decreased as higher amounts of ketorolac tromethamine is added in the formulation. This might be an indication that other residual compounds associated with the HA hydrogel formulation might strongly contribute to the large  $C4_{HAKT}$  amounts. The  $C5_{HA2KT}$  (0.5 at.%) and  $C5_{HA10KT}$  (0.8 at.%) amounts are attributed to carboxylic environments present in the HA hydrogel and ketorolac tromethamine structures. We can see that this is a minor chemical environment in HA hydrogel formulations containing ketorolac tromethamine and do not appear to be affected by the supposed presence of residues in the HA hydrogel formulations. Besides that, in this case, the carboxylic environment of ketorolac tromethamine appears to be decisive in increasing the  $C5_{HAKT}$  amounts, since  $C5_{HA10KT}$  shows slightly higher amounts than  $C5_{HA2KT}$ .

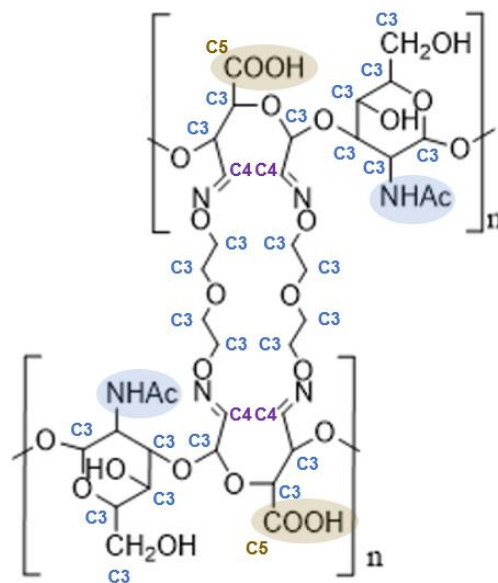


Figure 3.15. Molecular structure of HA hydrogel showing the C2: aliphatic carbon, C3: amine, hydroxyl or ether groups, C4: imine bond and C5: carboxyl environment.

The N 1s core level spectra from both freeze-dried HA hydrogel formulations containing ketorolac tromethamine (HA2KT and HA10KT) show two different nitrogen bonding states.

- The nitrogen of amino groups (N1: —N—H) at 398.5 eV,
- The carbon-nitrogen bond from imide environments or from the heterocyclic ring structure containing an atom of nitrogen (N2: —N=C—/—N—C—) at 400.0 eV.

In both HA hydrogel formulations containing ketorolac tromethamine, large amounts of  $N2_{HA2KT}$  (87.9 at. %) and  $N2_{HA10KT}$  (86.8 at. %) were found compared to  $N1_{HA2KT}$  (12.1 at. %) and  $N1_{HA10KT}$  (13.2 at. %). Unlike the result found for a dry drop of aqueous solution containing ketorolac tromethamine, which shows the biggest portion of nitrogen in the form of amine environments, in formulations of HA hydrogel containing ketorolac tromethamine most of the nitrogen seems to be in the form of carbon-nitrogen bond

from imide environments characteristic of the HA hydrogel structure but maybe also from the heterocyclic ring structure characteristic of the ketorolac tromethamine molecule. According to the stoichiometry of the cross-linked HA hydrogel molecule (see Figure 3.15), the imide amount should correspond to twice the amine content. However, according to the experimental stoichiometric values, the amount of  $N2_{\text{HAKT}}$  seems to correspond to almost five times that of  $N1$ , further suggesting that the carbon-nitrogen bond from the heterocyclic ring structure characteristic of the ketorolac tromethamine molecule might strongly contribute for the  $N2_{\text{HAKT}}$  amount over the single amine environment at the same molecular structure. However, we did not notice large variations between  $N2_{\text{HA2KT}}$  (87.9 at. %) and  $N2_{\text{HA10KT}}$  (86.8 at. %) amounts expected if the carbon-nitrogen from the ketorolac tromethamine have a strong influence over these stoichiometric values, which puts into doubt the real influence of ketorolac tromethamine on the amounts of  $N1_{\text{HAKT}}$  and  $N2_{\text{HAKT}}$ . In any case, a small trend of decreasing over  $N2_{\text{HAKT}}$  amounts as ketorolac is added in the HA hydrogel formulation could still be noticed.

Regarding the O 1s core level spectra from both freeze-dried HA hydrogel formulations containing ketorolac tromethamine (HA2KT and HA10KT) two different oxygen bonding states were found.

- The oxygen from the carbonyl or carboxyl groups (O1:  $\text{—C=O/O=C—OH}$ ) at 531.5 eV
- The oxygen from ether and hydroxyl groups (O2:  $\text{—C—O—C—/—C—OH}$ ) at 533.0 eV.
- Still in the O 1s spectrum is possible to see the auger Na KLL emission at energies around 536.0 eV.

The  $O2_{\text{HA2KT}}$  (77.2 at. %) and  $O2_{\text{HA10KT}}$  (78.0 at. %) show that most of the oxygen present in HA hydrogel formulations containing ketorolac tromethamine is present in the form of ether or hydroxyls environments, which are characteristic of the molecular structure of the HA hydrogel but also characteristic of the hydroxyls from the ketorolac tromethamine molecule. While the  $O1_{\text{HA2KT}}$  (22.8 at. %) and  $O1_{\text{HA10KT}}$  (22.0 at. %) amounts indicate that the smallest fraction of chemical oxygen environments in these formulations are present in the form of carbonyl or carboxyl environments. Nevertheless, the theoretical stoichiometric ratio between O1 and O2 should be almost 1:6 based on the HA hydrogel molecule (see Figure 3.15). While the ketorolac tromethamine molecule has an O1:O2 stoichiometry of 1:2. Therefore, it is actually expected that there is an increase in the amount of O2 over the amount of O1 in HA hydrogel formulations containing ketorolac tromethamine. However, between the  $O1_{\text{HA2KT}}$  and  $O1_{\text{HA10KT}}$  and between  $O2_{\text{HA2KT}}$  and  $O2_{\text{HA10KT}}$  there is little variation thus indicating that the amount of ketorolac tromethamine present in each formulation is not capable of significant changes in the amounts of  $O1_{\text{HA2KT}}$  and  $O2_{\text{HA2KT}}$  in both formulations. In addition, we know from previous results that other residual compounds from functionalization processes may also be present in these formulations, and consequently, might more significantly change the  $O1_{\text{HA2KT}}$  and  $O2_{\text{HA2KT}}$  amounts. This may be a possible explanation for why we have found an O1:O2 experimental stoichiometry of almost 1:4. The amount of  $O1_{\text{HA2KT}}$  and  $O2_{\text{HA2KT}}$  does not seem to show a tendency to decrease or increase with the increase of ketorolac tromethamine.

### 3.3.3.3 Comparison between C 1s, N 1s and O 1s chemical environments identified in pure ketorolac tromethamine and HA hydrogel-based formulations containing ketorolac tromethamine

In summary, what we must retain from the C 1s, N 1s and O 1s high-resolution analysis thus far, is that we were able to identify and quantify relative chemical amounts related to functional groups characteristic of ketorolac tromethamine in HA hydrogel formulations. From the analysis of a dry drop of an aqueous solution containing ketorolac tromethamine we highlighted the chemical environments of ketorolac tromethamine and then the effect of the addition of ketorolac tromethamine in HA hydrogel formulations. Although some explanations for the quantity of certain chemical environments are based on assumptions that need further analysis to be confirmed, we noticed a tendency of increase in the C2 and N1 amounts with the addition of ketorolac tromethamine in HA hydrogel formulations, while a trend of reduction in the C3, C4 and N2 amounts with the addition of ketorolac tromethamine in HA hydrogel formulations. No trends were specially found over the oxygen environments with the addition of ketorolac tromethamine in HA hydrogel formulations.

Figure 3.16 summarizes these tendencies in a comparison of all C 1s, N 1s and O 1s chemical environments identified.

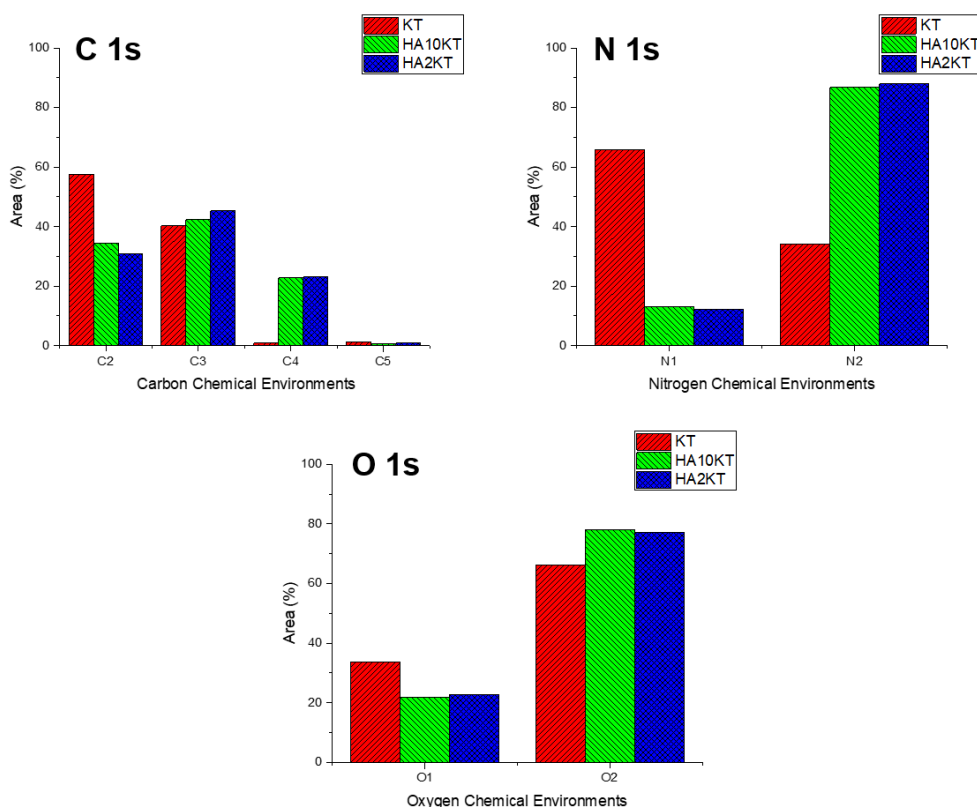


Figure 3.16. Relative chemical environments amount found over C 1s, N 1s and O 1s high-resolution spectra from a dry drop of aqueous solution containing ketorolac tromethamine and freeze-dried HA hydrogel containing ketorolac tromethamine. In the relative amounts of C1s, the C2<sub>KT</sub> correspond to the sum of the detected C1<sub>KT</sub> e do C2<sub>KT</sub> amounts related to hydrocarbon structures.

This analytical strategy demonstrates the ability of XPS to identify and quantify therapeutic drugs from their key chemical environments directly in hydrogel-based drug delivery systems. In addition of creating a surface chemical data basis for this kind of biomedical system, we also generated chemical information comparable with those previously obtained by ToF-SIMS analyses performed on HA hydrogel systems containing ketorolac tromethamine. It must be then emphasized that the C3 and C4 environments found here as chemical environments mainly characteristic of the HA hydrogel seems also to be characteristic of the fragments of HA hydrogel previously highlighted by ToF-SIMS analysis in Table 3.1. Similarly, the C1, C2, C5 and N1 environments found here as hydrocarbon and carboxylic environments mainly characteristic of ketorolac tromethamine represent the main functional groups of molecular ions appearing in Table 3.2, where the main fragments of ketorolac tromethamine were listed.

### 3.3.4 Survey spectra analysis of HA hydrogel containing gellan gum microcapsules

The same XPS approach was applied to a freeze-dried HA hydrogel formulation containing gellan gum microcapsules. Figure 3.17 shows the survey spectra obtained for this sample.

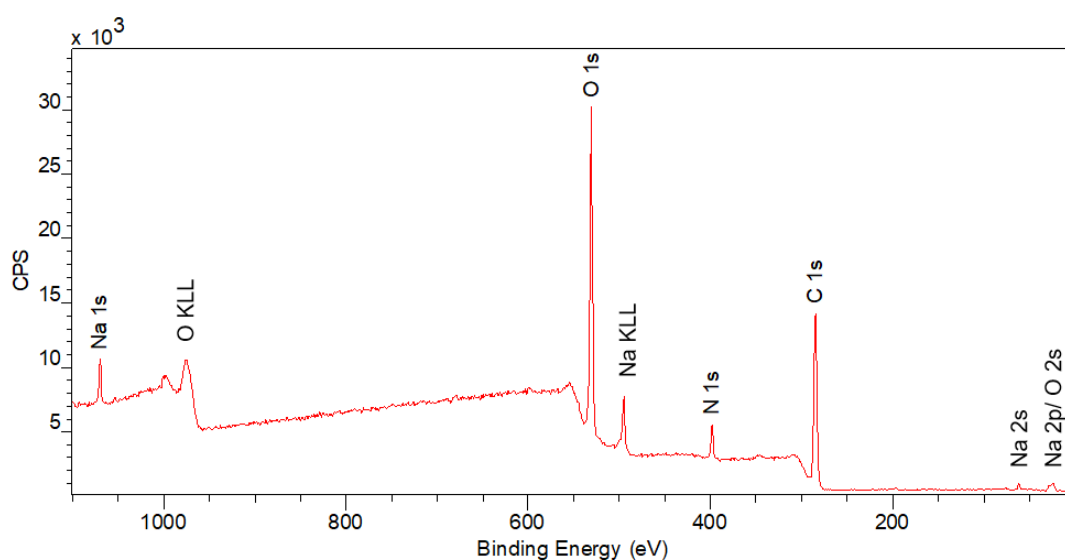


Figure 3.17. Survey spectra from lyophilized hydrogel containing gellan gum microcapsules.

We observe the quantifiable presence of carbon, nitrogen, oxygen and sodium. Sodium as we know is particularly present in HA hydrogel, while carbon, oxygen and nitrogen are atoms present in both HA hydrogel and gellan gum molecular structures.

The different atomic amounts for this formulation can be seen below in 3.7.

Table 3.7. Core levels and their corresponding peak binding energies (eV) and experimental atomic concentrations (at. %) from hydrogel containing gellan gum microcapsules (HAGGM). The rightmost column brings the atomic concentrations for the pure HA hydrogel found in a previous subsection.

Core level	Peak BE (eV)	HAGGM	HA
		at. %	at. %
C 1s	285	60.9	62.1
N 1s	398	5.0	5.2
O 1s	531	32.8	31.5
Na 1s	1070	1.3	1.2

In a general comparison between freeze-dried pure HA hydrogel and HA hydrogel containing gellan gum microcapsules, the amounts of C 1s, N 1s, O 1s and Na 1s does not present large differences. However, the stoichiometric differences found for these two samples [small increase in O 1s environments] are consistent with the addition of high acyl gellan molecules in formulations of pure HA hydrogel. This means that the small increases in the amount of oxygen and the reduction in the amount of carbon and nitrogen may be associated with the presence of high acyl gellan. The molecular structure of the high acyl gellan is given in Figure 3.18.

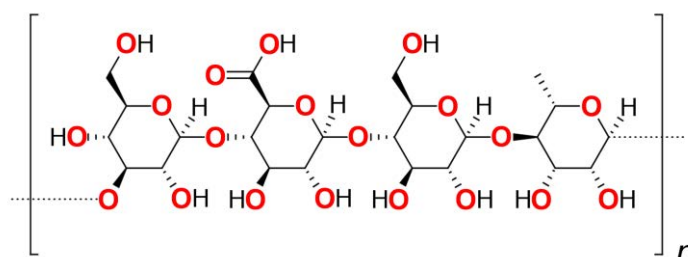


Figure 3.18. Molecular structure of acyl gellan with oxygen atoms highlighted in red.

### 3.3.5 Core level spectra analysis of HA hydrogel with gellan gum microcapsules

The high-resolution C 1s, N 1s, and O 1s core level spectra are also studied to identify and quantify the surface chemical bonding states in the HA hydrogel formulations containing gellan gum microcapsules.

These high-resolution spectra are shown below in Figure 3.19.

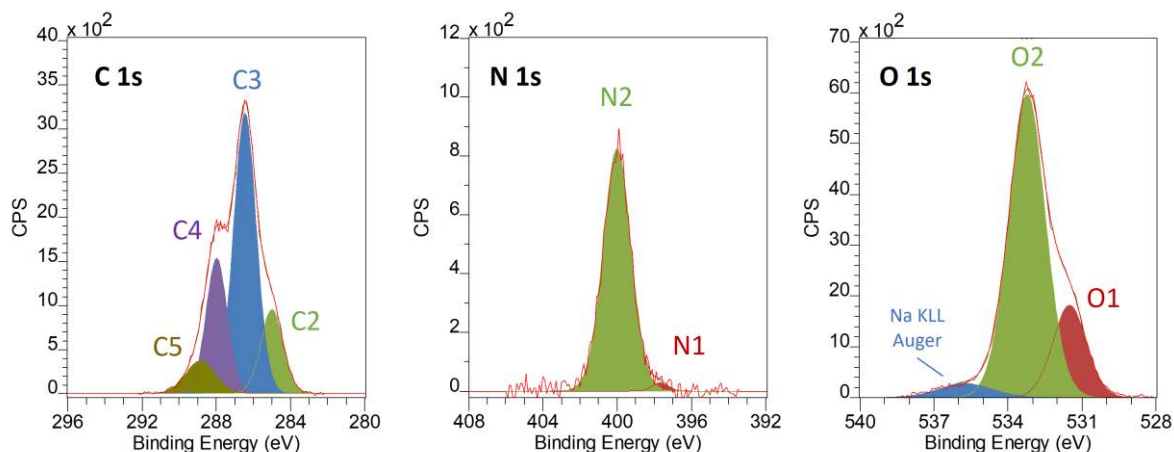


Figure 3.19. Curve fitting of the high-resolution spectra of C 1s, O 1s and N 1s core levels of freeze-dried HA hydrogel containing gellan gum microcapsules.

The identified amounts of C 1s, N 1s, and O 1s from freeze-dried HA hydrogel containing gellan gum microcapsules can be seen below in Table 3.8.

Table 3.8. Peak fitting parameters of high-resolution XPS analysis of freeze-dried HA hydrogel containing gellan gum microcapsules (HAGGM).

Core level	Position (eV)	Assignment	Bonding state	HAGGM
				Area (%)
C 1s	248.8	C2	C–H/C–C	15.7
	286.2, 286.3	C3	C–O–C/C–OH/C–N	52.7
	287.9, 288.0	C4	C=O/O=C–N	23.6
	289.2	C5	O=C–OR	8.0
N 1s	398.5	N1	N–H	4.6
	400.0	N2	C–N/C=N	95.4
O 1s	531.5, 532.0	O1	O=C–OH/ O=C–N	21.8
	533.0	O2	O–C–O/C–OH	78.2

### 3.3.5.1 Chemical state assignments for HA hydrogel containing gellan gum microcapsules

The freeze-dried HA hydrogel containing gellan gum microcapsules present four different types of carbon (see C 1s spectrum in Figure 3.19).

- The carbon from hydrocarbon structures (C2: —C—H/—C—C—) at 285.0 eV.
- The carbon from amine or hydroxyl or ether groups (C3: —C—N—/—C—OH/—C—O—C) at 286.2 eV.
- The carbon from the carbonyl and imine environments (C4: —C=O/—C=N—) at 288.0 eV.
- The carbon from the carboxylic acid environment (C5: O=C—OH) at 289.2 eV.

The  $C_{2\text{HAGGM}}$  (15.7 at.%) amount is related to the hydrocarbon environment existing in both HA hydrogel and gellan gum molecular structures. In a brief comparison with the  $C_{2\text{HA2KT}}$  and  $C_{2\text{HA10KT}}$  amounts found in the previous subsection, the  $C_{2\text{HAGGM}}$  amount is about the half of their amounts, as since these formulations share the same freeze-dried HA hydrogel base, it might confirm that a great part of  $C_{2\text{HA2KT}}$  and  $C_{2\text{HA10KT}}$  amounts comes from the ketorolac tromethamine. The large amount of  $C_{3\text{HAGGM}}$  (52.7 at.%) was already expected here because this amount is directly related to hydroxyl and ether contributions that are strongly present in HA hydrogel (see Figure 3.15) as well as in gellan gum (Figure 3.18). The  $C_{4\text{HAGGM}}$  (23.6 at.%) amount is similar to those found for  $C_{\text{HA2KT}}$  and  $C_{\text{HA10KT}}$ , indicating that the carbonyl environment is mainly related to the HA hydrogel structure. While the higher amount of  $C_{5\text{HAGGM}}$  (8.0 at.%), if compared to  $C_{5\text{HA2KT}}$  and  $C_{5\text{HA10KT}}$ , can be explained by the presence of sites of carboxylic acid in molecules of high acyl gellan.

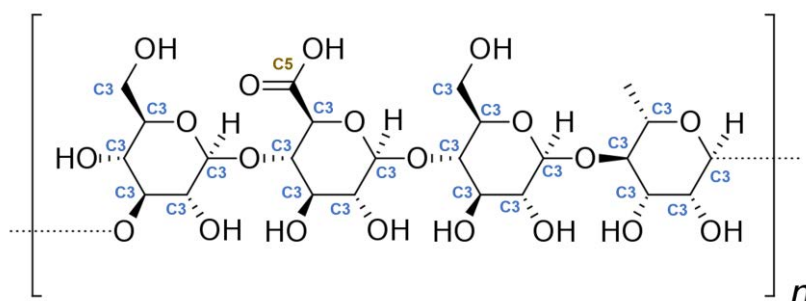


Figure 3.20. Molecular structure of acyl gellan hydrogel showing the C3: hydroxyl or ether groups and C5: carboxyl environment.

The N 1s core level spectra for freeze-dried HA hydrogel formulations containing gellan gum microcapsules show two different nitrogen bonding states (see N 1s spectrum in Figure 3.19).

- The nitrogen of amino groups (N1: —N—H) at 398.5 eV
- The carbon-nitrogen bond from imide environments (N2: —N=C—) at 400.0 eV.

The  $N_{1\text{HAGGM}}$  (4.6 at.%) and  $N_{2\text{HAGGM}}$  (95.4 at.%) amounts might be attributed to the carbon-nitrogen environments present only in the HA hydrogel molecule mainly because there are no chemical bonds containing nitrogen in the acyl gellan molecule.

Regarding the O 1s core level spectrum for freeze-dried HA hydrogel formulations containing gellan gum microcapsules, two different oxygen bonding states are indicated (see O 1s spectrum in Figure 3.19).

- The oxygen from the carbonyl or carboxyl groups (O1: —C=O/O=C—OH) at 531.5 eV
- The oxygen from ether and hydroxyl groups (O2: —C—O—C—/—C—OH) at 533.0 eV.
- Also, in the O 1s spectrum is possible to see the auger Na KLL emission at energies around 536.0 eV.

The  $O1_{HAGGM}$  (21.8 at. %) and  $O2_{HAGGM}$  (78.2 at. %) amounts obtained for freeze-dried HA hydrogel formulations containing gellan gum microcapsules are similar to those amounts obtained for  $O1_{HA2KT}/O1_{HA10KT}$  and  $O2_{HA2KT}/O2_{HA10KT}$  that indicates a strong influence of the chemical oxygen environments present in the hydrogel also in formulations containing gellan gum microcapsules.

### 3.3.5.2 Comparison among C 1s, N 1s and O 1s chemical environments identified in HA hydrogel formulations containing ketorolac tromethamine and gellan gum microcapsules

In summary, what we must retain from the C 1s, N 1s and O 1s high-resolution analysis thus far, is that we were also able to identify and quantify relative chemical amounts related to functional groups characteristic of gellan gum in HA hydrogel formulations. In a brief comparison with previous results, we noticed how the replacement of a free dispersion of ketorolac tromethamine in HA hydrogel by gellan gum microcapsules can affect the chemical environment in the biomedical system. We noticed a decreasing trend in the C2, N1 and O1 environments with the replacement of ketorolac tromethamine by gellan gum microcapsules. On the contrary, we noticed a tendency to increase in the C3, C4, C5, N2 and O2 environments with the replacement of ketorolac tromethamine by gellan gum microcapsules.

Figure 3.21 summarizes the tendencies mentioned above in a comparison of all C 1s, N 1s and O 1s chemical environments identified in HA hydrogel formulations containing ketorolac tromethamine and gellan gum microcapsules.

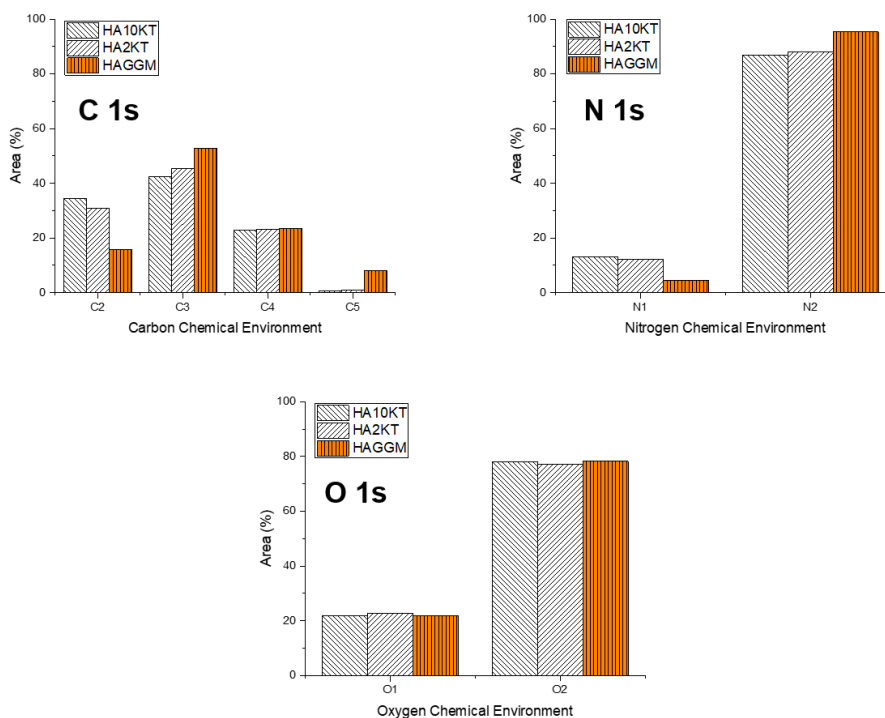


Figure 3.21. Relative chemical environments amount found over C 1s, N 1s and O 1s high-resolution spectra from freeze-dried HA hydrogel containing ketorolac tromethamine and gellan gum microcapsules.

This analytical strategy also demonstrates the ability of XPS to identify and quantify chemical environments from therapeutic vehicles directly in hydrogel-based drug delivery systems aiming to replace the free dispersion of therapeutic drugs by a prolonged drug delivery. It might be emphasized that the C3, C4, C5, N2 and O1 environments found here as chemical environments mainly characteristic of the HA hydrogel containing gellan gum microcapsules (in comparison with HA hydrogel formulations containing ketorolac tromethamine) can help identify the characteristic molecular fragments of gellan gum previously highlighted by ToF-SIMS analysis in Figure 3.4.

### 3.4 MULTIMODAL APPROACH DISCUSSION

The use of ToF-SIMS macro-imaging was a fundamental tool in the chemical mapping of HA hydrogel formulations containing ketorolac tromethamine and gellan gum microcapsules. This was reached first by identifying individually chemical markers of hydrogel, ketorolac tromethamine and gellan gum microcapsules. Then, by using different field-of-view (FoV) sizes ranging from  $500 \times 500 \mu\text{m}^2$  to  $1500 \times 1500 \mu\text{m}^2$  that allowed a large view of chemical markers in the surface of interest.

In addition, the use of AFM allowed the visualization of the fibrillar morphology of the surface of gellan gum microcapsules that might be an important information in the understanding of mechanisms of absorption and releasing of therapeutic drugs using this kind of drug delivery vehicle. However, areas in HA hydrogel formulations could not have its morphology imaged because AFM is limited to the analysis of areas with a maximum size of  $100 \times 100 \mu\text{m}^2$  (xy) that is a pretty much smaller FoV in comparison with those reached by ToF-SIMS. Besides that, HA hydrogel formulations have a topographical variation greater than  $10 \mu\text{m}$  that is more than the maximum variation limit in the z-direction supported by AFM analysis.

Then, identification and quantification of chemical environments on HA hydrogel-based drug delivery systems were performed through XPS analysis. Survey and core level spectra were obtained from formulations of pure HA hydrogel and HA hydrogel with ketorolac tromethamine and gellan gum microcapsules. A  $200 \mu\text{m}$  diameter x-ray spot was carefully set up on scanning x-ray images (SXI) acquired through a navigation FoV of  $1350 \times 1350 \mu\text{m}^2$  for analysis each of these surfaces. No specific region of interest was particularly searched for correlation with results obtained from ToF-SIMS.

Table 3.9. Advantages and disadvantages aspects of multimodal ToF-SIMS, AFM and XPS approach for analysis of HA hydrogel formulations with ketorolac tromethamine and gellan gum microcapsules.

Advantages	Disadvantages
ToF-SIMS macro imaging allows visualization of chemical markers of ketorolac tromethamine and gellan gum microcapsules in HA hydrogel	No quantitative information about the chemical compounds present in the sample is acquired through the ToF-SIMS analysis
AFM allowed the visualization of the fibrillar morphology of the surface of gellan gum microcapsules	AFM is limited to the analysis of areas with a maximum size of $100 \times 100 \mu\text{m}^2$ (xy) and a maximum topographical variation of up to $10 \mu\text{m}$ (z)
Molecular information obtained by ToF-SIMS is coherent with chemical environments quantified by XPS	

### 3.5 CONCLUSIONS

Therefore, we can conclude that we were able to successfully perform ToF-SIMS imaging of ketorolac tromethamine and gellan gum microcapsules in HA hydrogel-based drug delivery systems used in the treatment of glioblastoma that were not yet implanted in living brains. This was achieved primarily through the identification of molecular fragments characteristic of each of these systems before them being mixed together to form drug delivery systems. Three important groups of molecular ions can be distinguished. First, the group that contains low-mass oxygenated molecular fragments such as  $\text{COH}^+$  ( $m/z = 29.00$ ),  $\text{CH}_2\text{OH}^+$  ( $m/z = 31.01$ ),  $\text{CH}_3\text{CO}^+$  ( $m/z = 43.01$ ) and  $\text{CH}_5\text{CO}^+$  ( $m/z = 53.00$ ) that can be identified as characteristic of the HA hydrogel. The second group corresponds to nitrogenous molecular fragments such as  $\text{C}_{14}\text{H}_{12}\text{NO}^+$  ( $m/z = 210.10$ ),  $\text{C}_{14}\text{H}_{14}\text{NO}^+$  ( $m/z = 212.12$ ),  $\text{C}_{14}\text{H}_{14}\text{NO}_2^+$  ( $m/z = 228.10$ ) and  $\text{C}_{15}\text{H}_{14}\text{NO}_3^+$  ( $m/z = 256.12$ ) that appear to be characteristics of ketorolac tromethamine. The third group is composed of unassigned molecular ions that might be related to the D-glucose, D-glucuronate and L-rhamnose units characteristic of gellan gum. The assignment for each  $m/z$  is not shown in order to avoid false assignments since these  $m/z$  were identified directly in the mass spectrum and no reference about the gellan gum fragmentation in mass spectrometry was used to confirm the possible assignments. Then, we proceed in the identification of zones of chemical contrast based on these molecular fragments characteristic of each of HA hydrogel, ketorolac tromethamine and gellan gum microcapsules.

Furthermore, from the use of AFM we were able to focus on exploring the morphology of the gellan gum microcapsules and we discovered a fibrillar aspect on its surface. The morphology of these microcapsules is still poorly known and, therefore, the AFM may in the future represent a strong ally in

the study of absorption and release mechanisms of drugs through this fibrillar surface found in gellan gum microcapsules.

Besides that, we showed that the quantification of chemical environments of ketorolac tromethamine, gellan gum microcapsules in HA hydrogel formulations was possible. Survey and core level spectra were acquired in pure HA hydrogel and HA hydrogel-based formulations containing ketorolac tromethamine and gellan gum microcapsules, except for the core level spectra of pure HA hydrogel that was not possible to be acquired due to peak broadening resulting from surface charge effects. In summary, in terms of survey spectra of pure HA hydrogel, the approximate stoichiometric ratios found in freeze-dried formulations of pure HA hydrogel revealed that lower amounts of nitrogen and oxygen have been found in experimental data in comparison with those expected for theoretical values. Besides that, the identification of sodium in the HA hydrogel composition might indicate that residues from the process of functionalization of hydrogel may be present in these formulations.

Similarly, the approximate stoichiometric ratios found in the survey spectra of a dry drop of aqueous solution containing ketorolac tromethamine revealed that less carbon and more nitrogen and oxygen than expected were found for a ketorolac tromethamine molecule. On the other hand, in a direct comparison, the expected increase in the atomic percentage of carbon and nitrogen and a decrease in the atomic percentage of oxygen in formulations of HA hydrogel containing ketorolac tromethamine compared to pure HA hydrogel formulations was observed. In terms of core level analysis, although some explanations for the quantity of certain chemical environments are based on assumptions that need further analysis to be confirmed, we noticed a tendency of increase in the C2 (carbon from hydrocarbon structures) and N1 (nitrogen of amino groups) amounts with the addition of ketorolac tromethamine in HA hydrogel formulations. A trend of reduction was observed in the C3 (carbon from the heterocyclic ring structure containing an atom of nitrogen, amine or hydroxyl environments), C4 (carbon from the carbonyl environment) and N2 (carbon-nitrogen bond from the heterocyclic ring structure) amounts with the addition of ketorolac tromethamine in HA hydrogel formulations. As ketorolac tromethamine is richer in carbon chains compared to HA hydrogel, it is natural to see a significant increase in C2 in HA hydrogel formulations with a greater amount of ketorolac tromethamine whereas C3 and C4, which are characteristic of HA hydrogel, lose prominence due to the addition of ketorolac tromethamine. Besides that, the increase in N1 in relation to N2 is explained by the addition of ketorolac tromethamine in HA hydrogel formulations. It happens because N1 groups are present in both ketorolac tromethamine and HA hydrogel chemical structures while N2 is only present in ketorolac tromethamine.

In addition, a general comparison between the approximate stoichiometric ratios found in the survey spectra of freeze-dried pure HA hydrogel and HA hydrogel containing gellan gum microcapsules, the quantities of C 1s, N 1s, O 1s and Na 1s does not present large differences. However, the stoichiometric differences found for these two samples [small increase in O 1s environments] are consistent with the addition of high acyl gellan molecules in formulations of pure HA hydrogel. This means that the small increases in the amount of O 1s and the reduction in the amount of carbon and nitrogen may be

associated with the presence of high acyl gellan. In terms of core level analysis, we noticed a decrease for C2, N1 and O1 environments with the replacement of ketorolac tromethamine by gellan gum microcapsules. On the contrary, we noticed an increase for C3, C4, C5, N2 and O2 environments with the replacement of ketorolac tromethamine by gellan gum microcapsules. This increase in C3, C4, C5 and O2 can be explained by the introduction of chemical environments related to oxygen such as ether, hydroxyl and carboxyl groups strongly present in the composition of high acyl gellan. On the other hand, the reduction of N1 and the increase of N2 may be mostly associated with the nitrogen environment in the HA hydrogel.

At this point, we saw how the information obtained by ToF-SIMS and XPS was correlated. While the ToF-SIMS method was able to generate qualitative molecular information about a target surface and gave us the spatial distribution of these molecules in this same target surface, only with the use of XPS we were able to measure the chemical environments characteristic of the molecules highlighted by ToF-SIMS. Although we have used our multimodal surface imaging approach to study a drug delivery system designed for the treatment of glioblastoma pre-implant, these results bring to light the possibility of transferring this approach to the study of drug delivery systems pre-implant. In this regard, the direct correlation of the ToF-SIMS and XPS methods is promising in observing the resorption of hydrogel or microcapsules and diffusion of drugs in neural tissues, which is essential in understanding the behaviour of these drug deliverers and if the drug has reached or not its therapeutic target.

In other words, we can conclude that the multimodal ToF-SIMS, AFM and XPS surface analysis approach is compatible with the analysis of different regions of analysis in drug delivery systems with some caveats. Positive aspects in our multimodal surface analysis approach applied to the analysis of drug delivery systems include:

- ToF-SIMS macro imaging allows visualization of chemical markers of ketorolac tromethamine and gellan gum microcapsules in HA hydrogel
- AFM allowed the visualization of the fibrillar morphology of the surface of gellan gum microcapsules
- Molecular information obtained by ToF-SIMS is coherent with chemical environments quantified by XPS

The negative aspects in our multimodal surface analysis approach applied to drug delivery systems include:

- No quantitative information about the chemical compounds present in the sample is acquired through the ToF-SIMS analysis
- AFM is limited to the analysis of areas with a maximum size of  $100 \times 100 \mu\text{m}^2$  (xy) and a maximum topographical variation of up to  $10 \mu\text{m}$  (z)

In summary, the main objective of this chapter, which was to apply the first level of sophistication in multimodal surface chemical imaging in the analysis of different drug delivery systems, was achieved. This approach shows the complementarity of chemical analysis techniques such as ToF-SIMS and XPS and puts in perspective the use of AFM in problems related to drug delivery via gellan gum microcapsules.



## **4 MULTIMODAL TOF-SIMS, TANDEM MS, XPS AND XPEEM APPROACH FOR SURFACE CHEMICAL ANALYSIS OF OPTIMAL CUTTING TEMPERATURE COMPOUND**

---

In this fourth chapter, we will see application of the second level of sophistication of our multimodal surface imaging approach over an optimal cutting temperature (O.C.T.<sup>TM</sup>) Compound commonly used in the preparation of biological samples. Our multimodal approach in this chapter will be based on ToF-SIMS, Tandem MS, XPS and X-PEEM surface imaging analysis aiming at identifying and quantifying zones of chemical contrasts over a resin commonly used in the process of cutting of slices of biological samples: the O.C.T.<sup>TM</sup> Compound. The presentation of this resin and the process of sample preparation was already highlighted in section 2.2.2. The accomplishment of this analytical strategy on the O.C.T.<sup>TM</sup> compound will be extremely important in creating a know-how for accessing of regions of interest over a same sample for future analysis of biological surfaces. In the first section (4.1), we will see how ToF-SIMS imaging analysis is able to highlight chemical contrasts between the O.C.T.<sup>TM</sup> Compound and its embedded biological tissue but also between different regions in the O.C.T.<sup>TM</sup> Compound itself. In the second section (4.2), we will see how Tandem MS can be used to confirm assignments in the mass spectrum from a characteristic molecular fragmentation at a given  $m/z$ . In the third section (4.3), we will show how XPS is a fundamental tool in the quantification of chemical environments in regions that presents chemical contrasts and how the information generated from this technique can be correlated with the data obtained by mass spectrometry. In the fourth section (4.4), we will see the application of PEEM in the imaging of the different chemical contrast environments previously highlighted by ToF-SIMS, Tandem MS and XPS. In the fifth section (4.5) we will find a detailed discussion about the multimodal ToF-SIMS, Tandem MS, XPS and X-PEEM approach applied in the analysis of zones of interest in the O.C.T.<sup>TM</sup> Compound. Conclusions for this chapter will be found in the sixth section (4.6).

### **4.1 IMAGING CHEMICAL FEATURES IN THE RESIN HOSTING A BIOLOGICAL TISSUE BY TOF-SIMS**

Since chemical contrasts were generally absent in optical observations, ToF-SIMS images in both positive and negative ion modes were obtained using a wide FoV of  $4 \times 3 \text{ mm}^2$  in order to highlight chemical contrasts in the O.C.T.<sup>TM</sup> Compound in which biological tissue had been embedded. Figure 4.1 indicates the wide FoV of  $4 \times 3 \text{ mm}^2$  selected for ToF-SIMS imaging over the O.C.T.<sup>TM</sup> Compound hosting a biological tissue and the exact location of the O.C.T.<sup>TM</sup> Compound and the biological tissue.

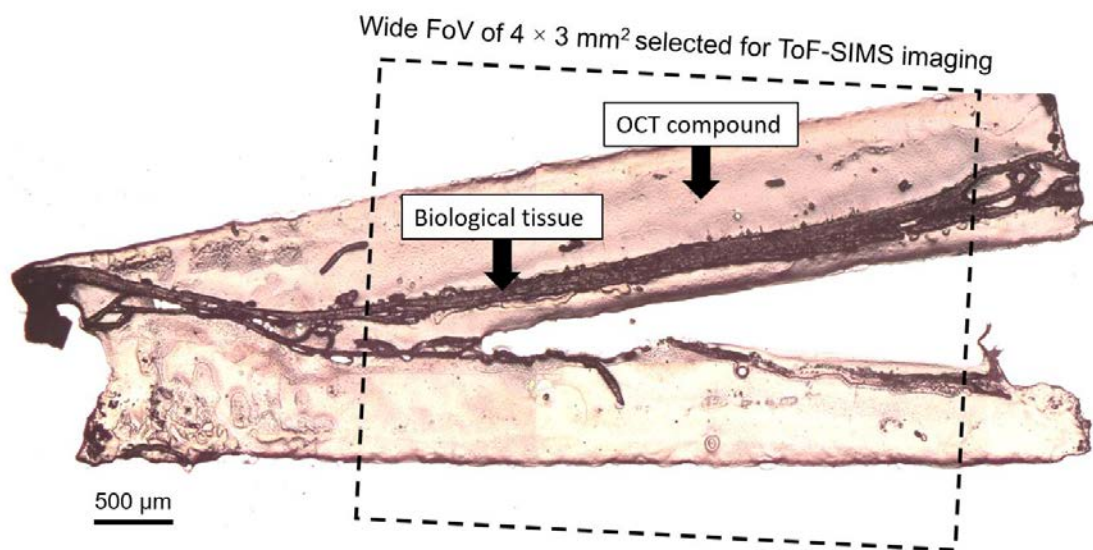


Figure 4.1. Optical imaging of the O.C.T.<sup>TM</sup> Compound embedding a biological tissue. The dotted line indicates the wide FoV of  $4 \times 3 \text{ mm}^2$  selected for ToF-SIMS imaging.

The spectra seen in Figure 4.2 and Figure 4.3 show the main ions identified in that target area.

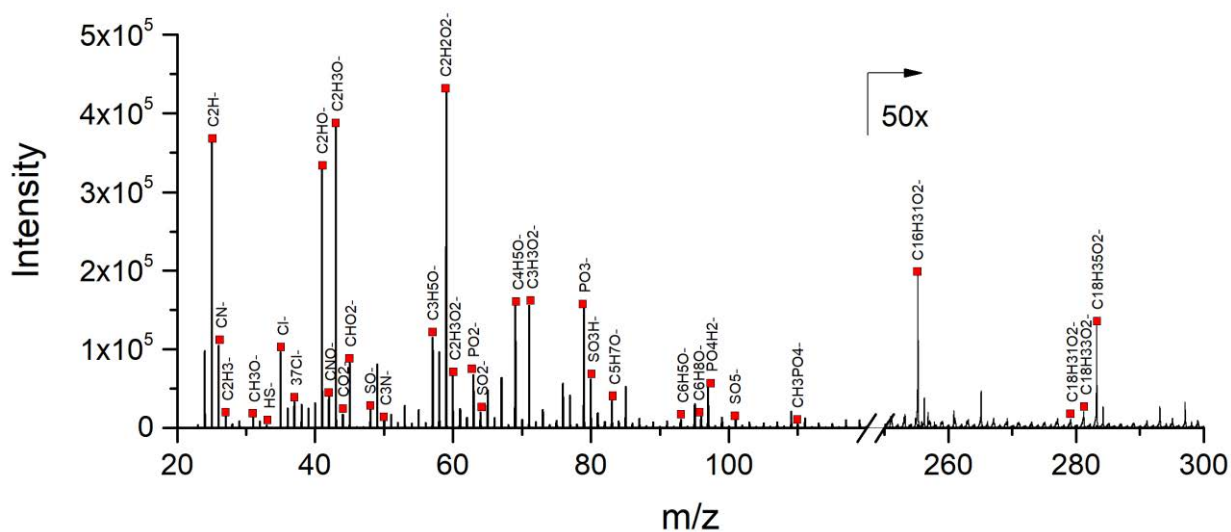


Figure 4.2. ToF-SIMS positive mass spectrum from the large  $4 \times 3 \text{ mm}^2$  area over the target system containing silicon substrate, biological tissue and the O.C.T.<sup>TM</sup> Compound.

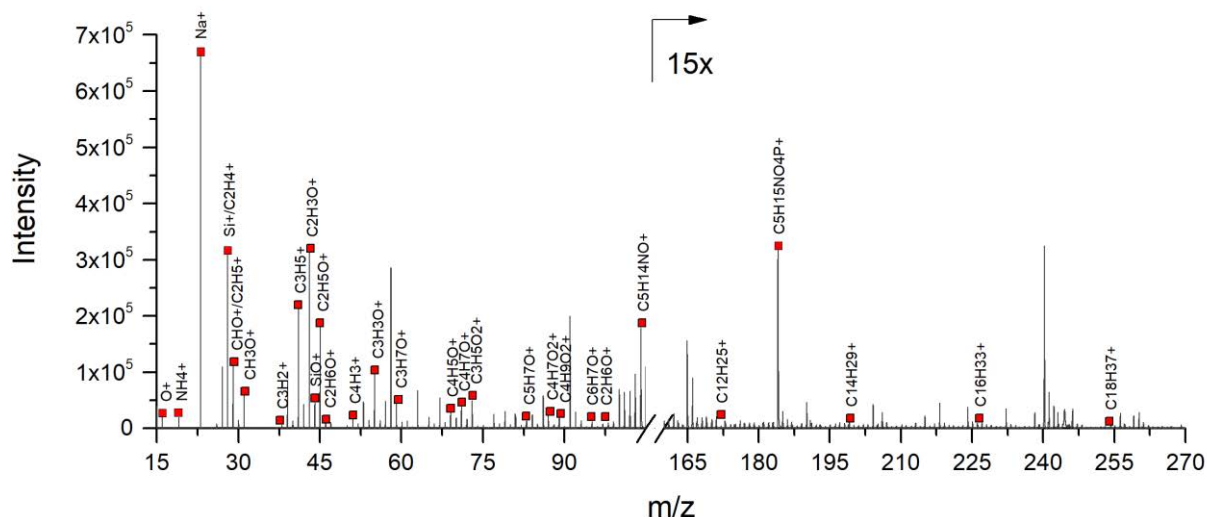


Figure 4.3. ToF-SIMS negative mass spectrum from the large 4 × 3 mm<sup>2</sup> area over the target system containing silicon substrate, biological tissue and the O.C.T.<sup>TM</sup> Compound.

The peaks that appear in these two mass spectra will be discussed in more details in the next subsections.

#### 4.1.1 Ions from silicon substrate

Among the positive ions identified there are O<sup>+</sup> (m/z = 15.99), Si<sup>+</sup> (m/z = 27.98) and SiO<sup>+</sup> (m/z = 43.97) that are characteristic of the silicon oxide thin layer on the surface of the silicon substrate used to support the biological tissue and the O.C.T.<sup>TM</sup> Compound.

The spatial distribution ions characteristic of the silicon substrate can be seen below in Figure 4.4.

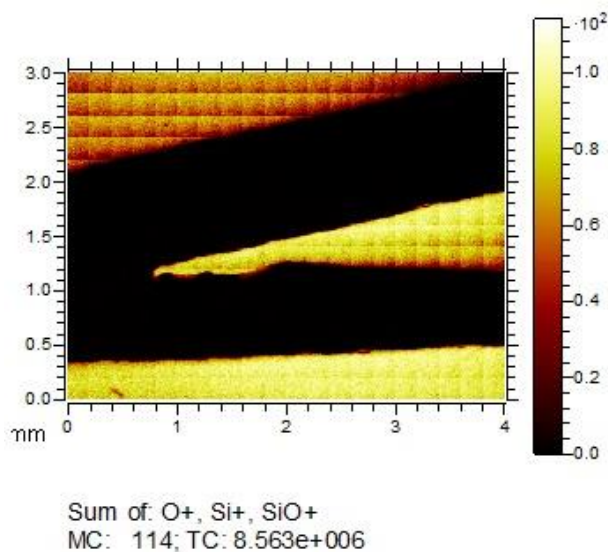


Figure 4.4. ToF-SIMS macro image showing the spatial distribution of ions characteristic of the silicon substrate.

#### 4.1.2 Ions from the biological tissue

Ions commonly found in biological tissues were also found to be intense in the large area analysed. It includes positive fragments of phospholipids such as the choline head group  $C_5H_{14}NO^+$  at  $m/z = 104.09$  and the phosphocholine head group  $C_5H_{15}NO_4P^+$  at  $m/z = 184.07$ . Similar fragments of phospholipids such as  $PO_4H^-$  ( $m/z = 95.95$ ),  $PO_4H_2^-$  ( $m/z = 96.95$ ) and  $CH_3PO_4^-$  ( $m/z = 109.94$ ) were found in the negative spectrum. The ions  $CN^-$  ( $m/z = 26.00$ ),  $CNO^-$  ( $m/z = 42.00$ ) and  $C_3N^-$  ( $m/z = 49.99$ ), which correspond to fragments of amino acids present in large proteins such as collagen were also identified occupying the same region as the fragments of phospholipids.

These positive and negative ions found in the biological tissue are listed below in Table 4.1.

Table 4.1. List of positive and negative ions appearing in the biological tissue.

	<b>m/z (experimental)</b>	<b>m/z (theoretical)</b>	<b>Assignment</b>
<b>Positive ions</b>	104.09	104.10	$C_5H_{14}NO^+$
	184.07	184.07	$C_5H_{15}NO_4P^+$
<b>Negative ions</b>	26.00	26.00	$CN^-$
	42.00	41.99	$CNO^-$
	49.99	50.00	$C_3N^-$
	95.95	95.96	$PO_4H^-$
	96.95	96.96	$PO_4H_2^-$
	109.97	109.97	$CH_3PO_4^-$

The spatial distribution of these positive and negative ions characteristic of the biological tissue can be seen in Figure 4.5.

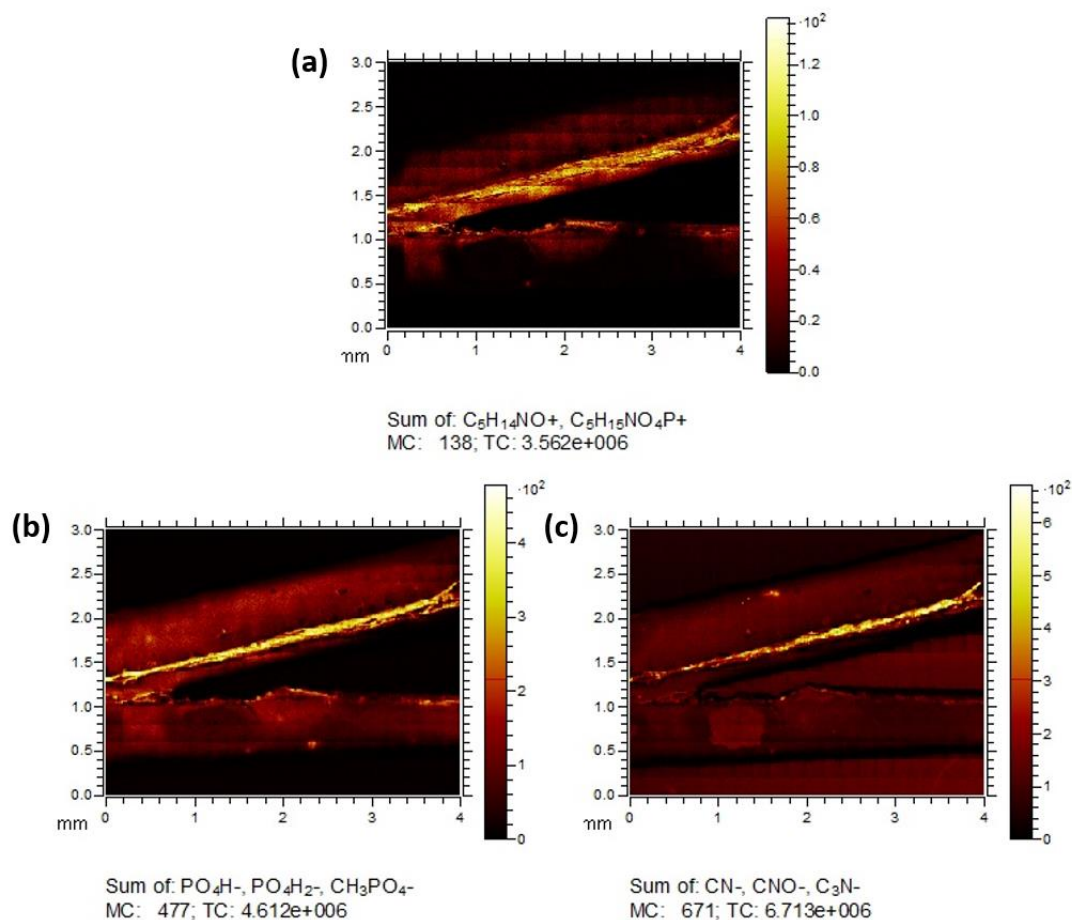


Figure 4.5. ToF-SIMS macro image showing the spatial distribution of (a) positive fragments of phospholipids and negative fragments of (b) phospholipids and (c) amino acids characteristic of the biological tissue.

#### 4.1.3 Ions from the resin

As the O.C.T.<sup>TM</sup> Compound consists mainly in glycols and water-soluble resins, hydrocarbons and oxygen-containing ions are widely expected in its composition. Using ToF-SIMS imaging, the existence of these hydrocarbons and ions containing oxygen was confirmed on the O.C.T.<sup>TM</sup> Compound. However, the distribution of these molecules is not observed homogeneously but it is present in two regions of chemical contrast on the O.C.T.<sup>TM</sup> Compound.

##### 4.1.3.1 Main chemical fragments identified in the S1-OCT regions

One of these regions of chemical contrast presents hydrocarbons and oxygen-containing ions in spots on the O.C.T.<sup>TM</sup> Compound that we will refer to as **S1-OCT** regions. In both positive and negative spectra, we can observe a large variety of fragments such as  $C_xH_y$ ,  $C_xH_yO$  and  $C_xH_yO_2$ . The list of the main positive and negative ions appearing in this region are listed below in Table 4.2.

Table 4.2. List of positive and negative hydrocarbons and oxygen-containing ions appearing in the S1-OCT region on the O.C.T.<sup>TM</sup> Compound.

	Compound	m/z (experimental)	m/z (theoretical)	Assignment	
<b>Positive ions</b>	<b>C<sub>x</sub>H<sub>y</sub><sup>+</sup></b>	28.02	28.03	C <sub>2</sub> H <sub>4</sub> <sup>+</sup>	
		29.03	29.03	C <sub>2</sub> H <sub>5</sub> <sup>+</sup>	
		41.03	41.03	C <sub>3</sub> H <sub>5</sub> <sup>+</sup>	
	<b>C<sub>x</sub>H<sub>y</sub>O<sup>+</sup></b>	29.00	29.00	CHO <sup>+</sup>	
		31.01	31.01	CH <sub>3</sub> O <sup>+</sup>	
		43.01	43.01	C <sub>2</sub> H <sub>3</sub> O <sup>+</sup>	
		45.03	45.03	C <sub>2</sub> H <sub>5</sub> O <sup>+</sup>	
		46.03	46.04	C <sub>2</sub> H <sub>6</sub> O <sup>+</sup>	
		59.04	59.04	C <sub>3</sub> H <sub>7</sub> O <sup>+</sup>	
		69.03	69.03	C <sub>4</sub> H <sub>5</sub> O <sup>+</sup>	
		71.04	71.04	C <sub>4</sub> H <sub>7</sub> O <sup>+</sup>	
	<b>C<sub>x</sub>H<sub>y</sub>O<sub>2</sub><sup>+</sup></b>	60.02	60.02	C <sub>2</sub> H <sub>4</sub> O <sub>2</sub> <sup>+</sup>	
		73.02	73.02	C <sub>3</sub> H <sub>5</sub> O <sub>2</sub> <sup>+</sup>	
		87.04	87.04	C <sub>4</sub> H <sub>7</sub> O <sub>2</sub> <sup>+</sup>	
		89.05	89.05	C <sub>4</sub> H <sub>9</sub> O <sub>2</sub> <sup>+</sup>	
		99.04	99.04	C <sub>5</sub> H <sub>7</sub> O <sub>2</sub> <sup>+</sup>	
	<b>Negative ions</b>	<b>C<sub>x</sub>H<sub>y</sub><sup>-</sup></b>	14.01	14.01	CH <sub>2</sub> <sup>-</sup>
			25.01	25.00	C <sub>2</sub> H <sup>-</sup>
27.01			27.02	C <sub>2</sub> H <sub>3</sub> <sup>-</sup>	
<b>C<sub>x</sub>H<sub>y</sub>O<sup>-</sup></b>		29.00	29.00	CHO <sup>-</sup>	
		31.01	31.01	CH <sub>3</sub> O <sup>-</sup>	
		41.00	41.00	C <sub>2</sub> HO <sup>-</sup>	
		43.02	43.01	C <sub>2</sub> H <sub>3</sub> O <sup>-</sup>	
<b>C<sub>x</sub>H<sub>y</sub>O<sub>2</sub><sup>-</sup></b>		44.00	43.99	CO <sub>2</sub> <sup>-</sup>	
		45.00	44.99	CHO <sub>2</sub> <sup>-</sup>	
		46.00	46.00	CH <sub>2</sub> O <sub>2</sub> <sup>-</sup>	
		46.99	47.01	CH <sub>3</sub> O <sub>2</sub> <sup>-</sup>	
		58.00	58.00	C <sub>2</sub> H <sub>2</sub> O <sub>2</sub> <sup>-</sup>	
		59.01	59.01	C <sub>2</sub> H <sub>3</sub> O <sub>2</sub> <sup>-</sup>	
		71.01	71.01	C <sub>3</sub> H <sub>3</sub> O <sub>2</sub> <sup>-</sup>	

The spatial distribution of these hydrocarbons and oxygen-containing ions within in the S1-OCT region on the O.C.T.<sup>TM</sup> Compound can be seen in Figure 4.6.

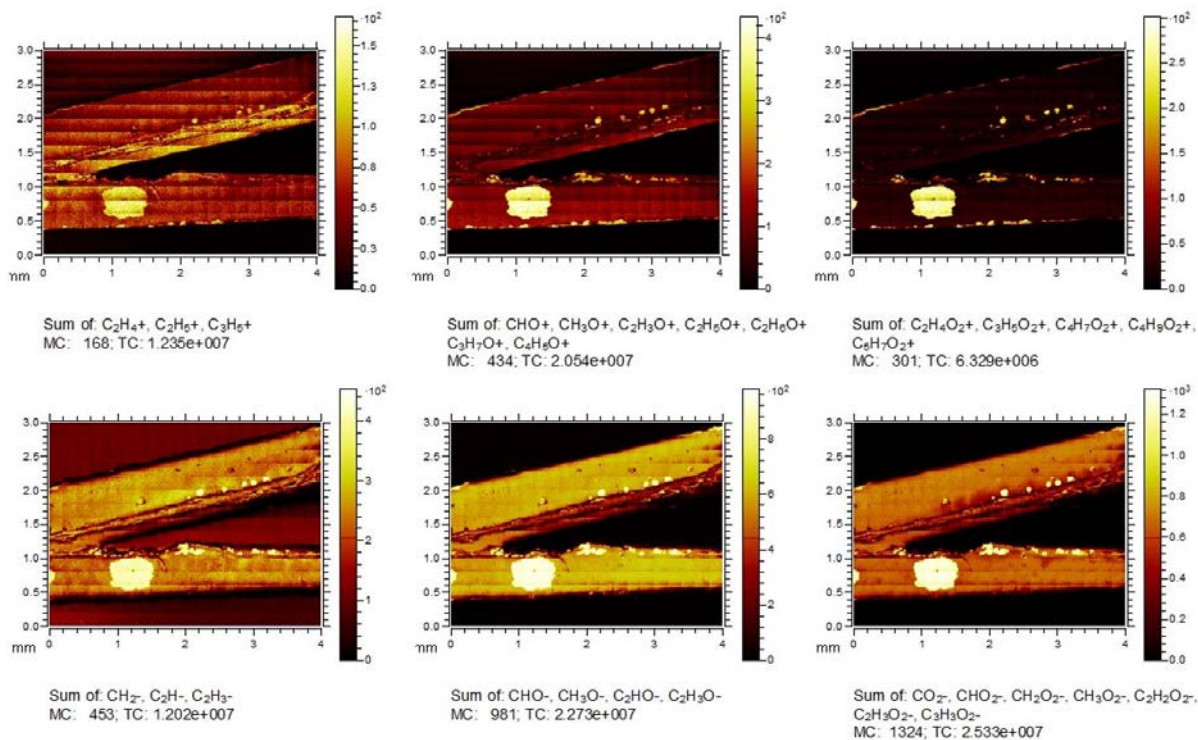


Figure 4.6. ToF-SIMS macro images showing the spatial distribution of hydrocarbons and oxygen-containing ions intensities within the S1-OCT region.

#### 4.1.3.2 Main chemical fragments identified in the S2-OCT region

The other region of chemical contrast presents hydrocarbons and oxygen-containing ions outside of the aforementioned spots on the O.C.T.<sup>TM</sup> Compound in the region that we will refer to as **S2-OCT**. In both positive and negative spectra, we can also observe a large variety of fragments such as C<sub>x</sub>H<sub>y</sub> and C<sub>x</sub>H<sub>y</sub>O.

The list of the main positive and negative ions that appear in this region are listed in Table 4.3.

Table 4.3. List of positive and negative hydrocarbons and oxygen-containing ions appearing in the S2-OCT region on the O.C.T.<sup>TM</sup> Compound.

	Compound	m/z (experimental)	m/z (theoretical)	Assignment	
<b>Positive ions</b>	<b>C<sub>x</sub>H<sub>y</sub><sup>+</sup></b>	13.01	13.00	CH <sup>+</sup>	
		14.01	14.01	CH <sub>2</sub> <sup>+</sup>	
		38.02	38.01	C <sub>3</sub> H <sub>2</sub> <sup>+</sup>	
		51.02	51.02	C <sub>4</sub> H <sub>3</sub> <sup>+</sup>	
		67.05	67.05	C <sub>5</sub> H <sub>7</sub> <sup>+</sup>	
		81.07	81.06	C <sub>6</sub> H <sub>9</sub> <sup>+</sup>	
		91.05	91.05	C <sub>7</sub> H <sub>7</sub> <sup>+</sup>	
	<b>C<sub>x</sub>H<sub>y</sub>O<sup>+</sup></b>	55.01	55.01	C <sub>3</sub> H <sub>3</sub> O <sup>+</sup>	
		81.03	81.05	C <sub>5</sub> H <sub>5</sub> O <sup>+</sup>	
		83.04	83.04	C <sub>5</sub> H <sub>7</sub> O <sup>+</sup>	
		95.04	95.04	C <sub>6</sub> H <sub>7</sub> O <sup>+</sup>	
		97.06	97.06	C <sub>6</sub> H <sub>9</sub> O <sup>+</sup>	
	<b>Negative ions</b>	<b>C<sub>x</sub>H<sub>y</sub>O<sup>-</sup></b>	57.03	57.03	C <sub>3</sub> H <sub>5</sub> O <sup>-</sup>
			69.03	69.03	C <sub>4</sub> H <sub>5</sub> O <sup>-</sup>
83.04			83.05	C <sub>5</sub> H <sub>7</sub> O <sup>-</sup>	
93.03			93.03	C <sub>6</sub> H <sub>5</sub> O <sup>-</sup>	
96.05			96.05	C <sub>6</sub> H <sub>8</sub> O <sup>-</sup>	

The presence of these hydrocarbons and oxygen-containing ions within in the S2-OCT region on the O.C.T.<sup>TM</sup> Compound can be seen in Figure 4.7.

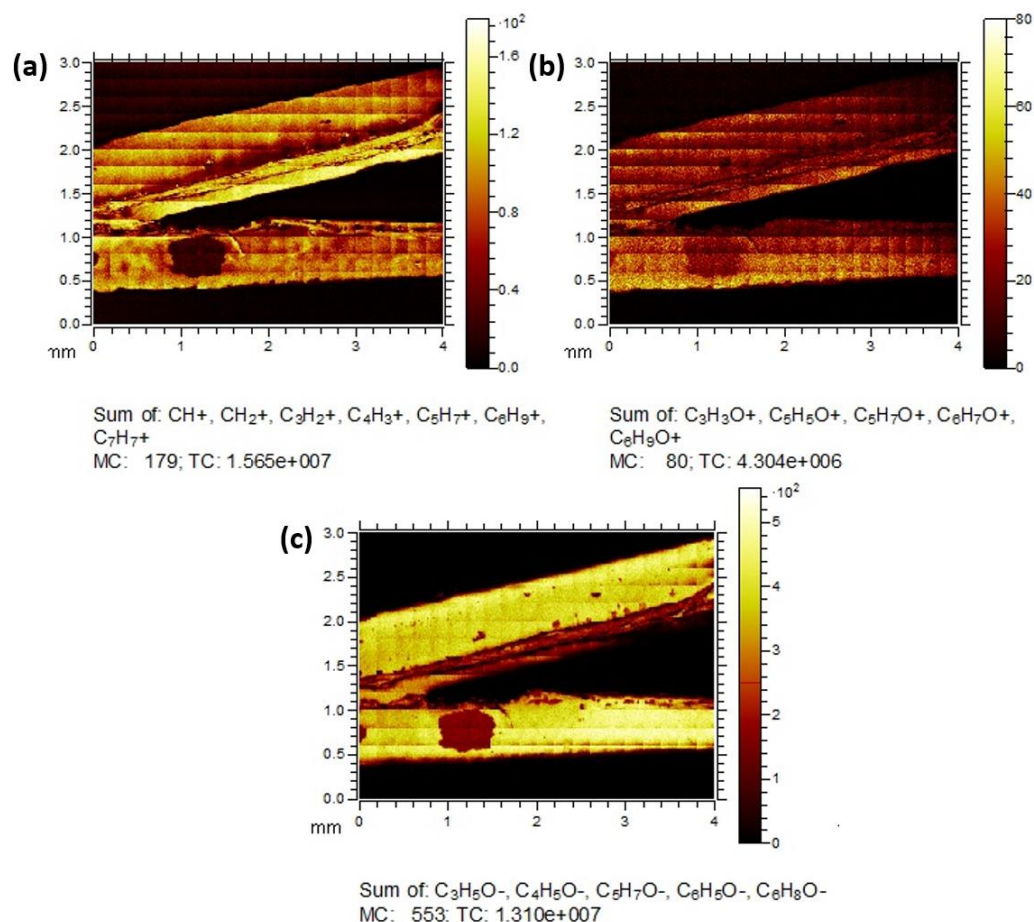


Figure 4.7. ToF-SIMS macro image showing the spatial distribution of (a) hydrocarbons and (b) and (c) oxygen-containing ions intensities within the S2-OCT region.

Although these two regions in the O.C.T.<sup>TM</sup> Compound differ in their chemical compositions in terms of fragments of hydrocarbons and oxygen-containing molecules this is not itself sufficient to explain the chemical difference between them.

#### 4.1.3.3 Belzalkonium salt fragments in the S2-OCT region

Other possible common key O.C.T.<sup>TM</sup> Compound peaks include the two negative chlorine isotopes  $\text{Cl}^-$  ( $m/z = 34.97$ ) and  $^{37}\text{Cl}^-$  ( $m/z = 36.96$ ) that might represent the benzalkonium additive used as an antiseptic in the formulation of the O.C.T.<sup>TM</sup> Compound. These two chlorine ions were found only in the S2-OCT region, which could indicate that the O.C.T.<sup>TM</sup> Compound could be covered with stains from some other chemical compound. However, the positive side chains of benzalkonium chloride such as  $\text{C}_{12}\text{H}_{25}^+$  ( $m/z = 169.08$ ),  $\text{C}_{14}\text{H}_{29}^+$  ( $m/z = 197.17$ ),  $\text{C}_{16}\text{H}_{33}^+$  ( $m/z = 225.20$ ) and  $\text{C}_{18}\text{H}_{37}^+$  ( $m/z = 253.24$ ) [30] were found on both S1-OCT and S2-OCT regions, which indicates that these long hydrocarbon chains can still be detected even if covered by some other chemical compound or that these long hydrocarbon chains belongs also to the supposed chemical compound covering the O.C.T.<sup>TM</sup> Compound. This question will be clarified in the next subsections. The ions characteristic of benzalkonium salt and identified in the O.C.T.<sup>TM</sup> Compound are listed below in Table 4.4.

Table 4.4. List of positive and negative ions characteristic of benzalkonium chloride identified the O.C.T.<sup>TM</sup> Compound.

	m/z (experimental)	m/z (theoretical)	Assignment
<b>Positive ions</b>	169.08	169.19	C <sub>12</sub> H <sub>25</sub> <sup>+</sup>
	197.17	197.09	C <sub>14</sub> H <sub>29</sub> <sup>+</sup>
	225.20	225.25	C <sub>16</sub> H <sub>33</sub> <sup>+</sup>
	253.24	253.30	C <sub>18</sub> H <sub>37</sub> <sup>+</sup>
<b>Negative ions</b>	34.97	34.96	Cl <sup>-</sup>
	36.96	36.96	<sup>37</sup> Cl <sup>-</sup>

The spatial distribution of the two negative chlorine isotopes and the long hydrocarbon chains of benzalkonium chloride can be seen in Figure 4.8.

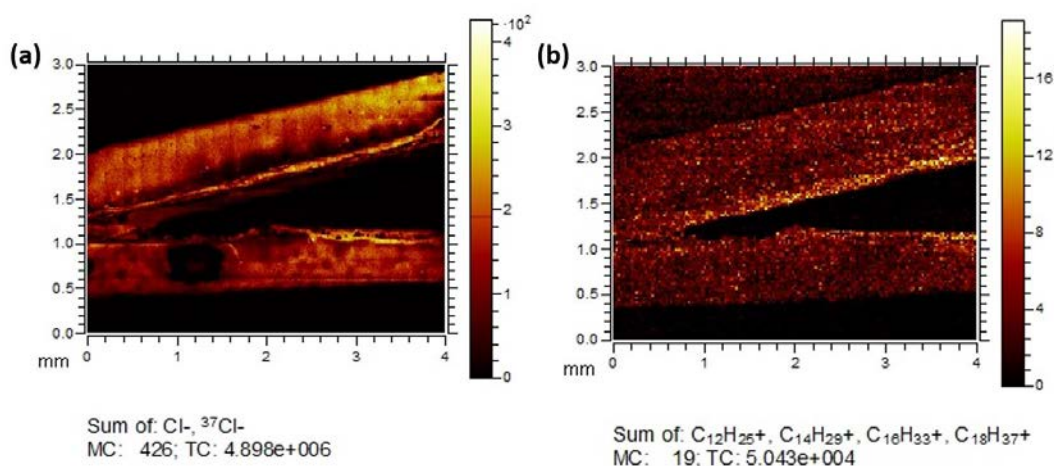


Figure 4.8. ToF-SIMS macro images showing the spatial distribution of (a) chlorine isotopes and (b) the long hydrocarbon chains of benzalkonium salt. The chlorine isotopes are present only in the S2-OCT region, while the long hydrocarbon chains are present in both S1-OCT and S2-OCT regions.

#### 4.1.3.4 Sulphate fragments in the S1-OCT and phosphate fragments in the S2-OCT region

Ions containing SO<sub>x</sub> and PO<sub>x</sub> functional groups have also been found on the O.C.T.<sup>TM</sup> Compound. The variations of SO<sub>x</sub> such as SO<sup>-</sup> (m/z = 47.96), SO<sub>2</sub><sup>-</sup> (m/z = 63.96) and SO<sub>3</sub><sup>-</sup> (m/z = 79.95) were strongly found in the S1-OCT region. The presence of other sulphated fragments in that same region such as HS<sup>-</sup> (m/z = 32.98), SO<sub>3</sub>H<sup>-</sup> (m/z = 80.96), H<sub>2</sub>S<sub>2</sub>O<sup>-</sup> (m/z = 81.95), SO<sub>5</sub><sup>-</sup> (m/z = 111.95) and SO<sub>5</sub>H<sup>-</sup> (m/z = 112.97) might indicate the presence of ammonium persulfate (NH<sub>4</sub>)<sub>2</sub>S<sub>2</sub>O<sub>8</sub> – an oxidizing agent commonly used in polymer chemistry. In the positive spectrum, the NH<sub>3</sub><sup>+</sup> (m/z = 17.02), NH<sub>4</sub><sup>+</sup> (m/z = 18.03), CH<sub>2</sub>N<sup>+</sup> (m/z = 28.01), CHO<sup>+</sup> (m/z = 29.00) and CH<sub>4</sub>N<sup>+</sup> (m/z = 30.03) fragments characteristic of ammonium persulfate (NH<sub>4</sub>)<sub>2</sub>S<sub>2</sub>O<sub>8</sub> also can be identified within the S1-OCT region. Similarly, the variations of PO<sub>x</sub>

such as PO<sup>-</sup> (m/z = 46.97), PO<sub>2</sub><sup>-</sup> (m/z = 62.96) and PO<sub>3</sub><sup>-</sup> (m/z = 78.95) were mainly found in the S2-OCT region (in addition to being strongly present on the biological tissue). It might be indicative of the close contact of the O.C.T.<sup>TM</sup> Compound with the biological tissue since no phosphorus-based molecules are expected in the composition of the O.C.T.<sup>TM</sup> Compound.

The fragments of ammonium persulfate identified in S1-OCT region of the O.C.T.<sup>TM</sup> Compound are listed in Table 4.5.

Table 4.5. List of positive and negative ions characteristic of ammonium persulfate identified in the S1-OCT region of the O.C.T.<sup>TM</sup> Compound.

	m/z (experimental)	m/z (theoretical)	Assignment
<b>Positive ions</b>	17.02	17.02	NH <sub>3</sub> <sup>+</sup>
	18.03	18.03	NH <sub>4</sub> <sup>+</sup>
	28.01	28.01	CH <sub>2</sub> N <sup>+</sup>
	29.00	29.00	CHO <sup>+</sup>
	30.03	30.03	CH <sub>4</sub> N <sup>+</sup>
<b>Negative ions</b>	32.98	32.98	HS <sup>-</sup>
	47.96	47.96	SO <sup>-</sup>
	63.96	63.96	SO <sub>2</sub> <sup>-</sup>
	79.95	79.95	SO <sub>3</sub> <sup>-</sup>
	80.96	80.96	SO <sub>3</sub> H <sup>-</sup>
	81.95	81.95	H <sub>2</sub> S <sub>2</sub> O <sup>-</sup>
	111.95	111.94	SO <sub>5</sub> <sup>-</sup>
	112.97	112.95	SO <sub>5</sub> H <sup>-</sup>

The spatial distribution of the ions containing SO<sub>x</sub> and PO<sub>x</sub> functional groups on the O.C.T.<sup>TM</sup> Compound can be seen in Figure 4.9.

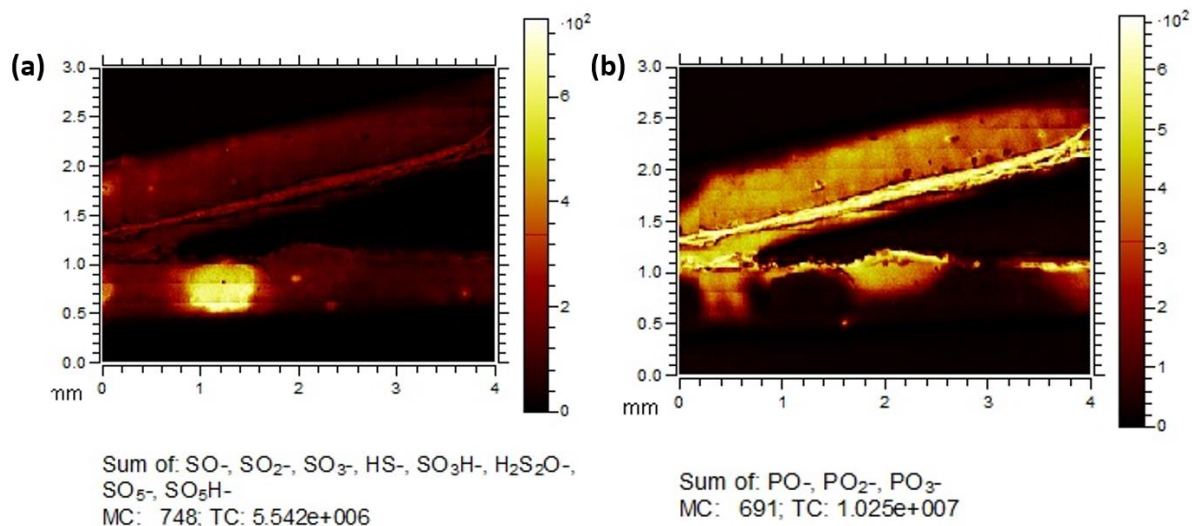


Figure 4.9. ToF-SIMS macro images showing the spatial distribution of ions containing (a) SO<sub>x</sub> and (b) PO<sub>x</sub> functional groups on the O.C.T.<sup>TM</sup> Compound. Sulphur-based ions were found mainly within the S1-OCT region, while phosphorus-based ions mainly on the S2-OCT region.

#### 4.1.3.5 Fatty acids fragments in the S1-OCT regions

Another additive potentially present in the formulation of the O.C.T.<sup>TM</sup> Compound used as plasticiser and stabiliser, and strongly appearing in the S1-OCT region, is the epoxidized linseed oil that contains variable amounts of unsaturated fatty acids such as C<sub>16</sub>H<sub>31</sub>O<sub>2</sub><sup>-</sup> (m/z = 255.22), C<sub>18</sub>H<sub>31</sub>O<sub>2</sub><sup>-</sup> (m/z = 279.16), C<sub>18</sub>H<sub>33</sub>O<sub>2</sub><sup>-</sup> (m/z = 281.23) and C<sub>18</sub>H<sub>35</sub>O<sub>2</sub><sup>-</sup> (m/z = 283.25), which might explain why long hydrocarbon chains that are also characteristic of benzalkonium salt were found in the S1-OCT region.

These fragments of fatty acids identified in S1-OCT region of the O.C.T.<sup>TM</sup> Compound are listed below in Table 4.6.

Table 4.6. List of fatty acids identified in the S1-OCT region of the O.C.T.<sup>TM</sup> Compound.

	m/z (experimental)	m/z (theoretical)	Assignment
<b>Negative ions</b>	255.22	255.23	C <sub>16</sub> H <sub>31</sub> O <sub>2</sub> <sup>-</sup>
	279.16	279.23	C <sub>18</sub> H <sub>31</sub> O <sub>2</sub> <sup>-</sup>
	281.23	281.24	C <sub>18</sub> H <sub>33</sub> O <sub>2</sub> <sup>-</sup>
	283.25	283.26	C <sub>18</sub> H <sub>35</sub> O <sub>2</sub> <sup>-</sup>

The spatial distribution of the aforementioned fatty acids can be seen in Figure 4.10.

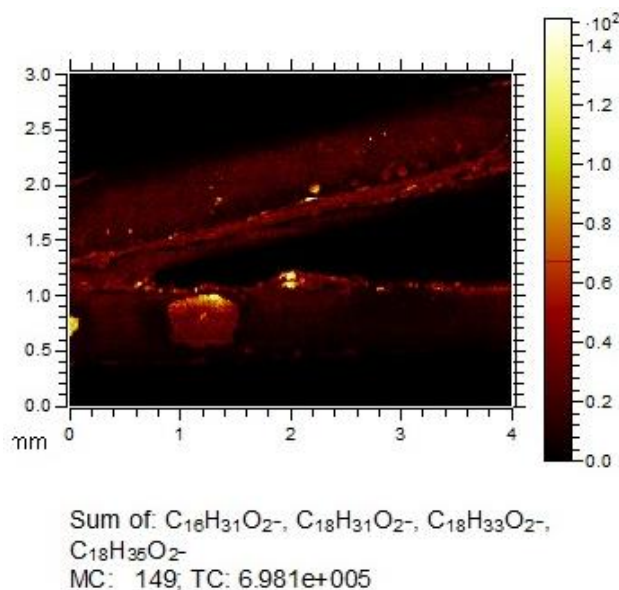


Figure 4.10. ToF-SIMS macro images showing the presence of unsaturated fatty acids mainly in the S1-OCT region.

#### 4.1.3.6 Summary of ToF-SIMS imaging analysis of S1- and S2-OCT regions

From this first investigation of an organic system hosting a biological tissue by ToF-SIMS, we could highlight how useful was the application of a wide field-of-view (FoV) in the identification of regions of interest (ROIs) for multimodal analysis. It allowed the identification of surfaces from the silicon substrate, the biological tissue and from zones of chemical contrast on the O.C.T.<sup>TM</sup> Compound. In addition to a large variety of hydrocarbons and oxygen-containing ions expected to be present in the composition of the O.C.T.<sup>TM</sup> Compound, we noticed that sulphur-based ions as well as fatty acids with their long carbon chains are strongly present in the S1-OCT region. This might be a strong indication that additives such as ammonium persulfate and epoxidized linseed oil, possibly incorporated into the O.C.T.<sup>TM</sup> Compound, are not homogeneously dispersed and form zones of high concentration of these additives. On the other hand, the additive benzalkonium chloride seem to be well incorporated in the O.C.T.<sup>TM</sup> Compound so that the intensity of the chlorine isotopes can be seen throughout the S2-OCT region.

#### 4.1.3.7 Zones of interest in the resin for multimodal analysis

To keep the main regions of contrast in this organic system in mind, Figure 4.11 shows an optical image of the O.C.T.<sup>TM</sup> Compound (resin) hosting a biological tissue and the large ToF-SIMS image in evidence overlapping the optical image. The ToF-SIMS image shows the chemical contrasts among biological tissue (in green) and O.C.T.<sup>TM</sup> Compound (in red and blue).

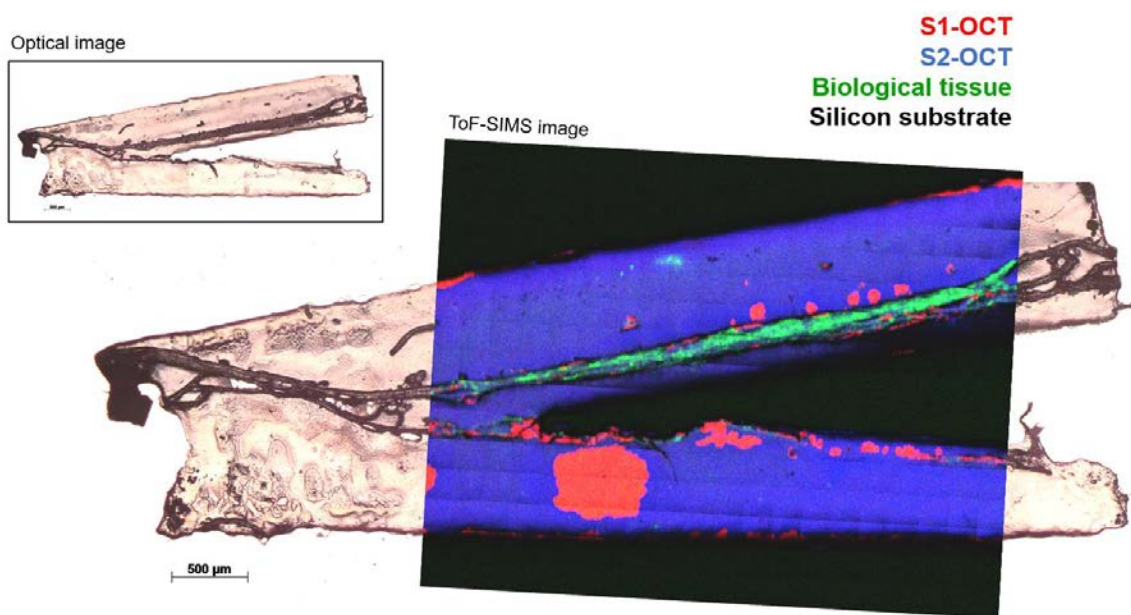


Figure 4.11. Optical image of a biological tissue cross section surrounded by O.C.T.<sup>TM</sup> Compound in the background, with a ToF-SIMS macro image in the foreground showing a RGB overlay where green is  $\text{CNO}^-$  ( $m/z = 41.99$ ) characteristic of the biological tissue, red is  $\text{C}_2\text{H}_2\text{O}_2^-$  ( $m/z = 58.00$ ) characteristic of the S1-OCT region and blue is  $\text{C}_4\text{H}_5\text{O}^-$  ( $m/z = 69.03$ ) characteristic of the S2-OCT region. Macro ToF-SIMS image size  $4 \times 3 \text{ mm}^2$  containing 300 ( $20 \times 15$ )  $200 \mu\text{m}^2$  tiles.

The chemical contrast among these three different areas showed in Figure 4.11 could not initially be seen in the organic system through the optical microscope. As the chemical differences of the S1-OCT (red) and S2-OCT (blue) regions is still an open question, we will focus on our multimodal analysis approach in the following subsections on these two contrasted regions.

## 4.2 IMAGING CHEMICAL FEATURES IN THE RESIN BY TANDEM MS

In order to refine the molecular assignment provided from specific  $m/z$  in the ToF-SIMS spectra in the previous section, we will now take the same organic system hosting a biological tissue to be analysed by Tandem MS. In Figure 4.12A below we see a ToF-SIMS image with a red and blue colour overlay representing the S1-OCT and S2-OCT regions, respectively. The region of interest for analysis by Tandem MS is highlighted with a square over a large red spot (region S1-OCT) on the O.C.T.<sup>TM</sup> Compound. In order to confirm the presence of fatty acids in the S1-OCT region, we will analyse in detail the fragmentation of the ion identified at  $m/z = 255.22$  assigned as a fragment of Palmitic acid ( $\text{C}_{16}:0$ ). The product spectrum of the  $m/z$  255 precursor from an ROI on the S1-OCT region on the O.C.T.<sup>TM</sup> Compound can be seen in Figure 4.12B.

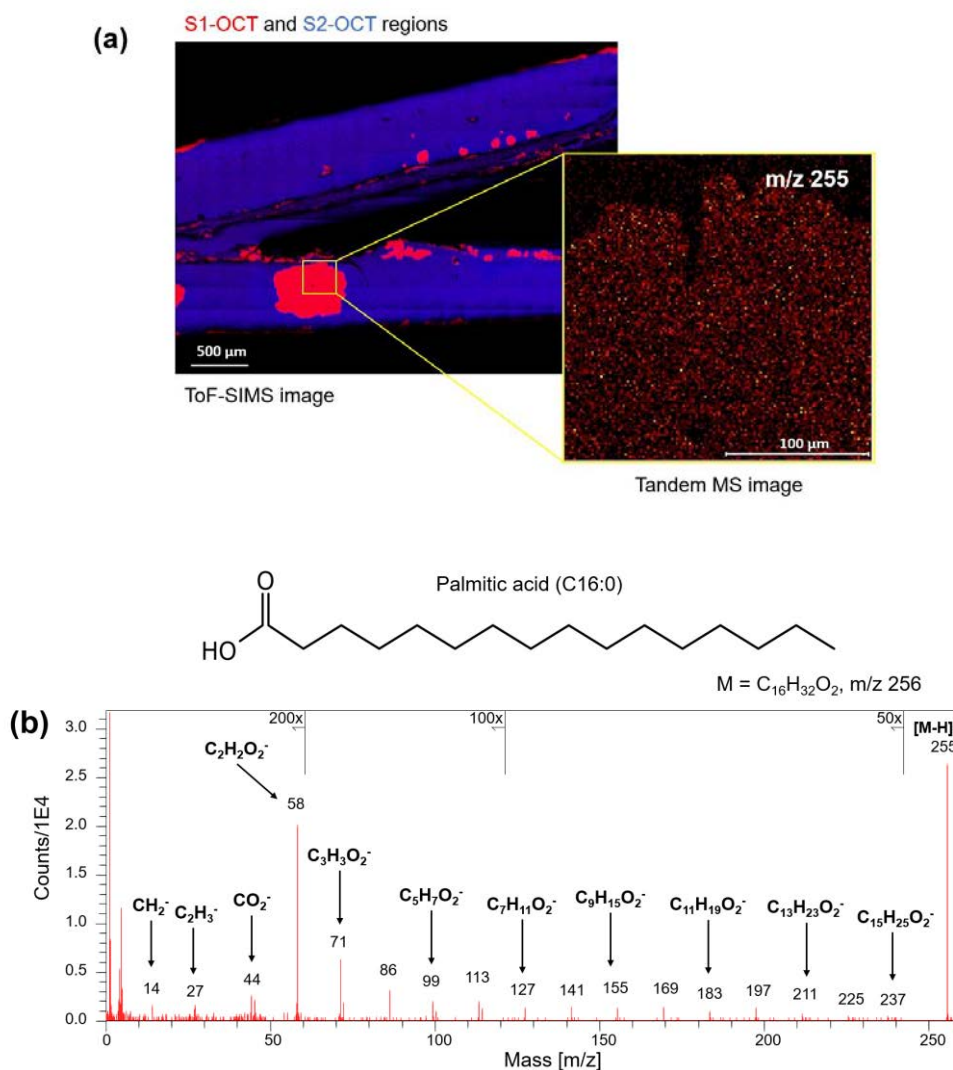


Figure 4.12. (a) Schematic view of a region of interest for Tandem MS analysis over the S1-OCT region on the O.C.T.<sup>TM</sup> Compound. The tandem MS image indicate the spatial distribution of the ion identified at  $m/z=255.22$  and assigned as Palmitic acid (C16:0). The ToF-SIMS image in the background show an overlay where red is  $C_2H_2O_2^-$  ( $m/z = 58.00$ ) characteristic of the S1-OCT region and blue is  $C_4H_5O^-$  ( $m/z = 69.03$ ) characteristic of the S2-OCT region. (b) Product spectrum of the  $m/z = 255.22$  precursor from an ROI on the S1-OCT region on the O.C.T.<sup>TM</sup> Compound.

The product spectrum of  $[M-H]^-$  at  $m/z$  255.22 seen above is consistent with the fragmentation of carboxylic acids that typically contain 16 carbon atoms. The key fragments below  $m/z$  255.22 indicate the preservation of the carboxylic functional group with a consequent loss of fragments from its carbon chain. For example, the fragment  $C_{15}H_{25}O_2^-$  at  $m/z$  237.18 is nothing more than the ion  $C_{16}H_{31}O_2^-$  at  $m/z$  255.22 with a loss of the fragments  $[CH_2+H_4]^-$ . Likewise, the fragment  $C_{13}H_{23}O_2^-$  at  $m/z$  211.17 is nothing more than the ion  $C_{15}H_{25}O_2^-$  at  $m/z$  237.18 with a loss of the fragments  $[CH+CH]^-$ . The same can be noticed for the fragment  $C_{11}H_{19}O_2^-$  at  $m/z$  183.13 that is actually the ion  $C_{13}H_{23}O_2^-$  at  $m/z$  211.17 with a loss of the fragments  $[CH_2+CH_2]^-$ . And so, the loss of part of the hydrocarbon chain of the main molecule is repeated for the other fragments. Among the fragments of  $[M-H]^-$  at  $m/z$  255.22 we can notice the low-mass fragments  $CH_2^-$  ( $m/z = 14.01$ ),  $C_2H_3^-$  ( $m/z = 27.01$ ),  $CO_2^-$  ( $m/z = 44.00$ ),  $C_2H_2O_2^-$  ( $m/z = 58.00$ ) that

had already been identified in the subsection 4.1.3 as fragments of hydrocarbon chains and oxygen-containing ions appearing in the S1-OCT region but that we didn't know until then which molecules in the S1-OCT region they belonged to.

In summary, Tandem MS has proven to be an essential tool in verifying the assignment given to peaks found in the ToF-SIMS spectrum. Thanks to the Tandem MS analysis we can now confirm that the fragments generated from the molecular ion identified at  $m/z$  255.22 are direct fragments of Palmitic acid (C16:0) as well as confirm the good assignment of fatty acids in the S1-OCT region that are possibly strongly related to the additive epoxidized linseed oil.

### **4.3 CHEMICAL QUANTIFICATION IN THE RESIN BY XPS**

From the mass spectrometry imaging analysis carried out in the previous sections that highlighted the existence of a chemical contrast on the surface of the O.C.T.<sup>TM</sup> Compound, it was possible to notice that both S1-OCT and S2-OCT regions showing contrast had fragments hydrocarbons or compounds containing oxygen in their composition. Aside the identification of fragments that might indicate the use of additives in the formulation of the O.C.T.<sup>TM</sup> Compound and that possibly explains why zones of chemical contrast exist on its surface, the distinction of two regions with their chemical contrast based on similar types of fragments can be a hard task. In addition, mass spectrometry does not provide any quantitative information that could be useful in distinguishing chemically different regions based on the same kind of fragments over biological samples. It is worth remembering that intensities in mass spectrometry are mostly associated with different ionization yields than related to quantities of certain ions in the sample.

#### **4.3.1 Survey spectra analysis from S1 and S2-OCT regions**

In this context, XPS analysis, which is able to identify and quantify elements and their chemical environments, can be useful in the characterization and consequent distinction of these regions of chemical contrast. Based on this, XPS analysis was performed on regions of chemical contrast previously highlighted by mass spectrometry imaging. Figure 4.13(a) shows a schematic view of the localization of the two spots of XPS analysis on S1-OCT and S2-OCT regions. Figure 4.13(b) indicates the localization of the spots of analysis in SXI images. The survey spectra obtained from the S2-OCT and S1-OCT spots are shown in Figure 4.13(c) and Figure 4.13(d).

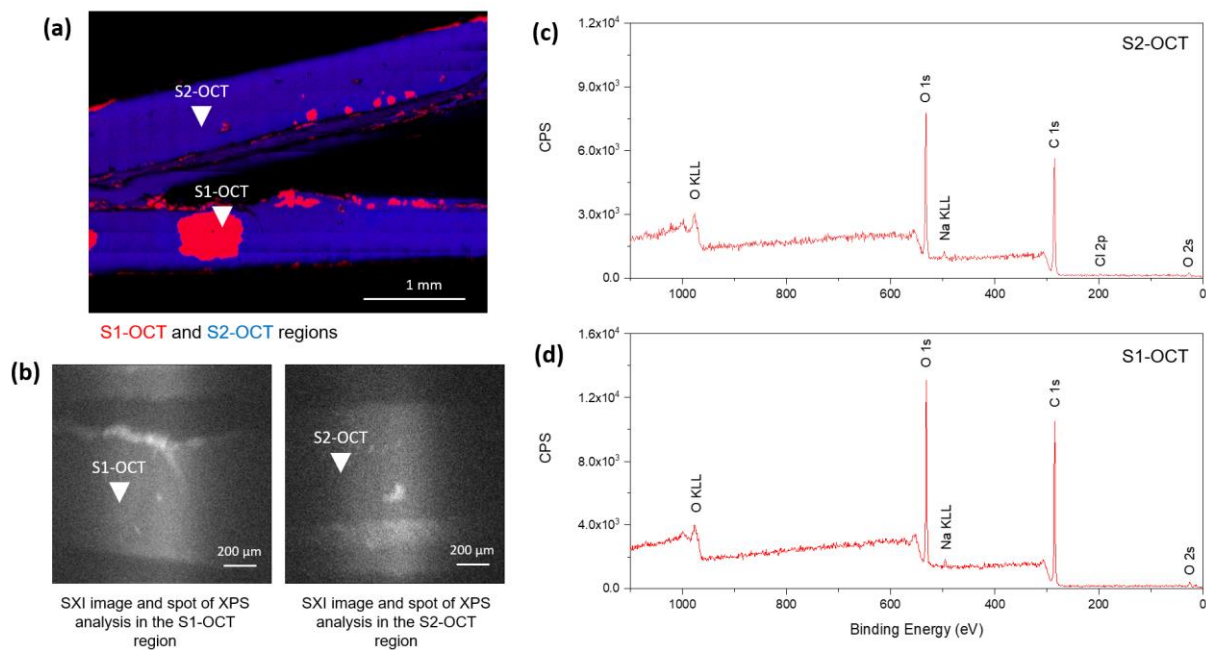


Figure 4.13. (A) ToF-SIMS macro image indicating an overlay of  $C_2H_2O_2^-$  in red and  $C_4H_5O^-$  in blue. The two zones of interest S1-OCT over the red region and S2-OCT over the blue region for XPS analysis are also indicated. (B) SXI images from S1-OCT and S2-OCT indicating the position of the X-ray spot for the XPS analysis: S1-OCT and S2-OCT, respectively. Survey spectra from (C) S1-OCT and (D) S2-OCT.

The survey spectra obtained from the S1-OCT and S2-OCT regions indicated the quantifiable presence of carbon and oxygen inside these two regions. Chlorine was only found in the S2-OCT region, which is in accordance with the ToF-SIMS imaging results. In the S1-OCT was found amounts of 72.3% carbon and 27.7% oxygen, while in the S2-OCT spot was found amounts of 71.4% carbon, 27.4% oxygen and 1.2% chlorine. These different amounts are reported in Table 4.7.

Table 4.7. Core levels and their corresponding peak binding energies (eV) and experimental atomic concentrations (at. %) from survey spectra from S1-OCT and S2-OCT spots.

Core level	Peak BE (eV)	S1-OCT	S2-OCT
		at. %	at. %
Cl 2p	199	–	1.2
C 1s	285	72.3	71.4
O 1s	531	27.7	27.4

While carbon and oxygen were expected for both spots on the O.C.T.<sup>TM</sup> Compound, the presence of chlorine in the S2-OCT can be explained by the presence of benzalkonium salt used in the formulation of the O.C.T.<sup>TM</sup> Compound but that only appears in the S2-OCT region. Neither sulphur nor phosphorus were identified in the two regions of contrast of the O.C.T.<sup>TM</sup> Compound. Probably compounds containing these elements are present in such low amounts that they are below the XPS detection limit and cannot be identified. The weak presence of sodium in both analysis spot (see Na KLL Auger emission in Figure 4.13C and Figure 4.13D) can be attributed to salts used in the formulation of the O.C.T.<sup>TM</sup> Compound.

### 4.3.2 Core level spectra analysis from S1 and S2-OCT regions

The high-resolution C 1s and O 1s core level spectra from S1-OCT and S2-OCT regions were also studied in order to identify and quantify the surface chemical bonding states in these two regions. The C 1s and O 1s core level spectra and their corresponding fitting are shown in Figure 4.14.

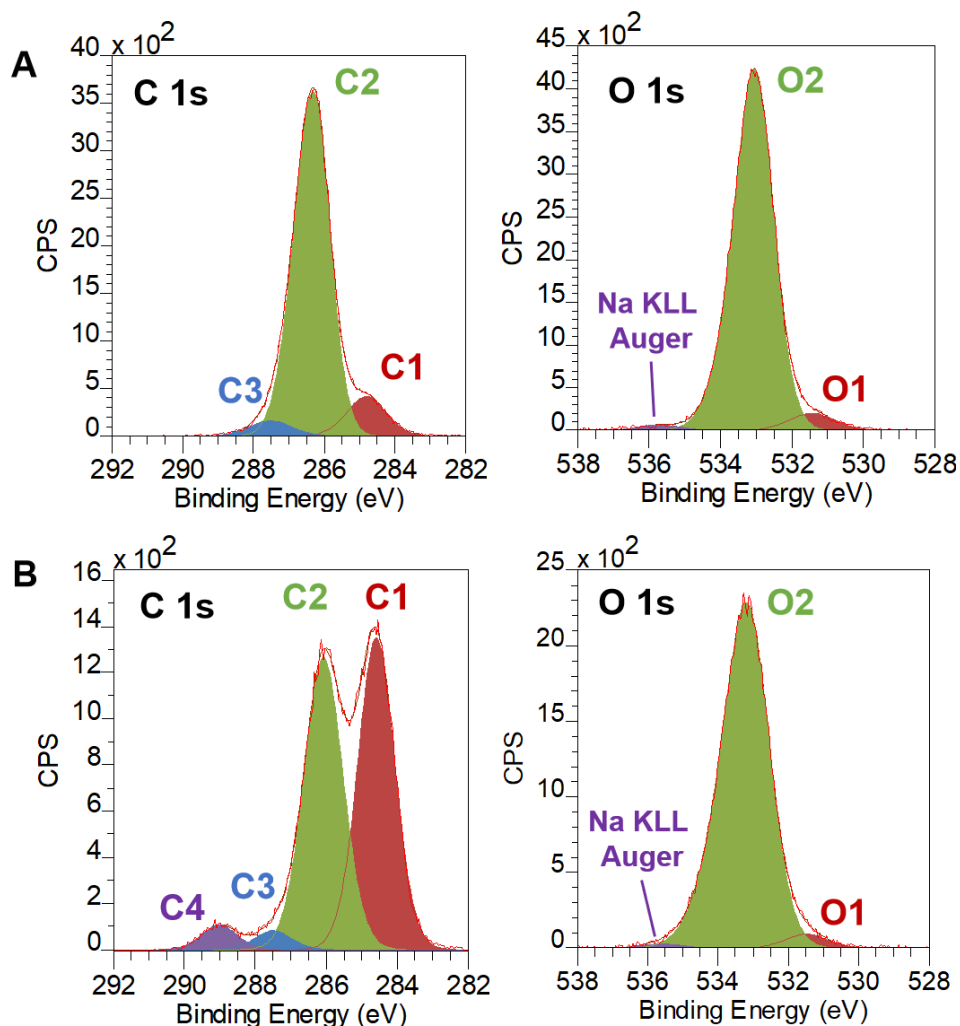


Figure 4.14. Curve fitting of the high-resolution spectra of C 1s and O 1s core levels of (A) S2-OCT and (B) S1-OCT.

The area percentage values for each C 1s and O 1s chemical states are shown below in Table 4.8.

Table 4.8. Peak fitting parameters of high-resolution XPS analysis of S1-OCT and S2-OCT spots on O.C.T.<sup>TM</sup> Compound.

Core level	Position (eV)	Assignment	FWHM	Bonding state	S1-OCT	S2-OCT
					Area (%)	Area (%)
<b>C 1s</b>	284.8	C1	1.2	C-H/C-C/C=C	10.7	47.2
	286.2 – 286.3	C2	1.3	C-O-C/C-OH	85.2	46.1
	287.9 – 288.0	C3	1.2	C=O	4.1	3.2
	289.2	C4	1.2	O=C-OH	–	3.5
<b>O 1s</b>	531.5 – 532.0	O1	1.1	C=O	5.3	4.8
	533.0	O2	1.3	C-O/C-O-C/C-OH	94.7	95.2

A comparative study of the C 1s and O 1s spectra show different bonding states for each region.

#### 4.3.2.1 Chemical state assignments in the S1-OCT region

There are three different carbon bonding states in the S1-OCT region as follows.

- The carbon from hydrocarbon structures (C1: —C—H/—C—C—/—C=C—) at 284.8 eV.
- The carbon from ether or hydroxyl environments (C2: —C—O—C—/—C—OH) at 286.2 eV.
- The carbon from carbonyl environments (C3: —C=O) is identified at 287.9 eV.

The remarkable difference between C1 (10.7 at. %) and C2 (85.2 at. %) amounts and between C2 and C3 (4.1 at. %) amounts indicates that the S1-OCT region is much richer in ether or hydroxyl bonds than hydrocarbon and carbonyl environments. This C2 (85.2 at. %) amount can be associated with a strong presence of glycols such as PEG that present a high concentration of ether bonds in its molecular structure. The low but not negligible C1 (10.7 at. %) amount in the S1-OCT region can be associated with the presence of fatty acids and their long hydrocarbon chains in that same region. The C3 (4.1 at. %) amount associated to carbonyl environments is associated with some other specific compounds present in the composition of the S1-OCT region that was not yet highlighted in our investigations.

Over the O 1s core level spectrum for the S1-OCT region, two different oxygen bonding states are indicated.

- The oxygen from the carbonyl group (O1: —C=O) at 531.3 eV.
- The oxygen from an ether or hydroxyl group (O2: —C—O—C—/—C—OH) at 532.5 eV.

These two O1 (5.3 at. %) and O2 (94.7 at. %) bonding states amounts are in total agreement with the carbon-oxygen states previously found for the C 1s environment. The O2 (94.7 at. %) amount is probably mostly associated with the ether environments present in the PEG structure while the O1 (5.3 at. %) amount remains associated with molecules containing carbonyl environments in its chemical structure that we are currently not sure of. The featuring appearing at higher energies around 536.0 eV is related to the X-ray excited Auger Na KLL emission.

Figure 4.15 below shows the C1, C2 and O2 chemical environments in molecules such as PEG and Palmitic acid already identified in the S1-OCT region.

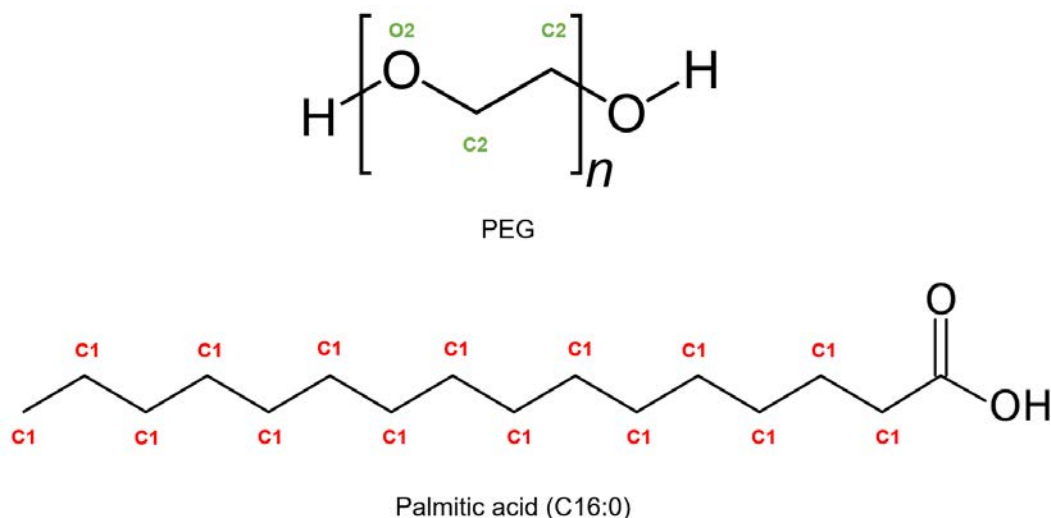


Figure 4.15. Chemical environments of carbon (C1 and C2) and oxygen (O2) identified in molecules such as PEG and Palmitic acid (C16:0) present in the S1-OCT region.

#### 4.3.2.2 Chemical state assignments in the S2-OCT region

Conversely, four different carbon bonding states were found in the S2-OCT region. They are as follows.

- The carbon from hydrocarbon structures (C1: —C—H/—C—C—/—C=C—) at 284.8 eV.
- The carbon from ether or hydroxyl environments (C2: —C—O—C—/—C—OH) at 286.2 eV.
- The carbon from carbonyl environments (C3: —C=O) at 287.9 eV.
- The carbon from carboxyl functionalities (C4: —O=C—OH) at 289.2 eV.

The similarity in C1 (47.2 at. %) and C2 (46.1 at. %) amounts indicates a S2-OCT region almost as rich in hydrocarbon bonds as in alcohol, ether or hydroxyl groups. Similarly, the C3 (3.2 at. %) and C4 (3.5 at. %) amounts indicates that the S2-OCT region is as rich in carbonyl as in carboxyl bonds. This similarity in C1 and C2 amounts might be associated with a strong presence of PVA, a molecule that is strongly balanced in C1 and C2 environments. The C1 environments constituting the benzalkonium chloride molecule might also have a contribution. The C3 and C4 environments are associated with some other specific compounds containing carbonyl and carboxyl environments present in the composition of the S2-OCT region that was not yet highlighted in our investigations.

Over the O 1s core level spectrum for the S2-OCT region, two different oxygen bonding states are indicated.

- The oxygen from the carbonyl and carboxyl groups (O1: —C=O) at 531.3 eV.
- The oxygen from an ether or hydroxyl group (O2: —C—O—C—/—C—OH) at 532.5 eV.

These two O1 (4.8 at. %) and O2 (95.2 at. %) bonding states amounts are in total agreement with the carbon-oxygen states previously found for the C 1s environment. The O2 (95.2 at. %) amount is probably mostly associated with the hydroxyl environments present in the PVA structure while the O1 (4.8 at. %) amount also remains associated with molecules containing carbonyl environments in its structure. The feature appearing at higher energies around 536.0 eV is also due X-ray excited Auger Na KLL emission.

Figure 4.17 below shows the C1, C2 and O2 chemical environments in molecules such as PVA and benzalkonium chloride already identified in the S2-OCT region.

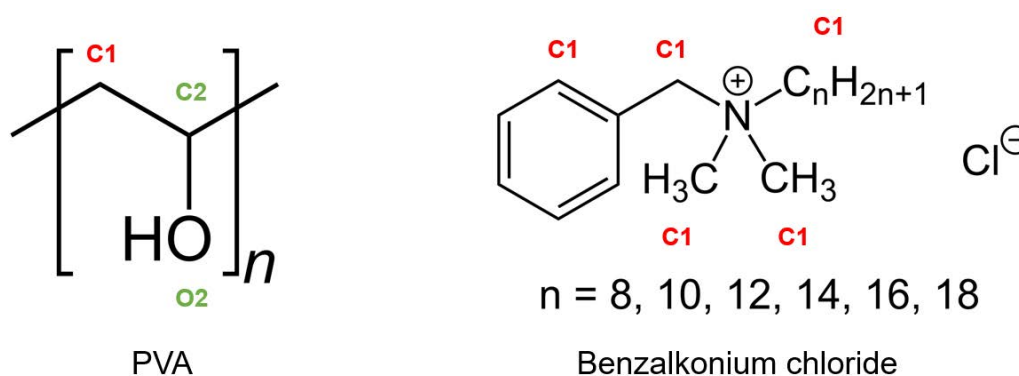


Figure 4.16. Chemical environments of carbon (C1 and C2) and oxygen (O2) identified in molecules such as PVA and Benzalkonium chloride present in the S2-OCT region.

#### 4.3.2.3 Comparison between C 1s and O 1s peak shapes from S1 and S2-OCT regions

Figure 4.17 shows a minimum to maximum normalised overlay of C 1s and O 1s from both S1-OCT and S2-OCT regions where we can better observe the different chemical environments mentioned above in each of these regions.

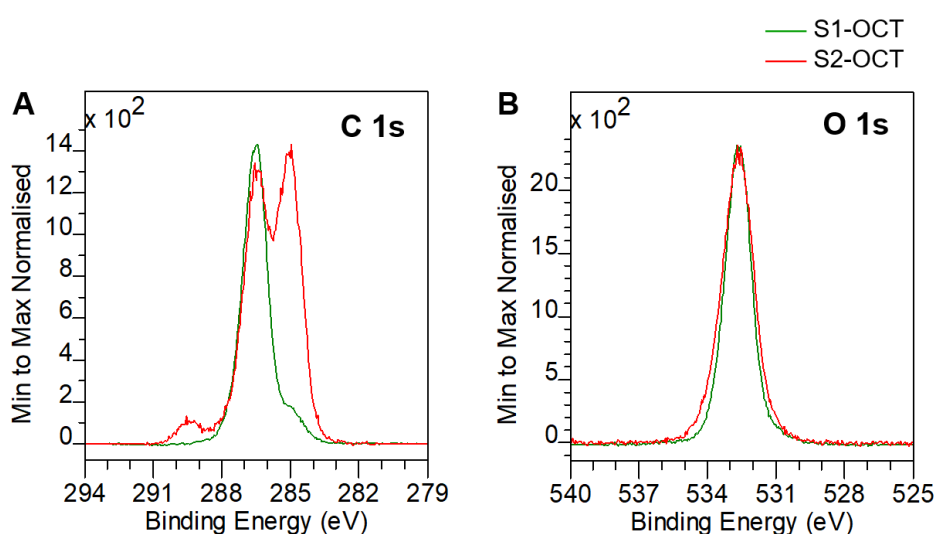


Figure 4.17. Minimum to maximum normalised high-resolution spectra of (A) C 1s and (B) O 1s core levels showing an overlay of S1-OCT (green) and S2-OCT (red) curve shapes.

From the XPS comparison based on the shape of the C 1s and O 1s high-resolution spectra we can see that the differences between the S1-OCT and S2-OCT regions are more associated with the C 1s environments than those of O 1s environments. The O 1s environments found in the S1-OCT and S2-OCT spots of analysis are quite similar for both regions. However, the O1 chemical feature identified in both O 1s core level peaks could only be explained for the S1-OCT region due the presence of fatty acids in this region, whereas no molecular fragments that could explain the O1 feature in the S2-OCT region were previously highlighted by ToF-SIMS.

#### 4.4 HIGH-RESOLUTION CHEMICAL STATE IMAGING OF CHEMICAL FEATURES IN THE RESIN BY X-PEEM

The imaging of the chemical bonding states present in the S1-OCT and S2-OCT was performed by X-PEEM spectromicroscopy, which can reach much smaller lateral scales than available by scanning x-ray photoelectron microprobes or other conventional XPS imaging instruments. In this subsection, we will find the spatial distribution of the main chemical environments present in the S1-OCT region from an area compatible in size with the largest field-of-view (FoV) available from energy-filtered X-PEEM imaging.

##### 4.4.1 Secondary electron PEEM images: identification of the S1 and S2-OCT regions

Figure 4.18 shows how the area of interest for analysis is localized, thanks to (a) the ToF-SIMS image, and (b) a secondary electron image (photoemission threshold spectral region) recorded at the micron scale in a region highlighted by ToF-SIMS imaging on the O.C.T.<sup>TM</sup> Compound.

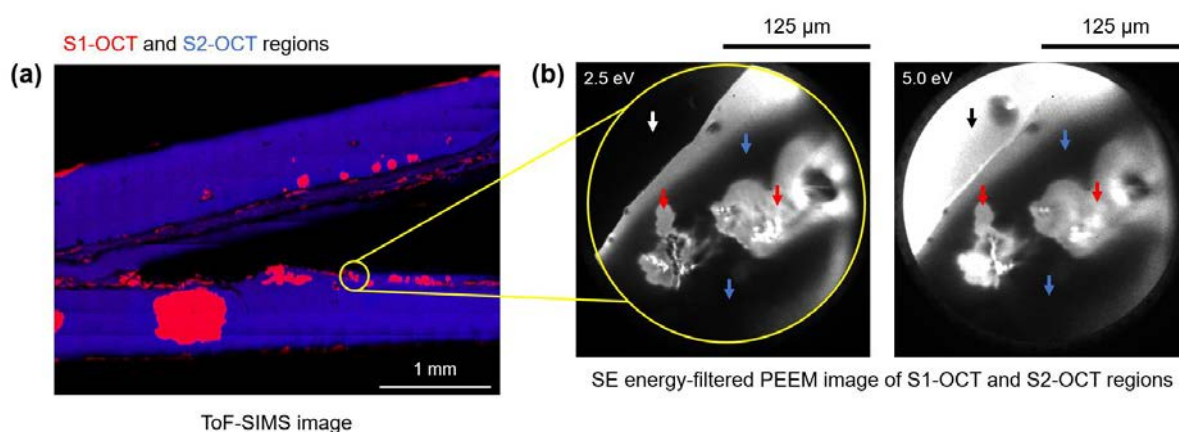


Figure 4.18. Identification of a zone of interest for PEEM analysis from ToF-SIMS image data. (a) ToF-SIMS image highlighting the S1-OCT regions (in red) and the S2-OCT region (in blue). (b) X-ray excited secondary electrons PEEM image at the microscale and at two different  $E-E_f$  energies: 2.5 eV and 5.0 eV from a small S1-OCT region on the O.C.T.<sup>TM</sup> Compound. The white and black arrows indicate the silicon substrate (appearing in dark scales at 2.5 eV and bright scales at 5.0 eV), the red arrows indicate the S1-OCT region (appearing in bright scales at both 2.5 and 5.0 eV) and the blue arrows indicate the S2-OCT region (appearing in dark scales at both 2.5 and 5.0 eV in the secondary electron image).

The gray-scale contrast seen in Figure 4.18(b) is due to the local work function (or surface potential) variations attributed to the different chemical composition found in the S1-OCT and S2-OCT regions according to both ToF-SIMS and XPS analyses. If we assume that the work function dominates the observed image, this means that the S1-OCT region has a lower work function than S2-OCT region and that is why it appears in brighter scales (see the red arrows in Figure 4.18(b)). This assumption is in agreement with the contrast seen in the silicon substrate region that appears in darker scales at 2.5 eV and in brighter scales at a much higher work function energy (5 eV).

A similar contrast on X-PEEM images of biological systems was observed in recent works [117] and it was found useful to discriminate chemically different regions at the micron scale. We must however keep in mind that charging is might have occurred in the present case, as seen from two experimental observations: first, the shift of the photoemission threshold to very low electron energies. Indeed, it is observed usually that an electrically conductive surface covered with hydrocarbons arising from air exposure shows up work function values around 3-3.5 eV (observed for the silicon region), which is much higher than the photoemission threshold well below 2.5 eV observed on the PEEM image of Figure 4.18(b) for the S1-OCT region. The second observation indicative of charging is, possibly, the dark halo surrounding the bright S1-OCT-related features of the PEEM image: although here, the effect of the pronounced topography (resulting from distortions of the strong surface electrical field induced by the extractor lens) may explain this contrast as well, we can assume that differential charge distributions over the surface would result in similar lateral changes of the electric field, thereby creating such dark regions on the image. In summary, we cannot totally exclude that charging and even maybe differential charging, was happened during the X-PEEM measurement. However, we will see in the next sub-section that, would this be the case, it would not hamper a proper laterally-resolved chemical-state determination.

#### **4.4.2 Core level X-PEEM images: chemical state analysis**

Similar energy-filtered (spectromicroscopic) analysis was performed across the characteristic C 1s and O 1s core level peaks acquired in these regions. The details of the acquisition are given in Table 4.9.

As raw signal-to-noise in each pixel from the images acquired is too low to meaningfully work with spectra at pixels, the corresponding datasets were post-processed using first an Outlier Filter and then PCA noise reduction to produce spatially resolved spectra of sufficient quality to perform X-PEEM spatially resolved quantification. The idea is that the Outlier Filter will remove much of the anomaly in terms of pixel intensity due to noise and systematic errors in the pixels and the PCA noise reduction will replace the resulting image by a linear combination of the most significant abstract factors.

Table 4.9. Experimental details of core level PEEM spectra acquisition.

	Core levels	
	C 1s	O 1s
<b>Spectrum acquisition order</b>	2 <sup>nd</sup>	1 <sup>st</sup>
<b>Energy range</b>	282 – 292 eV	528 – 538 eV
<b>Steps</b>	0.1 eV	0.1 eV
<b>Scans</b>	30 scans	30 scans
<b>Total time of analysis</b>	8 hours	8 hours

#### 4.4.2.1 C 1s high-resolution X-PEEM results

We start by presenting the C 1s X-PEEM results as they enable a direct identification of the S1- and S2-OCT regions. In Figure 4.19(a) we can see a PEEM image showing the lateral distribution at the micron scale of the integral intensity of the post-processed C 1s spectra related to S1-OCT and S2-OCT regions. A False Colour scale was used to assign colours to ranges of pixels intensities. This allows sets of pixels with similar intensities to be identified and then used to create spectra by summing spectra-at-pixel from pixels with the same false colour. We can observe that the clear separation between S1- (blue pixels) in the centre and S2-OCT (red pixels) in the surroundings in the O.C.T.<sup>TM</sup> Compound is coherent with the bright and dark scales found in the X-ray excited SE PEEM image at 2.5 eV (see Figure 4.19(b)).

In Figure 4.19(c) we can see the spectra generated from the C 1s spectra summation of the blue and red pixels for the S1- and S2-OCT regions, respectively.

The chemical differences highlighted by C 1s high-resolution core level mapping in the zone of interest is in complete agreement with the assignment of the coloured areas to the S1-OCT and S2-OCT regions of the O.C.T.<sup>TM</sup> Compound. This is further confirmed by the peak shape of the C 1s spectra: we can observe the similarity between the C 1s high-resolution (see Figure 4.19(C)) and the C 1s high-resolution spectra acquired by XPS analysis from a spot inside the S1-OCT and S2-OCT regions (see Figure 4.14). Indeed, we observe for S1-OCT a single, broad peak, whereas for S2-OCT, two distinct peaks are detected. This is a confirmation of our initial assignment from the X-PEEM image, of the two-coloured areas.

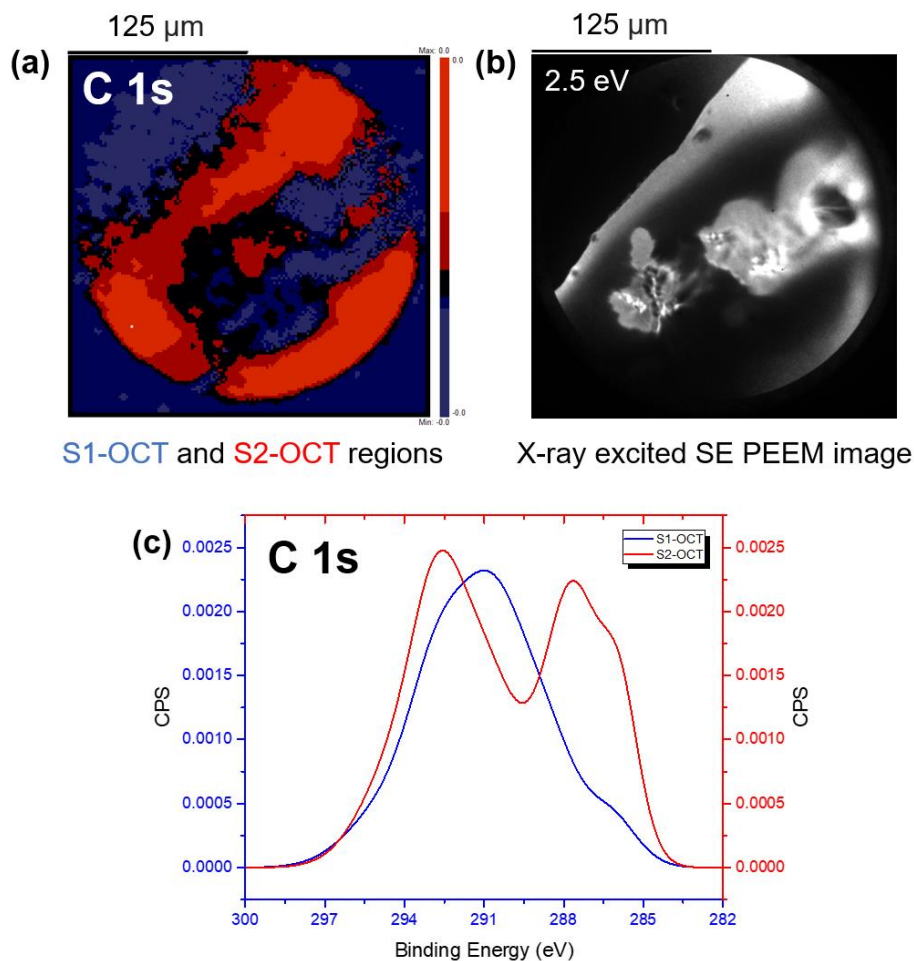


Figure 4.19. (a) X-PEEM image showing the lateral distribution at the micron scale of the integral intensity of the post-processed C 1s spectra over the region of interest. (b) X-ray excited secondary electrons PEEM image at the microscale and at  $E-E_F = 2.5$  eV from the area of interest (S1- and S2-OCT regions) in the O.C.T.<sup>TM</sup> Compound. (c) C 1s spectra generated from the summation of the blue and red pixels for the S1- and S2-OCT regions, respectively.

In the following we tentatively tried to perform the chemical-state assignment of the summed spectra-at-pixels from S1- and S2-OCT regions by discussing the overall broadening of the peaks: we see two spectral characteristics possibly related to charging effects: (1) a large broadening observed in the X-PEEM C 1s high-resolution spectra that can be a limiting factor in the fitting of component peaks representative of chemical environments present in both S1- and S2-OCT regions and (2) an overall binding energy shift for both spectra, as compared to the XPS spectra – the energy range for the X-PEEM C 1s spectra for both S1-OCT and S2-OCT regions is extending up to nearly 299 eV (compared to 291 eV for the XPS spectra) and that is directly related to the magnitude of the positive surface potential which builds-up upon photoemission: this can be an effect of the long-time of exposure to X-rays of the poorly-conductive organic surface during analysis, resulting in surface charging. We can quantify this energy shift by comparing the peak energy to the XPS case (Figure 4.14), and we see that this shift is relatively small (around 1.5 eV), meaning that the charge build-up during XPEEM analysis is limited. However, these charging effects are indeed difficult to cope with because no charge compensation system (such as an electron flood gun) is available on the X-PEEM setup.

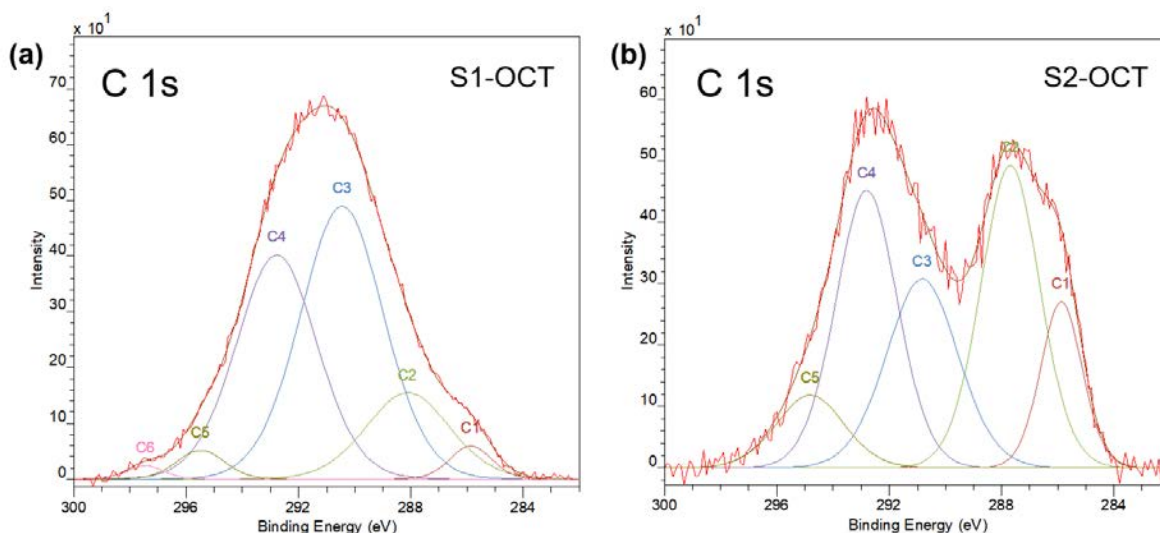


Figure 4.20. Curve fitting of the C 1s X-PEEM high-resolution spectra highlighting the chemical environments present in the (a) S1-OCT and (b) S2-OCT regions.

In Figure 4.20, we tentatively present a peak fitting of the X-PEEM C 1s spectra for each zone and observe that, there are more components identified (C1, C2, C3, C4, C5 and C6) than those found in the XPS spectra (C1, C2, C3 and C4, Figure 4.14). We can observe that after calibrating the C1 component at 284.8 eV the other components are found severely shifted to higher energies. Due to the broadening of the X-PEEM C 1s spectra, the component peaks are also broadened with respect to the XPS case.

Table 4.10 below shows the peak fitting parameters for C 1s high-resolution acquired from S1-OCT and S2-OCT regions through X-PEEM imaging.

Table 4.10. Peak fitting parameters for C 1s high-resolution X-PEEM spectra of S1-OCT and S2-OCT regions on the O.C.T.<sup>TM</sup> Compound.

Core level	Position (eV)	Assignment	FWHM	S1-OCT	S2-OCT
				Area (%)	Area (%)
C 1s	284.8	C1	1.7-2.2	2.7	11.4
	286.6-287.3	C2	2.5-3.5	14.1	30.0
	289.4-289.6	C3	2.8-3.5	44.3	19.7
	291.5-291.7	C4	2.7-3.4	35.4	31.7
	293.8-294.4	C5	2.0-2.8	2.6	7.4
	296.4	C6	1.5	0.9	–

One of the possible interpretations for XPEEM C 1s spectra is the determination of the C1 and C2 as components representative of the same chemical environment but which can be identified separately due to shifts to high energies probably caused by charging effects after long exposure of the region of interest to X-ray – note that the acquisition of the C 1s high-resolution spectrum happens after the O 1s acquisition as indicated in Table 4.9, that is, when the C 1s high-resolution spectrum acquisition is

performed the surface is already exposed to x-rays for more than 8 hours. The same behaviour can be observed for C3 and C4 as well as for C5 and C6 (in the C 1s spectra of the S1-OCT region).

#### 4.4.2.2 O 1s high-resolution X-PEEM results

We now address the O 1s X-PEEM results. In Figure 4.21(a) we can see a PEEM image showing the spatial distribution at micron scale of the integral intensity of the post-processed O 1s spectra related to S1-OCT and S2-OCT regions. A False Colour scale was also used here to assign colours to range of pixels intensities. We can observe that the clear separation between S1- (blue pixels) in the centre and S2-OCT (red pixels) in the surroundings in the O.C.T.<sup>TM</sup> Compound is also coherent with the bright and dark scales found in the X-ray excited SE PEEM image at 2.5 eV (see Figure 4.21(b)). In Figure 4.21(c) we can see the spectra generated from the O 1s spectra summation of the blue and red pixels for the S1- and S2-OCT regions, respectively.

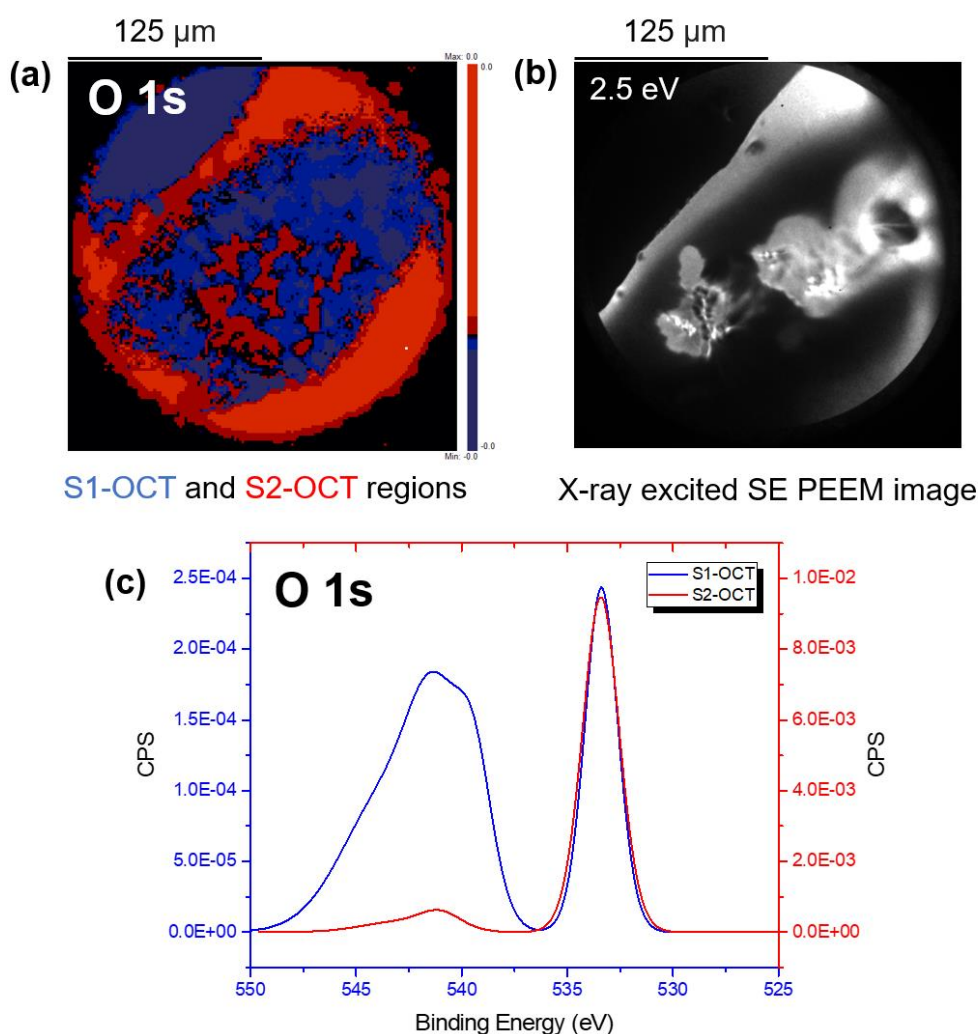
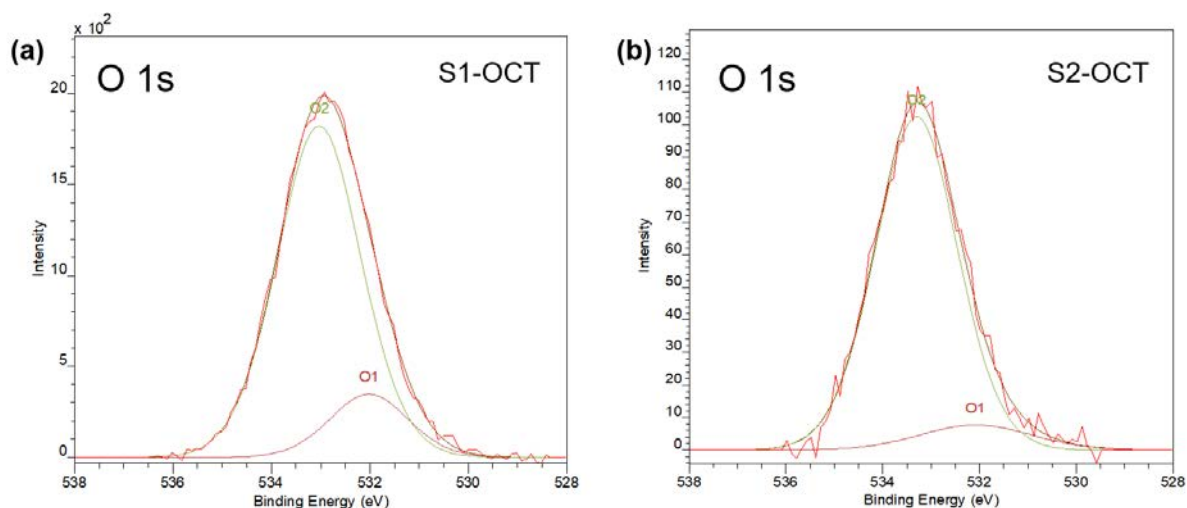


Figure 4.21. (a) X-PEEM image showing the lateral distribution at the micron scale of the integral intensity of the post-processed O 1s spectra over the region of interest. (b) X-ray excited secondary electrons PEEM image at the microscale and at  $E-E_f = 2.5$  eV from the area of interest (S1- and S2-OCT regions) in the O.C.T.<sup>TM</sup> Compound. (c)

*O 1s spectra generated from the summation of the blue and red pixels for the S1-OCT and S2-OCT regions, respectively.*

The chemical differences highlighted by O 1s high-resolution core level mapping in the zone of interest is also in agreement with the assignment of the coloured areas to the S1-OCT and S2-OCT regions of the O.C.T.<sup>TM</sup> Compound. This is confirmed by the peak shape of the O 1s spectra: if we disregard the peak appearing at higher energies associated with the Auger Na KLL emission, we can observe the similarity between the O 1s high-resolution (see Figure 4.21(c)) and the O 1s high-resolution spectra acquired by XPS analysis from a spot inside the S1-OCT and S2-OCT regions (see Figure 4.14).

In this case, charging effects such as peak broadening and overall binding energy shift seem to be less pronounced in the O 1s X-PEEM spectra. Note that the energy range for the O 1s X-PEEM high-resolution spectra for both S1-OCT and S2-OCT regions is placed between 529 eV and 536 eV in a very similar way we can find in the XPS case (Figure 4.14). The wide peak appearing at higher energies might be associated with the Auger Na KLL emission; however, the much higher energy of this Na KLL X-PEEM peak (540 eV) tells us that a pronounced charging effect has occurred in the region where the salt residues are present.



*Figure 4.22. Curve fitting of the O 1s X-PEEM high-resolution spectra highlighting the chemical environments present in the (a) S1-OCT and (b) S2-OCT regions.*

In Figure 4.22 we present a peak fitting of the O 1s X-PEEM spectra for each S1- and S2-OCT regions and observe that, the same components identified in the XPS case (O1 and O2) are also identified here. Table 4.11 below shows the peak fitting parameters for O 1s high-resolution acquired from S1-OCT and S2-OCT regions through X-PEEM imaging. The relative intensity difference between O1 and O2 for the S1-OCT region seen in X-PEEM spectra, however, is much clearer: this can be attributed to the higher spatial resolution of X-PEEM compared to the more localized spectroscopic character of the XPS analysis.

Table 4.11. Peak fitting parameters for O 1s high-resolution X-PEEM spectra of S1-OCT and S2-OCT regions on the O.C.T.<sup>TM</sup> Compound.

Core level	Position (eV)	Assignment	FWHM	S1-OCT	S2-OCT
				Area (%)	Area (%)
O 1s	532.0-532.1	O1	2.0-2.7	15.1	8.5
	533.0-533.3	O2	2.0	84.9	91.5

In general, the results suggest that the good agreement between the O 1s high-resolution spectra acquired by X-PEEM and XPS analysis may be explained by the experimental steps followed to apply the X-PEEM imaging (Table 4.9). Initially, X-PEEM high-resolution spectrum of the O 1s was acquired over the region of interest. As X-PEEM high-resolution spectra can only be acquired one at a time, after 8 hours of O 1s spectrum acquisition, the high-resolution C 1s spectrum was then acquired during 8 more hours over the same zone of interest that had already been exposed to the acquisition time of the O 1s spectrum. As the O 1s spectrum was the first X-PEEM high-resolution spectrum to be obtained, the area of interest did probably not yet have a history of long exposure to X-rays and consequently the charging effects were not as pronounced at the time of analysis. However, when the C 1s spectrum was acquired, it was possible that a pronounced charge effect was already present on the surface of the zone of interest, so the consequent high broadening and shifting to higher energies of the C 1s X-PEEM high-resolution spectra as well as the limitations imposed by the peak broadening in the fitting of component peaks were unavoidable.

## 4.5 MULTIMODAL APPROACH DISCUSSION

The use of ToF-SIMS macro-imaging was a fundamental tool in the chemical mapping of the O.C.T.<sup>TM</sup> Compound. Using ToF-SIMS imaging we were able to distinguish silicon substrate from biological tissue embedded in the O.C.T.<sup>TM</sup> Compound, as well as identifying chemically contrasted regions of interest (ROIs) for multimodal analysis that were labelled as S1- and S2-OCT regions. In addition to identifying the existence of compounds such as ammonium persulfate, epoxidized linseed oil and benzalkonium chloride in the O.C.T.<sup>TM</sup> Compound, the S1- and S2-OCT ROIs are distinguished by a wide variety of simple and oxygenated organic compounds. In the latter case, the interpretation of the differences between these two regions based only on these simple and oxygenated organic fragments is almost impossible and presents a specific difficulty of the ToF-SIMS analysis since no quantitative information is provided.

To validate the assignment of m/z identified in ToF-SIMS, Tandem MS was applied in the study of the fragmentation of the ion fragment at m/z 255.22, characteristic of the palmitic acid present in the composition of the epoxidized linseed oil. Thanks to this, we could confirm the existence of fatty acids such as the palmitic acid in the S2-OCT region in the O.C.T.<sup>TM</sup> Compound. The navigation in Tandem MS was not considered difficult mainly because a large FoV comparable to that used in ToF-SIMS

navigation is available as well as the possibility of acquiring macro images, which strongly contribute to find the same ROIs previously highlighted in ToF-SIMS exploration.

On the other hand, the difficulty in reoperating ROIs highlighted by ToF-SIMS and Tandem MS in XPS microscopy can be considered moderate mainly because although almost no contrast is generated on the surface of the O.C.T.<sup>TM</sup> Compound while using scanning x-ray image (SXI), the maximum field of view (FoV) of  $1350 \times 1350 \mu\text{m}^2$  allows for a wide view of landmarks in the sample that facilitates the XPS navigation. The reoperation and analysis of these same regions using XPS brings us the complementary quantitative information about the S1- and S2-OCT areas. Survey and high-resolution XPS spectra indicate a high number of chemical environments associated with ethers and hydroxyls in the S1-OCT region, while similar proportions of hydrocarbons and ethers and hydroxyls are indicated in the S2-OCT region. This quantitative information brings to light the real distribution of simple and oxygenated organic compounds evidenced by ToF-SIMS. Furthermore, it reiterates the assertion that fatty acids are present in the S2-OCT region due to its higher amounts of hydrocarbons associated to the long hydrocarbon chains of fatty acids in comparison with the hydrocarbon amount found in the S1-OCT region.

The difficulty in reoperate regions of interest for PEEM analysis is initially associated with the narrow FoV of about  $250 \mu\text{m}$  of diameter available for navigation. However, this situation can be overcome if we have the option to choose ROIs compatible in size with the narrow PEEM. In addition, the surface of the O.C.T.<sup>TM</sup> Compound behaves relatively well during navigation and exposure to X-rays and no charging effects were initially observed. This allowed PEEM navigation to rely on work function contrasts to find ROIs. The X-PEEM C 1s high-resolution spectra secondly acquired show extra components located at higher energies if compared with XPS spectra. However, we can still say that the same bonding states found in the XPS analyses (C1, C2, C3, C4) were also found by X-PEEM analysis. Nevertheless, in the X-PEEM O 1s high-resolution spectra acquired before the C 1s spectra, we can find the same O1 and O2 components found in the XPS analyses. Besides that, the difference of relative intensity of these components is much clearer in the X-PEEM analyses and can be attributed to the higher spatial resolution of X-PEEM compared to the more localized spectroscopic character of the XPS analysis. The results suggest then that the good agreement between the X-PEEM O 1s spectra and the XPS O 1s spectra may be explained by order of spectra acquisition in the X-PEEM experiment. This is a strong indication that the second analysis is strongly affected by the charging effects (peak broadening and shift to higher energies).

In summary, the ToF-SIMS and Tandem MS results complement each other in providing a molecular mapping and identification of ROIs on surfaces with more accurate m/z assignments. On the other hand, XPS and X-PEEM provide quantitative information about chemical environments present in contrast regions useful in describing differences especially when the regions of interest have similar molecular composition. In fact, the correlation between molecular information provided by ToF-SIMS and Tandem MS, and chemical environment information locally provided by XPS and laterally resolved provided by X-PEEM for both S1- and S2-OCT regions indicate a strong consistency in the output information of

these four complementary techniques. The summary of the coherences and incoherent aspects found in our multimodal approach applied to biological tissues can be found below in Table 4.12.

Table 4.12. Coherent and incoherent aspects of our multimodal ToF-SIMS, Tandem MS, XPS and X-PEEM approach for analysis of O.C.T.<sup>TM</sup> Compound.

Advantages	Disadvantages
ToF-SIMS macro imaging allows visualization of ROIs showing chemical contrast on the surface of the O.C.T. <sup>TM</sup> Compound	ToF-SIMS, Tandem MS, XPS and X-PEEM have different FoV sizes
ToF-SIMS has the ability to identify simple and oxygenated organic compounds among other compounds in different ROIs in a same sample	Impossible to perform interpretation of distinct chemical contrast regions based on similar molecular fragments acquired by ToF-SIMS
Tandem MS allows to refine the assignment of molecular ions found in the ToF-SIMS mass spectrum by the fragmentation of a specific m/z	Moderate difficult in reoperate ROIs highlighted by ToF-SIMS and analysed by Tandem MS in XPS
Easy reoperation of ROIs highlighted by ToF-SIMS in Tandem MS	Reoperation of the same ROIs by XPS and PEEM is not trivial due to its smaller FoV
PEEM imaging on the O.C.T. <sup>TM</sup> Compound is feasible and consistency between XPS and X-PEEM core-levels indicates surface stability during the first analysis	The surface of the O.C.T. <sup>TM</sup> Compound is easily charged after the first 8 hours of X-PEEM core level analysis and charging effects such as peak shifting and broadening are then frequently seen

## 4.6 CONCLUSIONS

In this second level of sophistication of application of our multimodal surface analysis approach, we made a step forward in the correlation of chemical surface analysis techniques such as ToF-SIMS, Tandem MS, XPS and PEEM in the analysis of regions of interest (ROIs) in a same organic sample. We observed how the use of ToF-SIMS allowed us to map a large area on the O.C.T.<sup>TM</sup> Compound hosting a biological tissue. Besides that, we were able to identify regions over the organic compound itself showing chemical contrasts. These were ROIs compatible in size with the field of view (FoV) of other analytical methods and consequently good for correlative analysis. Although the two ROIs (S1-OCT and S2-OCT) identified in the O.C.T.<sup>TM</sup> Compound were found to be basically constituted of hydrocarbons and oxygen-containing ions, the identification and mapping of other compounds possibly present in these regions such as benzalkonium chloride, ammonium persulfate and epoxidized linseed oil gives us a better idea of the composition of this organic material and how heterogeneous these molecular groups

are distributed spatially. Tandem MS proved to be an essential tool in confirming the existence of certain molecules in the composition of the O.C.T.<sup>TM</sup> Compound. Through the analysis of the fragmentation of a molecule at  $m/z$  255.23 we were able to prove that it is the palmitic acid that is present within the S1-OCT region, thus providing an adequate explanation for the origin of certain hydrocarbons and oxygen-containing ions already identified within the S1-OCT region and also discarding any possibility of overlapping and incorrect assignment of peaks.

From the XPS analysis we could quantify the chemical environments present in the S1-OCT and S2-OCT regions. The high-resolution C 1s and O 1s spectra suggest that the S1-OCT region is richer in functional groups such as ether and hydroxyl compared to hydrocarbon and carbonyl groups and this may be an indication that this region is richer in glycols such as PEG, while the S2-OCT region has a balance between hydrocarbons and ether and hydroxyl environments, thus being an indication of a region rich in alcohols such as PVA.

Once the chemical environments present in the S1-OCT and S2-OCT regions were properly quantified by XPS analysis, we took a step further in trying to image the chemical environments in these regions. With the limitation of the field-of-view for energy-filtered PEEM image analysis around 230  $\mu\text{m}$ , we should decide for a smaller region of analysis but that still has a chemical contrast between these two regions. An important aspect of XPS analysis is that we are able to obtain high-resolution spectra of a single 200  $\mu\text{m}$  spot on the sample lasting about 40 minutes. However, the spectromicroscopic analysis performed by PEEM in energy filtered PEEM imaging mode last around 6-8 hours for each high-resolution spectrum. So, the long exposure of the surface of interest for analysis to X-rays may be a fundamental factor contributing for the broadening and shifting to higher energies of high-resolution spectra and a complication in creating reliable fitting models aiming to highlight chemical environments present in these regions. Nevertheless, in more general terms despite the peaks broadening we were able to obtain curves for the C 1s and O 1s high-resolution spectra similar to those obtained by XPS.

In other words, we can conclude that our multimodal surface analysis approach is compatible with the analysis of a same organic sample with some caveats. Positive aspects in our multimodal surface analysis approach applied to the analysis of the O.C.T.<sup>TM</sup> Compound include:

- ToF-SIMS macro imaging allows visualization of ROIs showing chemical contrast on the surface of the O.C.T.<sup>TM</sup> Compound
- ToF-SIMS has the ability to identify simple and oxygenated organic compounds among other compounds in different ROIs in a same sample
- Tandem MS allows to refine the assignment of molecular ions found in the ToF-SIMS mass spectrum by the fragmentation of a specific  $m/z$
- Easy reoperation of ROIs highlighted by ToF-SIMS in Tandem MS
- PEEM imaging on the O.C.T.<sup>TM</sup> Compound is feasible and consistency between XPS and X-PEEM core-levels indicates surface stability during the first analysis

The negative aspects in our multimodal surface analysis approach applied to O.C.T.<sup>TM</sup> Compounds include:

- ToF-SIMS, Tandem MS, XPS and X-PEEM have different FoV sizes
- Impossible to perform interpretation of distinct chemical contrast regions based on similar molecular fragments acquired by ToF-SIMS
- Moderate difficulty in reoperating ROIs highlighted by ToF-SIMS and analysed by Tandem MS in XPS
- Reoperation of the same ROIs by XPS and PEEM is not trivial due to its small FoV
- The surface of the O.C.T.<sup>TM</sup> Compound is easily charged after the first 8 hours of X-PEEM core level analysis and charging effects such as peak shifting and broadening are then frequently seen

In summary, the main objective of this chapter, which was to apply a second level of sophistication in multimodal surface chemical imaging in the analysis of a same organic sample, was achieved. This approach shows the generated ability to re-operate the same sample using different techniques and paves the way for the application of the same approach in the analysis of biological samples.



## **5 MULTIMODAL TOF-SIMS, XPS AND X-PEEM APPROACH FOR SURFACE CHEMICAL ANALYSIS OF BRAIN AND GLIAL SCAR TISSUES IN CONTACT WITH IMPLANTABLE BIOMEDICAL TECHNOLOGIES**

---

In this fifth chapter, we will see the third level of application of our multimodal surface imaging approach over rodent and primate non-human brain tissues aiming to investigate the same zone of interest for analysis. The biological tissues discussed here were in close contact with implantable biomedical technologies such as HA hydrogel (drug delivery vehicle) and intracranial devices. The rodent's brain was the one that underwent a HA hydrogel implantation surgery for acting as a drug delivery vehicle in the treatment of glioblastoma. This HA hydrogel remained implanted for three months in its brain. The process of preparation of the rat brain tissue with hydrogel for surface analysis was previously described in section 2.2.3. The main interest in the analysis of the rodent's brain hosting the HA hydrogel is to find out if there is still HA hydrogel remaining even after the implantation period and if there has been any infiltration of this hydrogel to other regions of the brain that should not be affected. The analytical approach used to answer these questions is based on ToF-SIMS imaging. On the other hand, the non-human primate's brain underwent surgery for implantation of an intracranial device commonly used in the translation of electrocorticographic (EcoG) signals used in brain-computer interfaces (BCI). This intracranial device remained implanted in the non-human primate's brain for twelve months. The process of preparation of the non-human primate's brain and brain sectioning for surface analysis was also previously described in section 2.2.4. The main interest in analysing sections of the non-human primate's brain is to discover a possible explanation for the triggering of an acute inflammatory reaction that allowed the formation of a thick glial scar tissue around the intracranial device preventing then its functioning. In this case, we will perform our multimodal ToF-SIMS, XPS and X-PEEM surface imaging approach to investigate its interfaces. A schematic view of the rodent's and non-human primate's brain and their tissue sections of interest for analysis can be seen in Figure 5.1.

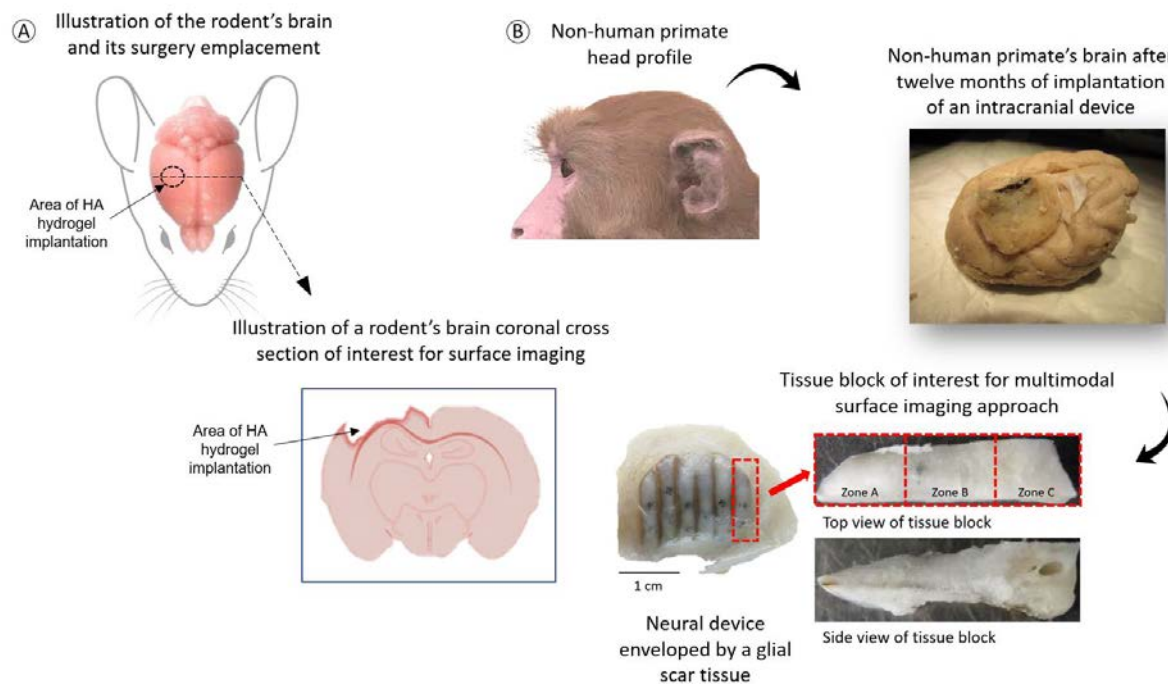
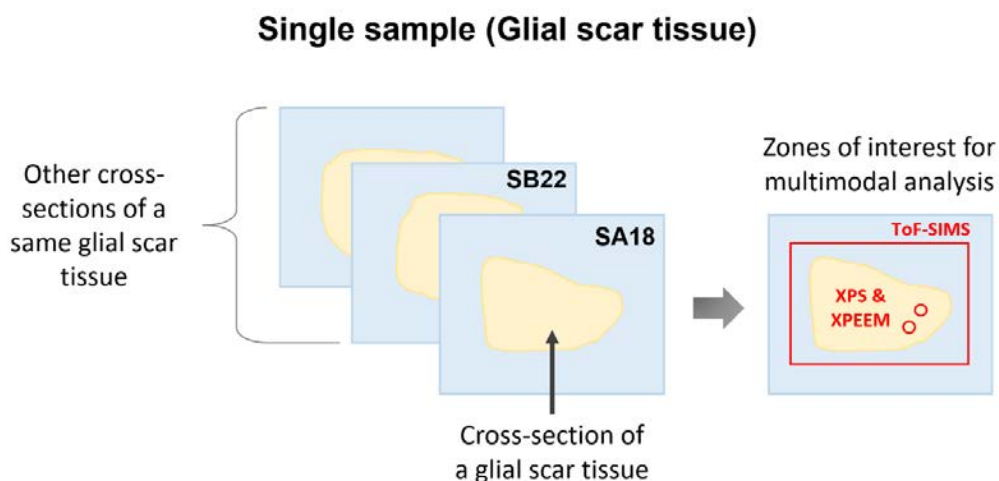


Figure 5.1. (A) Schematic view of a rodent's brain showing the area of implantation where hyaluronic acid (HA) hydrogel remained implanted for three months as well as an illustration of a brain coronal cross section of interest for surface imaging analysis. (B) A non-human primate head profile followed by a picture of a primate's non-human brain after hosting an intracranial device for one year enveloped by a thick fibrotic or glial tissue. The next picture shows the glial tissue block of interest for multimodal surface imaging approach.

In the first section (5.1), we firstly introduce the main characteristic of a rodent's brain. Then, we move on to the second section (5.2) and see how ToF-SIMS image analysis is a fundamental tool in detecting and mapping out HA hydrogel that remained implanted after three months of surgery in a rodent's brain tissue. In the third section of this chapter (5.3), we introduce what is a glial scar tissue and explain its formation around implantable medical devices. Then, we will move to the application of our multimodal ToF-SIMS, XPS and X-PEEM surface imaging approach on a glial scar tissue formed around an intracranial device after twelve months of implantation in a non-human primate's brain. Apart from using ToF-SIMS imaging to analyse coronal cross-sections of a rodent's brain tissue, our multimodal surface imaging approach focused on the analysis of a single sample, a cross section of a glial scar tissue formed around an intracranial device, and on the same area of interest for multimodal analysis. Figure 5.2 shows a schematic view of the same zone of interest on a same biological tissue. The exact location of these tissue slices with respect to the intracranial device can be seen in the section "Glial scar tissue and scheme of tissue cross section's location" in the appendix.



*Figure 5.2. Schematic view of cross sections of a glial scar tissue formed around an implanted intracranial device on non-human primate's brain. This is the single sample where multimodal ToF-SIMS, XPS and X-PEEM surface imaging will be performed over a same zone of interest. Other cross-section tissues will be occasionally analysed. In red we can see the zone of interest for analysis for each of analytical methods used.*

In the fourth section (5.4), we show ToF-SIMS imaging allied to principal component analysis (PCA) is a fundamental tool in highlighting the main biomolecules present in glial scar tissues and how this approach can help in identifying zones of chemical contrast in glial scar tissues. Furthermore, we show the high sensitivity of the ToF-SIMS analysis allows us to identify metals in the glial scar tissue thus raising the hypothesis of tissue contamination by contact with metallic components used to build the intracranial device. This could explain the acute inflammatory reaction triggered in the neural tissue after the implantation of the intracranial device. In the fifth section (5.5), we see how XPS is a fundamental tool in the identification and quantification of chemical environments in regions of the glial scar tissue that presents chemical contrasts. In the sixth section (6) we see the use of X-PEEM in the imaging of the different chemical contrast environments in the glial scar tissue. In the seventh section (5.7) we present a detailed discussion about the multimodal ToF-SIMS, XPS and XPEEM approach applied in the analysis of a rodent's brain tissue and a glial scar tissue formed on a non-human primate brain. Conclusions for this chapter are given in the eighth section (5.8).

## 5.1 BRAIN TISSUE

A rodent's brain tissue has basically the same structure of brains as others animals found inside the mammalian class. In terms of anatomy, the brain together with the spinal cord constitute the central nervous system (CNS) of the mammals. Both brain and spinal cord are made up nerve cells called neurons, and supporting cells called glial cells (astrocytes and oligodendrocytes). A typical neuron consists of a cell body and two sets of additional compartments. One of these sets are called axon; their job is to transmit information from the neuron on to others to which it is connected. The other set are called dendrites; their job is to receive the information being transmitted by the axons of other neurons. Both participate in the specialised contacts called synapses. The glial cells, on the other hand, long

thought to have purely supporting function to the neurons, are known to make an important contribution to the development of the CNS and to its function in the adult brain. While much more numerous, the glial cells do not transmit information in the way that neurons do [204]. The organization of these cells contributes to the existence of two major components in the brain: the gray matter and the white matter. The gray matter is the major component of the CNS, consisting of neuronal cell bodies, dendrites and unmyelinated axons, glial cells, synapses, and capillaries. The white matter, on the other hand, contains relatively few cell bodies and is composed chiefly of long-range myelinated axons [205]. The colour association arises mainly from the whiteness of myelin that is rich in cholesterol. Figure 5.3 shows the distribution of gray and white matters in a brain coronal cross-section.

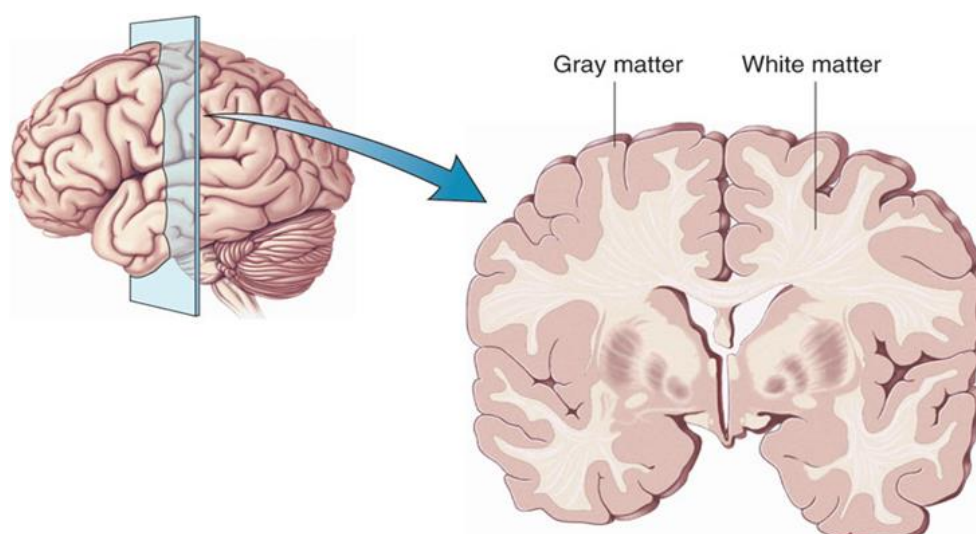


Figure 5.3. Brain coronal section showing the distribution of the gray and white matters. [206]

## 5.2 IMAGING HYDROGEL IN A RODENT'S BRAIN CORONAL SECTION BY TOF-SIMS

Given the successful application of ToF-SIMS imaging in the chemical mapping of ketorolac tromethamine and gellan gum microcapsules in HA hydrogel in Chapter 3, in this section we use the same ToF-SIMS imaging approach in the imaging of a rodent's brain tissue after 3 months of undergoing cortectomy surgery for HA hydrogel implantation as a drug delivery vehicle in the treatment of glioblastoma. The main interest in the analysis of a rodent's brain hosting the HA hydrogel is to find out if there is still hydrogel remaining even after the implantation period and if there has been any infiltration of the hydrogel to other regions of the brain that should not be affected.

### 5.2.1 Imaging of the main chemical structures present in the cortectomy region

Figure 5.4 shows the lateral signal intensity distributions of selected negative ions peaks from a coronal brain tissue section showing the surgical area after 3 months of HA hydrogel implantation.

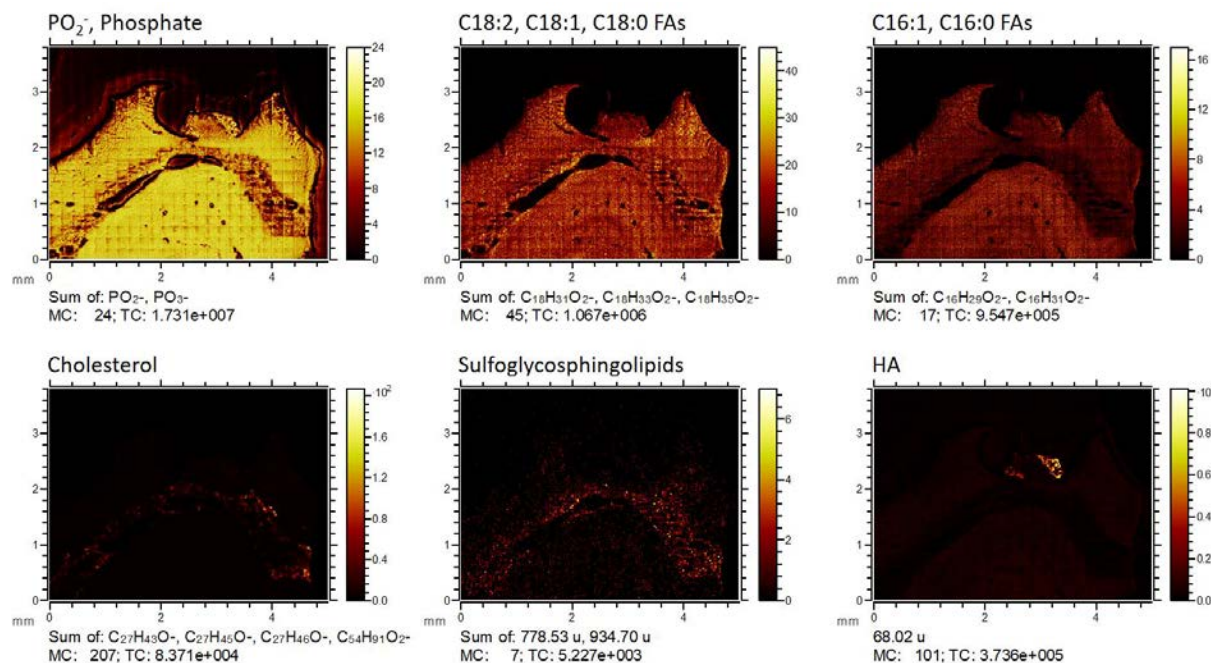


Figure 5.4. Negative ion ToF-SIMS macro-images ( $5.0 \times 3.8 \text{ mm}^2$ ) of brain tissue sections obtained after 3 months of implantation of HA hydrogel (HA) showing the distribution of phosphate, fatty acids, cholesterol and sulfoglycosphingolipid as well as the presence of HA residues.

The images of phosphate, fatty acids (FAs), cholesterol and sulfoglycosphingolipid present the distribution of common molecules on the surface of the tissue section indicating the stability of main structures in the brain after 3 months. In the top row we have the following three images. The image showing the sum of PO<sub>2</sub><sup>-</sup> and PO<sub>3</sub><sup>-</sup> signals at  $m/z = 62.97$  and  $78.97$  primarily represents the distribution of phospholipids on the tissue surface. The image showing the sum of C<sub>18</sub>H<sub>31</sub>O<sub>2</sub><sup>-</sup>, C<sub>18</sub>H<sub>33</sub>O<sub>2</sub><sup>-</sup> and C<sub>18</sub>H<sub>35</sub>O<sub>2</sub><sup>-</sup> signals at  $m/z = 279.25$ ,  $281.26$  and  $283.28$  corresponds to the distribution of linoleic (C18:2), oleic (C18:1) and stearic (C18:0) fatty acids, respectively. The image showing the sum of C<sub>16</sub>H<sub>29</sub>O<sub>2</sub><sup>-</sup> and C<sub>16</sub>H<sub>31</sub>O<sub>2</sub><sup>-</sup> signals at  $m/z = 253.23$  and  $255.25$  precisely present contributions of palmitoleic (C16:1) and palmitic (C16:0) fatty acids, respectively, and represents the distribution of palmitoleic/palmitic-containing phospholipids such as phosphatidylcholine. As expected, the image of the linoleic/oleic/stearic distribution is considered to be less structured than the image of the palmitoleic/palmitic distribution, indicating that these types of fatty acids do not occupy the same regions in the tissue [207]. On the other hand, the phosphate and palmitoleic/palmitic image have the same structured distribution, indicating that the phosphate signal may be primarily representative of palmitoleic/palmitic-containing phospholipids.

In the bottom row (Figure 5.4) we have the image showing the sum of C<sub>27</sub>H<sub>43</sub>O<sup>-</sup>, C<sub>27</sub>H<sub>45</sub>O<sup>-</sup>, C<sub>27</sub>H<sub>46</sub>O<sup>-</sup> and C<sub>54</sub>H<sub>91</sub>O<sub>2</sub><sup>-</sup> signals at  $m/z = 383.33$ ,  $385.35$ ,  $386.35$  and  $771.65$  characterizing cholesterol, while the image showing the sum of  $m/z = 778.53$  and  $934.70$  signals is presenting of sulfoglycosphingolipid distribution. Both cholesterol and sulfoglycosphingolipid intensities are showed occupying a curved feature in the centre of the brain tissue corresponding to the white matter. In general, these results are

expected since the white matter regions consist primarily of nerve fibres (axons) surrounded by myelin sheath, which are rich in cholesterol. Sulfoglycosphingolipids are also supposed to appear in higher intensities in the white matter. Grey matter, in contrast, consist of nerve cell bodies and glial cells rich in membrane phospholipids and lower concentrations of cholesterol and sulfoglycosphingolipids [21, 123]. The last image of the bottom row shows the  $m/z = 68.02$  signal intensity characteristic of the HA hydrogel that confirms its presence in the neural tissue even after 3 months. The Table 5.1 below lists the negative molecular ions identified on the rodent's coronal section.

*Table 5.1. List of the main negative molecular ions characteristic of a rodent's brain coronal section.*

<b>m/z (experimental)</b>	<b>m/z (theoretical)</b>	<b>Assignment</b>
62.97	62.96	$\text{PO}_2^-$
68.02	-	-
78.97	78.95	$\text{PO}_3^-$
253.23	253.21	$\text{C}_{16}\text{H}_{29}\text{O}_2^-$
255.25	255.23	$\text{C}_{16}\text{H}_{31}\text{O}_2^-$
279.25	279.23	$\text{C}_{18}\text{H}_{31}\text{O}_2^-$
281.26	281.24	$\text{C}_{18}\text{H}_{33}\text{O}_2^-$
283.28	283.26	$\text{C}_{18}\text{H}_{35}\text{O}_2^-$
383.33	383.63	$\text{C}_{27}\text{H}_{43}\text{O}^-$
385.35	385.37	$\text{C}_{27}\text{H}_{45}\text{O}^-$
386.35	386.37	$\text{C}_{27}\text{H}_{46}\text{O}^-$
771.65	771.78	$\text{C}_{54}\text{H}_{91}\text{O}_2^-$
778.53	-	-
934.70	-	-

### **5.2.2 Comparison between ToF-SIMS imaging and cresyl violet staining of a rodent's brain tissue**

A comparison between a ToF-SIMS image from the rat brain tissue after 3 months of implantation of HA cylinders and a subsequent tissue section that shared the same interface stained with cresyl violet is given in Figure 5.5.

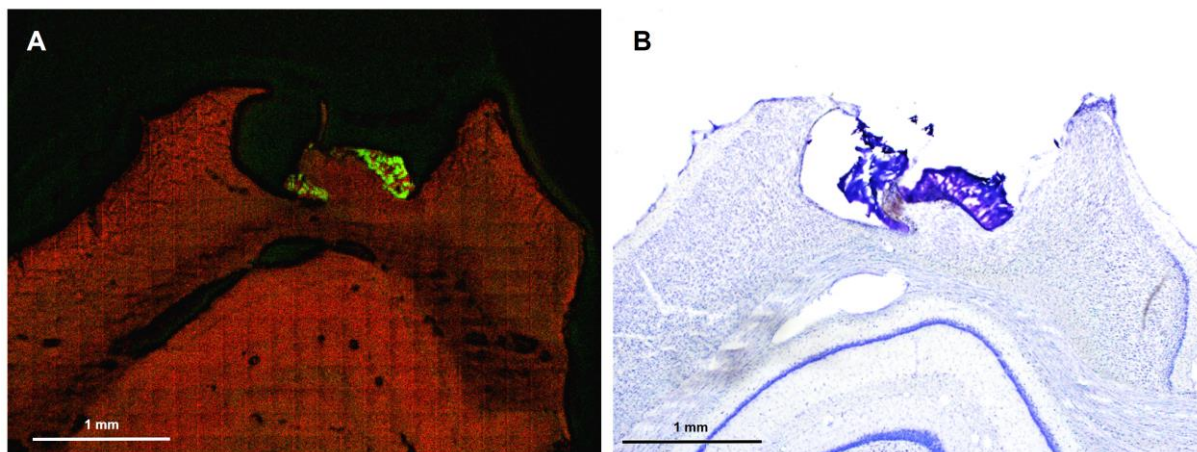


Figure 5.5. (a) Negative ion ToF-SIMS macro-image of brain tissue sections obtained after 3 months of implantation of hyaluronic acid (HA) hydrogel showing two colours overlay of red: FAs C16:1 and C16:0 at  $m/z = 253.23$  and  $255.25$ , respectively; green: HA hydrogel signal at  $m/z = 68.02$ . Image size  $5.0 \times 3.8 \mu\text{m}^2$  containing 475 ( $25 \times 19$ )  $200 \times 200 \mu\text{m}^2$  patches. (b) A subsequent tissue section cresyl violet stained.

The ToF-SIMS macro-image shows that the summation of FAs C16:1 and C16:0 at  $m/z = 253.23$  and  $255.25$  in red matches well with the tissue aspect from the cresyl violet staining. Additionally, the green colour represents the HA hydrogel signal intensity at  $m/z = 68.02$  that can be also identified in dark violet in the stained tissue. The particularity of the ToF-SIMS image is that we can observe the presence of FAs in red along with the presence of the HA hydrogel residue, indicating that the HA hydrogel residue was probably colonized by new brain cells. In summary, we conclude that from the ToF-SIMS imaging we were able to verify the existence of HA hydrogel remaining in the surgical area even after 3 months of implantation. We also conclude that there was no infiltration of the HA hydrogel into other areas of the brain that should not be affected because the main chemical structures in the deeper regions of the brain remain unchanged. This is a very important information for the development of effective drug delivery vehicles and might ensure the sustainability and controllability of drug delivery within the target tumour site while minimizing the adverse effects of systemic exposure to drugs transported by HA hydrogels.

### 5.3 GLIAL SCAR TISSUE

The glial scar tissue commonly formed around implantable neural technologies is part of the natural wound-healing mechanism that seeks to confine the inflammation due to implantation surgery to the lesion core and protect the intact neural tissue. It occurs when tissue regeneration fails and the injured tissue is rapidly replaced by a glial scar tissue. This glial scar tissue is mainly composed of glial cells such as resident astrocytes and ependymal neural stem cell-derived astrocytes localized at the lesion penumbra (see Figure 5.6).

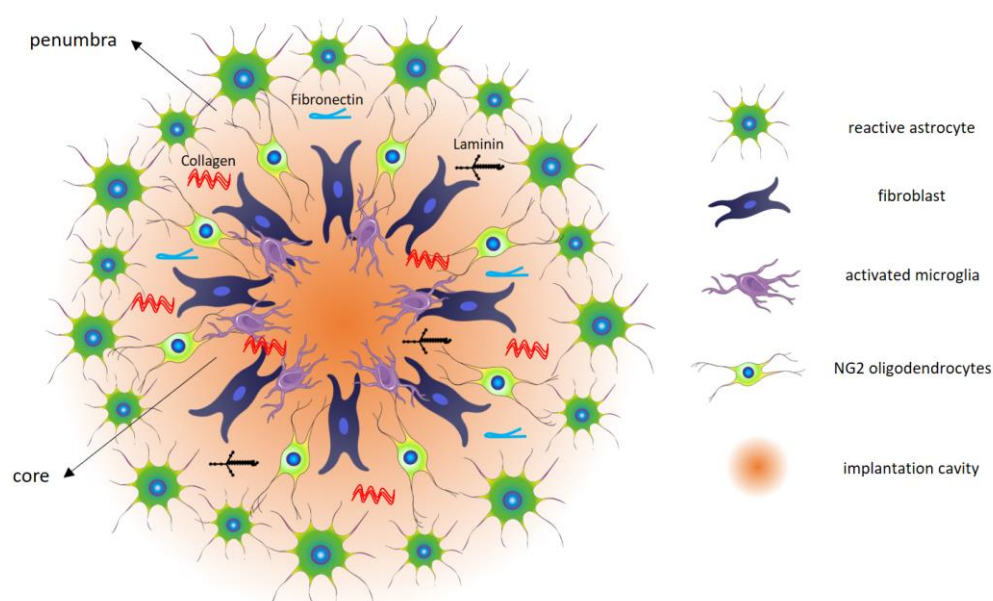


Figure 5.6. Anatomy of a glial scar formed after central nervous system (CNS) injury. The lesion has two distinct components – the lesion penumbra that is composed of reactive astrocytes, and the lesion core that is composed of NG2 oligodendrocytes precursor cells, meningeal and/or vascular derived fibroblasts, and microglia. The extracellular matrix (ECM) molecules (collagen, fibronectin, and laminin) synthesized by fibroblasts are also indicated inside the lesion core [208].

Since astrocytes are responsible for secreting growth-inhibitory chondroitin sulphate proteoglycans, the glial scar is also considered the major barrier to regenerating neurons around the implantation cavity [154, 208, 209]. In the lesion core, inflammatory cells such as neutrophils and microglia interact with meningeal and/or vascular derived fibroblasts that synthesize a dense fibrotic tissue composed of extracellular matrix (ECM) molecules such as fibronectin, collagen and laminin [210]. After damage due to implantation, immature cells such as NG2 oligodendrocyte progenitors are also present in the lesion core. These are related to dystrophic axons in the glial scar helping to stabilize them within the hostile lesion environment.

According to Lau *et al.*, 2013 [211], the fibrotic response is perhaps more detrimental in the central nervous system (CNS) compared to other tissues because the brain's ECM normally contains relatively small amounts of fibrous proteins (collagen and elastin) and adhesive glycoproteins (laminin and fibronectin). The adhesive glycoproteins are important molecules that bind to the fibrin network (thrombosis or clot) formed on the surface of the neural device in the early stages of the inflammatory response, as well as platelet granule components released during platelet aggregation [6].

This same layered structure composed of reactive astrocytes at the lesion penumbra and microglia at the lesion core, can be seen in the glial scar tissue extracted from the surrounding of the intracranial device implanted in a non-human primate's cortex in the context of this work. The glial scar tissue surrounding the intracranial device and the back of a piece of a similar intracranial device supposed to

be the same inside the glial scar tissue can be seen in Figure 5.7(B). The glial scar tissue was prepared as a cross section application of different staining techniques used with light microscopy. In Figure 5.7(C) we observe the Nissl staining of the scar tissue section indicating in violet the population of glial cells present in this fibrotic tissue, including astrocytes and microglia. The cavities in the tissue produced by the relief of the intracranial device are numbered from 1 to 6. In Figure 5.7(D), however, we observe in green thanks to staining of the glial fibrillary acidic protein (GFAP) the reactivity of astrocytes at the lesion penumbra, in contrast with other cell populations at the lesion core shown in red thanks to propidium iodide (PI) staining.

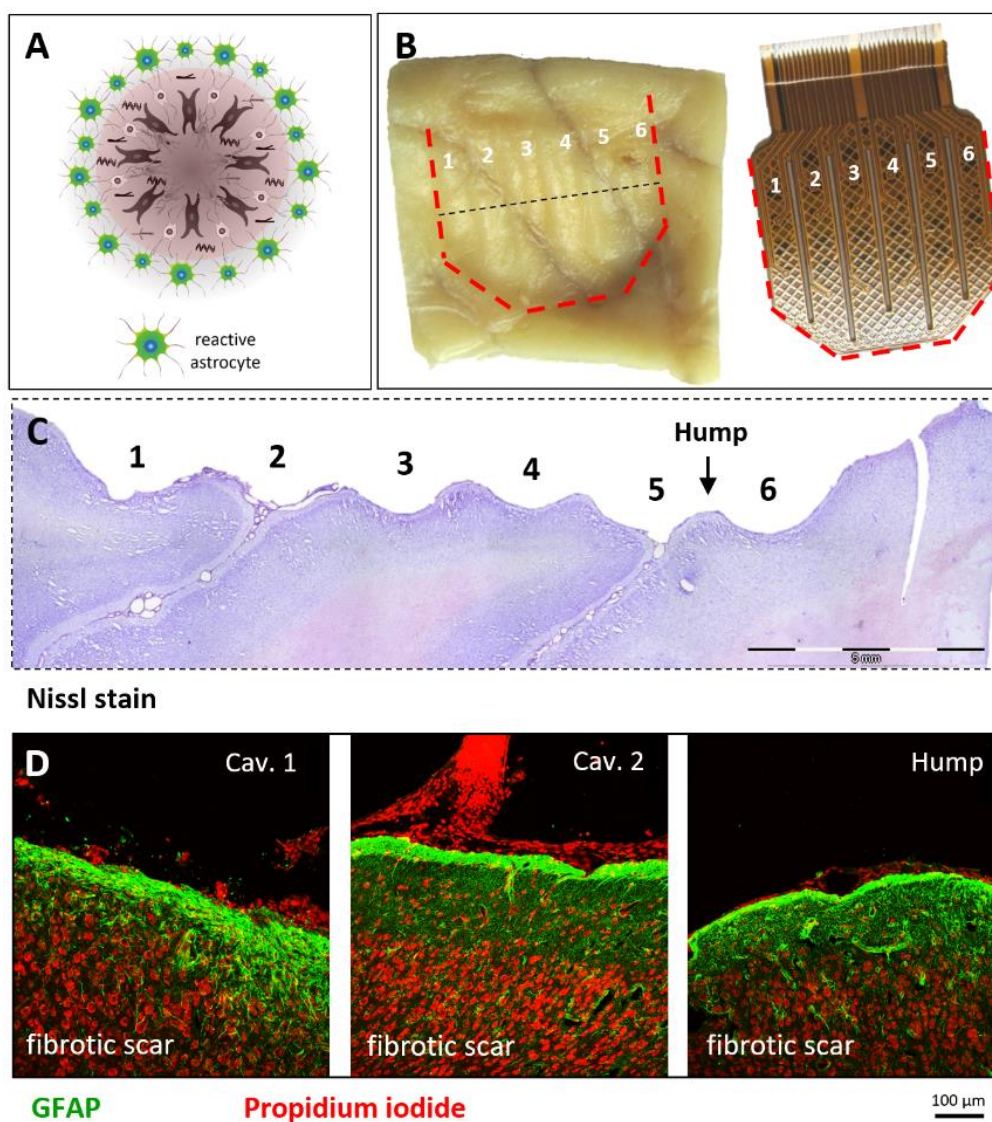


Figure 5.7. (A) Astrocytes become activated in response to the central nervous system (CNS) injury at the lesion penumbra. (B) Back of the neural device with and without the glial scar surrounding it. The dotted line over the glial scar tissue indicates the tissue cross section taken for staining. (C) Nissl stain of the glial scar tissue section showing in violet the population of glial cells present in the fibrotic tissue. The cavities in the tissue produced by the relief of the neural device are numbered from 1 to 6. (D) Glial fibrillary acidic protein (GFAP) and propidium iodide staining of the scar tissue from cavities 1 and 2, and from a hump between cavities 5 and 6, showing in green reactive astrocytes at the lesion penumbra, while in red other glial cells at the lesion core of the scar tissue.

Similarly, in Figure 5.8(B), we observe activated microglia at the lesion core in green thanks to staining of ionized calcium-binding adapter molecule (IBA1).

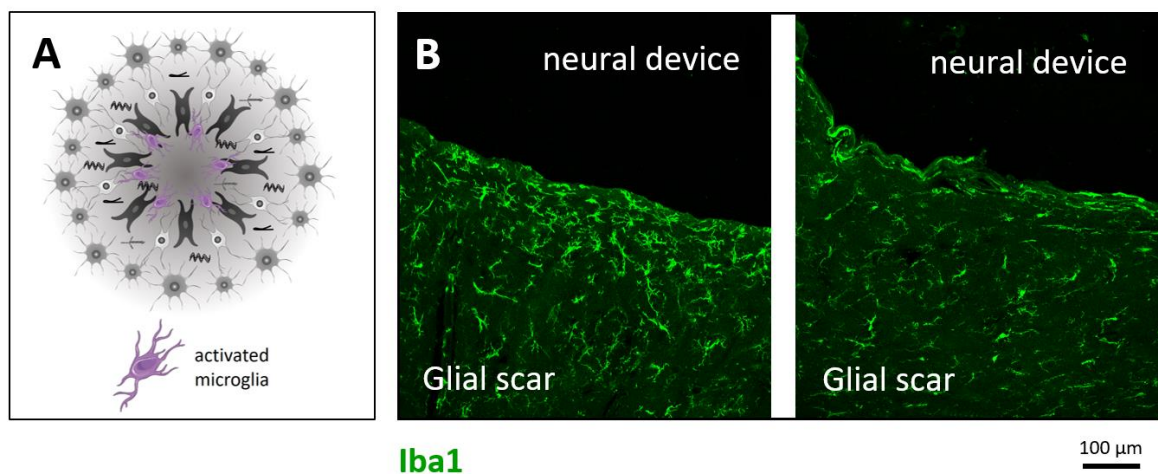


Figure 5.8. (A) Microglia accumulate within the lesion core after injury due to surgery for intracranial device implantation. (B) Ionized calcium-binding adapter molecule (IBA1) staining of the scar tissue layer in contact with the neural device (lesion core); activated microglia is shown in green.

## 5.4 IMAGING A GLIAL SCAR TISSUE BY TOF-SIMS

In this section we see how ToF-SIMS imaging allied to principal component analysis (PCA) is a fundamental tool in highlighting the main biomolecules present in glial scar tissues and how this approach can help in identifying zones of chemical contrast in glial scar tissues. In addition, we see how the high sensitivity of the ToF-SIMS analysis allows us to identify traces of metals in the glial scar tissue, thus raising the hypothesis of contamination of the biological tissue by metals from the intracranial device, explaining then the generation of an acute inflammatory reaction in the implantation site.

### 5.4.1 Identification of the main biomolecules present in the glial scar tissue by applying PCA on ToF-SIMS data

Although staining provides good contrast enhancement in biological samples providing localization of different structures in the fibrotic tissue, ToF-SIMS imaging can provide detailed molecular characterisation of the glial scar tissue. Two tissue sections will be target of analysis in this subsection, these are the slices of glial scar tissue labelled SA09 and SA18. The exact location of these tissue slices with respect to the intracranial device can be seen in the section “Glial scar tissue and scheme of tissue cross section’s location” in the appendix. Imaging the SA09 and SA18 slices, localized at approximately 350 μm and 100 μm of distance from the surface of the neural device, respectively, a limited number of main chemical elements were immediately identified (C, H, O, N, Cl, Na, S, P), however, the molecular combinations of these elements are numerous.

In Figure 5.9 is possible to observe the macro images from SA09 and SA18 slices with their respective mass spectrum showing countless molecules present on the top surface of these tissue sections. Molecules from the silicon substrate may also be present in the spectra.

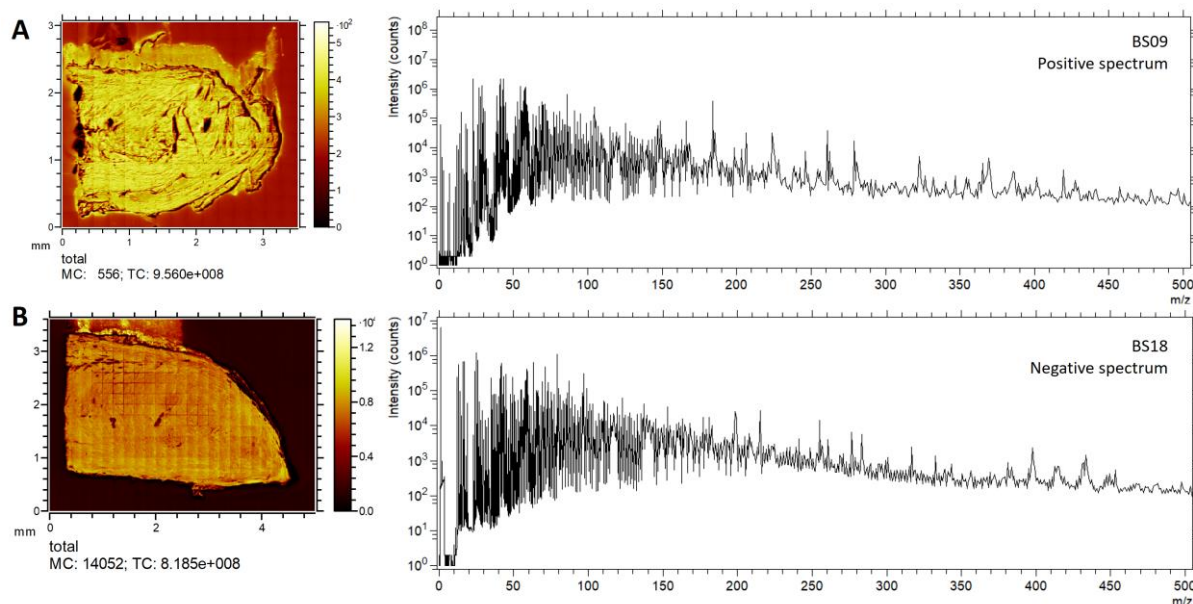


Figure 5.9. ToF-SIMS total image counts and mass spectra of (A) SA09 and (B) SA18 tissue sections showing intensity in log scale ranging from  $m/z=0$  to 510. A large variety of molecules is observed in both positive and negative ion extraction modes. Molecules from silicon substrate may also be present in the spectra.

To separate molecules characteristic of biological tissue and silicon substrate and highlight only molecules present in the biological tissue, we applied PCA to the image dataset based on all positive and negative spectrum information seen in Figure 5.9. The overall chemical differences between the glial scar tissue (slices SA09 and SA18) and the substrate were described in the first components PC1 and PC2, with an average 70% and 10% explanation of data variation.

#### 5.4.1.1 PCA scores of BS09 ToF-SIMS positive data

In Figure 5.10 we can see the red and green overlay of the PC1 and PC2 scores, respectively, from the positive spectrum data set of SA09 and its loadings in a  $m/z$  range from 80 to 280. The molecules corresponding to the  $m/z$  seen at positive values of loadings PC1 (Figure 5.10B in red) are detected in the glial scar tissue.

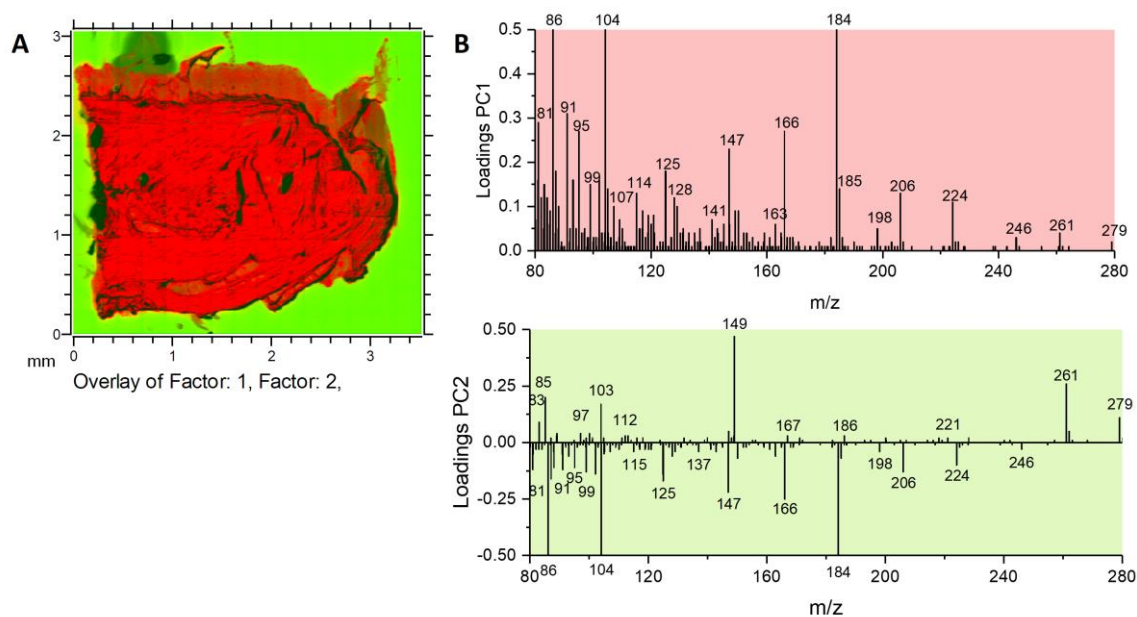


Figure 5.10. PCA analysis of positive data set acquired from SA09 tissue section. (A) Overlay of PC1 (factor 1) and PC2 (factor 2) scores in red and green, respectively, and (B) their respective loadings ranging from  $m/z=80$  to 280.

The loadings indicate that the glial scar tissue is made up of proteins due to the presence of the fragments  $C_4H_5N_2^+$  ( $m/z = 81.06$ ),  $C_5H_{12}N^+$  ( $m/z = 86.10$ ),  $C_7H_7^+$  ( $m/z = 91.04$ ),  $C_5H_7N_2^+$  ( $m/z = 95.08$ ) and  $C_4H_5NO_2^+$  ( $m/z = 99.04$ ) characteristics of amino acids such as histidine (His), phenylalanine (Phe) and leucine/isoleucine (Leu/Ile) presents in collagen, laminin and fibronectin [33, 212-215]. There is also a strong presence of phospholipids due to the detection of the fragments  $C_5H_{12}N^+$  ( $m/z = 86.10$ ),  $C_5H_{14}NO^+$  ( $m/z = 104.11$ ),  $C_2H_6O_4P^+$  ( $m/z = 125.00$ ),  $C_5H_6O_4P^+$  ( $m/z = 160.99$ ),  $C_5H_{15}NO_4P^+$  ( $m/z = 184.08$ ) and  $C_8H_{19}NO_4P^+$  ( $m/z = 224.10$ ). The fragments at  $m/z = 86.10$ ,  $104.11$  and  $184.08$  are specifically related to the choline head group present in phosphatidylcholine (PC) and sphingomyelin (SM) molecules [21, 171, 216]. These may constitute the plasma membrane of the variety of cells present in the scar tissue. The Table 5.2 below lists these main positive molecular ions found on the surface of the glial scar tissue.

Table 5.2. List of the main positive molecular ions characteristic of the glial scar tissue found on slice SA09.

<b><math>m/z</math> (experimental)</b>	<b><math>m/z</math> (theoretical)</b>	<b>Assignment</b>
81.06	81.04	$C_4H_5N_2^+$
86.10	86.09	$C_5H_{12}N^+$
91.04	91.05	$C_7H_7^+$
95.08	95.06	$C_5H_7N_2^+$
99.04	99.03	$C_4H_5NO_2^+$
104.11	104.10	$C_5H_{14}NO^+$
125.00	125.00	$C_2H_6O_4P^+$
160.99	161.00	$C_5H_6O_4P^+$
184.08	184.07	$C_5H_{15}NO_4P^+$
224.10	224.10	$C_8H_{19}NO_4P^+$

In addition, the molecules corresponding to the  $m/z$  seen at positive values of loadings PC2 (Figure 5.10B in green) are characteristic of the silicon substrate. The negative values of loadings PC2 confirm the previously mentioned  $m/z$  present in the fibrotic tissue as peaks strongly missing in the silicon substrate.

#### 5.4.1.2 PCA scores of SA18 ToF-SIMS negative data

Similarly, in Figure 5.11 we can see the red and green overlay of the PC1 and PC2 scores from the negative spectrum data set of SA18 and its loadings in a  $m/z$  range from 80 to 280. The molecules corresponding to the  $m/z$  seen at positive values of loadings PC1 (Figure 5.11B in red) are present in the glial scar tissue.

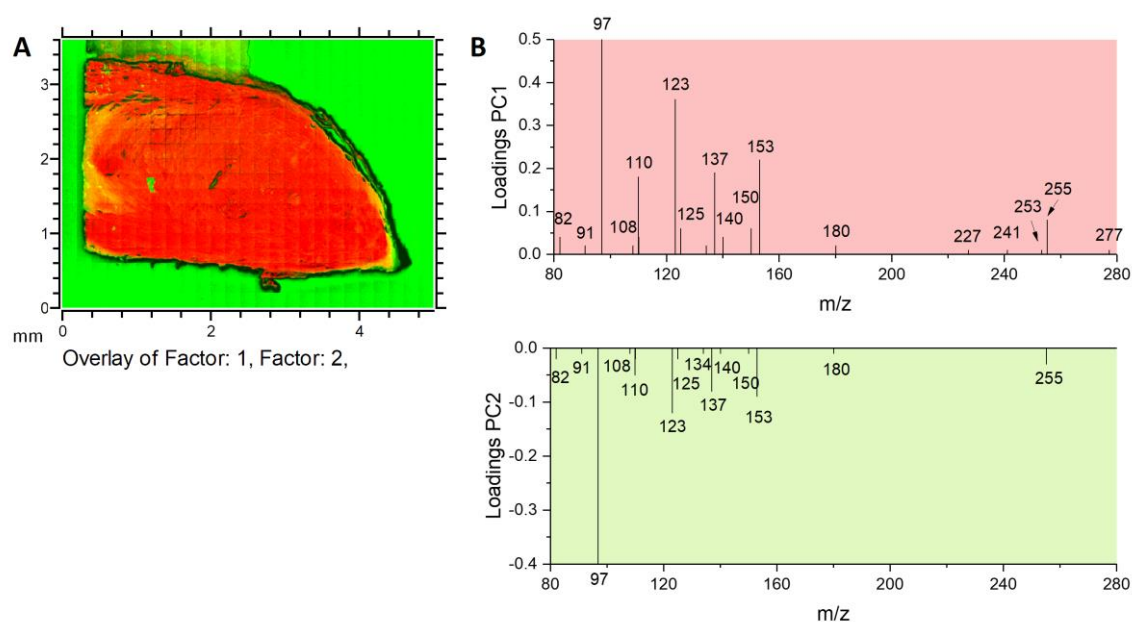


Figure 5.11. PCA analysis of negative data set acquired from SA18 tissue section. (A) Overlay of PC1 (factor 1) and PC2 (factor 2) scores in red and green, respectively, and (B) their respective loadings ranging from  $m/z=80$  to 280.

The loadings indicate the presence of the fragments  $C_4H_4NO^-$  ( $m/z = 82.03$ ),  $C_7H_7^-$  ( $m/z = 91.05$ ),  $C_5H_6N_3^-$  ( $m/z = 108.05$ ) or  $C_6H_6NO^-$  ( $m/z = 108.05$ ),  $C_5H_4NO_2^-$  ( $m/z = 110.02$ ) and  $C_6H_5N_2O_2^-$  ( $m/z = 137.00$ ) also characteristics of amino acids such as His and Phe presents in collagen, laminin and fibronectin [213, 217]. The presence of the following fragments of phospholipids is also indicated:  $PO_4H_2^-$  ( $m/z = 96.97$ ),  $C_2H_4O_4P^-$  ( $m/z = 122.98$ ),  $C_2H_7NO_4P^-$  ( $m/z = 140.00$ ),  $C_3H_8NO_4P^-$  ( $m/z = 153.00$ ),  $C_5H_{11}NO_4P^-$  ( $m/z = 180.03$ ),  $C_6H_{10}PO_8^-$  ( $m/z = 241.01$ ) and  $C_{14}H_{14}PO_4^-$  ( $m/z = 277.09$ ). Besides the fragment at  $m/z = 122.98$  be considered a common fragment of PCs, SMs and phosphatidylethanolamine (PE) molecules, fragments at  $m/z = 140.00$ ,  $153.00$  and  $180.03$  are supposed to be specifically related to Pes [218]. While the fragment at  $m/z = 241.01$  is related to phosphatidylinositol (PI). Fragments of fatty acid (FAs) chains such as  $C_{14}H_{27}O_2^-$  ( $m/z = 227.18$ ),  $C_{16}H_{29}O_2^-$  ( $m/z = 253.20$ ) and  $C_{16}H_{31}O_2^-$  ( $m/z = 255.21$ ) related to myristic acid (C14:0), palmitoleic acid

(C16:0), and palmitic acid (C16:1)<sup>1</sup>, respectively, are also highlighted [29, 172, 218, 219]. The Table 5.3 below lists these main negative molecular ions found on the surface of the glial scar tissue.

Table 5.3. List of the main negative molecular ions characteristic of the glial scar tissue found on slice SA18.

m/z (experimental)	m/z (theoretical)	Assignment
82.03	82.02	C <sub>4</sub> H <sub>4</sub> NO <sup>-</sup>
91.05	91.05	C <sub>7</sub> H <sub>7</sub> <sup>-</sup>
96.97	96.96	PO <sub>4</sub> H <sub>2</sub> <sup>-</sup>
108.05	108.05	C <sub>5</sub> H <sub>6</sub> N <sub>3</sub> <sup>-</sup>
108.05	108.05	C <sub>6</sub> H <sub>6</sub> NO <sup>-</sup>
110.02	110.02	C <sub>5</sub> H <sub>4</sub> NO <sub>2</sub> <sup>-</sup>
122.98	122.98	C <sub>2</sub> H <sub>4</sub> O <sub>4</sub> P <sup>-</sup>
137.00	137.03	C <sub>6</sub> H <sub>5</sub> N <sub>2</sub> O <sub>2</sub> <sup>-</sup>
140.00	140.01	C <sub>2</sub> H <sub>7</sub> NO <sub>4</sub> P <sup>-</sup>
153.00	153.01	C <sub>3</sub> H <sub>8</sub> NO <sub>4</sub> P <sup>-</sup>
180.03	180.04	C <sub>5</sub> H <sub>11</sub> NO <sub>4</sub> P <sup>-</sup>
227.18	227.20	C <sub>14</sub> H <sub>27</sub> O <sub>2</sub> <sup>-</sup>
241.01	241.01	C <sub>6</sub> H <sub>10</sub> PO <sub>8</sub> <sup>-</sup>
253.20	253.21	C <sub>16</sub> H <sub>29</sub> O <sub>2</sub> <sup>-</sup>
255.21	255.23	C <sub>16</sub> H <sub>31</sub> O <sub>2</sub> <sup>-</sup>
277.09	277.06	C <sub>14</sub> H <sub>14</sub> PO <sub>4</sub> <sup>-</sup>

The molecules corresponding to the m/z seen at positive values of PC2 loadings (Figure 5.11Figure 5.10B in green) are also here characteristic of the silicon substrate. The negative values of loadings PC2 also confirm the negative molecular ions m/z present in the glial scar tissue as peaks strongly missing in the silicon substrate. The “Parameters used for principal component analysis of slices SA09 and SA18” can be found in the appendix.

#### 5.4.2 Imaging chemically distinct features in the scar tissue by applying PCA on ToF-SIMS data

As seen in the previous subsection, the most striking patterns in positive and negative ToF-SIMS data set were described in the first components PC1 and PC2 concerning the chemical differences between the silicon substrate and the biological tissue. The subsequent components highlighted special features surrounding the biological tissue that belongs to the O.C.T.<sup>TM</sup> Compound used for sectioning. However, specific subsequent components such as PC6 and PC8 also presented important information concerning the distribution of biomolecules in the glial scar tissue. For instance, the PCA analysis of the SA18 negative data set had verified, from component PC8 (0.08% explanation of data variation), the existence of two chemically distinct regions specifically in the glial scar tissue. All “PCA scores from ToF-SIMS negative spectrum of slice SA18” can be found in the appendix.

<sup>1</sup> Fatty acids (FAs) are often designed by the abbreviation C<sub>x</sub>:y, where x is the number of carbons in chain and y is the number of double bonds between carbons.

The low explanation of data variation in higher components such as PC8 is expected and indicates that chemical contrasts that have a greater number of variables are evidenced in lower components. This scenario is consistent with our PCA analysis as our approach includes all peaks from the negative mass spectrum and many of them are related to the silicon substrate and the O.C.T.<sup>TM</sup> compound used in the sectioning of the biological tissue. As proof of this, if we do the same PCA analysis on the same dataset but this time excluding all masses below 200 Daltons (mostly related to the silicon substrate and the O.C.T.<sup>TM</sup> compound), we can see that the most striking differences highlighted in the components PC1 and PC2 become those found in the biological tissue as we can see in Figure 5.12.

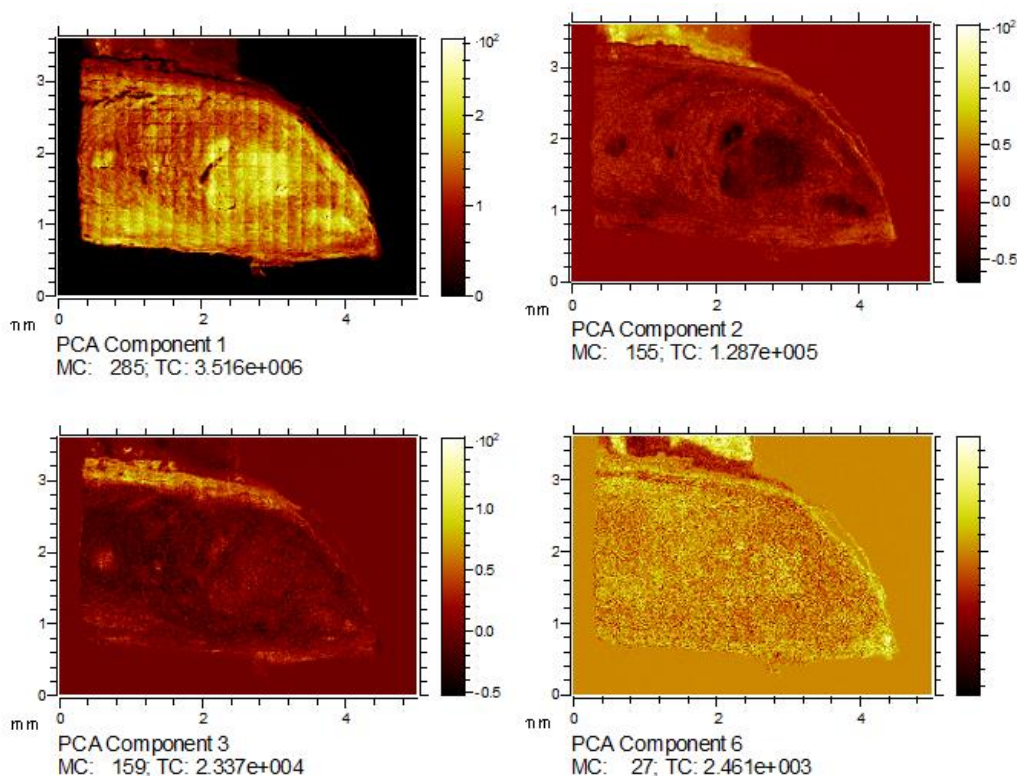


Figure 5.12. New PCA analysis of SA18 image data when mass below 200 Daltons are excluded. The same features found on PC8 of previous analysis considering all peaks were found here on PC1.

Taking then PC8 image for deeper discussion in this section, in Figure 5.13 we can see the image scores and its load peaks in a  $m/z$  range from 0 to 300.

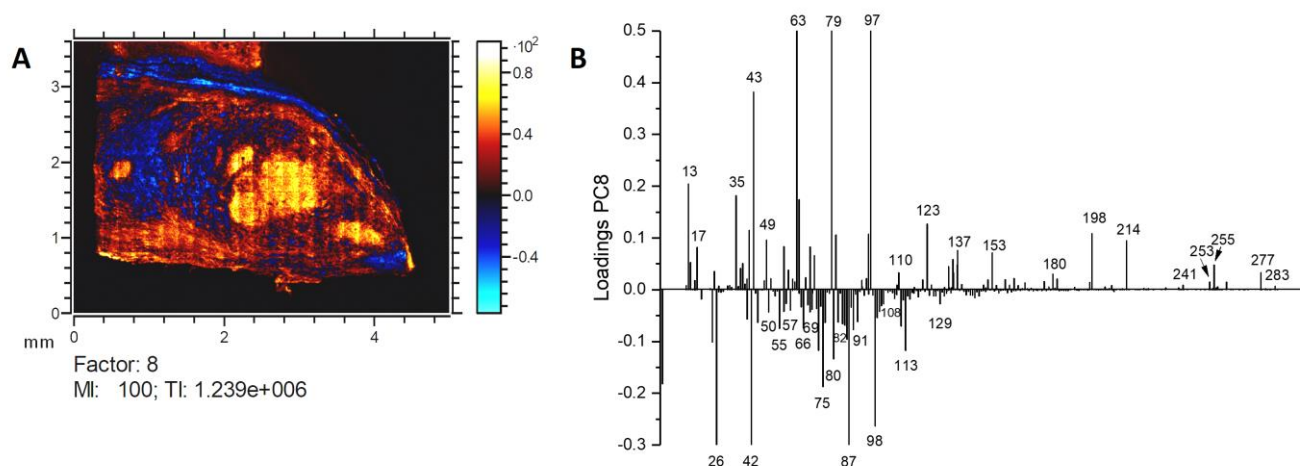


Figure 5.13. (A) PC8 (factor 8) scores image and (B) loadings from TOF-SIMS negative ions data of SA18 tissue section.

As we can notice, the PC8 image scores (Figure 5.13A) highlighted rounded regions coloured in yellow mainly concentrated in the middle of the tissue.

#### 5.4.2.1 Positive loadings of PC8

According to the positive PC8 load peaks (Figure 5.13B), these are regions of higher presence of fragments of phospholipid membranes (PM) and Fas. Among the fragments of phospholipids, we found  $\text{PO}_2^-$  ( $m/z = 62.96$ ),  $\text{PO}_3^-$  ( $m/z = 78.96$ ),  $\text{H}_2\text{PO}_4^-$  ( $m/z = 96.97$ ),  $\text{CH}_3\text{PO}_4^-$  ( $m/z = 109.97$ ),  $\text{C}_2\text{H}_4\text{PO}_4^-$  ( $m/z = 122.98$ ),  $\text{C}_3\text{H}_6\text{PO}_4^-$  ( $m/z = 137.00$ ),  $\text{C}_3\text{H}_8\text{NPO}_4^-$  ( $m/z = 153.00$ ),  $\text{C}_5\text{H}_{11}\text{NPO}_4^-$  ( $m/z = 180.03$ ),  $\text{C}_6\text{H}_{10}\text{PO}_8^-$  ( $m/z = 241.01$ ), and  $\text{C}_{14}\text{H}_{14}\text{PO}_4^-$  ( $m/z = 277.09$ ). While among the fragments of FAs we have  $\text{C}_{16}\text{H}_{29}\text{O}_2^-$  ( $m/z = 253.20$ ),  $\text{C}_{16}\text{H}_{31}\text{O}_2^-$  ( $m/z = 255.21$ ), and  $\text{C}_{18}\text{H}_{35}\text{O}_2^-$  ( $m/z = 283.23$ ) attributed to palmitoleic (C16:1), palmitic (C16:0), and stearic (C18:0) Fas, respectively. The regions rich in phospholipids and FAs may indicate a clinical scenario of severe inflammation with an early case of necrosis containing “exploded” cells. The same zones of necrosis were not highlighted in the SA09 PCA data set, indicating that this is an exclusive characteristic of the SA18 tissue section. This may be related to the closer localization of SA18 at 100  $\mu\text{m}$  of distance of the implantation core in comparison with the SA09 that is located at 350  $\mu\text{m}$ .

#### 5.4.2.2 Negative loadings of PC8

The same highlighted region also indicate a deficiency in  $\text{C}_3\text{N}^-$  ( $m/z = 50.00$ ),  $\text{C}_2\text{HS}^-$  ( $m/z = 56.99$ ),  $\text{C}_3\text{NO}^-/\text{C}_4\text{H}_4\text{N}^-$  ( $m/z = 66.03$ ),  $\text{C}_4\text{H}_4\text{N}_2^-$  ( $m/z = 80.03$ ),  $\text{C}_4\text{H}_4\text{NO}^-$  ( $m/z = 82.03$ ),  $\text{C}_7\text{H}_7^-$  ( $m/z = 91.05$ ),  $\text{C}_5\text{H}_6\text{N}_3^-$  ( $m/z = 108.05$ ) and  $\text{C}_8\text{H}_2\text{N}_3^-$  ( $m/z = 140.00$ ), according to negative PC8 load peaks (Figure 5.13B). These are fragments of multiple amino acids as diverse as cysteine (Cys), methionine (Met), hydroxyproline (Hyp), proline (Pro), His, Phe, tryptophan (Trp), and tyrosine (Tyr) [217] constituting the proteins collagen, fibronectin and elastin [30, 33, 212, 220, 221]. The negative load peaks also indicated a lower presence of  $m/z = 75.00$  and  $123.99$  corresponding to  $\text{C}_2\text{H}_3\text{SO}^-$  and  $\text{C}_6\text{H}_4\text{SO}^-$  ions, respectively. These are direct fragments of chondroitin sulphate [222] secreted by astrocytes to inhibit neuronal

growth during the glial scar tissue formation [154, 209]. The  $m/z = 26.00$  and  $41.99$  ions corresponding to  $\text{CN}^-$  and  $\text{CNO}^-$  are common structural units from both all amino acids and proteoglycans [201, 212, 214], and appear on PC8 negative load peaks.

The Table 5.4 below lists these main negative molecular ions appearing in positive and negative loadings of PC8 from ToF-SIMS data of glial scar tissue.

*Table 5.4. List of the main negative molecular ions appearing in positive and negative loadings of PC8 from ToF-SIMS data of glial scar tissue slice SA18.*

Positive loadings of PC8			Negative loadings of PC8		
$m/z$ (experimental)	$m/z$ (theoretical)	Assignment	$m/z$ (experimental)	$m/z$ (theoretical)	Assignment
62.96	62.96	$\text{PO}_2^-$	26.00	26.00	$\text{CN}^-$
78.96	78.96	$\text{PO}_3^-$	41.99	42.00	$\text{CNO}^-$
96.97	96.97	$\text{H}_2\text{PO}_4^-$	50.00	50.00	$\text{C}_3\text{N}^-$
109.97	109.97	$\text{CH}_3\text{PO}_4^-$	56.99	56.98	$\text{C}_2\text{HS}^-$
122.98	122.98	$\text{C}_2\text{H}_4\text{PO}_4^-$	65.99	65.99	$\text{C}_3\text{NO}^-$
137.00	137.00	$\text{C}_3\text{H}_6\text{PO}_4^-$	66.03	66.03	$\text{C}_4\text{H}_4\text{N}^-$
153.00	153.00	$\text{C}_3\text{H}_8\text{NPO}_4^-$	75.00	74.99	$\text{C}_2\text{H}_3\text{SO}^-$
180.03	180.04	$\text{C}_5\text{H}_{11}\text{NPO}_4^-$	80.03	80.03	$\text{C}_4\text{H}_4\text{N}_2^-$
241.01	241.01	$\text{C}_6\text{H}_{10}\text{PO}_8^-$	82.03	82.02	$\text{C}_4\text{H}_4\text{NO}^-$
253.20	253.21	$\text{C}_{16}\text{H}_{29}\text{O}_2^-$	91.05	91.05	$\text{C}_7\text{H}_7^-$
255.21	255.23	$\text{C}_{16}\text{H}_{31}\text{O}_2^-$	108.05	108.05	$\text{C}_5\text{H}_6\text{N}_3^-$
277.09	277.06	$\text{C}_{14}\text{H}_{14}\text{PO}_4^-$	123.99	123.99	$\text{C}_6\text{H}_4\text{SO}^-$
283.23	283.26	$\text{C}_{18}\text{H}_{35}\text{O}_2^-$	140.00	140.02	$\text{C}_8\text{H}_2\text{N}_3^-$

#### **5.4.2.3 Zones of interest in the glial scar tissue for multimodal analysis**

In summary, just as the yellower regions in Figure 5.13A are related to the positive load peaks, the bluer regions are related to negative load peaks of PC8. In this way, the fragments of amino acids and proteoglycans that are less intense in the yellower regions should be more intense in the bluer regions. This complementarity is shown in the summed intensity image of fragments of amino acids + proteoglycans and fragments of phospholipids + FAs in Figure 5.14. Since fragments of amino acids and proteoglycans are representative of macromolecules in the three-dimensional extracellular space, the regions where amino acids and proteoglycans related fragments are most intense will be considered as an extracellular matrix (ECM)-rich region for further discussion. Similarly, since phospholipids and FAs are common constituents of the plasma membrane that forms the external boundary of the cytoplasm of cells, the regions where phospholipids and FAs fragments are most intense will be considered as a plasma membrane (PM)-rich region.

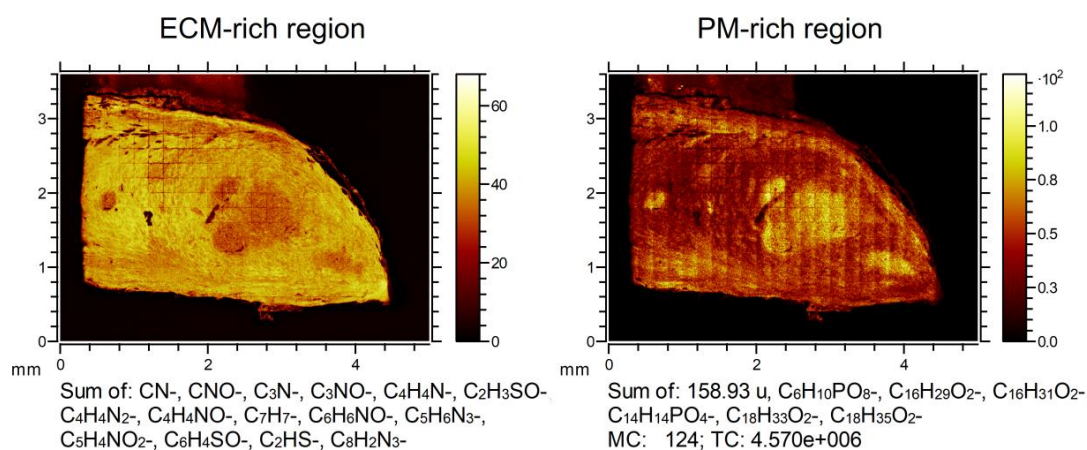


Figure 5.14. Negative ion ToF-SIMS image from SA18 tissue section. Summed intensity images of complementary regions containing fragments of amino acids (left) and phospholipids and FAs (right). The images are made up of 468 (26 × 18) 100 × 100 μm<sup>2</sup> tiles stitched together.

#### 5.4.2.4 Comparison between ToF-SIMS imaging and H&E staining

In addition, a comparison between a ToF-SIMS image cropped without the original black background, and a subsequent tissue section that shared the same interface with SA18 stained with hematoxylin and eosin (“H&E stain”) shows that the same histological features can be correlated in both images. As we can see in Figure 5.15, some characteristics of the tissue can be distinguished in the ToF-SIMS image even without the aid of histological information. Figure 5.15A shows that the summation of fragments of amino acids at  $m/z = 66.03$ ,  $80.03$ , and  $91.05$  peaks (in red) matches well the collagen type I features in the H&E stained image. Similarly, other chemically distinct regions on tissue can be seen in the ToF-SIMS image. The blue colour represents the summation of FAs at  $m/z = 253.20$ ,  $255.21$ , and  $283.23$  peaks, which matches the cell nuclei indicated on the H&E stained image.

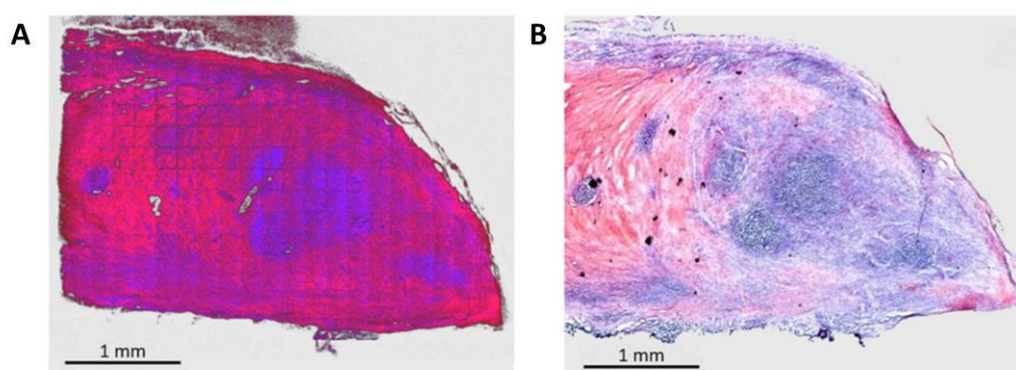


Figure 5.15. (A) Negative ion ToF-SIMS image from SA18 tissue section cropped without the original black background showing two colours overlay of red: Pro, His, and Phe at  $m/z = 66.03$ ,  $80.03$  and  $91.05$ , respectively; blue: FAs C<sub>16</sub>:1, C<sub>16</sub>:0, and C<sub>18</sub>:0 at  $m/z = 253.20$ ,  $255.21$  and  $283.23$ , respectively. Image is an excerpt from the original image, which is 4.5 × 3.8 mm<sup>2</sup> and contains 468 (26 × 18) 100 × 100 μm<sup>2</sup> tiles. Image contrast enhanced for clearer presentation of colours. (B) A subsequent tissue section that shared the same interface with SA18 H&E stained.

### 5.4.3 Identification of metals in the glial scar tissue by ToF-SIMS

In a more comprehensive exploration of the glial scar tissue surrounding the neural device, we can see that the excellent detection limit of ToF-SIMS in the ppm range also allowed the detection of traces of metals in the glial scar tissue sections may indicating a chemical instability of the intracranial device. Metals such as copper and nickel were identified in different locations in different sections of glial scar tissue. The presence of copper, nickel, and their respective isotopes in different tissue sections is shown in Figure 5.16.

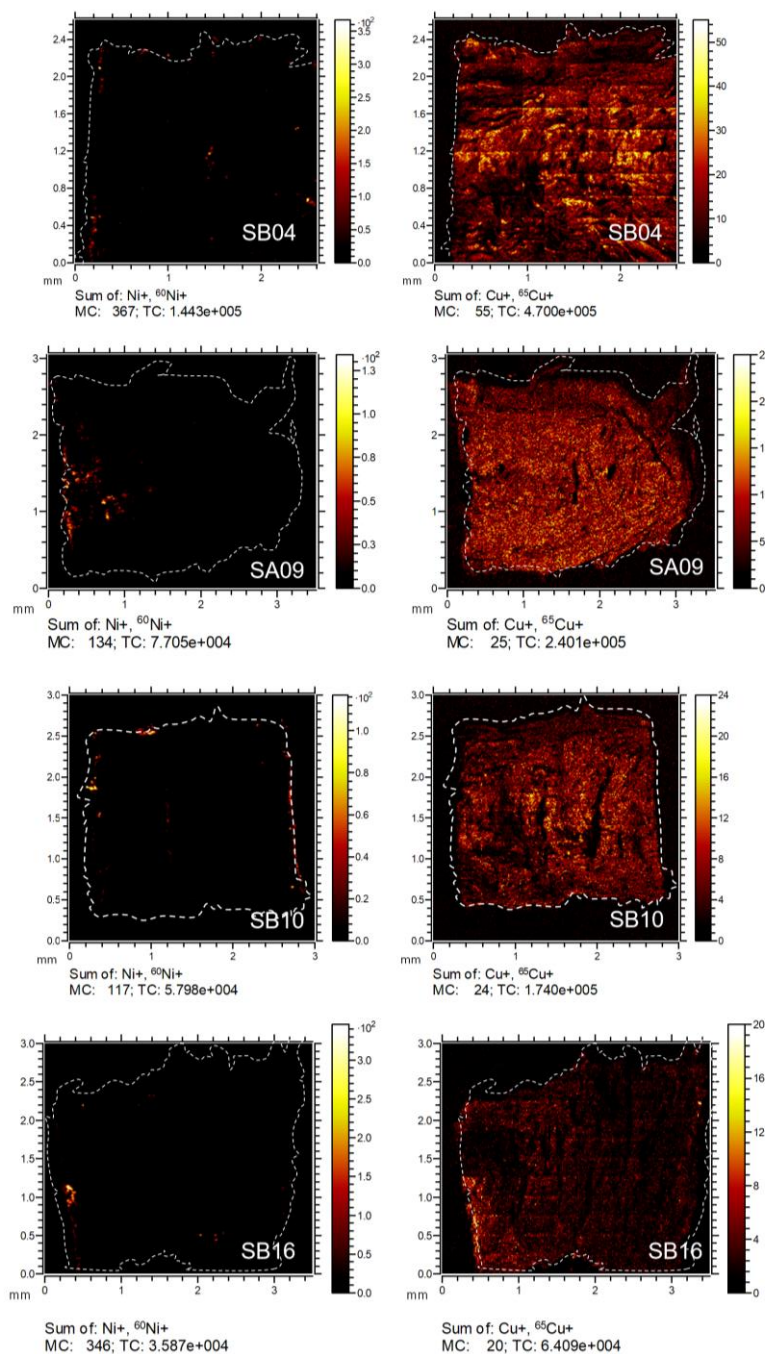


Figure 5.16. ToF-SIMS images showing the distribution of isotopes of copper and nickel in different tissue sections. The distance of these tissue sections from the top surface of the intracranial device are about 400  $\mu\text{m}$  for the SB04 tissue section, about 350  $\mu\text{m}$  for the SA09 and SA10 tissue sections and about 100  $\mu\text{m}$  for the SB16 tissue section.

As we can notice, nickel seems to be locally present in a few isolated spots whilst copper is present in everywhere in the tissue sections. The origin of nickel is certainly the intracranial device since nickel is one of the main components of the electrodes in the neural device, as presented in the subsection 2.2.4.2. However, the presence of copper in the tissue is more complex to explain since it is a dietary metal present in the organism. Despite the fact that copper composes the tracks inside the Kapton® flex that link the electrode network in the neural device, it is also associated with the synthesis of elastin and collagen present in the glial scar tissue. It is normally used as a cofactor by the enzyme lysyl oxidase to catalyse the formation of cross-linkages of collagen fibrils recently released from fibroblasts in the extracellular space [223-225].

#### 5.4.3.1 In-depth identification of copper and nickel

In-depth analysis of the SB10 tissue section also indicated the presence of copper and nickel in the tissue volume as we can see in the 3D reconstruction in Figure 5.17. The copper signal is spread over all the sputtered volume from the top of the tissue until the bottom in contact with the silicon substrate. The nickel signal is also spread in the volume but is less intense and shows some agglomerations as the red arrow indicates.

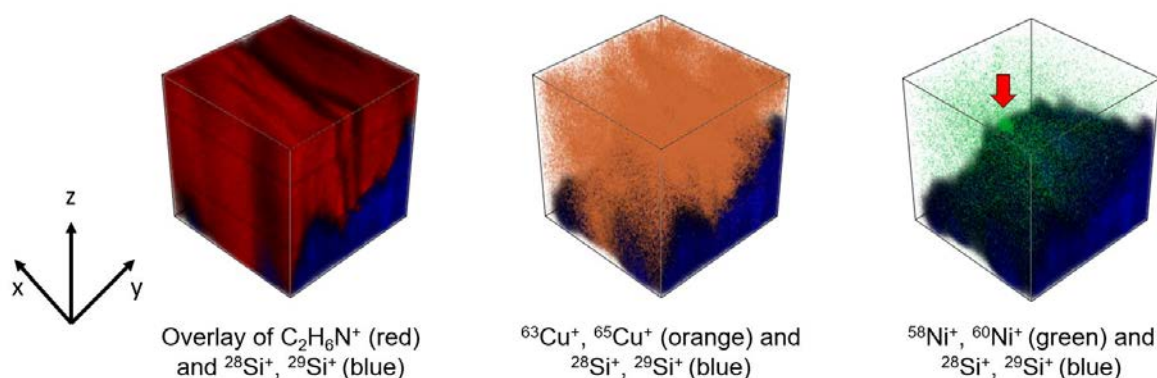


Figure 5.17. 3D reconstruction of the sputtered volume, exemplified with the sum of different secondary ions over the whole thickness of  $z = 20 \mu m$  of the SB10 tissue section, localized about  $350 \mu m$  of distance of the surface of the neural device, and a FoV of  $x \times y = 200 \times 200 \mu m^2$ . Overlay of a fragment of Ala and other amino acids characteristic of the scar tissue in red, the sum of copper isotopes in orange and the sum of nickel isotopes in green on the sum of silicon isotopes characteristic of the substrate in blue. The dark lines crossing the volume correspond to a crack in the tissue. Dietary copper is commonly found in tissues of living beings and in this case become hard to distinguish of any copper from the neural device. The nickel present in the scar tissue, however, belongs to the neural device.

#### 5.4.3.2 Spatial distribution of MWCNTs and nickel

Nickel was also found to be closely related to the presence of multi-walled carbon nanotubes (MWCNTs) in the glial scar tissue. The MWCNTs presence can be seen through the alternating dark dots in the glial scar tissue of Figure 5.18(A). The structure of the neural device containing multi-walled carbon

nanotubes was already highlighted in section 2.2.4.2. These particles of MWCNTs isolated in the tissue localized at about 500  $\mu\text{m}$  from the surface of the neural device may have been ripped out from electrodes by phagocyte cells (microglia) in the glial scar tissue upon contact with the biological matter. In Figure 5.18(B) is possible to see the particles of MWCNTs spread on the surface of a scar tissue section. The agglomeration of nickel isotopes coinciding with the distribution of the particles of MWCNTs is seen in Figure 5.18(C). MWCNTs could not be highlighted in the same way as nickel in Figure 5.18(C) because ToF-SIMS is not an appropriated technique to distinguished carbons from MWCNTs from the biomolecules in the scar tissue.

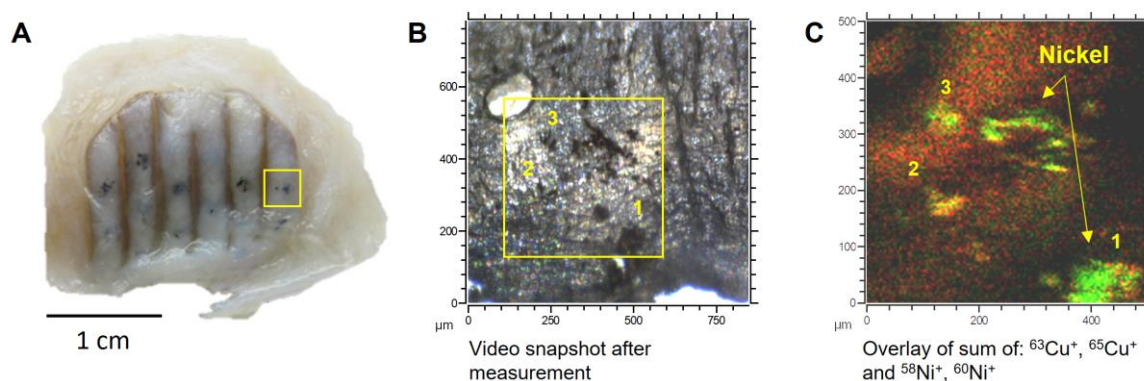


Figure 5.18. (A) Glial scar tissue surrounding the neural device after implantation period. The dark dots are particles of multi-walled carbon nanotubes (MWCNTs) isolated in the biological tissue at few hundred micrometres from the surface of the neural device. (B) Video snapshot at the end of ToF-SIMS analysis of a tissue section extracted from the region inside the yellow square from (A). The particles of MWCNTs are the dark dots in the surface of the tissue. (C) ToF-SIMS image of the region inside the yellow square seen in (B) showing the overlay of copper isotopes (in red) and nickel isotopes (in green). Nickel distribution presents the same pattern showed by the distribution of the particles of MWCNTs in (B). The numbers 1, 2 and 3 present in (B) and (C) were used to indicate similarities between both images.

## 5.5 CHEMICAL QUANTIFICATION PERFORMED IN THE GLIAL SCAR TISSUE BY XPS

The quantification of the elemental chemical composition on the surface of the scar tissue was possible thanks to XPS analysis. The same ECM-rich and PM-rich regions previously highlighted by ToF-SIMS imaging on the SA18 slice were subsequently located for XPS analysis by using real-time in situ x-ray induced secondary electron (SE) [scanning x-ray image (SXI)] images with a maximum FoV of  $1350 \times 1350 \mu\text{m}^2$ . Once the ECM-rich and PM-rich regions of interest were identified, a SXI image was acquired and a  $200 \mu\text{m}$  x-ray analysis microspot carefully set over each region. An additional charge compensation procedure is applied with low-energy electron flood gun and complementary low-energy ion gun. Before analysis, surface cleaning was carried employing gas cluster ion beam  $\text{Ar}_{2500}$  (2 nA,  $2 \times 2 \text{ mm}^2$  raster area, 1 min).

### 5.5.1 Survey spectra analysis from ECM and PM-rich regions

The analysis of the two chemically distinct ECM-rich and PM-rich regions indicates the quantifiable presence of carbon, nitrogen, oxygen, chlorine, phosphorus, sodium, and sulphur according to the survey spectra of Figure 5.19. The ECM fragments-rich region was found to have the following composition 68.6% carbon, 8.8% nitrogen, 20.9% oxygen, 0.9% chlorine, 0.5% phosphorus, 0.2% sodium, and 0.1% sulphur, while on the PM fragments-rich region, amounts of 80.0% carbon, 2.2% nitrogen, 16.5% oxygen, 0.5% chlorine, and 0.6% phosphorus were found. These different amounts can be seen in Table 5.5.

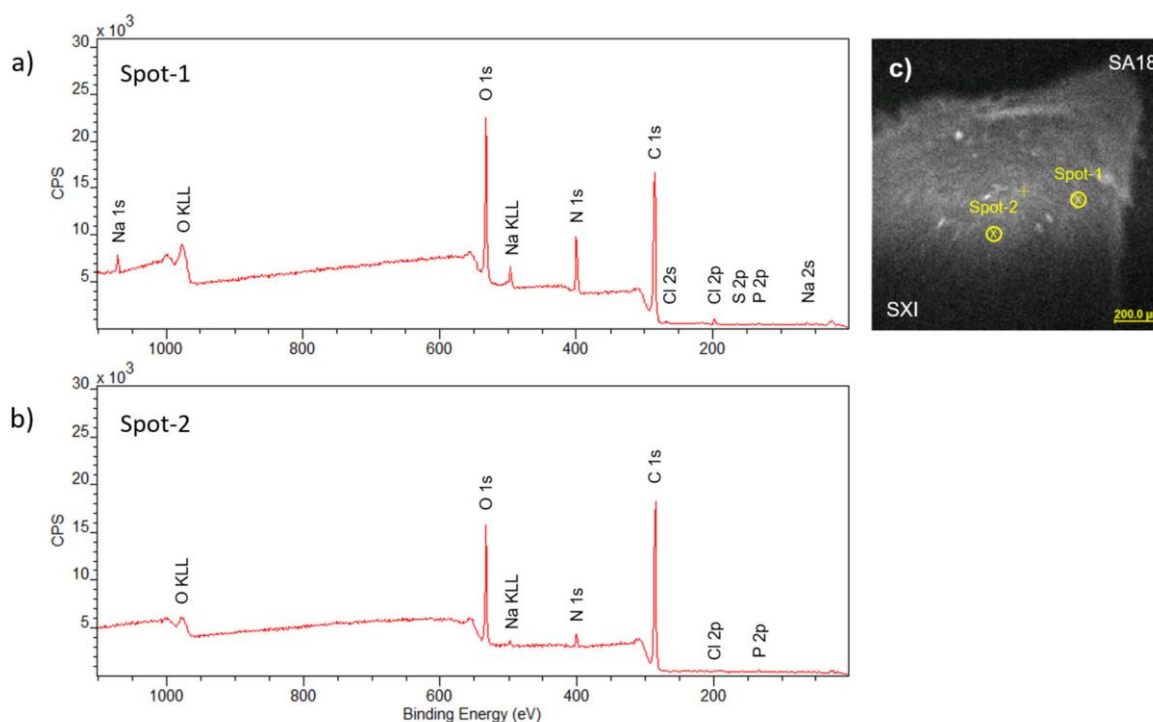


Figure 5.19. Survey spectra from (a) ECM and (b) PM-rich environments. (c) Scanning X-ray image (SXI) of SA18 tissue section showing the two target spots: spot-1 on ECM-rich and spot-2 on PM-rich regions.

Table 5.5. Core levels and their corresponding peak binding energies (eV) and atomic concentrations (at. %) from survey spectra of ECM-rich and PM-rich regions on SA18 tissue section.

Core level	Peak BE (eV)	ECM-rich region (spot-1)	PM-rich region (spot-2)
		at. %	at. %
<b>C 1s</b>	285	68.6	80.0
<b>N 1s</b>	398	8.8	2.2
<b>O 1s</b>	531	20.9	16.7
<b>Cl 2p</b>	196	0.9	0.5
<b>P 2p</b>	131	0.5	0.6
<b>Na 1s</b>	1070	0.2	-
<b>S 2p</b>	162	0.1	-

As expected, large amounts of carbon and oxygen in their respective stoichiometry were found in both regions of the biological tissue, as these are fundamental elements (as well as hydrogen) in the composition of organic and biological matter. The higher amount of nitrogen present in the ECM-rich region is related to the greater number of proteins present in that region. Following this reasoning, the higher amount of chlorine may indicate the presence of specific amino acids such as alanine (Ala) and Phe [214], while sulphur may indicate the presence of proteoglycans such as chondroitin sulphate and heparan sulphate. Sodium is a common constituent of the ECM with different functions, including regulation of homeostatic mechanisms of the extracellular fluid that bathes all cells in the body [226], while phosphorous is part of cell membrane composition. On the other hand, the higher amounts of carbon and phosphorous together with a decrease in the amount of nitrogen in the PM-rich region are consistent with a cell membrane-rich environment. The same coherence is applied for the weak presence of sodium (see Na KLL Auger emission in Figure 5.19) and chlorine in this region since they are also present in the cytosol of cells developing an important role in osmotic pressure and fluids balance. In addition, despite the detection of metals such as copper and nickel by ToF-SIMS imaging in several glial scar tissue slices (including the SA18 slice), we were not able to identify these same elements by XPS analysis. This can be explained by the fact that the detection limit of the XPS technique ranges from 1.0 – 0.5% atomic not allowing trace analysis.

### 5.5.2 Core level spectra analysis from ECM and PM-rich regions

The high-resolution C 1s, N 1s, and O 1s core level spectra from ECM-rich and PM-rich regions are also studied to identify and quantify the surface chemical bonding states in these two regions. The C 1s, N 1s and O 1s core level spectra and their corresponding fitting are shown in Figure 5.20.

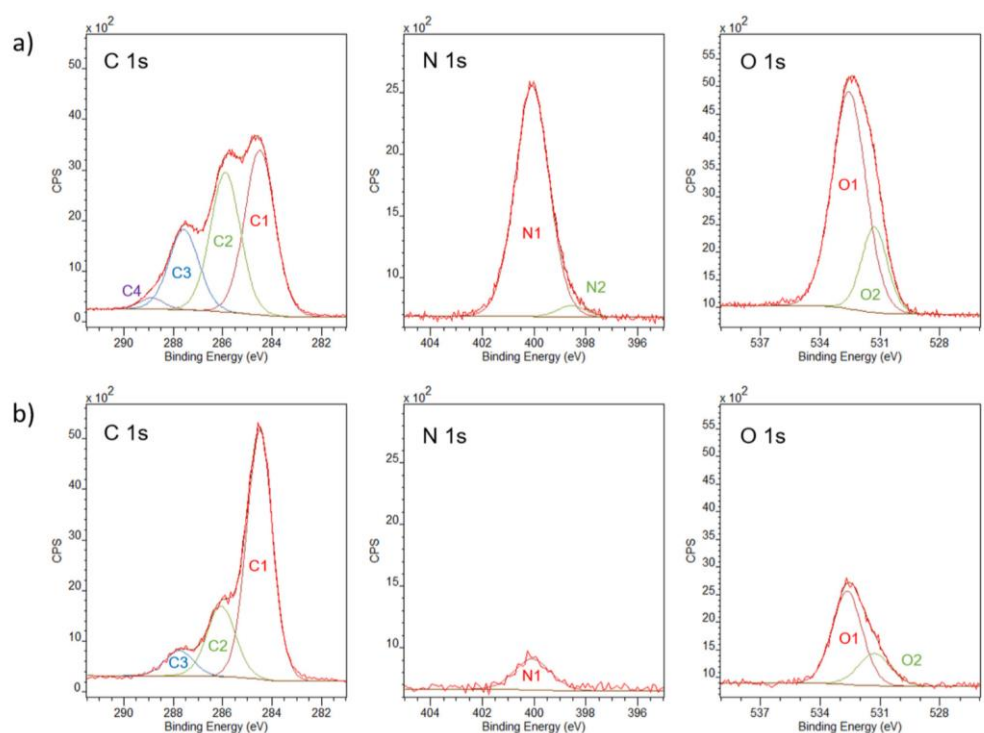


Figure 5.20. Curve fitting of the high-resolution spectra of C 1s, O 1s and N 1s core levels of different (a) extracellular matrix (ECM)- and (b) phospholipids membrane (PM)-rich environments on SA18 tissue section.

The same C 1s, O 1s, and N 1s environments have been evidenced by Rouxhet *et al.* [186, 187, 227] in their studies about the surface chemical composition of bio-organic systems and cells, and similarly assigned by Coullerez *et al.* [228] in their chemical studies of melamine-formaldehyde resins. The area percentage values for each C 1s, N 1s and O 1s chemical states are shown below in Table 5.6.

Table 5.6. Peak fitting parameters of high-resolution XPS analysis of ECM-rich and PM rich regions on SA18 tissue section.

Core level	Position (eV)	Assignment	Bonding state	ECM-rich region	PM-rich region
				(spot-1)	(spot-2)
				Peak area (%)	Peak area (%)
<b>C 1s</b>	248.8	C1	C–H/C–C/C=C	41.8	70.1
	286.2 – 286.3	C2	C–O/C–N	35.6	22.1
	287.9 – 288.0	C3	C=O/O=C–N	20.4	7.7
	289.2	C4	O=C–OH	2.2	–
<b>O 1s</b>	532.6	O1	C–O–C	77.1	73.0
	531.3	O2	O=C–OH	22.9	27.0
<b>N 1s</b>	400	N1	N–C/N=C	96.2	100
	398.5	N2	N–H	3.8	–

A comparative study of the C 1s, N 1s and O 1s spectra shows different bonding states for each region.

### 5.5.2.1 Chemical state assignments in the ECM-rich region

There were found four different carbon bonding states over the ECM-rich region as follows.

- The carbon from hydrocarbon structures (C1: —C—H/—C—C—/—C=C—) at 284.8 eV.
- The carbon from ether and amine environments (C2: —C—O—C—/—C—N—) at 286.2 eV.
- The carbon from carbonyl and amide environments (C3: —C=O—/—O=C—N—) at 287.9 eV.
- The carbon from carboxyl functionalities (C4: —O=C—OH) at 289.2 eV.

The similarity in C1 (41.8 at. %) and C2 (35.6 at. %) amounts indicates an ECM-rich region almost as rich in hydrocarbon bonds as in ether and amine groups that is in agreement with the chemical composition of this particular region, since proteoglycans are commonly made of ether bonds in their repetitive disaccharide units [201, 229] and amino acids made of amine bonds [215]. The following C3 (20.4 at. %) and C4 (2.2 at. %) amounts can be explained by the presence of amide groups found in some amino acids and chondroitin sulphate, and the presence of carboxyl groups found in amino acids and some proteoglycans.

Figure 5.21 below shows the carbon chemical environments (C1, C2, C3 e C4) in common amino acids and proteoglycan molecules already identified in the ECM-rich region.



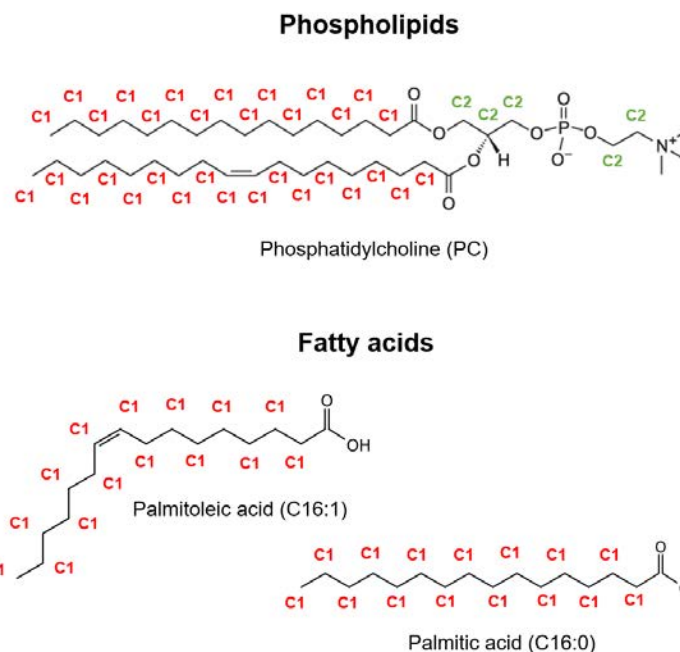


Figure 5.22. Chemical environments of carbon identified in some common phospholipids and fatty acids molecules found in the plasma membrane (PM)-rich region on the slice SA18.

The N 1s core level spectra shows only one nitrogen bonding state of low intensity, *i.e.*, the carbon—nitrogen bond from amine structures (N1: —N—C—) or the nitrogen of the ring structures of nitrogenous bases (N1: —N=C—) at 400.0 eV, still related to the low presence of amino acids in this region.

As regard the O 1s core level spectra, two different oxygen bonding states are shown, *i.e.*, the oxygen from an ether group (O1: —C—O—C—) at 532.5 eV and the oxygen from the carbonyl group (O2: —O=C—OH) at 531.3 eV. The O1 (73 at. %) and O2 (27 at. %) amounts have almost the same proportion found previously in the ECM-rich region and may indicate the same ether and carboxyl groups present in proteoglycans. Although the additional carbonyl content (~4 at.%) on this PM-rich region may be attributed to the presence of ester bonds between glycerol and FA molecules, it is not believed that the proportions of O1 and O2 bonding states differs significantly in the ECM-rich and the PM-rich regions.

## 5.6 HIGH-RESOLUTION CHEMICAL STATE MAPPING BY X-PEEM

In order to image the main chemical environments present in glial scar tissue, we observed the SA18 slice using PEEM for localization of the ECM-rich and PM-rich regions. However, no analysis could be performed on this glial scar tissue slice because little or almost no photoelectric emission was detected in the regions of interest for multimodal analysis. This may be an effect of the long exposure of the biological tissue to X-rays during the reoperation of the zones of interest inside the PEEM. After numerous attempts to obtain some photoelectric emission on the SA18 tissue, we then proceeded to the exploration and analysis of the SB22 slice. The exact location of the SB22 slice is about 80  $\mu\text{m}$  of distance of the intracranial device and can be schematically seen at “Glial scar tissue and scheme of

tissue cross section's location" in the appendix. Figure 5.23 below shows a schematic view of the new zone of interest for X-PEEM analysis.

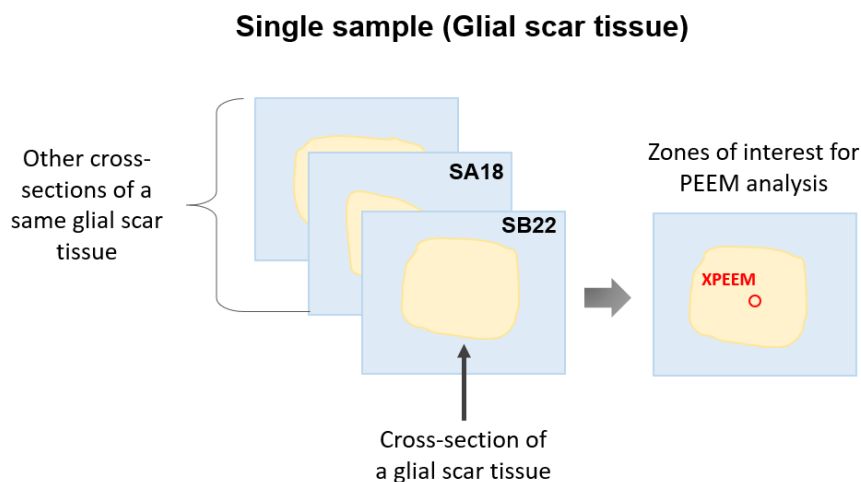


Figure 5.23. Schematic view of cross sections of a glial scar tissue formed around an implanted intracranial device on non-human primate's brain. A new region of interest on the SB22 is defined for X-PEEM analysis. This is the single sample where multimodal ToF-SIMS, XPS and X-PEEM surface imaging will be performed.

### 5.6.1 Secondary electron X-PEEM image: identification of a zone of interest

X-PEEM images at the photoemission threshold (secondary electrons) over a field-of-view (FoV) diameter of 160  $\mu\text{m}$  were recorded to obtain an overview of the sample surface and locate interesting features for further analysis. Please note that the lateral scales attainable with this technique are much smaller than that available by scanning x-ray photoelectron microprobes or other conventional XPS imaging instruments. Figure 5.24 shows a secondary electron image (photoemission threshold spectral region) recorded at the micron scale in a region on the SB22 slice of glial scar tissue.

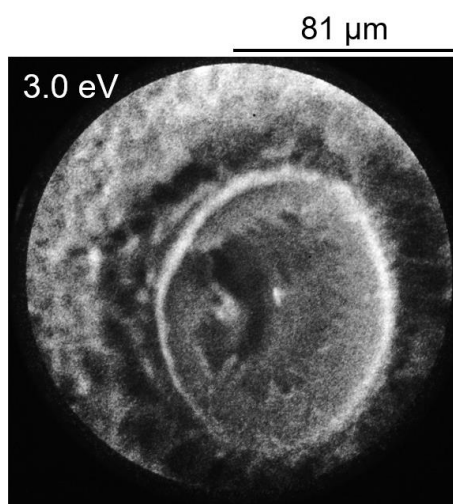


Figure 5.24. X-ray excited secondary electrons PEEM image at the microscale and at 3.0 eV from a small circular pattern in the SB22 slice of glial scar tissue.

The gray-scale contrast seen in Figure 5.24 might be due to the local work function (or surface potential) variations attributed to the different chemical composition found in this region containing a circular pattern. The application of XPS imaging techniques at high magnification and lateral resolution such as X-PEEM for analysis of biological surfaces is still rarely reported in the literature although some studies were published recently [115-117].

### **5.6.2 C 1s core level X-PEEM imaging: chemical-state analysis**

The imaging of the chemical bonding states of the SB22 glial scar tissue section was achieved by X-PEEM spectromicroscopy. As seen in the previous chapter, the first high-resolution spectrum acquired using X-PEEM analysis is benefited with the fact that the surface of interest has not yet been long exposed to X-rays. Knowing this, we will preferentially be interested in the acquisition of the C 1s X-PEEM high-resolution spectra. As raw signal-to-noise in each pixel from the images acquired by X-PEEM is too low to meaningfully work with spectra at pixels, the corresponding datasets were post-processed using first an Outlier Filter and then PCA noise reduction to produce spatially resolved spectra of sufficient quality to perform X-PEEM spatially resolved quantification.

In Figure 5.25(a) we can see a X-PEEM image showing the lateral distribution at the micron scale of the integral intensity of the post-processed C 1s spectra over the region of a circular pattern in the SB22 glial scar tissue section. A False Colour scale was used to assign colours to ranges of pixels intensities. This allows sets of pixels with similar intensities to be identified and then used to create spectra by summing spectra-at-pixel from pixels with the same false colour. We can observe a clear separation between two zones that we will call by R1 (blue pixels) and R2 (red pixels) in the centre of the region of interest that seems to follow the same circular pattern found in the X-ray excited SE PEEM image at 3.0 eV (see Figure 5.25(b)). In Figure 5.25(c) we can see the spectra generated from the C 1s spectra summation of the blue and red pixels for the R1 and R2 regions, respectively.

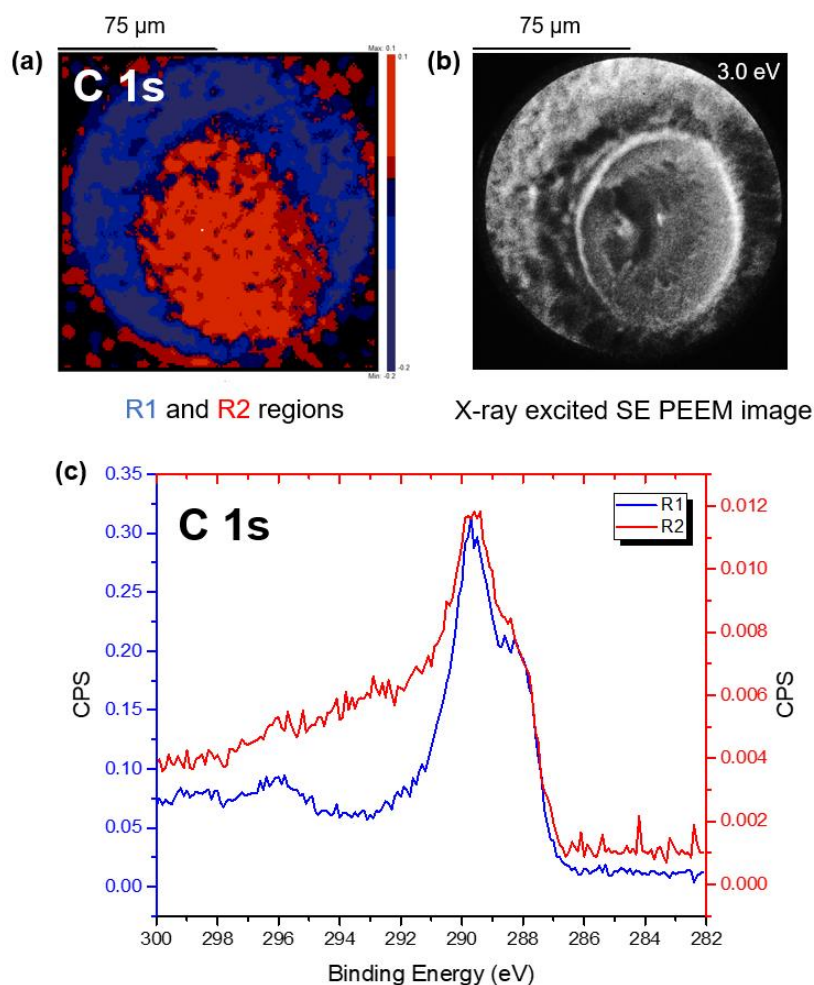


Figure 5.25. (a) X-PEEM image showing the lateral distribution at the micron scale of the integral intensity of the post-processed C 1s spectra over the region of interest. (b) X-ray excited secondary electrons PEEM image at the microscale and at  $E-E_f = 3.0$  eV from the region of interest (circular pattern) in the SB22 slice of glial scar tissue. (c) C 1s spectra generated from the summation of the blue and red pixels for the R1 and R2 regions, respectively.

In Figure 5.25(c) we can see that the shape of the C 1s X-PEEM summed spectra-at-pixels for R1 and R2 show a clear chemical contrast between both regions associated with chemical environments located at higher binding energies. Furthermore, both peak shapes appear very similar to the C 1s high-resolution spectrum for the ECM-rich region in the XPS case (Figure 5.20(a)). This allows us to assign the R1 region to the ECM- and the R2 region to the PM-related area.

In the following we tried to perform the chemical-state assignment of the summed spectra-at-pixels from R1 and R2 regions by discussing the overall binding energy shift for both spectra, as compared to the XPS spectra – the energy range for the X-PEEM C 1s spectra for both R1 and R2 regions begins around 286 eV and extends up to nearly 300 eV (compared to the range 283-290 eV for the XPS spectra, Figure 5.20(a)) and that is directly related to the magnitude of the positive surface potential which builds-up upon photoemission. Even despite C 1s was the first spectrum acquired in the zone of interest, this can be an effect of the exposure time to X-rays for this poorly-conductive biological surface during analysis,

possibly resulting in surface charging. However, because of the internal consistency between the XPS and the X-PEEM spectra, we can reasonably assume that the surface remained stable, chemically speaking, during the X-PEEM analysis.

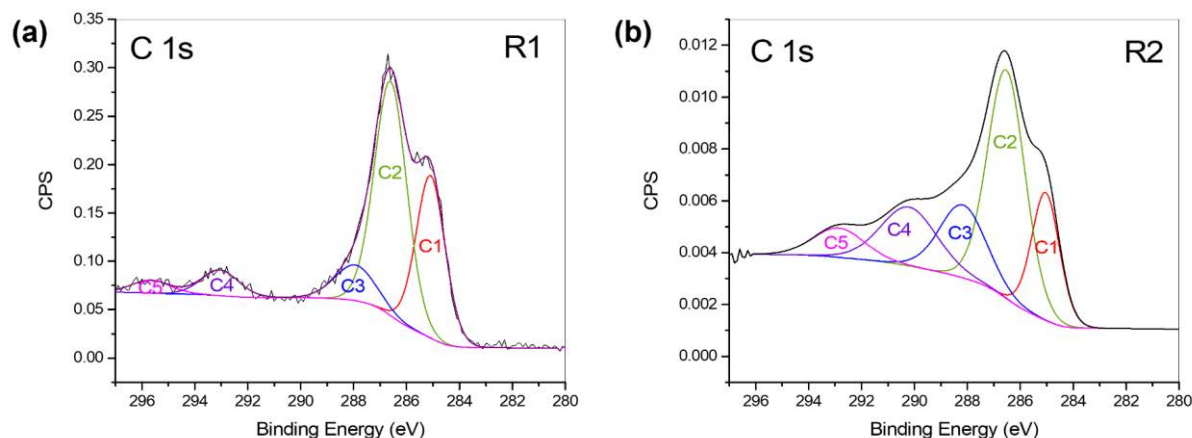


Figure 5.26. Curve fitting of the recalibrated C 1s X-PEEM high-resolution highlighting the chemical environments present in the (a) R1 and (b) R2 regions in the SB22 glial scar tissue section. The energy calibration shifted the C1 component to 284.8 eV.

In Figure 5.26 we present the peak fitting of the X-PEEM C 1s spectra for each R1 and R2 regions. As we can observe, the same bonding states found in ECM-rich regions of SA18 section in C 1s XPS spectrum (C1, C2, C3, C4) were also found in SB22 tissue section as shown in Figure 5.20(a) (exception for the C5 component that do not appears in the C 1s XPS spectrum): the agreement between XPS and X-PEEM on the one hand, and the internal consistency of C1s XPEEM spectra can be an indicative that despite some indicatives of surface charging – such as the C4 and C5 components being found severely shifted to higher energies, we can still correlate data from XPS and XPEEM high-resolution analysis.

Table 5.7 below shows the peak fitting parameters for C 1s high-resolution acquired from R1 and R2 regions through X-PEEM imaging.

Table 5.7. Peak fitting parameters for the recalibrated C 1s high-resolution X-PEEM spectra of R1 and R2 regions in the SB22 glial scar tissue section. The energy calibration shifted the C1 component to 284.8 eV.

Core level	Assignment	R1			R2		
		Position (eV)	FWHM	Area (%)	Position (eV)	FWHM	Area (%)
C 1s	C1	284.8	1.3	31.0	284.8	1.2	17.5
	C2	286.3	1.4	50.0	286.3	1.6	42.2
	C3	287.6	1.8	9.5	287.9	2.0	16.7
	C4	292.7	1.6	6.2	290.0	2.5	16.2
	C5	295.4	1.7	3.3	292.6	2.2	7.4

Besides the peak broadening at higher energies possibly due to charging effects, another possible explanation for the appearance of the C5 component, which differs from the components found by XPS,

may be associated with the detection of a chemical artifact in this specific region. In addition, if we associate the components from C1 to C3 (without considering the C4 and C5 components severely shifted to higher energies) to chemical environments that we already know from the XPS analysis, we will have the following scenario: the carbon from hydrocarbon structures (C1:  $\text{—C—H/—C—C—/—C=C—}$ ) up to 284.8 eV. The carbon from ether and amine environments (C2:  $\text{—C—O—C—/—C—N—}$ ) at 286.3 eV. The carbon from carbonyl and amide environments (C3:  $\text{—C=O—/—O=C—N—}$ ) at 287.9 eV. Considering the quantitative values of C1, C2 and C3 for each R1 and R2 regions, it is reasonable to say that higher amounts of C1 and C2 were found in the R1 region, which indicates a region of tissue especially rich in proteins, while higher amounts of C3 were found in the R3 region, otherwise indicating a region mainly rich in proteoglycans. The accumulation of proteoglycans surrounded by proteins on the glial scar tissue remains unexplained, maybe being part of the natural distribution of biomolecules on tissue or even a specific behaviour given by the previous contact with the intracranial device.

## 5.7 MULTIMODAL APPROACH DISCUSSION

The use of ToF-SIMS imaging was fundamental in addressing the questions involving biological tissues hosting implantable technologies such as drug delivery vehicles and intracranial devices. From the ToF-SIMS macro-imaging we were able to observe qualitative chemical contrasts based on different molecules over large areas on the surface of biological tissues. So far, we can mention the observation of HA hydrogel reabsorption in rodent brain tissue without infiltration to other areas of the brain. Further on, in a context of multimodal analysis and the use of principal component analysis in data processing, we can mention the identification of areas of necrosis and acute inflammation in regions of the glial scar tissue. In this case, we understood that regions showing phospholipids and fatty acids are representative of areas full of "exploded" cells while regions showing amino acids and proteoglycans are more associated with an extracellular environment.

The difficulty in reoperating zones of interest highlighted by ToF-SIMS in XPS microscopy can be considered moderate mainly because although almost no contrast is generated on the surface of the biological tissue while using scanning x-ray image (SXI), the maximum field of view of  $1350 \times 1350 \mu\text{m}^2$  allows for a wide view of landmarks in the sample ideal for navigating to the zones of interest. The reoperation and analysis of these same regions using XPS brings us the complementary quantitative information about these two areas. Survey and high-resolution XPS spectra indicate chemical environments rich in carbon bonds for the same regions where we found phospholipids and fatty acids by ToF-SIMS imaging. Similarly, survey and high-resolution XPS spectra indicate a balance between carbon bonds and ether and amine environments for the same regions of glial scar tissue where we found amino acids and proteoglycans by ToF-SIMS imaging. In fact, this correlation between molecular information and chemical environments for both of these regions are true, which indicates a strong consistency in the output information of these two techniques.

The difficulty of reoperating areas of interest highlighted by ToF-SIMS and analysed by XPS in X-PEEM starts with the easy charging of biological surfaces during navigation and exposure to x-rays. This causes local changes in the extraction electrical field and consequently little or no photoelectron is extraction from the regions of interest. Furthermore, the maximum field of view in X-PEEM imaging mode is about a few hundred micrometres of diameter and only allows for a narrow view of patterns in the surface of the biological tissue. Due to charge effects found during reoperation of zones of interest highlighted by ToF-SIMS and analysed by XPS, another zone of interest on another slice of the same glial tissue was finally analysed by PEEM. The high-resolution C 1s and O 1s spectrum acquired through X-PEEM analysis shows extra components located at higher energies. However, we can still say that the same bonding states found through XPS analysis (C1, C2, C3, C4) were also found through X-PEEM analysis. The consistency found between XPS and X-PEEM core-level spectra indicates that there is no significant detrimental effect of X-PEEM regarding surface stability upon X-ray exposure during analysis. However, it has been found that after 8-16 hours of exposure to x-rays, the zone of interest cannot be revisited for any other analysis due to its accentuated degradation.

Another aspect of the multimodal approach that must be taken into account is the detection limits of each technique. For the study of traces of metals in the glial scar tissue, for example, ToF-SIMS proved to be an excellent technique due to its high detection range from ppm to ppb. However, traces of copper and nickel identified by ToF-SIMS were not able to be identified by XPS and X-PEEM due to their lower sensitivities. The summary of the coherences and incoherent aspects found in our multimodal approach applied to biological tissues can be found below in Table 5.8.

*Table 5.8. Coherent and incoherent aspects of our multimodal ToF-SIMS, XPS and X-PEEM approach for analysis of biological tissues.*

Advantages	Disadvantages
ToF-SIMS macro imaging allows visualization of large areas on the surface of biological tissues	The biological surface is easily charged during PEEM navigation and damage after X-PEEM analysis
Moderate difficulty for reoperating zones of interest highlighted by ToF-SIMS in XPS	Reoperation of the same zones of interest by PEEM is not trivial due to its small FoV
Molecular information obtained by ToF-SIMS is coherent with chemical environments quantified by XPS	8-16 hours of exposure to x-rays leads to accentuated degradation of the zone of interest on the biological tissue
PEEM imaging on biological tissues is feasible and consistency between XPS and X-PEEM core-levels indicates surface stability during analysis	Detection limit of XPS and PEEM are insufficient to identify traces of metals such as copper and nickel in the biological tissue

## 5.8 CONCLUSIONS

In summary, using the ToF-SIMS imaging we had access to the lateral distribution of small molecules (0 - 1000 Da) present on the top surface of the biological system. We verify the remaining existence of HA hydrogel as a drug delivery vehicle used in the treatment of glioblastoma inside the surgical area of a rodent's brain even after 3 months of implantation. We also observed that there was no indication of infiltration of the HA hydrogel into other areas of the brain that should not be affected and, besides that, the main chemical structures in the deeper regions of the brain (e.g., phospholipids, fatty acids, cholesterol, sulfoglycosphingolipids, etc.) remained unchanged. At this point, we must emphasize how important this information is in the development of effective drug delivery vehicles that ensure the sustainability and controllability of drug delivery within the target tumour site and that minimizes the adverse effects of systemic exposure to drugs carried by HA hydrogels. Later, we observed that ToF-SIMS imaging combined with PCA data processing proved to be an essential tool in evidencing chemical contrasts present in a glial scar tissue developed around an intracranial device used in brain-computer interfaces. In addition to being able to identify the main molecules present in the glial scar tissue, we observed an abnormal distribution of phospholipids and fatty acids (PM-rich region) among amino acids and proteoglycans (ECM-rich region). This abnormal distribution of phospholipids and fatty acids may be associated with the plasma membrane of “exploded” cells in the glial scar tissue, thus indicating that part of the inflammation generated by the implantation of an intracranial device was not reversible and part of the glial scar tissue became necrotic. Further on, the excellent limit of detection of ToF-SIMS ranging from ppm to ppb allowed for the imaging of copper and nickel traces in several slices of glial scar tissue. Copper presented a more homogeneous distribution on glial scar tissue slices while nickel was seen in localized spots. Besides that, nickel was also found close to black spots in the glial scar tissue associated with MWCNTs that may have been snatched from the intracranial device electrodes along the implantation period. Although copper is part of the composition of the intracranial device, its homogeneous distribution indicates that the identified copper might be actually from metalloproteins associated with the synthesis of elastin and collagen abundant in glial scar tissues. On the other hand, the presence of nickel can only be explained through a chemical instability of the intracranial device and its physical proximity to MWCNTs reinforces the idea that the immune system considered both nickel and MWCNTs fragments as foreign invaders and tried to isolate them in the glial scar tissue.

The quantification of the surface composition in glial scar tissue was achieved through XPS analysis. The same PM-rich and ECM-rich regions previously analysed by ToF-SIMS were reoperated in XPS and variable amounts of carbon, oxygen, nitrogen, chlorine, phosphorous, sodium, and sulphur were detected on the top surface of the glial scar tissue through the XPS survey spectra. Besides that, several chemical environments could be identified and quantified on the top surface of each PM-rich and ECM-rich region regions in the glial scar tissue. In the ECM-rich regions, there was found almost similar amounts of hydrocarbons, esters and amines, the presence of amides and carbonyls are also remarkable in this region, which seems coherent with environments of amino acids and proteoglycans. In the PM-rich regions, on the other hand, there was an additional presence of hydrocarbon environments attributed to the large chains of fatty acids connected to phospholipid molecules.

The imaging of the chemical environments present in the glial scar tissue was performed at the micrometre scale by X-PEEM analysis. However, the same PM-rich and ECM-rich region could not be reoperated inside the PEEM equipment due to excessive charge effects generated on the surface of the biological sample upon X-ray exposure thus leading us to analyse another slice of glial scar tissue instead. In this new slice of glial scar tissue, a region containing a circular pattern was identified and imaged with secondary electrons (photoemission threshold) at the microscale in the energy-filtered PEEM mode. From this same circular region in the glial scar tissue, we obtained high-resolution C 1s spectra from which we can identify the existence of the same chemical environments found in the ECM-rich regions by XPS (C1, C2, C3, C4). The C5 component detected in the C 1s X-PEEM spectrum might be probably associated with a chemical artifact in that specific region or to the peak broadening due to charge effects. The consistency found between XPS and X-PEEM core-level spectra indicated that there is no significant detrimental effect of X-PEEM regarding surface stability upon X-ray exposure during analysis. Furthermore, we were able to visualize the distribution of chemical environments in the circular pattern. Hydrocarbon bonds were found throughout the analysed area, while amino environments related to proteins were found mainly outside the circular region and carbonyl environments related to proteoglycans mainly inside. This chemical distribution inside a circular pattern in the glial scar tissue remains unexplained.

In other words, we can conclude that our multimodal surface analysis approach is compatible with biological systems hosting implantable biomedical technologies with some caveats. Positive aspects in our multimodal surface analysis approach applied to biological systems include:

- ToF-SIMS imaging provides visualization of large areas on the surface of biological tissues ideal for navigation and identification of zones of interest for further multimodal analysis,
- There is a moderate difficulty for reoperating zones of interest highlighted by ToF-SIMS in XPS,
- Molecular information obtained by ToF-SIMS is coherent with chemical environments quantified by XPS,
- PEEM imaging on biological tissues is feasible and consistency between XPS and X-PEEM core-levels indicates biological surface stability during analysis.

The negative aspects in our multimodal surface analysis approach applied to biological systems include:

- The biological surface is easily charged during exposure to X-rays for PEEM navigation,
- Reoperation of same zones of interest by PEEM is not trivial due to its small field of view,
- Hours of surface exposure to x-rays leads to accentuated degradation of zones of interest on the biological tissue,
- Detection limit of XPS and PEEM are insufficient to identify traces of metals such as copper and nickel in the biological tissue.

As we can notice, the negative aspects of the multimodal approach on biological samples are more associated with the use of X-PEEM. However, despite the difficulties encountered, the balance is still positive and the XPEEM results are providing a proof of concept showing the complement imaging

capabilities of complex biological tissues for chemical surface analysis in combination with ToF-SIMS and XPS.



## FINAL CONCLUSIONS AND PROSPECTS

---

The use of multimodal and multiscale approaches to characterize biomedical surfaces and interfaces has proved to be an essential tool for providing a better understanding of chemical process that occur at the outermost part of such materials. We have seen in this work different multimodal approaches applied to solve healthcare issues associated to biomedical interfaces at different levels of sophistication based on the complexity of navigation to the same areas of interest.

- 1) ***At the first level of sophistication***, we explored different drug delivery systems for the treatment of glioblastoma before implantation in a non-human brain. At this level, no zone of interest was particularly defined for multimodal analysis (Chapter 3). We were able to **(i) map by ToF-SIMS the distribution** of ketorolac tromethamine and gellan gum microcapsules in HA hydrogel used in drug delivery in glioblastoma cases. HA hydrogel formulations containing 10 mg of ketorolac tromethamine showed more heterogeneous distribution compared to formulations with 2 mg, possibly indicating formulation saturation given the greater amount of ketorolac tromethamine used; **(ii) image by AFM the fibrillar morphology** of gellan gum microcapsules; **(iii) quantify by XPS chemical environments** of HA hydrogel, ketorolac tromethamine and gellan gum microcapsules, as well as observe the effect of the addition of ketorolac tromethamine and gellan gum microcapsules in HA hydrogel in terms of chemical environments.
- 2) ***At the second level of sophistication***, we started to focus on the analysis of the same sample: O.C.T.<sup>TM</sup> compound, but still in two different regions of analysis showing chemical contrast on this sample (Chapter 4). Here, we were able to **(i) map by ToF-SIMS the existence** of two chemical contrast zones (S1- and S2-OCT) in the O.C.T.<sup>TM</sup> compound. These two chemical contrast zones were found to consist of oxygenated organic compounds, while groups of phosphates, sulphates, benzalkonium chloride and fatty acids were found separately distributed in these two regions; **(ii) confirm by Tandem MS the existence** of fatty acids in one of the zones of chemical contrast (S1-OCT) based on the study of ion fragmentation at  $m/z$  255.22 found as a characteristic of palmitic acid; **(iii) quantify by XPS chemical environments** of the S1- and S2-OCT regions. In agreement with the ToF-SIMS results, we found in the S1-OCT region chemical environments characteristic of PEG and fatty acids. While in the S2-OCT region we found chemical environments of PVA and benzalkonium chloride. This indicates a possible heterogeneity in the distribution of these compounds in the composition of the O.C.T.<sup>TM</sup> compound; **(iv) imaging by X-PEEM the chemical environments** found in the S1- and S2-OCT regions. With the limitation of the field-of-view for energy-filtered PEEM image analysis around 230  $\mu\text{m}$ , we decided to proceed with analysis in a smaller S1-OCT region. Large broadening and shifting to higher energies of high-resolution spectra were probably observed due to long exposure to X-rays of the area of interest. This represented a complication in

creating reliable fitting models aiming to highlight chemical environments presents in these regions. Nevertheless, in more general terms, despite the peak broadening, we were able to obtain curves for the C1s and O1s high-resolution spectra similar in shape to those obtained by XPS.

- 3) ***At the third level of sophistication***, in addition to focusing on the analysis of the same sample: neural tissues of a rodent and a non-human primate, we tried to correlate information acquired from the analysis of the same area of interest specifically in the neural tissue of a non-human primate (Chapter 5). At this level, we were able to **(i) verify by ToF-SIMS the existence** of HA hydrogel as a drug delivery vehicle used in the treatment of glioblastoma inside the surgical area of a rodent's brain even after 3 months of implantation, as well as observe an abnormal distribution of phospholipids and fatty acids (PM-rich region) among amino acids and proteoglycans (ECM-rich region) in a glial scar tissue formed around an implanted intracranial device. This abnormal distribution of phospholipids and fatty acids may be associated with the plasma membrane of “exploded” cells in the glial scar tissue, thus indicating that part of the inflammation generated by the implantation of an intracranial device was not reversible and part of the glial scar tissue became necrotic; **(ii) quantify by XPS the surface composition** in PM- and ECM-rich regions previously analysed. In the ECM-rich regions, hydrocarbons, esters, amines, amides and carbonyls were found in coherent amounts with environments of amino acids and proteoglycans. In the PM-rich regions, on the other hand, there was noticed an additional presence of hydrocarbon environments attributed to the large chains of fatty acids connected to membrane phospholipids; **(iii) imaging by X-PEEM of the chemical environments** present in the glial scar tissue at the  $\mu\text{m}$  scale. The same PM-rich and ECM-rich region could not be reanalysed inside the PEEM equipment due to excessive charge effects generated on the surface of the SA18 slice upon X-ray exposure thus leading us to analyse another slice of glial scar tissue instead. From this new region in the glial scar tissue, we obtained high-resolution C 1s spectra from which we can identify the existence of the same chemical environments found in the ECM-rich regions by XPS. The extra components detected in the C1s X-PEEM spectrum might be associated with a chemical artefact in that specific region or to the peak broadening due to charge effects similarly observed in the second level of sophistication.

The ToF-SIMS has proven to be an excellent exploratory tool at all levels of sophistication of the multimodal surface imaging approach. This technique allowed us to reach two of the main intermediate objectives proposed in this work, which are: identification of chemical surface species and chemically distinct regions in biomedical surfaces. This was achieved primarily due to the ability to generate laterally resolved molecular information in large areas on the surface of the sample. Besides that, ToF-SIMS offers the option of acquiring mm size images over biomedical surfaces from putting images or tiles up to  $500\ \mu\text{m} \times 500\ \mu\text{m}$  together. This tool is of great importance in identifying areas of interest on the sample. The pixel size was chosen to be  $1.95\ \mu\text{m}$  (close to the lateral resolution used and allowed us to distinguish small features on our samples of interest. The high mass resolution of ToF-SIMS for these

imaging parameters is also an advantage and allowed us to analyse the chemical structure of the sample with good accuracy. However, when smaller features are desired to be imaged (using e.g., a FoV smaller than 100  $\mu\text{m}$ ), better lateral resolutions are required and then parameters that support a balance between mass resolution and lateral resolution should be preferred. Another aspect that must be taken into consideration is the topography of the analysed surface mainly because sharp topographical differences can create zones of little or no secondary emission over the analysed surface. The excellent detection limit of ToF-SIMS in the ppm-ppb range is also a great tool in detecting traces of possible contaminants in biomedical systems. Furthermore, when ToF-SIMS mass spectrum are treated with PCA data processing, we can reduce noise and highlight trends and patterns in the data that can be useful in discerning the chemical composition of ROIs. This set of possibilities allowed ToF-SIMS to image (i) drugs and microcapsules in drug delivery systems based on HA hydrogel not yet implanted in non-human brains, (ii) regions on a same O.C.T. compound sample that could be easily confused with biological tissue due to presence of similar chemical markers, (iii) the reabsorption of HA hydrogel directly into a cross-section of rodent's brain tissue and the imaging of contaminants such as nickel that possibly caused severe inflammation in the glial scar tissue formed around an intracranial device implanted in a primate non-human brain.

The Tandem MS is a similar technique to ToF-SIMS, however, this technique disposes of a second mass analyser where a breakdown of selected ions (precursor ions) into fragments (product ions) occurs. These product fragments reveal then aspects of the chemical structure of the precursor ion that is extremely useful in refining the assignment of molecular ions initially identified in the ToF-SIMS mass spectrum. We observed the Tandem MS successful employment at the second level of sophistication of the multimodal approach where it is used in the study of palmitic acid  $m/z$  255.22 fragmentation and confirms the assignment of fragments of fatty acids in one of the regions of interest in the O.C.T.<sup>TM</sup> compound.

The AFM was used in this work as a complementary tool (as well as Tandem MS) that was intended to identify morphologically distinct regions in biomedical systems. However, AFM is limited to analysis of areas with a maximum size of  $100 \times 100 \mu\text{m}^2$  (xy) and a maximum topographical variation of up to 10  $\mu\text{m}$  (z), which restricted its application in the analysis of most biomedical interfaces discussed in this work. It was applied at the first level of sophistication in the visualization of the fibrillar morphology of the surface of gellan gum microcapsules. The results obtained showed a great potential for future studies in giving indications of how the absorption and release of therapeutic drugs can happen through these surfaces. However, AFM was not found to be an appropriate tool in the multimodal and multiscale observation of biomedical surfaces in the second and third levels of sophistication. However, for other biological systems the AFM can be extremely pertinent.

The XPS was used at all levels of sophistication of the multimodal surface imaging approach (as well as ToF-SIMS). It was the tool that allowed us to reach our third intermediate goal which was to quantify chemical environments directly on the surface of biomedical systems in precise regions of interest. Some poorly conductive biomedical systems presented difficulties to be analysed because charge effects were found on their surface, notably on the surface of freeze-dried HA hydrogels. In general, we

were able to quantify through characteristic spectra the influence of the addition of ketorolac tromethamine and gellan gum microcapsules in HA hydrogels, the chemical environments present in chemically contrasting zones in O.C.T.<sup>TM</sup> Compound, as well as quantifying chemical environments related to zones of necrosis and severe inflammation directly in biological tissues. We could notice that one of the limitations of XPS in this work was its relatively low detection limit (1.0 – 0.5% atomic). Traces of metals such as nickel that were identified in glial scar tissue by ToF-SIMS could not be identified by XPS either. In general, we observed that chemical information obtained from both XPS and ToF-SIMS presented coherence over the same samples or same regions of interest for analysis.

PEEM imaging was used at the second level of sophistication of the multimodal surface imaging approach for chemical environment imaging of ROIs in the O.C.T.<sup>TM</sup> compound but also at the third level of sophistication for chemical environment imaging of ROIs in glial scar tissues. In both cases we observed grey scale contrast due to the work function variations attributed to the different chemical composition found in these regions. The reoperation of the same ROIs analysed by ToF-SIMS and XPS in PEEM was found not trivial due to its smaller FoV (around 200  $\mu\text{m}$  of diameter). Then, we observed that PEEM imaging on the O.C.T.<sup>TM</sup> compound was feasible and that the consistency between XPS and X-PEEM core-levels indicated surface stability during the first analysis. However, after the second analysis we observed that the surface of the O.C.T.<sup>TM</sup> compound underwent charging after the first 8 hours of X-PEEM core level analysis and charging effects such as peak shifting and broadening are then frequently seen. The same behaviour was observed over biological samples in addition of a strong charge effect that do not allowed correlative X-PEEM imaging analysis at the same SA18 slice of glial scar tissue analysed by ToF-SIMS and XPS. Nevertheless, quantification of chemical states was observed to be potentially more accurate in PEEM than in XPS due to the higher lateral resolution of the analysis.

In terms of future works, we can mention the following topics:

- a) The development of protocols of sample preparation adapted to biological samples that allow thinner slices of biological tissue to be obtained (less than 20  $\mu\text{m}$ ) may be one of the possible solutions for decreasing the charge effects during PEEM imaging of biological surfaces.
- b) Due to the specific difficulties attributed to the navigation and reoperation of areas of interest in PEEM analysis, other techniques such as FIB can be used to intentionally produce landmarks on the surface of the sample that help to indicate the location of areas of interest.
- c) For a more adequate study of the morphology of gellan gum microcapsules by AFM, it is advised that microcapsules might be analysed already in their hydrated state without the use of any solution (such as aqueous or saline solutions used in this work), this should be essential to avoid the formation of clusters of gellan gum microcapsules allowing the analysis of the morphology of these microcapsules individually.
- d) After the successful imaging ketorolac tromethamine and gellan gum microcapsules in HA hydrogel, as well as the imaging of the reabsorption of pure HA hydrogel in rodent brain tissue, we can put into perspective the imaging of HA hydrogel formulations containing ketorolac tromethamine and gellan gum microcapsules directly into non-human brains for the study of

drug liberation and drug absorption after implantation. This was one of the initial objectives of this work, however, with the advent of the covid-19 pandemic and with the period of lockdown and stoppage of work in laboratories, the preparation of this type of sample was delayed and we reached the end of this thesis without being able to access them. However, the protocols developed in this thesis should allow such analysis in the future.



## BIBLIOGRAPHY

---

1. Gao, P., et al., *Biomedical applications of 2D monoelemental materials formed by group VA and VIA: a concise review*. Journal of Nanobiotechnology, 2021. **19**(1): p. 96.
2. Clegg, J.R. and N.A. Peppas, *Molecular recognition with soft biomaterials*. Soft Matter, 2020. **16**(4): p. 856-869.
3. Gong, X., *Self-Assembly Technique for Biomedical Applications*. Nano LIFE, 2015. **05**(02): p. 1542002.
4. David G. Castner, B.D.R., *Biomedical surface science: Foundations to frontiers*. Elsevier, 2002. **500**(1-3): p. 28-60.
5. Kasemo, B., *Biological surface science*. Surface Science, 2002. **500**(1): p. 656-677.
6. Anderson, J.M., *Biological Responses to Materials*. Annual Review of Materials Research, 2001. **31**(1): p. 81-110.
7. Rosso, F., et al., *From Cell-ECM interactions to tissue engineering*. Journal of Cellular Physiology, 2004. **199**(2): p. 174-180.
8. Muniyandi, P.P., V.; Veerananarayanan, S.; Ukai, T.; Maekawa, T.; Hanajiri, T.; Mohamed, M.S., *ECM Mimetic Electrospun Porous Poly (L-lactic acid) (PLLA) Scaffolds as Potential Substrates for Cardiac Tissue Engineering*. Polymers, 2020. **12**(2): p. 451.
9. Zemans, R.L., et al., *Conceptual Approaches to Lung Injury and Repair*. Annals of the American Thoracic Society, 2015. **12**(Supplement 1): p. S9-S15.
10. Olajuyin, A.M., X. Zhang, and H.-L. Ji, *Alveolar type 2 progenitor cells for lung injury repair*. Cell Death Discovery, 2019. **5**(1): p. 63.
11. Basil, M.C., et al., *The Cellular and Physiological Basis for Lung Repair and Regeneration: Past, Present, and Future*. Cell Stem Cell, 2020. **26**(4): p. 482-502.
12. Stock, S.R., *The Mineral-Collagen Interface in Bone*. Calcified Tissue International, 2015. **97**(3): p. 262-280.
13. Errassifi, F., et al., *Infrared, Raman and NMR investigations of risedronate adsorption on nanocrystalline apatites*. Journal of Colloid and Interface Science, 2014. **420**: p. 101-111.
14. Saidak, Z. and P.J. Marie, *Strontium signaling: Molecular mechanisms and therapeutic implications in osteoporosis*. Pharmacology & Therapeutics, 2012. **136**(2): p. 216-226.
15. Rachner, T.D., S. Khosla, and L.C. Hofbauer, *Osteoporosis: now and the future*. The Lancet, 2011. **377**(9773): p. 1276-1287.
16. Shahmoradi, M., et al., *Fundamental Structure and Properties of Enamel, Dentin and Cementum*, in *Advances in Calcium Phosphate Biomaterials*, B. Ben-Nissan, Editor. 2014, Springer Berlin Heidelberg: Berlin, Heidelberg. p. 511-547.
17. Tirrell, M., E. Kokkoli, and M. Biesalski, *The role of surface science in bioengineered materials*. Surface Science, 2002. **500**(1): p. 61-83.
18. Decelle, J., et al., *Algal Remodeling in a Ubiquitous Planktonic Photosymbiosis*. Current Biology, 2019. **29**(6): p. 968-978.e4.
19. Solé-Domènech, S., et al., *Localization of cholesterol, amyloid and glia in Alzheimer's disease transgenic mouse brain tissue using time-of-flight secondary ion mass spectrometry (ToF-SIMS) and immunofluorescence imaging*. Acta Neuropathologica, 2013. **125**(1): p. 145-157.
20. Stauber, J., et al., *On-tissue protein identification and imaging by MALDI-Ion mobility mass spectrometry*. Journal of the American Society for Mass Spectrometry, 2010. **21**(3): p. 338-347.
21. Peter Sjövall, B.J., Jukka Lausmaa, *Localization of lipids in freeze-dried mouse brain sections by imaging TOF-SIMS*. Elsevier, 2006(Applied Surface Science).
22. Fletcher, J.S. and J.C. Vickerman, *A new SIMS paradigm for 2D and 3D molecular imaging of bio-systems*. Analytical and Bioanalytical Chemistry, 2010. **396**(1): p. 85-104.
23. Xia, N., et al., *Time-of-Flight Secondary Ion Mass Spectrometry Analysis of Conformational Changes in Adsorbed Protein Films*. Langmuir, 2002. **18**(10): p. 4090-4097.

24. Kompauer, M., S. Heiles, and B. Spengler, *Atmospheric pressure MALDI mass spectrometry imaging of tissues and cells at 1.4-um lateral resolution*. *Nature Methods*, 2017. **14**(1): p. 90-96.
25. Schaepe, K., et al., *Imaging of Lipids in Native Human Bone Sections Using TOF–Secondary Ion Mass Spectrometry, Atmospheric Pressure Scanning Microprobe Matrix-Assisted Laser Desorption/Ionization Orbitrap Mass Spectrometry, and Orbitrap–Secondary Ion Mass Spectrometry*. *Analytical Chemistry*, 2018. **90**(15): p. 8856-8864.
26. Patel, D.I., et al., *Introduction to near-ambient pressure x-ray photoelectron spectroscopy characterization of various materials*. *Surface Science Spectra*, 2019. **26**(1): p. 016801.
27. Delcorte, A., et al., *Large cluster ions: soft local probes and tools for organic and bio surfaces*. *Physical Chemistry Chemical Physics*, 2020. **22**(31): p. 17427-17447.
28. Fletcher, J.S., et al., *TOF-SIMS 3D Biomolecular Imaging of Xenopus laevis Oocytes Using Buckminsterfullerene (C60) Primary Ions*. *Analytical Chemistry*, 2007. **79**(6): p. 2199-2206.
29. Bich, C., et al., *Argon Cluster Ion Source Evaluation on Lipid Standards and Rat Brain Tissue Samples*. *Analytical Chemistry*, 2013. **85**(16): p. 7745-7752.
30. Gamble, L.J., et al., *ToF-SIMS of tissues: “Lessons learned” from mice and women*. *Biointerphases*, 2015. **10**(1): p. 019008.
31. Castner, D.G., *Biomedical surface analysis: Evolution and future directions (Review)*. *Biointerphases*, 2017. **12**(2): p. 02C301.
32. Robinson, M.A., D.J. Graham, and D.G. Castner, *ToF-SIMS Depth Profiling of Cells: z-Correction, 3D Imaging, and Sputter Rate of Individual NIH/3T3 Fibroblasts*. *Analytical Chemistry*, 2012. **84**(11): p. 4880-4885.
33. Barnes, C.A., et al., *The surface molecular functionality of decellularized extracellular matrices*. *Biomaterials*, 2011. **32**(1): p. 137-143.
34. Vaidyanathan, S., et al., *Explanatory multivariate analysis of ToF-SIMS spectra for the discrimination of bacterial isolates*. *Analyst*, 2009. **134**(11): p. 2352-2360.
35. Sämfors, S., et al., *Localised lipid accumulation detected in infarcted mouse heart tissue using ToF-SIMS*. *International Journal of Mass Spectrometry*, 2019. **437**: p. 77-86.
36. Bluestein, B.M., et al., *An unsupervised MVA method to compare specific regions in human breast tumor tissue samples using ToF-SIMS*. *Analyst*, 2016. **141**(6): p. 1947-1957.
37. Brulet, M., et al., *Lipid mapping of colonic mucosa by cluster TOF-SIMS imaging and multivariate analysis in cfr knockout mice*. *Journal of Lipid Research*, 2010. **51**(10): p. 3034-3045.
38. Shannon, R.R.a.F., . Brian J. *Microscope*. *Encyclopedia Britannica* 2020; Available from: <https://www.britannica.com/technology/microscope>.
39. Thorn, K., *A quick guide to light microscopy in cell biology*. *Molecular biology of the cell*, 2016. **27**(2): p. 219-222.
40. Johansson, P.K., L. Schmäser, and D.G. Castner, *Nonlinear Optical Methods for Characterization of Molecular Structure and Surface Chemistry*. *Topics in Catalysis*, 2018. **61**(9): p. 1101-1124.
41. Depciuch, J., et al., *Raman and FTIR spectroscopy in determining the chemical changes in healthy brain tissues and glioblastoma tumor tissues*. *Spectrochimica Acta Part A: Molecular and Biomolecular Spectroscopy*, 2020. **225**: p. 117526.
42. Elshemey, W.M., A.M. Ismail, and N.S. Elbialy, *Molecular-Level Characterization of Normal, Benign, and Malignant Breast Tissues Using FTIR Spectroscopy*. *Journal of Medical and Biological Engineering*, 2016. **36**(3): p. 369-378.
43. Walsh, M.J., et al., *Attenuated total reflectance Fourier-transform infrared spectroscopic imaging for breast histopathology*. *Vibrational Spectroscopy*, 2012. **60**: p. 23-28.
44. Bird, B., et al., *Detection of breast micro-metastases in axillary lymph nodes by infrared micro-spectral imaging*. *Analyst*, 2009. **134**(6): p. 1067-1076.
45. Kallenbach-Thieltges, A., et al., *Label-free, automated classification of microsatellite status in colorectal cancer by infrared imaging*. *Scientific Reports*, 2020. **10**(1): p. 10161.
46. Kallenbach-Thieltges, A., et al., *Immunohistochemistry, histopathology and infrared spectral histopathology of colon cancer tissue sections*. *Journal of Biophotonics*, 2013. **6**(1): p. 88-100.

47. Nallala, J., et al., *Infrared imaging as a cancer diagnostic tool: Introducing a new concept of spectral barcodes for identifying molecular changes in colon tumors*. *Cytometry Part A*, 2013. **83A**(3): p. 294-300.
48. Chrabaszcz, K., et al., *Label-free FTIR spectroscopy detects and visualizes the early stage of pulmonary micrometastasis seeded from breast carcinoma*. *Biochimica et Biophysica Acta (BBA) - Molecular Basis of Disease*, 2018. **1864**(11): p. 3574-3584.
49. Bird, B., et al., *Infrared spectral histopathology (SHP): a novel diagnostic tool for the accurate classification of lung cancer*. *Laboratory Investigation*, 2012. **92**(9): p. 1358-1373.
50. Rzeznik, L., et al., *Microscopic Insight into the Sputtering of Thin Polystyrene Films on Ag{111} Induced by Large and Slow Ar Clusters*. *The Journal of Physical Chemistry C*, 2008. **112**(2): p. 521-531.
51. Song, C.L., et al., *Thermal effect on dispersive infrared spectroscopic imaging of prostate cancer tissue*. *Journal of Biophotonics*, 2018. **11**(12): p. e201800187.
52. Baker, M.J., et al., *Investigating FTIR based histopathology for the diagnosis of prostate cancer*. *Journal of Biophotonics*, 2009. **2**(1-2): p. 104-113.
53. Hands, J.R., et al., *Investigating the rapid diagnosis of gliomas from serum samples using infrared spectroscopy and cytokine and angiogenesis factors*. *Analytical and Bioanalytical Chemistry*, 2013. **405**(23): p. 7347-7355.
54. Walsh, M.J., et al., *IR microspectroscopy: potential applications in cervical cancer screening*. *Cancer Letters*, 2007. **246**(1): p. 1-11.
55. Sitnikova, V.E., et al., *Breast cancer detection by ATR-FTIR spectroscopy of blood serum and multivariate data-analysis*. *Talanta*, 2020. **214**: p. 120857.
56. Ferreira, I.C.C., et al., *Attenuated Total Reflection-Fourier Transform Infrared (ATR-FTIR) Spectroscopy Analysis of Saliva for Breast Cancer Diagnosis*. *Journal of Oncology*, 2020. **2020**: p. 4343590.
57. Gajjar, K., et al., *Fourier-transform infrared spectroscopy coupled with a classification machine for the analysis of blood plasma or serum: a novel diagnostic approach for ovarian cancer*. *Analyst*, 2013. **138**(14): p. 3917-3926.
58. Lyng, F.M., et al., *Discrimination of breast cancer from benign tumours using Raman spectroscopy*. *PLOS ONE*, 2019. **14**(2): p. e0212376.
59. Abramczyk, H., et al., *Raman 'optical biopsy' of human breast cancer*. *Progress in Biophysics and Molecular Biology*, 2012. **108**(1): p. 74-81.
60. Pacia, M.Z., et al., *Estimation of the content of lipids composing endothelial lipid droplets based on Raman imaging*. *Biochimica et Biophysica Acta (BBA) - Molecular and Cell Biology of Lipids*, 2020. **1865**(9): p. 158758.
61. Zheng, X., et al., *Rapid and non-invasive screening of high renin hypertension using Raman spectroscopy and different classification algorithms*. *Spectrochimica Acta Part A: Molecular and Biomolecular Spectroscopy*, 2019. **215**: p. 244-248.
62. Pacia, M.Z., et al., *Rapid biochemical profiling of endothelial dysfunction in diabetes, hypertension and cancer metastasis by hierarchical cluster analysis of Raman spectra*. *Journal of Raman Spectroscopy*, 2016. **47**(11): p. 1310-1317.
63. Duncan, M.D., J. Reintjes, and T.J. Manuccia, *Scanning coherent anti-Stokes Raman microscope*. *Optics Letters*, 1982. **7**(8): p. 350-352.
64. Zumbusch, A., G.R. Holtom, and X.S. Xie, *Three-Dimensional Vibrational Imaging by Coherent Anti-Stokes Raman Scattering*. *Physical Review Letters*, 1999. **82**(20): p. 4142-4145.
65. Evans, C.L., et al., *Chemical imaging of tissue in vivo with video-rate coherent anti-Stokes Raman scattering microscopy*. *Proceedings of the National Academy of Sciences of the United States of America*, 2005. **102**(46): p. 16807.
66. Potma, E.O. and X.S. Xie, *Direct Visualization of Lipid Phase Segregation in Single Lipid Bilayers with Coherent Anti-Stokes Raman Scattering Microscopy*. *ChemPhysChem*, 2005. **6**(1): p. 77-79.
67. Potma, E.O. and X.S. Xie, *CARS Microscopy for Biology and Medicine*. *Optics and Photonics News*, 2004. **15**(11): p. 40-45.

68. Hughes, C., et al., *Enhanced FTIR bench-top imaging of single biological cells*. *Analyst*, 2015. **140**(7): p. 2080-2085.
69. Pilling, M. and P. Gardner, *Fundamental developments in infrared spectroscopic imaging for biomedical applications*. *Chemical Society Reviews*, 2016. **45**(7): p. 1935-1957.
70. Amrania, H., et al., *New IR imaging modalities for cancer detection and for intra-cell chemical mapping with a sub-diffraction mid-IR s-SNOM*. *Faraday Discussions*, 2016. **187**(0): p. 539-553.
71. Halliwell, D.E., et al., *Imaging cervical cytology with scanning near-field optical microscopy (SNOM) coupled with an IR-FEL*. *Scientific Reports*, 2016. **6**(1): p. 29494.
72. Hermann, P., et al., *Comparative Study of Far-Field and Near-Field Raman Spectra from Silicon-Based Samples and Biological Nanostructures*. *The Journal of Physical Chemistry C*, 2011. **115**(50): p. 24512-24520.
73. Wysocki, B., et al., *Post Processing and Biological Evaluation of the Titanium Scaffolds for Bone Tissue Engineering*. *Materials*, 2016. **9**(3).
74. Liu, X. and P.X. Ma, *Polymeric Scaffolds for Bone Tissue Engineering*. *Annals of Biomedical Engineering*, 2004. **32**(3): p. 477-486.
75. Ghosh, U., et al., *Molecular structure of a prevalent amyloid- $\beta$  fibril polymorph from Alzheimer's disease brain tissue*. *bioRxiv*, 2020: p. 2020.03.06.981381.
76. Kollmer, M., et al., *Cryo-EM structure and polymorphism of A $\beta$  amyloid fibrils purified from Alzheimer's brain tissue*. *Nature Communications*, 2019. **10**(1): p. 4760.
77. Hayworth, K.J., et al., *Ultrastructurally smooth thick partitioning and volume stitching for large-scale connectomics*. *Nature Methods*, 2015. **12**(4): p. 319-322.
78. Karreman, M.A., et al., *Fast and precise targeting of single tumor cells in vivo by multimodal correlative microscopy*. *Journal of Cell Science*, 2016. **129**(2): p. 444.
79. Binnig, G. and H. Rohrer, *Scanning tunneling microscopy*. *Surface Science*, 1985. **152-153**: p. 17-26.
80. Binnig, G., et al., *Surface Studies by Scanning Tunneling Microscopy*. *Physical Review Letters*, 1982. **49**(1): p. 57-61.
81. Binnig, G., C.F. Quate, and C. Gerber, *Atomic Force Microscope*. *Physical Review Letters*, 1986. **56**(9): p. 930-933.
82. Lewis, A., et al., *Development of a 500 Å spatial resolution light microscope: I. light is efficiently transmitted through  $\lambda/16$  diameter apertures*. *Ultramicroscopy*, 1984. **13**(3): p. 227-231.
83. Pohl, D.W., W. Denk, and M. Lanz, *Optical stethoscopy: Image recording with resolution  $\lambda/20$* . *Applied Physics Letters*, 1984. **44**(7): p. 651-653.
84. Bard, A.J., et al., *Scanning electrochemical microscopy. Introduction and principles*. *Analytical Chemistry*, 1989. **61**(2): p. 132-138.
85. Xu, L.-P., Y. Liu, and X. Zhang, *Interfacial self-assembly of amino acids and peptides: Scanning tunneling microscopy investigation*. *Nanoscale*, 2011. **3**(12): p. 4901-4915.
86. Otero, R., F. Rosei, and F. Besenbacher, *SCANNING TUNNELING MICROSCOPY MANIPULATION OF COMPLEX ORGANIC MOLECULES ON SOLID SURFACES*. *Annual Review of Physical Chemistry*, 2006. **57**(1): p. 497-525.
87. Kuznetsov, Y.G., et al., *Atomic force microscopy investigation of Mason–Pfizer monkey virus and human immunodeficiency virus type 1 reassembled particles*. *Virology*, 2007. **360**(2): p. 434-446.
88. Kuznetsov, Y.G., et al., *Atomic Force Microscopy Investigation of Human Immunodeficiency Virus (HIV) and HIV-Infected Lymphocytes*. *Journal of Virology*, 2003. **77**(22): p. 11896.
89. Malkin, A.J., M. Plomp, and A. McPherson, *Application of atomic force microscopy to studies of surface processes in virus crystallization and structural biology*. *Acta Crystallographica Section D*, 2002. **58**(10 Part 1): p. 1617-1621.
90. Lyubchenko, Y.L. and L.S. Shlyakhtenko, *Imaging of DNA and Protein-DNA Complexes with Atomic Force Microscopy*. *Critical reviews in eukaryotic gene expression*, 2016. **26**(1): p. 63-96.

91. Hoshi O., U.T., *Atomic Force Microscopy Imaging of Human Metaphase Chromosomes in Liquid*. Atomic Force Microscopy in Biomedical Research. Methods in Molecular Biology (Methods and Protocols), 2011. **736**.
92. Ribeiro, M.M.B., et al., *Antimicrobial properties of analgesic kyotorphin peptides unraveled through atomic force microscopy*. Biochemical and Biophysical Research Communications, 2012. **420**(3): p. 676-679.
93. Yang, L., et al., *Atomic Force Microscopy Study of Different Effects of Natural and Semisynthetic  $\beta$ -Lactam on the Cell Envelope of Escherichia coli*. Analytical Chemistry, 2006. **78**(20): p. 7341-7345.
94. Liou, J.-W., et al., *Visible Light Responsive Photocatalyst Induces Progressive and Apical-Terminus Preferential Damages on Escherichia coli Surfaces*. PLOS ONE, 2011. **6**(5): p. e19982.
95. Kim, K.S., et al., *AFM-Detected Apoptotic Changes in Morphology and Biophysical Property Caused by Paclitaxel in Ishikawa and HeLa Cells*. PLOS ONE, 2012. **7**(1): p. e30066.
96. McAllister, C., et al., *Protein Interactions and Misfolding Analyzed by AFM Force Spectroscopy*. Journal of Molecular Biology, 2005. **354**(5): p. 1028-1042.
97. Ning, X., et al., *Identification of Cell Status via Simultaneous Multitarget Imaging Using Programmable Scanning Electrochemical Microscopy*. Analytical Chemistry, 2020. **92**(18): p. 12111-12115.
98. Filice, F.P. and Z. Ding, *Analysing single live cells by scanning electrochemical microscopy*. Analyst, 2019. **144**(3): p. 738-752.
99. Conzuelo, F., A. Schulte, and W. Schuhmann, *Biological imaging with scanning electrochemical microscopy*. Proceedings of the Royal Society A: Mathematical, Physical and Engineering Sciences, 2018. **474**(2218): p. 20180409.
100. Martin J. Hearn, B.D.R., and David Briggs, *SIMS and XPS Studies of Polyurethane Surfaces. I. Preliminary Studies*. Macromolecules, 1988. **21**: p. 2950-2959.
101. Viornerly, C., et al., *Surface Modification of Titanium with Phosphonic Acid To Improve Bone Bonding: Characterization by XPS and ToF-SIMS*. Langmuir, 2002. **18**(7): p. 2582-2589.
102. Vanea, E. and V. Simon, *XPS study of protein adsorption onto nanocrystalline aluminosilicate microparticles*. Applied Surface Science, 2011. **257**(6): p. 2346-2352.
103. McArthur, S.L., *Applications of XPS in bioengineering*. Surface and Interface Analysis, 2006. **38**(11): p. 1380-1385.
104. Graf, N., et al., *Application of XPS and ToF-SIMS for surface chemical analysis of DNA microarrays and their substrates*. Analytical and Bioanalytical Chemistry, 2009. **393**(8): p. 1907-1912.
105. Lee, C.-Y., et al., *Fluorescence, XPS, and TOF-SIMS Surface Chemical State Image Analysis of DNA Microarrays*. Journal of the American Chemical Society, 2007. **129**(30): p. 9429-9438.
106. Brünche, V.E., *Elektronenmikroskopische abbildung mit lichtelektrischen elektronen*. Z. Phys., 1933. **86**: p. 448-450.
107. Griffith, O.H., et al., *Photoelectron Microscopy: A New Approach to Mapping Organic and Biological Surfaces*. Proceedings of the National Academy of Sciences, 1972. **69**(3): p. 561.
108. Habliston, D.L., et al., *Photoelectron imaging of cells: photoconductivity extends the range of applicability*. Biophysical Journal, 1995. **69**(4): p. 1615-1624.
109. Nadakavukaren, K.K., G.F. Rempfer, and O.H. Griffith, *Photoelectron microscopy of cell surface topography*. Journal of Microscopy, 1981. **122**(3): p. 301-307.
110. Dam, R.J., K.K. Nadakavukaren, and O.H. Griffith, *Photoelectron microscopy of cell surfaces*. Journal of Microscopy, 1977. **111**(2): p. 211-217.
111. Birrell, G.B., D.L. Habliston, and O.H. Griffith, *Photoelectron imaging of viruses and DNA: evaluation of substrates by unidirectional low angle shadowing and photoemission current measurements*. Biophysical Journal, 1994. **67**(5): p. 2041-2047.
112. Houle, W.A. and O.H. Griffith, *Photoelectron microscopy of viruses*. Ultramicroscopy, 1983. **11**(1): p. 71-74.

113. Griffith, O.H., et al., *Photoelectron imaging of DNA*. Biopolymers, 1990. **29**(10-11): p. 1491-1493.
114. Houle, W.A. and O. Hayes Griffith, *Imaging of DNA by photoelectron microscopy*. Micron and Microscopica Acta, 1983. **14**(4): p. 351-352.
115. Skallberg, A., et al., *Neutrophils Activated by Nanoparticles and Formation of Neutrophil Extracellular Traps: Work Function Mapping and Element Specific Imaging*. Analytical Chemistry, 2019. **91**(21): p. 13514-13520.
116. Skallberg, A., C. Brommesson, and K. Uvdal, *Imaging XPS and photoemission electron microscopy; surface chemical mapping and blood cell visualization*. Biointerphases, 2017. **12**(2): p. 02C408.
117. Skallberg, A., et al., *New Tools for Imaging Neutrophils: Work Function Mapping and Element-Specific, Label-Free Imaging of Cellular Structures*. Nano Letters, 2020.
118. Greco, V., et al., *Applications of MALDI-TOF mass spectrometry in clinical proteomics*. Expert Review of Proteomics, 2018. **15**(8): p. 683-696.
119. Schubert, K.O., et al., *The use of MALDI-MSI in the investigation of psychiatric and neurodegenerative disorders: A review*. PROTEOMICS, 2016. **16**(11-12): p. 1747-1758.
120. Arafah, K., et al., *Lipidomics for Clinical Diagnosis: Dye-Assisted Laser Desorption/Ionization (DALDI) Method for Lipids Detection in MALDI Mass Spectrometry Imaging*. OMICS: A Journal of Integrative Biology, 2014. **18**(8): p. 487-498.
121. Yuki, D., et al., *DHA-PC and PSD-95 decrease after loss of synaptophysin and before neuronal loss in patients with Alzheimer's disease*. Scientific Reports, 2014. **4**(1): p. 7130.
122. Cersoy, S., et al., *Cluster TOF-SIMS imaging of human skin remains: analysis of a South-Andean mummy sample*. Journal of Mass Spectrometry, 2012. **47**(3): p. 338-346.
123. Melissa K. Passarelli, N.W., *Lipid imaging with time-of-flight secondary ion mass spectrometry (ToF-SIMS)*. Elsevier, 2011.
124. Burns, S.A. and J.A. Gardella, *Quantitative ToF-SIMS Studies of Protein Drug Release from Biodegradable Polymer Drug Delivery Membranes*. Applied surface science, 2008. **255**(4): p. 1170-1173.
125. Belu, A.M., et al., *TOF-SIMS Characterization and Imaging of Controlled-Release Drug Delivery Systems*. Analytical Chemistry, 2000. **72**(22): p. 5625-5638.
126. Judd, A.M., et al., *Distribution and Visualisation of Chlorhexidine Within the Skin Using ToF-SIMS: A Potential Platform for the Design of More Efficacious Skin Antiseptic Formulations*. Pharmaceutical Research, 2013. **30**(7): p. 1896-1905.
127. Mary L Kraft, A.N.Y., Peter K Weber, Joshua Zimmerberg, *Is the Site of Influenza Virus Assembly and Budding Enriched with Cholesterol and Sphingolipids?* Biophysical Journal, 2017. **112**(3): p. 318a-319a.
128. Kern, C., et al., *New insights into ToF-SIMS imaging in osteoporotic bone research*. Biointerphases, 2020. **15**(3): p. 031005.
129. Philipsen, M.H., et al., *Mass Spectrometry Imaging Shows Cocaine and Methylphenidate Have Opposite Effects on Major Lipids in Drosophila Brain*. ACS Chemical Neuroscience, 2018. **9**(6): p. 1462-1468.
130. Philipsen, M.H., et al., *Interplay between Cocaine, Drug Removal, and Methylphenidate Reversal on Phospholipid Alterations in Drosophila Brain Determined by Imaging Mass Spectrometry*. ACS Chemical Neuroscience, 2020. **11**(5): p. 806-813.
131. Peteranderl, R. and C. Lechene, *Measure of carbon and nitrogen stable isotope ratios in cultured cells*. Journal of the American Society for Mass Spectrometry, 2004. **15**(4): p. 478-485.
132. Decelle, J., et al., *Subcellular Chemical Imaging: New Avenues in Cell Biology*. Trends in Cell Biology, 2020. **30**(3): p. 173-188.
133. He, C., et al., *High-resolution visualization and quantification of nucleic acid-based therapeutics in cells and tissues using Nanoscale secondary ion mass spectrometry (NanoSIMS)*. Nucleic Acids Research, 2020.

134. Kabatas, S., et al., *Fluorinated nanobodies for targeted molecular imaging of biological samples using nanoscale secondary ion mass spectrometry*. *Journal of Analytical Atomic Spectrometry*, 2019. **34**(6): p. 1083-1087.
135. Proetto, M.T., et al., *Tumor Retention of Enzyme-Responsive Pt(II) Drug-Loaded Nanoparticles Imaged by Nanoscale Secondary Ion Mass Spectrometry and Fluorescence Microscopy*. *ACS Central Science*, 2018. **4**(11): p. 1477-1484.
136. Alkass, K., et al., *No Evidence for Cardiomyocyte Number Expansion in Preadolescent Mice*. *Cell*, 2015. **163**(4): p. 1026-1036.
137. Tang, S.S., et al., *Quantitative imaging of selenoprotein with multi-isotope imaging mass spectrometry (MIMS)*. *Surface and Interface Analysis*, 2014. **46**(S1): p. 154-157.
138. Goulbourne, Chris N., et al., *The GPIHBP1–LPL Complex Is Responsible for the Margination of Triglyceride-Rich Lipoproteins in Capillaries*. *Cell Metabolism*, 2014. **19**(5): p. 849-860.
139. Takado, Y., et al., *Imaging liver and brain glycogen metabolism at the nanometer scale*. *Nanomedicine: Nanotechnology, Biology and Medicine*, 2015. **11**(1): p. 239-245.
140. Biesemeier, A., et al., *Elemental mapping of Neuromelanin organelles of human Substantia Nigra: correlative ultrastructural and chemical analysis by analytical transmission electron microscopy and nano-secondary ion mass spectrometry*. *Journal of Neurochemistry*, 2016. **138**(2): p. 339-353.
141. Hassouna, I., et al., *Revisiting adult neurogenesis and the role of erythropoietin for neuronal and oligodendroglial differentiation in the hippocampus*. *Molecular Psychiatry*, 2016. **21**(12): p. 1752-1767.
142. Forecast, M.D., *Global Active Implantable Medical Devices Market Size, Share, Trends & Growth Analysis Report – Segmented By Product & Region - Industry Forecast (2020 to 2025)*. 2020. p. 185.
143. Sobot, R., *Implantable systems – Retrospective tutorial review*. *Microelectronics Journal*, 2019. **88**: p. 190-198.
144. Hong, G. and C.M. Lieber, *Novel electrode technologies for neural recordings*. *Nature Reviews Neuroscience*, 2019.
145. Buzsáki, G., *Theta Oscillations in the Hippocampus*. *Neuron*, 2002. **33**(3): p. 325-340.
146. Buzsáki, G., C.A. Anastassiou, and C. Koch, *The origin of extracellular fields and currents — EEG, ECoG, LFP and spikes*. *Nature Reviews Neuroscience*, 2012. **13**(6): p. 407-420.
147. Taylor, J.P., J. Hardy, and K.H. Fischbeck, *Toxic Proteins in Neurodegenerative Disease*. *Science*, 2002. **296**(5575): p. 1991.
148. Breit, S., J.B. Schulz, and A.-L. Benabid, *Deep brain stimulation*. *Cell and Tissue Research*, 2004. **318**(1): p. 275-288.
149. Perlmuter, J.S. and J.W. Mink, *DEEP BRAIN STIMULATION*. *Annual Review of Neuroscience*, 2006. **29**(1): p. 229-257.
150. Fried, I., *Brain Stimulation in Alzheimer's Disease*. *Journal of Alzheimer's Disease*, 2016. **54**: p. 789-791.
151. Eliseyev, A., et al. *CLINATEC® BCI platform based on the ECoG-recording implant WIMAGINE® and the innovative signal-processing: Preclinical results*. in *2014 36th Annual International Conference of the IEEE Engineering in Medicine and Biology Society*. 2014.
152. Shih, J.J., D.J. Krusienski, and J.R. Wolpaw, *Brain-Computer Interfaces in Medicine*. *Mayo Clinic Proceedings*, 2012. **87**(3): p. 268-279.
153. Jonathan R Wolpaw, N.B., William J Heetderks, Dennis J McFarland, P Hunter Peckham, Gerwin Schalk, Emanuel Donchin, Louis A Quatrano, Charles J Robinson, Theresa M Vaughan, *Brain-computer interface technology: a review of the first international meeting*. *IEEE transactions on rehabilitation engineering*, 2000. **8**(2): p. 164-173.
154. Jitte Groothuis, N.F.R., Geert M.J. Ramakers, Geoffrey van der Plasse, *Physiological Challenges for Intracortical Electrodes*. Elsevier, 2014(Brain Stimulation).
155. van Kuyck, K., et al., *Histological Alterations Induced by Electrode Implantation and Electrical Stimulation in the Human Brain: A Review*. *Neuromodulation: Technology at the Neural Interface*, 2007. **10**(3): p. 244-261.

156. Biran, R., D.C. Martin, and P.A. Tresco, *Neuronal cell loss accompanies the brain tissue response to chronically implanted silicon microelectrode arrays*. *Experimental Neurology*, 2005. **195**(1): p. 115-126.
157. Bao, G. and S. Suresh, *Cell and molecular mechanics of biological materials*. *Nature Materials*, 2003. **2**(11): p. 715-725.
158. Singh, A.P., et al., *Targeted therapy in chronic diseases using nanomaterial-based drug delivery vehicles*. *Signal Transduction and Targeted Therapy*, 2019. **4**(1): p. 33.
159. Lombardo, D., M.A. Kiselev, and M.T. Caccamo, *Smart Nanoparticles for Drug Delivery Application: Development of Versatile Nanocarrier Platforms in Biotechnology and Nanomedicine*. *Journal of Nanomaterials*, 2019. **2019**: p. 3702518.
160. David Ratel, B.V.D.S., Didier Wion, *Glioma resection and tumor recurrence: back to Semmelweis*. 2016.
161. Hamard, L., et al., *The brain tissue response to surgical injury and its possible contribution to glioma recurrence*. *J Neurooncol*, 2016. **128**(1573-7373 (Electronic)).
162. Fan, D.-y., Y. Tian, and Z.-j. Liu, *Injectable Hydrogels for Localized Cancer Therapy*. *Frontiers in Chemistry*, 2019. **7**(675).
163. Norouzi, M., B. Nazari, and D.W. Miller, *Injectable hydrogel-based drug delivery systems for local cancer therapy*. *Drug Discovery Today*, 2016. **21**(11): p. 1835-1849.
164. Wu, X., et al., *Synergistic therapeutic effects of Schiff's base cross-linked injectable hydrogels for local co-delivery of metformin and 5-fluorouracil in a mouse colon carcinoma model*. *Biomaterials*, 2016. **75**: p. 148-162.
165. Xiong, L., et al., *An injectable drug-loaded hydrogel based on a supramolecular polymeric prodrug*. *Chemical Communications*, 2015. **51**(78): p. 14644-14647.
166. Desmedt, C., et al., *Potential Benefit of Intra-operative Administration of Ketorolac on Breast Cancer Recurrence According to the Patient's Body Mass Index*. *JNCI: Journal of the National Cancer Institute*, 2018. **110**(10): p. 1115-1122.
167. Baio, J.E., D.J. Graham, and D.G. Castner, *Surface analysis tools for characterizing biological materials*. *Chemical Society Reviews*, 2020. **49**(11): p. 3278-3296.
168. Liu, J., et al., *Control of neuronal network organization by chemical surface functionalization of multi-walled carbon nanotube arrays*. *Nanotechnology*, 2011. **22**(19): p. 195101.
169. Kollmer, F., *Cluster primary ion bombardment of organic materials*. *Applied Surface Science*, 2004. **231-232**: p. 153-158.
170. Weibel, D., et al., *A C60 Primary Ion Beam System for Time of Flight Secondary Ion Mass Spectrometry: Its Development and Secondary Ion Yield Characteristics*. *Analytical Chemistry*, 2003. **75**(7): p. 1754-1764.
171. Brunelle, A., D. Touboul, and O. Lapr evote, *Biological tissue imaging with time-of-flight secondary ion mass spectrometry and cluster ion sources*. *Journal of Mass Spectrometry*, 2005. **40**(8): p. 985-999.
172. Vanbellinghen, Q.P., et al., *Time-of-flight secondary ion mass spectrometry imaging of biological samples with delayed extraction for high mass and high spatial resolutions*. *Rapid Communications in Mass Spectrometry*, 2015. **29**(13): p. 1187-1195.
173. Kirkpatrick, A., *Gas cluster ion beam applications and equipment*. *Nuclear Instruments and Methods in Physics Research Section B: Beam Interactions with Materials and Atoms*, 2003. **206**: p. 830-837.
174. Vickerman, J.C. and D.R. Briggs. *ToF-SIMS : materials analysis by mass spectrometry*. 2013.
175. Stroobant, E.H.a.V., *Mass spectrometry: principles and applications*. 2007: John Wiley & Sons.
176. Gross, J.H., *Mass spectrometry: a textbook*. 2006: Springer Science & Business Media.
177. Fisher, G.L., et al., *Parallel imaging MS/MS TOF-SIMS instrument*. *Journal of Vacuum Science & Technology B*, 2016. **34**(3): p. 03H126.
178. Liang, W., et al., *Recent advances in AFM-based biological characterization and applications at multiple levels*. *Soft Matter*, 2020. **16**(39): p. 8962-8984.
179. Maghsoudy-Louyeh, S., M. Kropf, and B. Tittmann, *Review of Progress in Atomic Force Microscopy*. *The Open Neuroimaging Journal*, 2018. **12**: p. 86-104.

180. Alford, T.L., L.C. Feldman, and J.W. Mayer, *Fundamentals of Nanoscale Film Analysis*. 2007: Springer US.
181. Scofield, J.H., *Hartree-slater subshell photoionization cross-sections at 1254 and 1487 eV*. Journal of Electron Spectroscopy and Related Phenomena, 1976. **8**: p. 129-137.
182. Yeh, J.J. and I. Lindau, *Atomic subshell photoionization cross sections and asymmetry parameters:  $1 \leq Z \leq 103$* . Atomic Data and Nuclear Data Tables, 1985. **32**(1): p. 1-155.
183. Akar, A., H. Gümüş, and N.T. Okumuşoğlu, *Electron inelastic mean free path formula and CSDA-range calculation in biological compounds for low and intermediate energies*. Applied Radiation and Isotopes, 2006. **64**(5): p. 543-550.
184. DUC, T.M. *Analyse de surface par ESCA - Analyse élémentaire et applications*. Techniques de l'ingénieur, 1998. **1**.
185. John F. Watts, J.W., *Electron Spectroscopy. An Introduction to Surface Analysis by XPS and AES*, 2019: p. 1-18.
186. Rouxhet, P.G. and M.J. Genet, *XPS analysis of bio-organic systems*. Surface and Interface Analysis, 2011. **43**(12): p. 1453-1470.
187. Dufrêne, Y.F., et al., *X-ray photoelectron spectroscopy analysis of whole cells and isolated cell walls of gram-positive bacteria: comparison with biochemical analysis*. Journal of Bacteriology, 1997. **179**(4): p. 1023.
188. Sherwood, P.M.A., *The use and misuse of curve fitting in the analysis of core X-ray photoelectron spectroscopic data*. Surface and Interface Analysis, 2019. **51**(6): p. 589-610.
189. Hofmann, S., *Auger- and X-Ray Photoelectron Spectroscopy in Materials Science*, ed. S.S.i.S. Sciences. 2013.
190. Peles, D.N. and J.D. Simon, *Challenges in Applying Photoemission Electron Microscopy to Biological Systems†*. Photochemistry and Photobiology, 2009. **85**(1): p. 8-20.
191. Barrett, N. and O. Renault, *La spectromicroscopie XPEEM avec le rayonnement synchrotron\**. Mater. Tech., 2009. **97**(2): p. 101-122.
192. Escher, M., et al., *Applications of high lateral and energy resolution imaging XPS with a double hemispherical analyser based spectromicroscope*. Journal of Electron Spectroscopy and Related Phenomena, 2010. **178-179**: p. 303-316.
193. Schneider, C.M. and G. Sch nhenese, *Investigating surface magnetism by means of photoexcitation electron emission microscopy*. Reports on Progress in Physics, 2002. **65**(12): p. 1785-1839.
194. Anders, S., et al., *Photoemission electron microscope for the study of magnetic materials*. Review of Scientific Instruments, 1999. **70**(10): p. 3973-3981.
195. Escher, M., et al., *Nanoelectron spectroscopy for chemical analysis: a novel energy filter for imaging x-ray photoemission spectroscopy*. Journal of Physics: Condensed Matter, 2005. **17**(16): p. S1329-S1338.
196. Tromp, R.M., W. Wan, and S.M. Schramm, *Aberrations of the cathode objective lens up to fifth order*. Ultramicroscopy, 2012. **119**: p. 33-39.
197. Tromp, R.M., *Measuring and correcting aberrations of a cathode objective lens*. Ultramicroscopy, 2011. **111**(4): p. 273-281.
198. Gang Xiong, Y.A.G.J., W P Hess, Ming-dong Cai, T J Dickinson, *Introduction to photoelectron emission microscopy : principles and applications*. Journal of Chinese Electron Microscopy Society, 2006. **25**(1): p. 1000-6281.
199. Barrett, N., et al., *X-ray Photoelectron Spectromicroscopy of Doped Silicon Patterns*. AIP Conference Proceedings, 2009. **1173**(1): p. 99-103.
200. Halas, S., *100 years of work function* Materials Science-Poland, 2006. **24**(4).
201. Shard, A.G., et al., *X-ray Photoelectron Spectroscopy and Time-of-Flight SIMS Investigations of Hyaluronic Acid Derivatives*. Langmuir, 1997. **13**(10): p. 2808-2814.
202. Raju, B., et al., *Development and validation of liquid chromatography–mass spectrometric method for simultaneous determination of moxifloxacin and ketorolac in rat plasma: application to pharmacokinetic study*. Biomedical Chromatography, 2012. **26**(11): p. 1341-1347.

203. Raju, B., et al., *Identification and structural characterization of in vivo metabolites of ketorolac using liquid chromatography electrospray ionization tandem mass spectrometry (LC/ESI-MS/MS)*. *Journal of Mass Spectrometry*, 2012. **47**(7): p. 919-931.
204. Association, B.N., *Neuroscience Science of the brain An Introduction for Young Students*.
205. Mercadante AA, T.P. *Neuroanatomy, Gray Matter*. 2020; Available from: <https://www.ncbi.nlm.nih.gov/books/NBK553239/>.
206. Wakana, S., et al., *Fiber Tract-based Atlas of Human White Matter Anatomy*. *Radiology*, 2004. **230**(1): p. 77-87.
207. Sjövall, P., J. Lausmaa, and B. Johansson, *Mass Spectrometric Imaging of Lipids in Brain Tissue*. *Analytical Chemistry*, 2004. **76**(15): p. 4271-4278.
208. Cregg, J.M., et al., *Functional regeneration beyond the glial scar*. *Experimental Neurology*, 2014. **253**: p. 197-207.
209. Karumbaiah, L., et al., *Targeted downregulation of N-acetylgalactosamine 4-sulfate 6-O-sulfotransferase significantly mitigates chondroitin sulfate proteoglycan-mediated inhibition*. *Glia*, 2011. **59**(6): p. 981-996.
210. Fernández-Klett, F. and J. Priller, *The Fibrotic Scar in Neurological Disorders*. *Brain Pathology*, 2014. **24**(4): p. 404-413.
211. Lau, L.W., et al., *Pathophysiology of the brain extracellular matrix: a new target for remyelination*. *Nature Reviews Neuroscience*, 2013. **14**(10): p. 722-729.
212. Sosnik, A., et al., *Surface study of collagen/poloxamine hydrogels by a 'deep freezing' ToF-SIMS approach*. *Biomaterials*, 2006. **27**(11): p. 2340-2348.
213. McArthur, S.L., et al., *Characterization of sequentially grafted polysaccharide coatings using time-of-flight secondary ion mass spectrometry (ToF-SIMS) and principal component analysis (PCA)*. *Surface and Interface Analysis*, 2002. **33**(12): p. 924-931.
214. Benninghoven, A., D. Jaspers, and W. Sichtermann, *Secondary-ion emission of amino acids*. *Applied physics*, 1976. **11**(1): p. 35-39.
215. Tidwell, C.D., et al., *Static time-of-flight secondary ion mass spectrometry and x-ray photoelectron spectroscopy characterization of adsorbed albumin and fibronectin films*. *Surface and Interface Analysis*, 2001. **31**(8): p. 724-733.
216. Parry, S. and N. Winograd, *High-Resolution TOF-SIMS Imaging of Eukaryotic Cells Preserved in a Trehalose Matrix*. *Analytical Chemistry*, 2005. **77**(24): p. 7950-7957.
217. Kawecki, M. and L. Bernard, *Database of proteinogenic amino acid reference spectra for Bismuth-cluster ToF-SIMS. I. Negative polarity*. *Surface Science Spectra*, 2018. **25**(1): p. 015001.
218. Amaya, K.R., J.V. Sweedler, and D.F. Clayton, *Small molecule analysis and imaging of fatty acids in the zebra finch song system using time-of-flight-secondary ion mass spectrometry*. *Journal of Neurochemistry*, 2011. **118**(4): p. 499-511.
219. Van Nuffel, S., et al., *Multimodal Imaging Mass Spectrometry to Identify Markers of Pulmonary Arterial Hypertension in Human Lung Tissue Using MALDI-ToF, ToF-SIMS, and Hybrid SIMS*. *Analytical Chemistry*, 2020. **92**(17): p. 12079-12087.
220. Henry, M. and P. Bertrand, *Surface composition of insulin and albumin adsorbed on polymer substrates as revealed by multivariate analysis of ToF-SIMS data*. *Surface and Interface Analysis*, 2009. **41**(2): p. 105-113.
221. Lhoest, J.B., et al., *Fibronectin adsorption, conformation, and orientation on polystyrene substrates studied by radiolabeling, XPS, and ToF SIMS*. *Journal of Biomedical Materials Research*, 1998. **41**(1): p. 95-103.
222. Charbonneau, C., et al., *Stimulation of cell growth and resistance to apoptosis in vascular smooth muscle cells on a chondroitin sulfate/epidermal growth factor coating*. *Biomaterials*, 2011. **32**(6): p. 1591-1600.
223. Rodríguez, C., et al., *Regulation of lysyl oxidase in vascular cells: lysyl oxidase as a new player in cardiovascular diseases*. *Cardiovascular Research*, 2008. **79**(1): p. 7-13.
224. Rucker, R.B., et al., *Copper, lysyl oxidase, and extracellular matrix protein cross-linking*. *Am J Clin Nutr*, 1998. **67**(5 Suppl)(0002-9165 (Print)): p. 996S-1002S.

225. Harris, E.D., et al., *Copper and the Synthesis of Elastin and Collagen*. Ciba Foundation Symposium 79 - Biological Roles of Copper, 1980: p. 163-182.
226. Derrickson, G.J.T.a.B., *Principles of Anatomy and Physiology*, ed. t. Edition. 2011: Wiley.
227. Rouxhet, P.G., et al., *Application of X-ray photoelectron spectroscopy to microorganisms*. Colloids and Surfaces B: Biointerfaces, 1994. **2**(1): p. 347-369.
228. Coullerez, G., et al., *XPS and ToF-SIMS study of freeze-dried and thermally cured melamine-formaldehyde resins of different molar ratios*. Surface and Interface Analysis, 2000. **29**(7): p. 431-443.
229. KIM S. SIOW, L.B., SUNIL KUMAR & HANS J GRIESSER, *XPS Study of Sulfur and Phosphorus Compounds with Different Oxidation States*. Sains Malaysiana, 2018. **47**(8): p. 1913–1922.



# APPENDIX

## 1. GLIAL SCAR TISSUE AND SCHEME OF TISSUE CROSS SECTION'S LOCATION

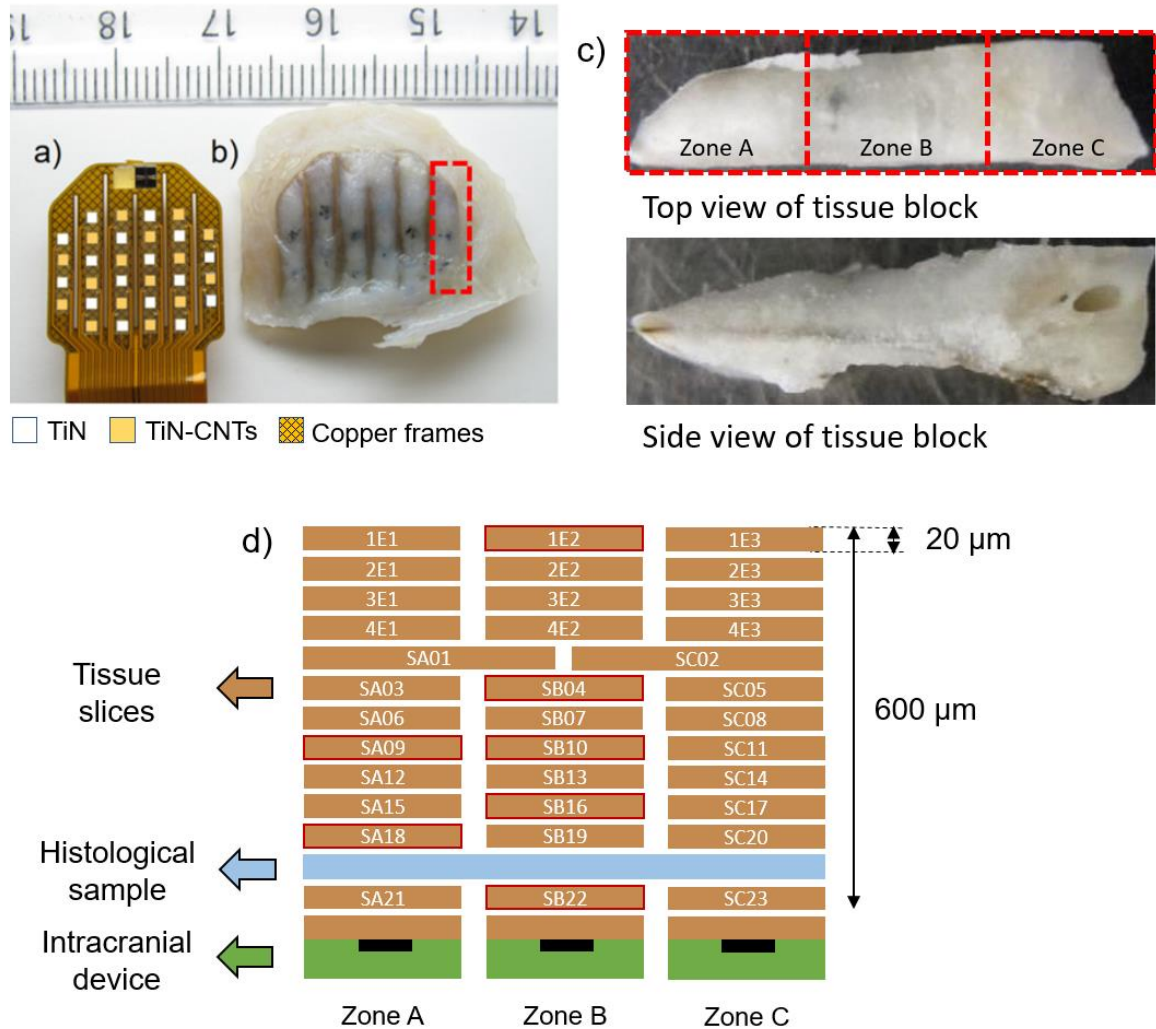


Figure A 1. (A) Intracranial device image of TiN and TiN-Carbon nanotubes (CNTs) based electrodes linked by copper frames embedded in polyimide. (B) The same intracranial device after one year of implantation on a nonhuman primate cortex completely enveloped by the glial scar tissue. The black spots seen on tissue were CNTs agglomerations displaced from the surface of the neural device and isolated in the tissue few hundred micrometres from device. The dotted rectangle indicates the region from which the tissue block was extracted. (C) Top view and side view of the tissue block indicating zones A, B and C. (D) Scheme showing the location of different glial scar tissue slices on the intracranial device.

## 2. PARAMETERS USED FOR PRINCIPAL COMPONENT ANALYSIS OF SLICES SA09 AND SA18

PCA was used to analyse the spectra and process images obtained from ToF-SIMS measurements. ToF-SIMS data sets were integrally treated by SURFACELAB 7 software (ION-TOF GmbH, Munster, Germany) besides used to calibrate all spectra, generate peak lists, and export data. For imaging processing, a region of interest of  $1 \times 1 \text{ mm}^2$  was selected on tissue surface image, aiming to preserve spectra quality from surface morphology effects. Then, peaks were automatically chosen in a mass range of 0–300 following 100 min counts, 1.0 min signal noise ratio, and 0.8 max background default conditions. A manual check was then performed to make sure that all peaks in the range were selected. The peak intensities were automatically mean centered and normalized during PCA processing.

### 3. PCA SCORES FROM TOF-SIMS NEGATIVE SPECTRUM OF SLICE SA18

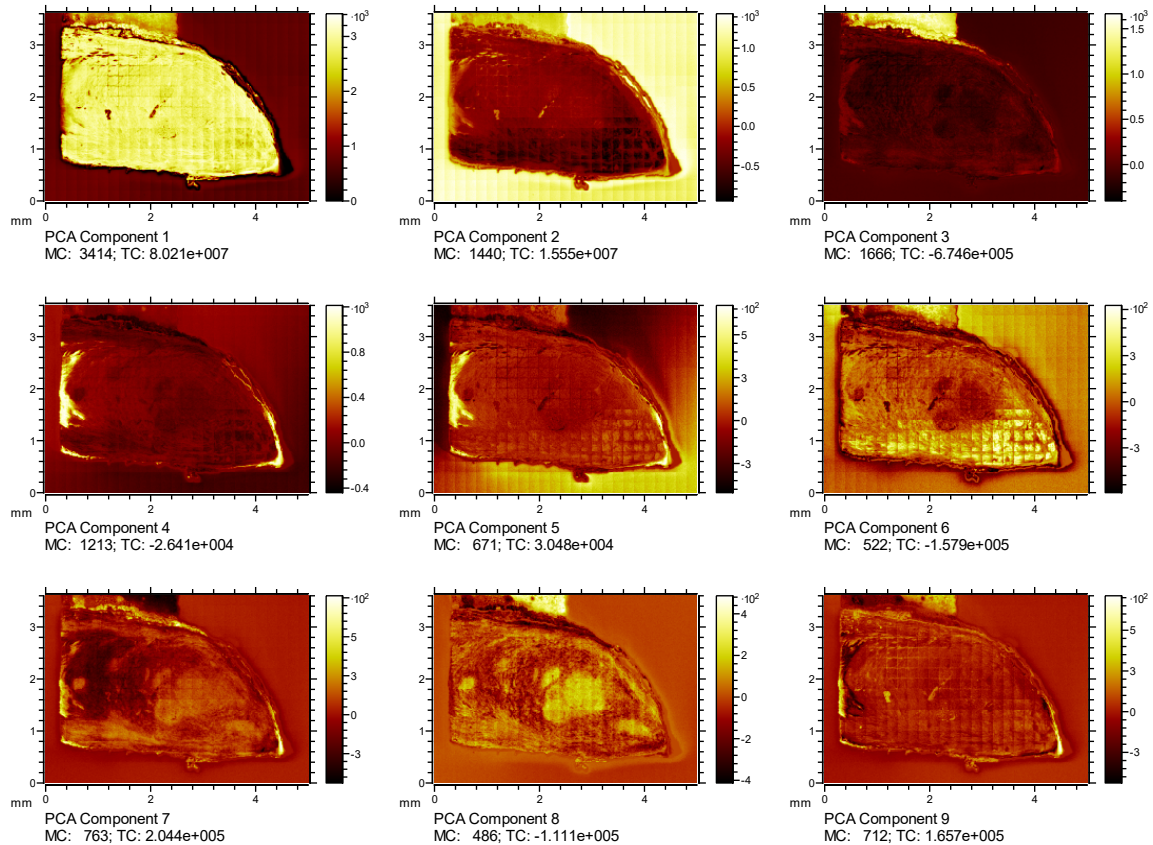


Figure A 2. PCA analysis of SA18 image data containing all negative peaks. The most striking patterns were described in the first PC1 and PC2 and concerned the chemical differences between the silicon substrate and the biological tissue. The subsequent components mainly highlighted special features surrounding the biological tissue that belongs to the O.C.T.<sup>TM</sup> Compound used for sectioning. The PC6 and PC8 were exceptions and verified the existence of two chemically distinct regions on tissue.

# EXTENDED SUMMARY OF THE THESIS IN FRENCH

---

## MICROSCOPIE MULTIMODALE DE SURFACE POUR DES APPLICATIONS EN TECHNOLOGIES POUR LA SANTE

Pour répondre à la complexité de la biologie dans les dispositifs biomédicaux, des outils de caractérisation chimique des surfaces performants sont nécessaires. L'objectif de cette thèse consiste à mettre en œuvre une approche de caractérisation de tissus et dispositifs pour le biomédical par imagerie chimique de surface multimodale. En combinant les méthodes d'analyse de surface, on peut acquérir des informations chimiques et morphologiques d'interfaces biomédicales telles que celles présentes dans les tissus cérébraux non humains contenant des technologies implantées, ou dans les systèmes d'administration de médicaments utilisés dans le traitement du glioblastome et les dispositifs neuronaux utilisés comme interface cerveau-ordinateur. Ces méthodes d'analyse ont pu être combinées à plusieurs niveaux de sophistication (jusqu'à 3) et les résultats du travail sont présentés en 3 chapitres, outre un chapitre bibliographique situant l'état de l'art sur cette approche, et un chapitre présentant les méthodes et outils expérimentaux utilisés en détails.

Nous avons utilisé plusieurs techniques de caractérisation chimique des surfaces à l'état de l'art, la spectrométrie ToF-SIMS, la spectrométrie de masse (MS) en tandem, la spectroscopie XPS, la microscopie électronique à photoémission (PEEM) ainsi que la microscopie AFM.

En quelques mots introductifs, la spectrométrie ToF-SIMS est un excellent outil d'exploration chimique des surfaces pour tous les systèmes étudiés par imagerie. Cette technique nous a permis d'atteindre deux des principaux objectifs intermédiaires proposés dans ce travail, qui sont l'identification (i) d'espèces chimiques de surface et (ii) de régions chimiquement distinctes en surface des échantillons. Ceci a été possible grâce à la résolution latérale utilisée pour de grandes zones d'analyse, en surface de l'échantillon. En effet, la spectrométrie ToF-SIMS offre la possibilité d'acquérir des images de taille millimétrique en assemblant des images continues (ou tuiles) de 500  $\mu\text{m}$  de large. La haute résolution massique du ToF-SIMS est également un avantage majeur qui nous a permis d'analyser la structure chimique de l'échantillon avec une bonne précision. Cependant, lorsque l'on souhaite imager des régions plus petites (inférieures à 100  $\mu\text{m}$  de largeur par exemple), de meilleures résolutions latérales sont nécessaires, qui ne peuvent s'obtenir qu'au détriment de la résolution en masse, ou bien par compromis entre résolution en masse et résolution latérale. Un autre aspect qui doit être pris en considération est la topographie de la surface analysée, principalement parce que de fortes différences topographiques peuvent créer des zones de peu ou pas d'émission secondaire. Mais comme nous avons pu le remarquer dans ce travail, des différences topographiques de l'ordre du micromètre restent peu significatives dans des régions analysées de dimension millimétrique. Cependant, ces mêmes variations topographiques (de l'ordre du micromètre) pourraient avoir des conséquences plus importantes pour des régions analysées de taille micrométrique. L'excellente limite de détection de ToF-SIMS, dans la gamme ppm-ppb, est également un atout pour détecter les traces de contaminants dans

les systèmes biomédicaux. Les spectres de masse ToF-SIMS, traités par outil statistique PCA, permettent une réduction du bruit et une mise en évidence des tendances dans les données, qui peuvent être utiles pour déterminer la composition chimique des zones analysées.

La spectrométrie de masse en tandem (Tandem MS) est une technique similaire à la spectrométrie ToF-SIMS, cependant, cette technique dispose d'un deuxième analyseur de masse où se produit une nouvelle décomposition des ions sélectionnés (ions précurseurs) en fragments (ions produits). Ces fragments de produits révèlent alors des aspects de la structure chimique de l'ion précurseur qui sont extrêmement utiles pour affiner l'attribution des ions moléculaires initialement identifiés dans le spectre de masse ToF-SIMS. Cette technique a été utilisée ponctuellement en complément de la spectrométrie ToF-SIMS.

La microscopie à champ proche AFM a été utilisée dans ce travail également comme un outil complémentaire qui visait à identifier des régions morphologiquement distinctes dans les systèmes biomédicaux. Le scanner de notre AFM est limité à l'analyse de zones d'une taille maximale de  $100 \times 100 \mu\text{m}^2$  (xy) et d'une variation topographique maximale de  $10 \mu\text{m}$  (z), ce qui a restreint son utilisation dans l'étude de la plupart des interfaces étudiées dans ce travail.

La spectroscopie XPS a été utilisée systématiquement, comme la spectrométrie ToF-SIMS. C'est l'outil qui nous a permis d'atteindre notre troisième objectif intermédiaire qui était de quantifier les environnements chimiques présents en surface des systèmes biomédicaux dans des régions d'intérêt précises. Certains systèmes biomédicaux peu conducteurs ont présenté des difficultés à l'analyse car ils possédaient des effets de charge difficiles à compenser, notamment les hydrogels HA lyophilisés. De manière générale, nous avons pu quantifier, à partir de l'intensité des niveaux de cœur analysés à haute résolution en énergie, (i) l'influence de l'ajout de kétorolac trométhamine et de microcapsules de gomme gellane dans les hydrogels HA, (ii) les environnements chimiques présents dans les zones chimiquement contrastées du composé « support » O.C.T.<sup>TM</sup>, ainsi que (iii) les environnements chimiques liés aux zones de nécrose et d'inflammation sévère des tissus biologiques. Nous avons pu remarquer que l'une des limitations de la spectroscopie XPS dans ce travail était sa limite de détection moins performante (1,0 – 0,5% atomique) par rapport à la spectrométrie ToF-SIMS. Les traces de métaux tels que le nickel, qui ont été identifiées dans le tissu cicatriciel glial par ToF-SIMS, n'ont pas pu être identifiées par XPS. Sinon, en général, nous avons observé que les informations chimiques obtenues à la fois par XPS et par ToF-SIMS présentaient une grande cohérence.

La microscopie électronique en photoémission XPEEM, à haute résolution en énergie et latérale, a été utilisée pour l'imagerie des environnements chimiques du composé O.C.T.<sup>TM</sup> et des tissus cicatriciels gliaux. Dans les deux cas, nous avons observé un contraste d'échelle dû aux variations de la fonction de travail, attribuées à la composition chimique différente de ces régions. L'analyse par PEEM des régions identifiées par ToF-SIMS et XPS n'a pas été triviale, en raison du champ de vision plus petit (un spot d'environ  $200 \mu\text{m}$  de diamètre seulement). L'information importante est que l'imagerie PEEM sur le composé O.C.T.<sup>TM</sup> a été réalisée et que la cohérence entre les spectres des niveaux de cœur XPS et X-PEEM indiquait une bonne stabilité de surface, lors de la première analyse. Cependant,

des effets de charge accumulés ont été fréquemment observés avec le durée de l'analyse (cela se traduit par un déplacement du spectre et/ou un élargissement des pics). Néanmoins, lorsque la mesure était possible, la quantification des états chimiques s'est avérée plus pertinente en PEEM qu'en XPS, en raison de la résolution latérale plus élevée.

Les résultats de notre travail peuvent s'organiser selon 3 niveaux de sophistication en ce qui concerne la combinaison des images/informations chimiques obtenues.

Le chapitre 3 du manuscrit présente un premier niveau de sophistication, au cours duquel nous présentons les résultats de l'étude de différents systèmes d'administration de médicaments pour le traitement du glioblastome, avant implantation dans un cerveau non humain. Par « premier niveau » de sophistication, nous entendons qu'il n'y avait aucune zone analysée particulière définissant un système d'étude en elle-même, mais plutôt que nous avons comparé des informations de surface de composés de référence, seuls ou en mélange avant implantation. Ainsi, nous avons pu (i) cartographier la distribution des microcapsules de kétorolac trométhamine et de gomme gellane dans l'hydrogel HA par ToF-SIMS. Ceci est illustré dans la Figure 1 de ce résumé.

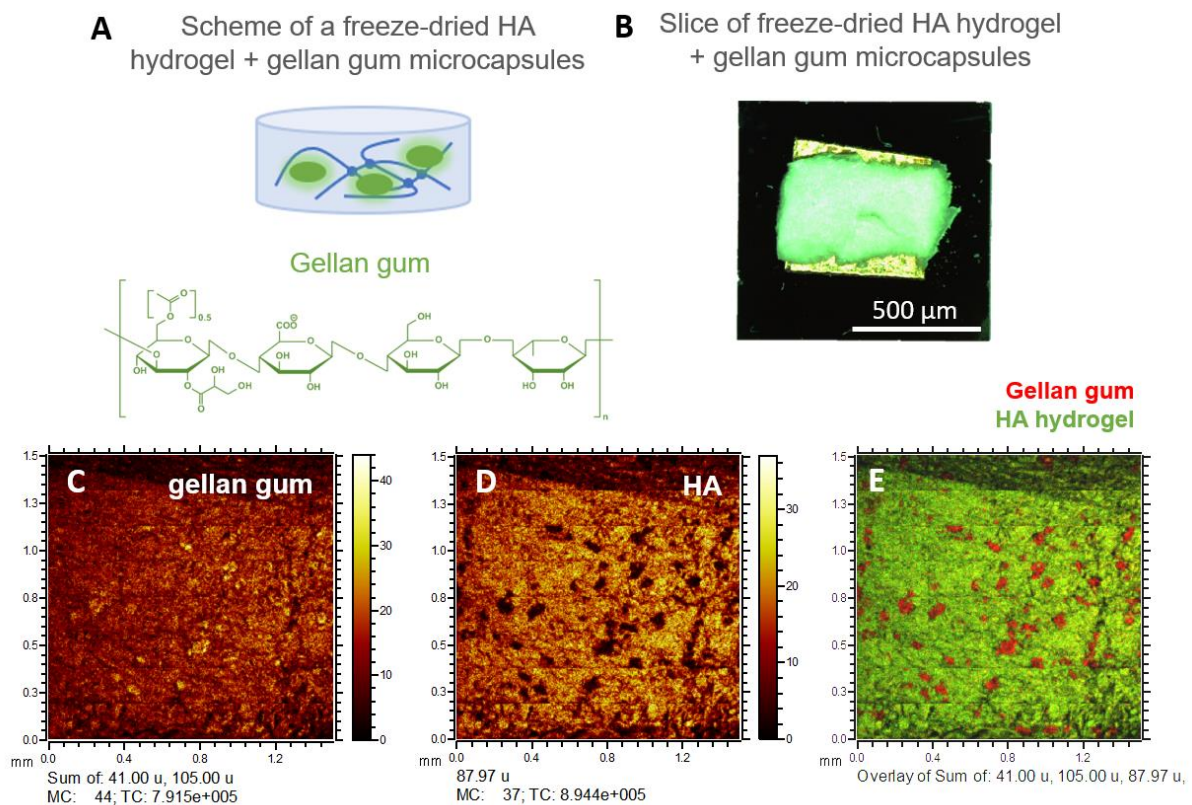


Figure 1. (A) Schéma de l'échantillon d'hydrogel HA contenant des microcapsules de gomme gellan. (B) Image optique des échantillons d'hydrogel HA contenant des microcapsules de gomme gellan déposées sur un substrat de silicium grâce à un ruban adhésif en cuivre. Image ToF-SIMS avec champ de vision de  $1500 \times 1500 \mu\text{m}^2$  (C) somme des signaux à  $m/z = 41.00$  et  $105.00$ , correspondant aux microcapsules, (D)  $m/z = 87.97$  correspondant à l'hydrogel HA, et (E) superposition de (C) en rouge et (D) en vert.

Les formulations d'hydrogel HA contenant 10 mg de kétorolac trométhamine présentent une répartition plus hétérogène que les formulations contenant 2 mg, indiquant la possibilité d'une ségrégation du kétorolac trométhamine dans le mélange. Nous avons pu également (ii) imager par AFM la morphologie fibrillaire de microcapsules de gomme gellane et enfin (iii) quantifier par XPS les environnements chimiques des microcapsules d'hydrogel HA, de kétorolac trométhamine et de gomme gellane, ainsi (iv) qu'observer l'effet de l'ajout de microcapsules de kétorolac trométhamine et de gomme gellane dans l'hydrogel HA, en termes d'environnements chimiques. Figure 2 présente les images AFM de la gomme gellan.

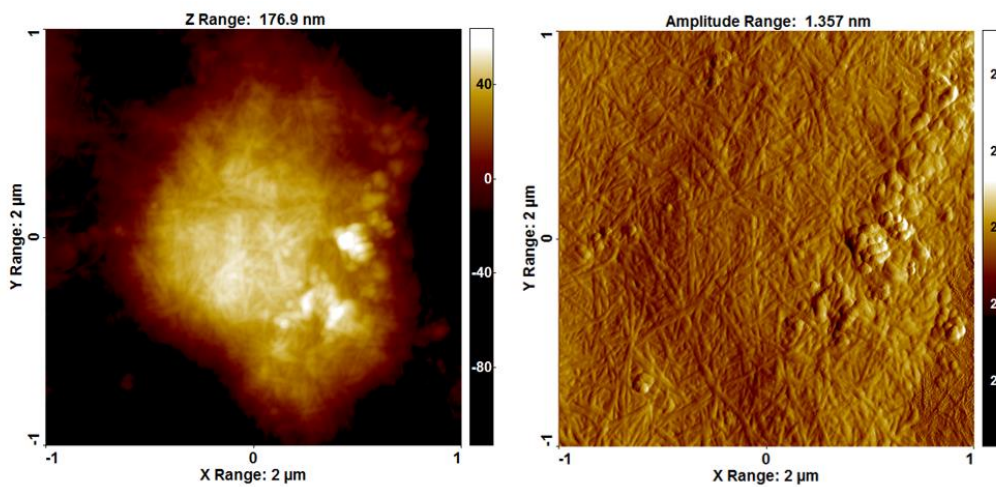


Figure 2. Images AFM de la surface d'une microcapsule de gomme gellan. À gauche, l'image de topographie et à droite l'image en mode erreur (image dérivée de l'image topographique) provenant de la même zone. Champ de vision de  $2 \times 2 \mu\text{m}^2$ .

Le chapitre 4 du manuscrit présente un niveau plus poussé de sophistication de notre étude (second niveau), consistant en l'analyse d'un unique et même échantillon, le composé bioorganique support qu'est le tissu O.C.T.<sup>TM</sup>, par différentes techniques, sondant deux régions d'analyse différentes. Dans cette partie, nous présentons (i) la cartographie de l'existence de deux zones de contraste chimique (S1- et S2-OCT) par ToF-SIMS. Ces deux zones de contraste chimique présentent toutes deux des fragments ioniques de composés organiques oxygénés, tandis que des fragments de phosphates et d'acides gras ou de sulfates et de chlorure de benzalkonium ont été observés respectivement dans la région S1-OCT et S2-OCT seulement. La cartographie ToF-SIMS de ces zones est présentée en Figure 3 de ce résumé.

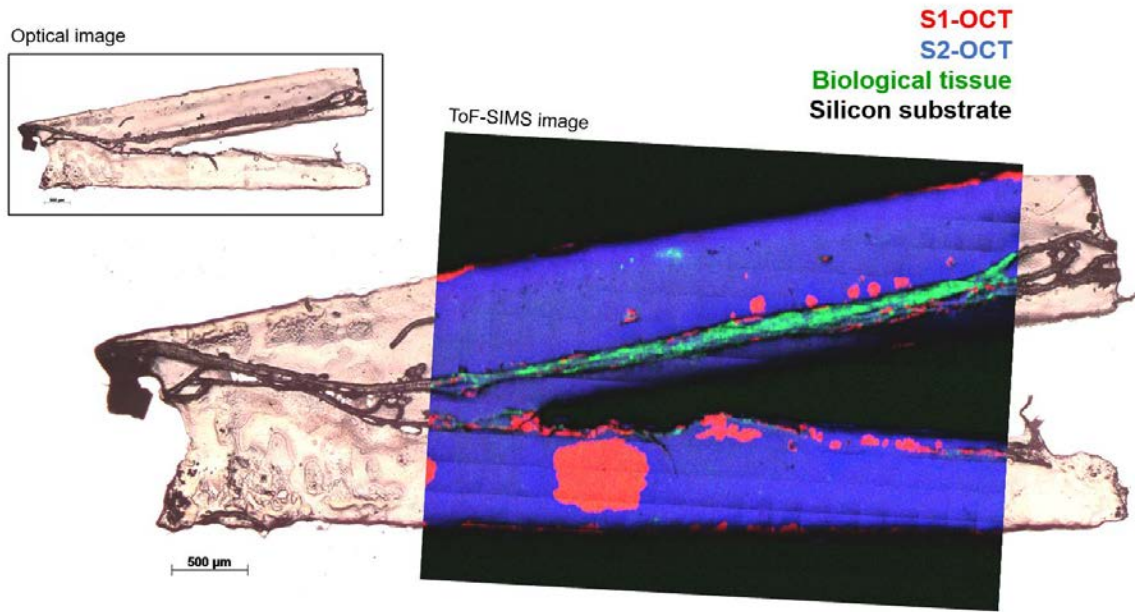


Figure 3. Image optique d'un tissu biologique en section transverse entouré de résine O.C.T.<sup>TM</sup> en image de fond avec superposition d'une image ToF-SIMS RGB. Vert =  $CNO^-$  ( $m/z = 41.99$ ) caractéristique du tissu biologique, rouge =  $C_2H_2O_2^-$  ( $m/z = 58.00$ ) caractéristique de la région S1-OCT et bleue =  $C_4H_5O^-$  ( $m/z = 69.03$ ) caractéristique de la région S2-OCT. Le champ de vision de l'image ToF-SIMS est de  $4 \times 3 \text{ mm}^2$  contenant 300 ( $20 \times 15$ ) tuiles de  $200 \mu\text{m}^2$ .

Nous avons également démontré dans ce chapitre (ii) la confirmation de l'existence d'acides gras dans la zone S1-OCT, sur la base de l'étude de la fragmentation ionique à  $m/z$  255.22, caractéristique de l'acide palmitique par spectrométrie Tandem MS. Nous présentons également (iii) le dosage quantitatif des environnements chimiques des régions S1- et S2-OCT par XPS. Les spectres de la Figure 4 de ce résumé illustrent ces mesures.

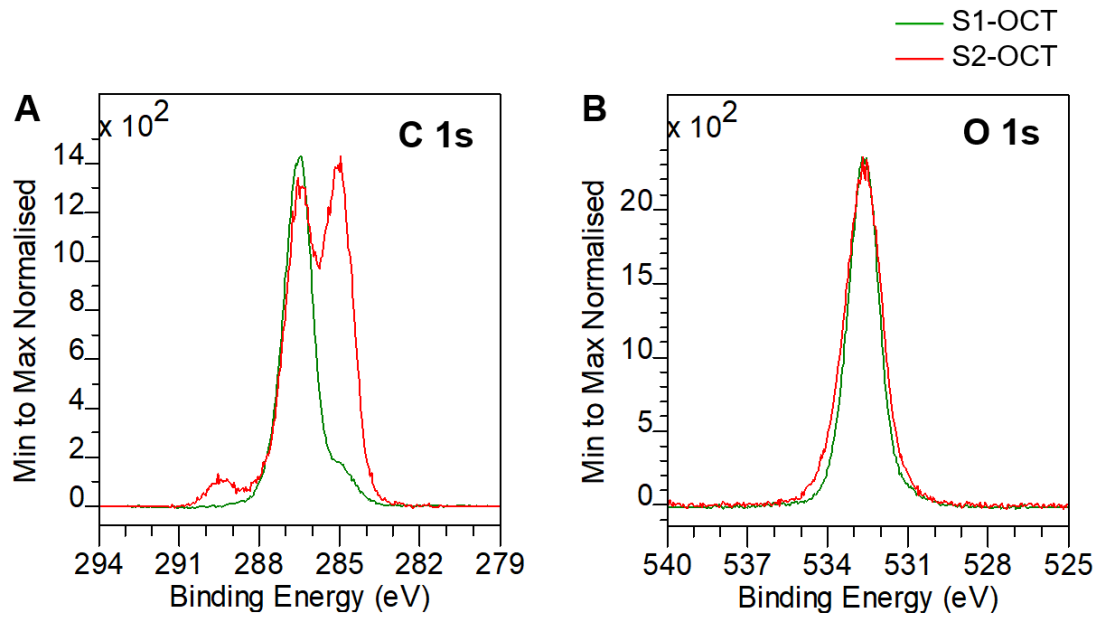


Figure 0. Spectres XPS à haute-résolution, normalisés au minimum et maximum des niveaux de coeur (A) C 1s et (B) O 1s. Les résultats des régions appelées S1-OCT (vert) et S2-OCT (rouge) sont superposés.

En accord avec les résultats de ToF-SIMS, nous avons trouvé dans la région S1-OCT des environnements chimiques caractéristiques du PEG (PolyEthylène Glycol) et des acides gras. Alors que dans la région S2-OCT, nous avons trouvé des environnements chimiques de PVA (Alcool PolyVinyle) et de chlorure de benzalkonium. Ceci indique une possible hétérogénéité dans la répartition de ces composés dans la composition de l'échantillon O.C.T.<sup>TM</sup>. Enfin, nous avons identifié par imagerie X-PEEM (iv) les environnements chimiques des régions S1- et S2-OCT, présentés en Figure 5.

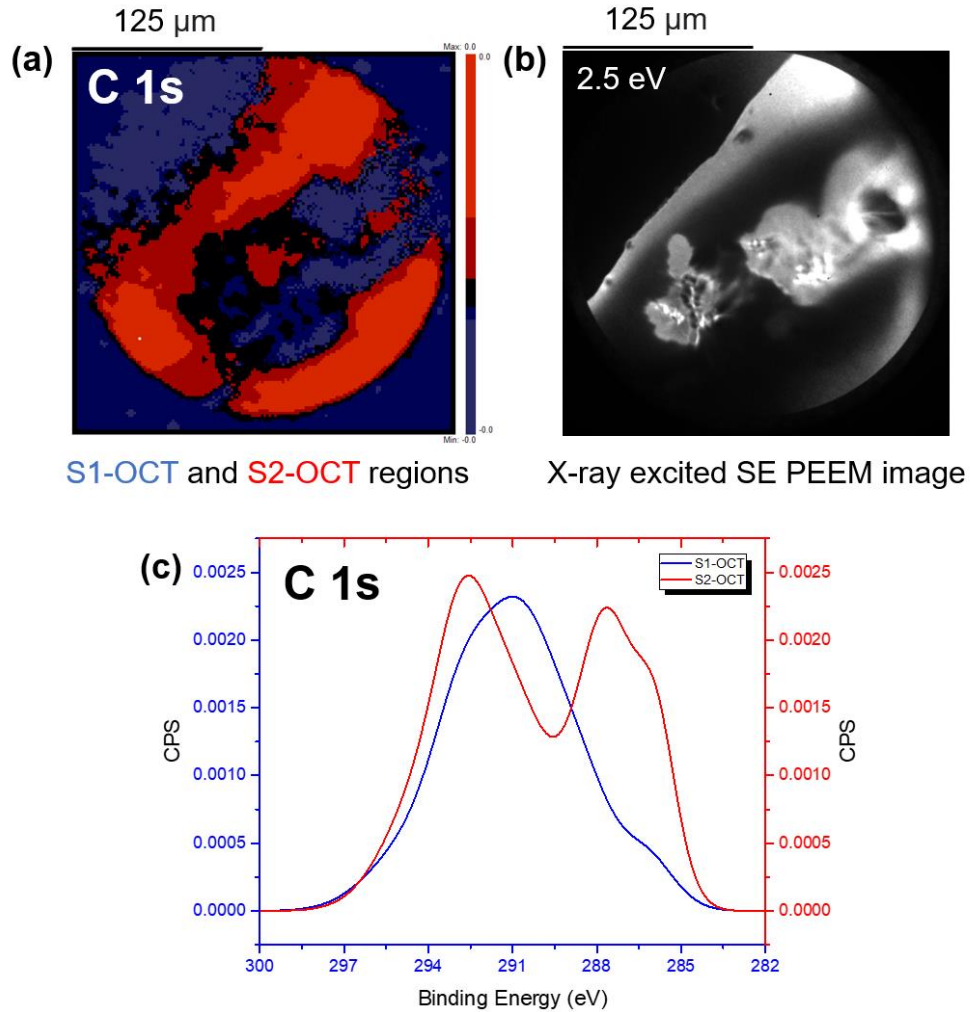


Figure 5. (a) Image X-PEEM qui illustre la répartition latérale, à l'échelle du micromètre, de l'intensité du signal du niveau de cœur C 1s. (b) Image PEEM des électrons secondaires générés par rayon X à l'énergie de  $E-E_F = 2.5$  eV. (c) Spectres superposés du niveau de cœur C 1s des régions S1-OCT (bleu) and S2-OCT (rouge).

À cause de la limitation du champ de vision par imagerie PEEM à 230  $\mu\text{m}$  de large environ, nous avons décidé de procéder à l'analyse d'une région plus petite de S1-OCT. Les spectres à haute résolution des niveaux de cœur ont malheureusement présenté des élargissements importants et des déplacements à plus hautes énergies de liaison, caractéristiques d'effets de charge probablement induits par une longue exposition aux rayons X de la zone d'intérêt. Cela a présenté une sérieuse complication pour décomposer les spectres des niveaux de cœur, et mettre en évidence les environnements chimiques présents dans ces régions. Néanmoins, malgré l'élargissement des pics, nous avons pu obtenir des spectres à haute résolution des niveaux de cœur du C 1s et O 1s de forme similaire à ceux obtenus par XPS.

Au troisième et dernier niveau de sophistication de notre étude, nous avons non seulement combiné les mesures sur un même échantillon, le tissu neuronal d'un rongeur ou d'un primate non humain, mais avons aussi corrélié les informations acquises à partir de l'analyse d'une même zone

d'intérêt, repérée spécifiquement dans le tissu neural d'un primate non humain (Chapitre 5). La Figure 6 présente les images ToF-SIMS d'une section de tissu biologique (cerveau) après implantation.

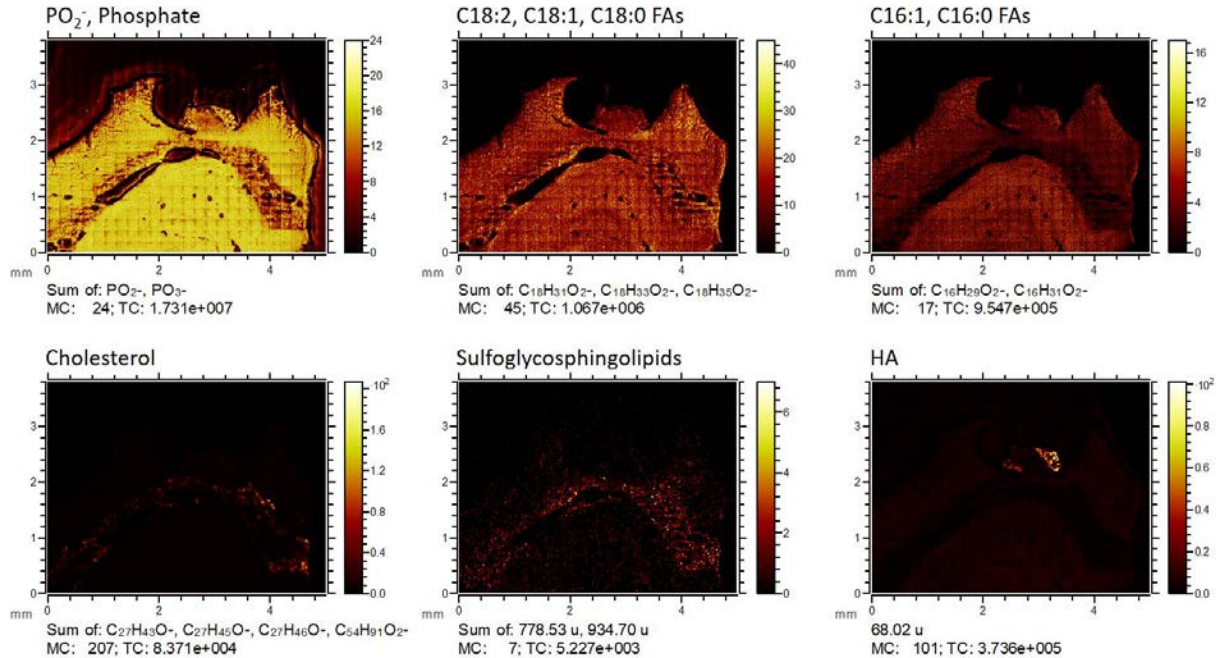


Figure 6. Images ToF-SIMS en mode négatif ( $5.0 \times 3.8 \mu\text{m}^2$ ) d'une coupe de tissu de cerveau après 3 mois d'implantation en présence des hydrogels. La répartition des espèces phosphate, acides gras, cholestérol et des sulfoglycosphingolipides est mise en évidence, en plus de la détection des résidus d'hydrogel HA.

Dans ce cas le plus poussé de la combinaison des informations chimiques obtenues dans notre travail, nous avons pu (i) vérifier l'existence de l'hydrogel HA en tant que véhicule d'administration de médicament dans le traitement du glioblastome, à l'intérieur de la zone chirurgicale du cerveau d'un rongeur, même après 3 mois d'implantation, (ii) ainsi qu'observer, par ToF-SIMS, une répartition anormale des phospholipides et des acides gras (région riche en MP, membrane plasmique) parmi les acides aminés et les protéoglycanes (région riche en MEC, matrice extra-cellulaire) dans un tissu cicatriciel glial formé autour d'un dispositif intracrânien implanté. Cette répartition anormale de phospholipides et d'acides gras peut être associée à la membrane plasmique de cellules « explosées » dans le tissu cicatriciel glial, indiquant ainsi qu'une partie de l'inflammation générée par l'implantation d'un dispositif intracrânien n'était pas réversible et que dans une partie de la cicatrice gliale, le tissu est devenu nécrotique. Nous avons pu également (iii) quantifier la composition de surface dans les régions riches en PM et ECM préalablement analysées par ToF-SIMS (Figure 7).

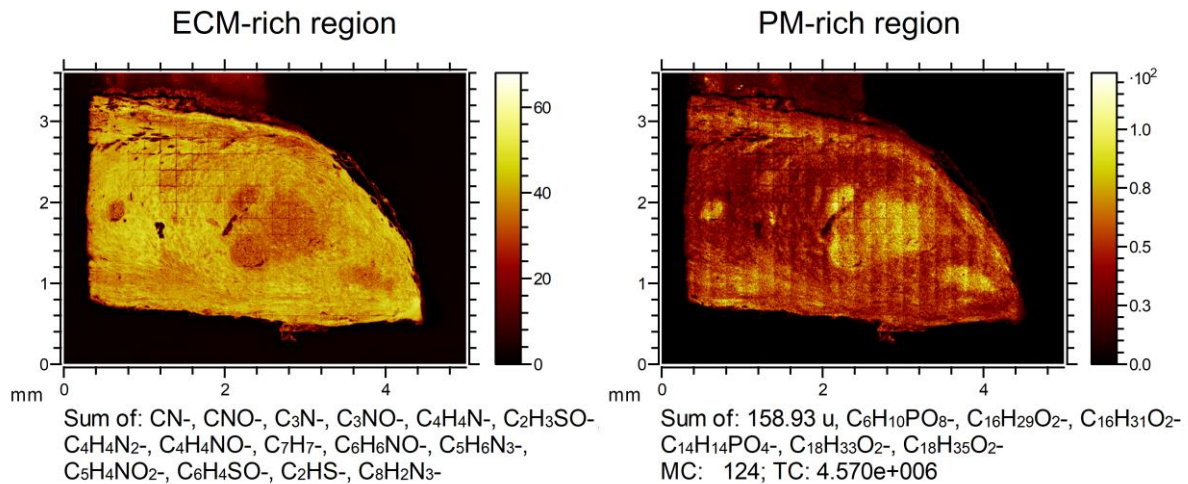


Figure 7. Images ToF-SIMS en mode négatif de la coupe SA18. À gauche, intensités totales des fragments caractéristiques des acides aminés, et à droite, intensités totales des fragments caractéristiques des phospholipides et des acides gras. Les images sont constituées de 468 (26 × 18) tuiles de 100 × 100 μm<sup>2</sup>.

Dans les régions riches en ECM, des espèces caractéristiques d'hydrocarbures, des espèces caractéristiques des fonctions esters, des amines, des amides et des carbonyles ont été trouvées en quantité cohérente avec les structures des acides aminés et des protéoglycane. Dans les régions riches en PM, en revanche, on a remarqué la présence supplémentaire d'environnements hydrocarbonés attribués aux grandes chaînes d'acides gras connectées aux phospholipides membranaires. Nous avons aussi obtenu (iii) des images des environnements chimiques présents dans le tissu cicatriciel glial à l'échelle du micromètre par X-PEEM. La région riche en PM et riche en ECM identifiée par ToF-SIMS n'a malheureusement pas pu être réanalysée par PEEM, en raison d'effets de charge excessifs générés par la tranche de l'échantillon, lors de l'exposition aux rayons X. Dans une nouvelle région du tissu cicatriciel glial, nous avons obtenu par PEEM un des spectres du niveau de cœur C 1s, à haute résolution en énergie, à partir desquels nous pouvons confirmer l'existence des mêmes environnements chimiques que ceux trouvés par XPS dans les régions riches en ECM. Les composants supplémentaires détectés dans le spectre C 1s X-PEEM pourraient être associés à un artefact chimique de cette région spécifique ou à l'élargissement du pic en raison d'effets de charge différentiels, déjà observés dans l'étude des échantillons du chapitre 4. Ces images sont présentées en Figure 8.

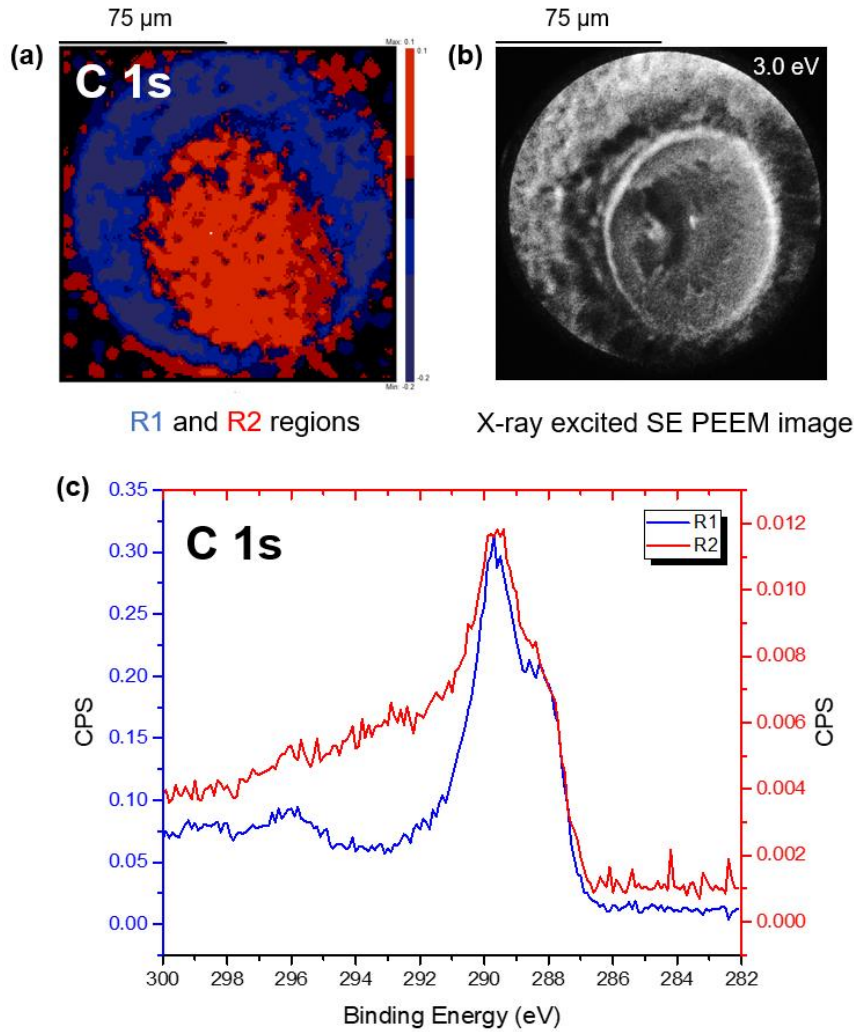


Figure 8. (a) Image X-PEEM de la répartition latérale, à l'échelle du micromètre, de l'intensité du spectre du niveau de cœur C 1s. (b) Image PEEM d'électrons secondaires générés par rayon X à l'énergie  $E-E_F = 3.0$  eV de la région d'intérêt (motif circulaire) dans la coupe SB22 du tissu glial. (c) Spectres du niveau de cœur C 1s des zones bleu (R1) et rouge (R2) superposés.

En termes de perspectives pour le futur, nous envisageons les axes de travail suivant :

- Travailler sur des coupes d'échantillon plus fines pour minimiser les effets de charge en PEEM.
- Améliorer les protocoles de repositionnement de l'échantillon entre techniques. Cela pourrait être réalisé à l'aide de gravure ionique par FIB ou d'autre type de repères.
- Pour l'étude des microcapsules de gomme gellan, il serait préférable de les étudier dans leur état hydraté. Avec les évolutions récentes de la technique AFM, cela est désormais possible mais pose des contraintes en termes de préparation d'échantillons et de possibilité de transfert vers les techniques d'UHV (besoin de cryogénie etc.).

Après avoir démontré la faisabilité d'imager chimiquement la répartition de ketorolac trométhamine dans un hydrogel, et la présence de l'hydrogel pur dans une coupe de cerveau, nous pourrions traiter la question de la répartition, dans une zone d'analyse, d'un médicament comme le ketorolac en

condition post-mortem, pour mieux comprendre les mécanismes de libération et d'absorption après implantation. Cette expérience était planifiée dans la thèse, mais la crise sanitaire a repoussé la préparation des échantillons et la mesure n'a pas pu être faite. Cependant les protocoles développés pendant ce travail de thèse devraient permettre de telles études dans un futur proche.



## RÉSUMÉ

---

Les propriétés interfaciales des dispositifs des technologies de la santé sont très importantes, car la plupart des réactions en biologie ont lieu aux interfaces. Alors que la médecine est engagée dans les technologies implantables, l'étude des interfaces devient de plus en plus importante pour l'innovation. Pour répondre à la complexité de la biologie en surfaces, des outils de caractérisation chimique de surfaces performantes sont nécessaires. L'objectif de cette thèse est de mettre en œuvre une approche d'imagerie chimique de surface multimodale qui utilise les techniques ToF-SIMS, Tandem MS, AFM, XPS et X-PEEM à trois niveaux de sophistication. Cette approche multimodale permet l'acquisition d'informations chimiques et morphologiques détaillées à partir d'interfaces biologiques telles que celles constituées par des tissus cérébraux non humains au contact de technologies implantées telles que les systèmes d'administration de médicaments utilisés dans le traitement du glioblastome et les dispositifs neuronaux utilisés comme interface cerveau-ordinateur.

## MOTS CLÉS

---

Technologies de la santé, approche multimodale, ACP, ToF-SIMS, Tandem MS, AFM, XPS et PEEM

## ABSTRACT

---

The interfacial properties of devices for healthcare technology are very important, because most reactions in biology take place at interfaces. As implantable technologies are developed for medical applications, the study of interfaces is becoming increasingly important for innovation. To adapt to the complexity of biology at surfaces, tools for the chemical characterization of high-performance surfaces are necessary. The objective of this thesis is to implement a multimodal chemical surface imaging approach that uses ToF-SIMS, Tandem MS, AFM, XPS and X-PEEM techniques at three levels of sophistication. This multimodal approach allows acquisition of detailed chemical and morphological information from biological interfaces such as those present in non-human brain tissue containing implanted technologies such as drug delivery systems used in the treatment of glioblastoma and neural devices used as a brain-computer interface.

## KEYWORDS

---

Healthcare technologies, multimodal approach, PCA, ToF-SIMS, Tandem MS, AFM, XPS and PEEM